PIV Investigation of Acoustic Transmission through Curved Duct Bends for the Optimisation of Thermoacoustic Systems

David Wee Shuon Tzern

THESIS SUBMITTED TO THE UNIVERSITY OF NOTTINGHAM

FOR THE DEGREE OF DOCTOR OF PHILOSOPHY

2013

Abstract

The efficiency of travelling wave thermoacoustic system, for a given operating temperature difference, is determined by the acoustic wave transmission through its feedback resonator loop system. Curved duct bends are one of the most repeated components used in the construct of these feedback resonator systems and thus require acoustic transmission optimisation.

This research investigates the transmission of low frequency, high amplitude acoustic waves propagating through duct bends with different radius of curvatures using Particle Image Velocimetry (PIV). The experimental PIV investigation was conducted on the axial plane of the bend. The velocity vector maps obtained from each run was analysed using both the newly developed Velocity based Wave Decomposition (VWD) technique as well as the Proper Orthogonal Decomposition (POD) technique. The POD technique was shown to successfully separate the different flow component of the acoustic wave in the respective Proper Orthogonal Modes (POMs). The acoustic transmission was thus computed based on the strength of these POMs. The POMs also allowed for the flow visualisation of the different loss mechanism that exists within the wave propagating through the bend (most notably, the energy cascade loss mechanism).

Based on the quantitative measurement of the acoustic transmission as well as the qualitative flow observation of the different loss mechanism, a non-dimensional parameter was developed in order to characterise the acoustic transmission through curved duct bend systems. This parameter is known as the Strouhal-Dean number. Based on this parameter, the acoustic transmission can be characterised into 3 acoustic flow regimes: Viscous dominated oscillation, Inertia dominated oscillation and the Transition regime between the first two oscillation regimes. The optimum acoustic transmission range corresponded to the transition regime where the inertia generated secondary circulation was balanced by its viscous loss suppression. The optimal Strouhal Dean number for acoustic transmission was found to be approximately 10.8.

Acknowledgement

You'll meet more angels on a winding path than on a straight one.

- Terri Guillements

This PhD has not only been a journey of intellectual research but also one of self-discovery. My best and worst moments in this journey were shared with many people. I would thus like to express my sincerest gratitude to those that have given me this experience of a life time.

To my supervisors, Dr Yousif Abdalla Abakr and Dr David Brian Hann, my deepest gratitude for their inspirations to take on this research, their guidance and motivation to persist through, and their support to complete it. Their thought provoking ideas and continuous intellectual challenges have been of tremendous help towards my personal and professional development, and their "trial by fire" supervision technique has taught me resilience and independence.

To Mr Paul Riley, the SCORE-UK project director, for sharing his technical knowledge as well as his life experiences. His mentorship has taught me to view the world from a whole new perspective.

To the University of Nottingham, for the MIDAS research scholarship that has made all this possible.

To the friendliest post doctorates, Chitta Saha, Tim Jukes and Faycal Bahri, for their counsel, advice in conducting experiments and assistance with the PIV system.

To my fellow PhD mates from NB04 and L4, who are responsible for keeping my sanity intact. Their companionship has indeed made this journey a very colourful one.

To my friends, for their patience, encouragement and reminder, that there is still life outside of research.

To my family, for their love and unyielding support, especially:

My father, for his kind reminder: not to take life too seriously;
and, my mother, for the arduous task of proof reading this thesis.

To Jacinta, for teaching me the most valuable lesson of appreciation.

For from Him and through Him and to Him are all things. To Him be the glory forever

Thank you.

Table of Contents

Table of Contents

List of Figures

List of Figures

List of Figures

List of Figures

List of Figures

List of Tables

List of Equations, Abbreviations and Symbols

Chapter 1

Thermoacoustics

$$\delta_{thermal\ penetration} = \sqrt{\frac{2k}{\omega \rho c_p}} \tag{1.1}$$

$$\mathrm{N}_L = \frac{r_h}{\delta_{thermal\ penetration}} \tag{1.2}$$

$$\Delta \mathrm{T}_{crit} = \frac{\omega\ A\ p}{\rho_m\ c_p\ u} \tag{1.3}$$

$$\Delta \mathrm{T} > \Delta \mathrm{T}_{onset} > \Delta \mathrm{T}_{crit} \tag{1.4}$$

$$r_h = \frac{V_{working\ fluid}}{A_{wetted}} \tag{1.5}$$

$$Z_{\ travelling\ wave} = \frac{p}{U} = \frac{\rho_m c}{A} \tag{1.6}$$

$$Z_{\ regenerator} = \frac{p}{U} \gg \frac{\rho_m c}{A} \tag{1.7}$$

Symbol and abbreviation	*Description*	*Units*
$\delta_{thermal\ penetration}$	Thermal penetration depth	(m)
k	Thermal Conduction Coefficient	(W $m^{-1}K^{-1}$)
ω	Angular Frequency	(s^{-1})
ρ , ρ_m	Fluid density	(kg m^{-3})
c_p	Specific Heat Capacity	(J kg^{-1} K^{-1})
N_L	Laucret Number	(dimensionless)
r_h	Hydraulic Radius	(m)
T_{crit}	Critical Temperature	(K)
T_{onset}	Onset Temperature	(K)
A	Cross Sectional Area	(m^2)
A_{wetted}	Wetted Area	(m^2)
p	Pressure	(kg $m^{-1}s^{-2}$)
u	Velocity	(ms^{-1})

$V_{working\ fluid}$	Volumetric Flow Rate	($m^3\ s^{-1}$)
Z	Acoustic Impedance	(kg $m^{-2}\ s^{-1}$)
$Z_{\ travelling\ wave}$	Travelling Wave Impedance	(kg $m^{-2}\ s^{-1}$)
$Z_{\ regenerator}$	Impedance of Regenerator	(kg $m^{-2}\ s^{-1}$)
c	Speed of sound	(m s^{-1})

Literature of acoustic wave propagating through curved duct bend systems

$$\mathrm{De} = \left(\frac{ur}{\nu}\right)\left(\frac{r}{\mathrm{R}}\right)^{\frac{1}{2}} \tag{1.8}$$

$$\alpha = \frac{\sqrt{2}\ r}{\delta_{viscous\ penetration}} = \mathrm{r}\left(\frac{\omega}{\nu}\right)^{\frac{1}{2}} \tag{1.9}$$

$$\frac{\partial u}{\partial t} + u\frac{\partial u}{\partial r} + \frac{w}{r+R}\left(\frac{\partial w}{\partial \theta} - w\right) = -\frac{1}{\rho}\frac{\partial p}{\partial r} + \upsilon f_{\upsilon} \tag{1.10}$$

$$\frac{\partial u}{\partial t} + u\frac{\partial u}{\partial r} - \frac{w^2}{r+R} \approx -\frac{1}{\rho}\frac{\partial p}{\partial r} \tag{1.11}$$

Symbol and abbreviation	*Description*	*Units*
De	Dean Number	(dimensionless)
α	Womersley Number	(m)
r	Hydraulic Radius	(m)
u	Axial Free Stream Velocity Amplitude	(m s^{-1})
ν	Kinematic Viscosity	($m^2\ s^{-1}$)
$\delta_{viscous\ penetration}$	Viscous Penetration Depth	(m)
ω	Angular Frequency	(s^{-1})

Chapter 2

Acoustic Wave Measurement and Analytical Techniques

Acoustic Impedance

$$Z = \frac{p}{U} \tag{1.12}$$

Standing Wave Ratio

$$SWR = \frac{A + B}{A - B} \tag{1.13}$$

Cut-off frequency for plane wave mode of propagation

For circular duct:

$$f_c = \zeta_0 \frac{c}{\pi d} \tag{1.14}$$

For square duct:

$$f_c = \frac{c}{2d} \tag{1.15}$$

Transfer Matrix

$$\begin{bmatrix} p_{output} \\ U_{output} \end{bmatrix} = \begin{bmatrix} T_{11} & T_{12} \\ T_{21} & T_{22} \end{bmatrix} \begin{bmatrix} p_{input} \\ U_{input} \end{bmatrix} \tag{1.16}$$

Mobility Matrix

$$\begin{bmatrix} p_{input} \\ p_{output} \end{bmatrix} = \begin{bmatrix} Z_{11} & Z_{12} \\ Z_{21} & Z_{22} \end{bmatrix} \begin{bmatrix} U_{input} \\ U_{output} \end{bmatrix} \tag{1.17}$$

Scattering Matrix

$$\begin{bmatrix} p_{incident,downstream} \\ p_{reflected,upstream} \end{bmatrix} = \begin{bmatrix} T_i & R_r \\ R_i & T_r \end{bmatrix} \begin{bmatrix} p_{incident,upstream} \\ p_{reflected,downstream} \end{bmatrix} \tag{1.18}$$

$$\widetilde{p_1}(x_1, t) = \tilde{a}(t) e^{i(\omega t - k_i x_1)} + \tilde{b}(t) e^{i(\omega t + k_r x_1)} \tag{1.19}$$

$$\widetilde{p_2}(x_1, t) = \tilde{a}(t) e^{i(\omega t - k_i x_2)} + \tilde{b}(t) e^{i(\omega t + k_r x_2)} \tag{1.20}$$

$$\begin{bmatrix} S_{PAA} \\ S_{PBB} \\ C_{PAB} \\ Q_{PAB} \end{bmatrix} = [TM_P]^{-1} \begin{bmatrix} S_{P11} \\ S_{P22} \\ C_{P12} \\ Q_{P12} \end{bmatrix} \tag{1.21}$$

$$S_{AB}(f) = C_{AB}(f) + j\, Q_{AB}(f) \tag{1.22}$$

$$S_{12}(f) = C_{12}(f) + j\, Q_{12}(f) \tag{1.23}$$

Inverse of Scatteing Matrix

$$\delta \begin{bmatrix} 1 & 1 & -2\cos k_r(x_1 - x_2) & 2\sin k_r(x_1 - x_2) \\ 1 & 1 & -2\cos k_i(x_1 - x_2) & -2\sin k_i(x_1 - x_2) \\ -\cos(k_i + k_r)x_2 & -\cos(k_i + k_r)x_1 & \cos(k_r x_1 + k_i x_2) + \cos(k_i x_1 + k_r x_2) & \sin(k_i x_1 + k_r x_2) - \sin(k_r x_1 + k_i x_2) \\ -\sin(k_i + k_r)\, x_2 & -\sin(k_i + k_r)\, x_1 & \sin(k_r x_1 + k_i x_2) + \sin(k_i x_1 + k_r x_2) & \cos(k_r x_1 + k_i x_2) - \cos(k_i x_1 + k_r x_2) \end{bmatrix}$$

$$\delta = \frac{1}{4}\sin^2\left[\frac{1}{2}(k_i + k_r)(x_1 - x_2)\right] \quad (1.24)$$

Wave Number

$$k_i = \frac{2\pi f}{c(1+M)} \text{ and } k_r = \frac{2\pi f}{c(1-M)} \quad (1.25)$$

$$R_{mech} = \frac{m\omega_n}{Q_{mech}} \quad (1.26)$$

$$\Omega_{min} = -0.0011f^2 + 0.0933f + 3.3021 \quad (1.27)$$

$$\phi = \tau + \pi \quad (1.28)$$

$$\phi = -9.01f + 792.48 \quad (1.29)$$

$$T_c = \frac{p_T}{p_a} \quad (1.30)$$

$$\begin{bmatrix} p_c \\ p_b \end{bmatrix} = \begin{bmatrix} T_f & R_b \\ R_f & T_b \end{bmatrix} \begin{bmatrix} p_a \\ p_d \end{bmatrix} \quad (1.31)$$

$$T_f = T_b = T = |T|e^{i\Phi_T}$$

$$R_f = R_b = R = |R|e^{i\Phi_R} \quad (1.32)$$

$$\xi_{ac} = \frac{P_a}{2\pi f \cdot \rho c} \quad (1.33)$$

Symbol and abbreviation	*Description*	*Units*
p	Pressure	(kg $m^{-1}s^{-2}$)
U	Volumetric Velocity	(m^3 s^{-1})
$Z_{1,1}, Z_{1,2,}\ Z_{2,1}, Z_{2,2}$	Coefficient of Mobility Matrix	(dimensionless)
$T_{1,1}, T_{1,2,}\ T_{2,1}, T_{2,2}$	Coefficient of Transfer Matrix	(dimensionless)
ζ_0	Zeroth Order Bessel function of the first kind	(dimensionless)
c	Speed of sound	(ms^{-1})
d	Hydraulic diameter	(m)
T_i	Scattering Matrix Incident Transmitted Coefficient	(dimensionless)
T_r	Scattering Matrix ReflectedTransmitted Coefficient	(dimensionless)
R_i	Scattering Matrix Incident Reflected Coefficient	(dimensionless)
R_r	Scattering Matrix Reflected Reflected Coefficient	(dimensionless)
$\tilde{p}$	Complex pressure component	(kg $m^{-1}s^{-2}$)
$\tilde{a}$	Amplitude of Incident complex pressure component	(kg $m^{-1}s^{-2}$)

$\tilde{b}$	Amplitude of Reflected complex pressure component	(kg $m^{-1}s^{-2}$)
x	Axial distance	(m)
t	Time Component	(s)
ω	Angular Frequency	(s^{-1})
k	Wave Number	(m^{-1})
S_{PXX}	Auto Power Spectral Density of Pressure X	(kg m^2s^{-3})
C_{PXY}	Real Component of the Cross Power Spectral Density between Pressure X and Y	(kg m^2s^{-3})
Q_{PXY}	Imaginary Component of the Cross Power Spectral Density between Pressure X and Y	(kg m^2s^{-3})
R_{mech}	Mechanical Stiffness of the Speakers diaphragm suspension	(kg m^2s^{-1})
Q_{mech}	Mechanical Quality property of Speaker	(dimensionless)
m	Mass of the speaker's diaphragm	(kg)
Ω_{min}	Resistive Load value giving the lowest attainable SWR value for the investigate frequency	(Ohms)
f	frequency	(s^{-1})
ϕ	Phase difference	(radians)
τ	Time it takes for signal to travel between source and termination	(s)
ξ_{ac}	Acoustic Displacement Amplitude	(m)

Chapter 3

Particle Image Velocimetry

$$g(m,n) = [f(m,n) * s(m,n)] + d(m,n) \quad (1.34)$$

$$\phi_{fg}(m,n) = E[f(m,n)\,, g(m,n)] \quad (1.35)$$

$$\phi_{fg}(m,n) = E[f(m,n)\,, [f(m,n) * s(m,n)] + d(m,n)] \quad (1.36)$$

$$\phi_{fg}{}'(m,n) = E[f(m,n)\,, f(m,n) * s(m,n)]$$

$$= \phi_{ff(m,n)} * s(m,n) \quad (1.37)$$

$$\Phi'(u,v) = F(u,v) \cdot G(u,v) \quad (1.38)$$

$$f'(x,y) = \phi'(m,n) \cdot h(x,y) \quad (1.39)$$

$$d_p = 0.34\left(\frac{8\pi\sigma}{\rho f^2}\right)^{\frac{1}{3}} \quad (1.40)$$

Symbol and abbreviation	*Description*	*Units*
$g(m,n)$	Output Image Function	-
$f(m,n)$	Input Image Function	-
$s(m,n)$	Transfer Function	-
$d(m,n)$	Noise Function	-
$\phi_{fg}(m,n) =$	Cross-correlation Function	-
d_p	Mean Seeding Particle Size	(m)

Chapter 4

Velocity based Wave Decomposition Technique

$$\tilde{p}(x,t) = \tilde{p_i}(x,t) + \tilde{p_r}(x,t) \tag{1.41}$$

$$\tilde{\boldsymbol{v}}(x,t) = \tilde{\boldsymbol{v_i}}(x,t) - \tilde{\boldsymbol{v_r}}(x,t) \tag{1.42}$$

$$\tilde{\boldsymbol{v_i}}(x,t) = \tilde{a}(t)e^{i\omega t - ik_i x} \tag{1.43}$$

$$\tilde{\boldsymbol{v_r}}(x,t) = \tilde{b}(t)e^{i\omega t + ik_r x} \tag{1.44}$$

$$\begin{bmatrix} S_{V11} \\ S_{V22} \\ C_{V12} \\ Q_{V12} \end{bmatrix} = [TM_v] \begin{bmatrix} S_{VAA} \\ S_{VBB} \\ C_{VAB} \\ Q_{VAB} \end{bmatrix} \tag{1.45}$$

$$\begin{bmatrix} 1 & 1 & -2\cos[(k_i + k_r)x_1] & -2\sin[(k_i + k_r)\,x_1] \\ 1 & 1 & -2\cos[(k_i + k_r)x_2] & -2\sin[(k_i + k_r)\,x_2] \\ \cos[k_i(x_1 - x_2)] & \cos[k_r(x_1 - x_2)] & -\cos[k_i x_1 + k_r x_2] - \cos[k_r x_1 + k_i x_2] & -\sin(k_i x_2 + k_r x_1) - \sin\left(k_r x_2 + k_i x_1\right) \\ \sin[k_i(x_1 - x_2)] & \sin\left(k_r\left(x_1 - x_2\right)\right) & -\sin(k_i x_1 + k_r x_2) + \sin(k_r x_1 + k_i x_2) & -\cos[k_r x_1 + k_i x_2] + \cos[k_i x_1 + k_r x_2] \end{bmatrix} \tag{1.46}$$

$$S_{VAA} = \frac{S_{V11} + S_{V22} - 2C_{V12}\cos k(x_1 - x_2) + 2Q_{V12}\sin k(x_1 - x_2)}{4\sin^2 k(x_1 - x_2)} \tag{1.47}$$

$$S_{VBB} = \frac{S_{V11} + S_{V22} - 2C_{V12}\cos k(x_1 - x_2) - 2Q_{V12}\sin k(x_1 - x_2)}{4\sin^2 k(x_1 - x_2)} \tag{1.48}$$

$$C_{VAB} = \frac{S_{V11}\cos 2kx_2 + S_{V22}\cos 2kx_1 - 2C_{V12}\cos k(x_1 + x_2)}{4\sin^2 k(x_1 - x_2)} \tag{1.49}$$

$$Q_{VAB} = \frac{S_{V11}\sin 2kx_2 + S_{V22}\sin 2kx_1 - 2C_{V12}\sin k(x_1 + x_2)}{4\sin^2 k(x_1 - x_2)} \tag{1.50}$$

$$S_{PU}(f,x) = \rho c[S_{AA}(f) - S_{BB}(f) - 2iQ_{AB}(f)] \tag{1.51}$$

$$S_{UU}(f,x) = S_{AA}(f) + S_{BB}(f) - 2C_{AB}(f) \tag{1.52}$$

$$\frac{Z(f,x)}{\rho c} = \frac{S_{PU}(f,x)}{S_{UU}(f,x)} = \frac{S_{AA}(f) - S_{BB}(f)}{S_{AA}(f) + S_{BB}(f) - 2C_{AB}(f)} + i\frac{-2\,Q_{AB}(f)}{S_{AA}(f) + S_{BB}(f) - 2C_{AB}(f)} \tag{1.53}$$

$$\theta_{AB} = tan^{-1}\left(\frac{Q_{AB}}{C_{AB}}\right) \tag{1.54}$$

$$\tilde{p}(x,t) = \left[A_1 e^{i\omega_1 t - ikx} + B_1 e^{i\omega_1 t + ikx}\right] + \left[A_2 e^{i\omega_2 t - ikx} + B_2 e^{i\omega_2 t + ikx}\right] \tag{1.55}$$

$$\tilde{v}(x,t) = \frac{1}{\rho c}\left(\left[A_1 e^{i\omega_1 t - ikx} - B_1 e^{i\omega_1 t + ikx}\right] + \left[A_2 e^{i\omega_2 t - ikx} + B_2 e^{i\omega_2 t + ikx}\right]\right) \tag{1.56}$$

$$f_c = \frac{j_0' c_0}{2\pi r} \tag{1.57}$$

$$SWR = \frac{A + B}{A - B} \tag{1.58}$$

$$t_{res} = \frac{(\varepsilon - 1){d_p}^2}{18\upsilon} \tag{1.59}$$

$$Z = R + i\omega L - \frac{1}{i\omega C} \tag{1.60}$$

$$\alpha_{approx} = \frac{1}{2}\left[\frac{r_m\, k\, \omega\ t_{res}}{1 + (\omega\, t_{res})^2}\right] \tag{1.61}$$

$$\tilde{v}(x,t) = \frac{1}{\rho c}\left(\left[A_1 e^{i\omega_1 t - ikx} - B_1 e^{i\omega_1 t + ikx}\right] \times \left[e^{-\alpha_{approx}\, x}\right]\right) \tag{1.62}$$

$$Max\ Percentage\ Error = 34.61 \times e^{-0.133(S/N)} \tag{1.63}$$

Symbol and abbreviation	*Description*	*Units*
$\tilde{p}$	Complex Presssure Component	(kg $m^{-1}s^{-2}$)
$\widetilde{p_i}$	Incident Pressure Component	(kg $m^{-1}s^{-2}$)
$\widetilde{p_r}$	Reflected Pressure Component	(kg $m^{-1}s^{-2}$)
$\tilde{v}$	Complex VelocityComponent	(m s^{-1})
$\widetilde{v_i}$	Incident VelocityComponent	(m s^{-1})
$\widetilde{v_r}$	Reflected VelocityComponent	(m s^{-1})

S_{PXX}	Auto Power Spectral Density of Pressure X	(kg m^2s^{-3})
C_{PXY}	Real Component of the Cross Spectral Density between Pressure X and Y	(kg m^2s^{-3})
Q_{PXY}	Imaginary Component of the Cross Spectral Density between Pressure X and Y	(kg m^2s^{-3})
j_0'	the first non-negative zero of the ordinary Bessel function of the first kind	(dimensionless)
c	Speed of sound	(m s^{-1})
k	Wave Number	(m^{-1})
x	Axial Distance	(m)
A	Incident Wave Amplitude Component	(value dependent)
B	Reflected Wave Amplitude Component	(value dependent)
SWR	Standing Wave Ratio	(dimensionless)
t_{res}	Seeding particle response time	(s)
ε	Ratio between particle and fluid density	(dimensionless)
d_p	Average seeding particle diameter	(m)
υ	Kinematic Viscousity of the fluid medium	(m^2 s^{-1})
Z	Complex Acoustic Impedance	(kg m^{-2} s^{-1})
R	Resistive Component of the Acoustic Impedance	(kg m^{-2} s^{-1})
L	Inductive Reactance Component of the Acoustic Impedance	(kg m^{-2} s^{-1})
C	Capacitive Reactance Component of the Acoustic Impedance	(kg m^{-2} s^{-1})
α_{approx}	Attenuation Coefficient Approximation	(m^{-1})
r_m	Ratio of total mass of seeding particles per unit volume of the acoustic medium	(kg m^{-3})
ω	Angular Frequency	(s^{-1})
(S/N)	Signal to Noise Ratio	(dimensionless)

Chapter 5

Proper Orthogonal Decomposition Technique

$$\vec{\mathbf{u}}(\boldsymbol{x},\boldsymbol{y},\boldsymbol{t}) = \sum_{i=1}^{T_N} a_i(t)\phi_i(x,y) \tag{1.64}$$

$$\overrightarrow{\mathbf{Vel}} = \begin{bmatrix} u_{1,1,1} & \cdots & u_{1,1,T_N} \\ v_{1,1,1} & \cdots & v_{1,1,T_N} \\ u_{2,1,1} & \cdots & u_{2,1,T_N} \\ v_{2,1,1} & \cdots & v_{2,1,T_N} \\ \vdots & \ddots & \vdots \\ u_{x_N,y_N} & \cdots & u_{x_N,y_N,T_N} \\ v_{x_N,y_N} & \cdots & v_{x_N,y_N,T_N} \end{bmatrix} \tag{1.65}$$

$$\boldsymbol{C}\mathbf{A}^{\boldsymbol{i}} = \boldsymbol{\lambda}^{\boldsymbol{i}}\mathbf{A}^{\boldsymbol{i}} \tag{1.66}$$

$$\mathbf{C}_{topos} = \overrightarrow{\mathbf{Vel}} \cdot \overrightarrow{\mathbf{Vel}}^{\mathbf{T}} \tag{1.67}$$

$$\mathbf{C}_{chronos} = \overrightarrow{\mathbf{Vel}}^{\mathbf{T}} \cdot \overrightarrow{\mathbf{Vel}}. \tag{1.68}$$

$$\lambda^i = \sum_{l=1}^{T_N}\sum_{n=1}^{x_N}\sum_{m=1}^{y_N} [\, a_i(t_l)\phi_i(x_n, y_m)\,]^2 \tag{1.69}$$

$$\phi^i = \frac{\sum_{n=1}^{N} A_n^i u^n}{\left\|\sum_{n=1}^{N} A_n^i u^n\right\|} \tag{1.70}$$

$$\mathrm{a}^{\boldsymbol{i}} = \phi^i u^n \tag{1.71}$$

$$\boldsymbol{i^{th}}\ \mathbf{POM} = a_i(t)\phi_i(x,y) \tag{1.72}$$

$$\overrightarrow{\mathbf{Vel}} = \mathbf{U\Sigma V}^{\boldsymbol{T}} \tag{1.73}$$

$$\begin{bmatrix} \overrightarrow{\mathbf{Vel}} \\ ([x_{N\times}y_N]\ \mathrm{x}\ T_N) \end{bmatrix} = \begin{bmatrix} \mathbf{U} \\ Topos\ matrix \\ ([x_{N\times}y_N]\ \mathrm{x}\ [x_{N\times}y_N]) \end{bmatrix} \begin{bmatrix} \mathbf{\Sigma} \\ diagonal\ matrix \\ ([x_{N\times}y_N]\ \mathrm{x}\ T_N) \end{bmatrix} \begin{bmatrix} \mathbf{V}^{\boldsymbol{T}} \\ Chronos\ Matrix \\ (T_N\ \mathrm{x}\ T_N) \end{bmatrix} \tag{1.74}$$

$$\overrightarrow{\mathbf{Vel}}\ \overrightarrow{\mathbf{Vel}}^{\mathbf{T}} = \mathbf{C}_{topos} = \mathbf{U\Sigma^2 U}^{\boldsymbol{T}} \tag{1.75}$$

$$\overrightarrow{\mathbf{Vel}}^{\mathbf{T}}\ \overrightarrow{\mathbf{Vel}} = \mathbf{C}_{chronos} = \mathbf{V\Sigma^2 V}^{\boldsymbol{T}} \tag{1.76}$$

$$\begin{aligned} \mathbf{C}_{topos} &= \mathbf{U}\,\mathbf{\Sigma^2}\,\mathbf{U^{-1}} \\ \mathbf{C}_{topos}\,\mathbf{U} &= \mathbf{U}\,\mathbf{\Sigma^2} \end{aligned} \tag{1.77}$$

$$\mathbf{C}_{chronos}\,\mathbf{V} = \mathbf{V}\,\boldsymbol{\Sigma}^{\mathbf{2}} \tag{1.78}$$

$$\lambda_i = \sqrt{\sigma_i} \tag{1.79}$$

$$\begin{aligned}\overrightarrow{\mathrm{Vel}} &= \mathrm{u}_1\sigma_1\mathrm{v}^T{}_1 + \mathrm{u}_2\sigma_2\mathrm{v}^T{}_2 + \cdots + \mathrm{u}_{T_N}\sigma_{T_N}\mathrm{v}^T{}_{T_N} \\ &= \sum_{i=1}^{T_N} \mathrm{u}_i\sigma_i\mathrm{v}^T{}_i\end{aligned} \tag{1.80}$$

$$i^{th}\ \mathrm{Mode} = \mathrm{u}_i\sigma_i\mathrm{v}^T{}_i = \begin{bmatrix} u_{1,1,1}{}^{i} & \cdots & u_{1,1,T_N}{}^{i} \\ v_{1,1,1}{}^{i} & \cdots & v_{1,1,T_N}{}^{i} \\ u_{2,1,1}{}^{i} & \cdots & u_{2,1,T_N}{}^{i} \\ v_{2,1,1}{}^{i} & \cdots & v_{2,1,T_N}{}^{i} \\ \vdots & \ddots & \vdots \\ u_{x_N,y_N}{}^{i} & \cdots & u_{x_N,y_N,T_N}{}^{i} \\ v_{x_N,y_N}{}^{i} & \cdots & v_{x_N,y_N,T_N}{}^{i} \end{bmatrix} \tag{1.81}$$

Symbol and abbreviation	*Description*	*Units*
$a_i(t)$	Temporal Coefficient	-
$\phi_i(x,y)$	Spatial Orthogonal Basis Function	-
$\overrightarrow{\mathbf{Vel}}$	Velocity Vector Response Matrix	-
$\mathbf{A}^{\boldsymbol{i}}$	Eigenvalue Matrix	-
$\boldsymbol{\lambda}^{\boldsymbol{i}}$	Diagonal Eigenvalue Matrix	-
$\mathbf{C}_{topos}$	Cross Correlation Matrix (against space)	-
$\mathbf{C}_{chronos}$	Cross Correlation Matrix (against time)	-
$\mathbf{U}$	Topos Matrix	-
$\boldsymbol{\Sigma}$	Diagonal Matrix	-
$\mathbf{V}^{\boldsymbol{T}}$	Chronos Matrix	-

Chapter 6

Analysis of the Proper Orthogonal Decomposition Technique

$$\lambda^i = \sum_{l=1}^{T_N} \sum_{n=1}^{x_N} \sum_{m=1}^{y_N} [\, a_i(t_l)\phi_i(x_n, y_m)\,]^2 \tag{1.82}$$

$$\mathbf{POM\ 1-2}_{\boldsymbol{Primary\ Oscillation}}(x, y, t) = a_1(t)\phi_1(x, y) + a_2(t)\phi_2(x, y) \tag{1.83}$$

$$\begin{aligned} \Gamma_{centre}(x, y, t) &= \frac{1}{N}\sum_{S} \frac{(PM \otimes U_M)\cdot z}{\|PM\| \cdot \|U_M\|} \\ &= \frac{1}{N}\sum_{S} \sin(\theta_M) \end{aligned} \tag{1.84}$$

Symbol and abbreviation	*Description*	*Units*
λ^i	Eigenvalue for POD Mode *i*	($m^2\ s^{-2}$)
$a_i(t_l)$	Temporal Coefficient for POD Mode *i*	-
$\phi_i(x_n, y_m)$	Spatial Orthogonal Basis Function for POD Mode *i*	-
$\Gamma_{centre}(x, y, t)$	Circulation Strength for each point in the velocity vector field	(dimensionless)
P	The investigated point in the velocity vector field	-
M	The neighbouring point surrounding point P	-
U_M	Magnitude of the velocity vector corresponding to point M	(ms^{-1})
θ_M	Angle between the velocity vector, U_M, and the vector PM	(degress)

Chapter 7

Acoustic Transmission through Curved Duct Systems

$$\mathrm{I}_{aa} = (V_{aa})^2 \rho c \tag{1.85}$$

$$\text{Acoustic Transmission} = \frac{\sum_1^2 \lambda^i}{\sum_1^{T_N} \lambda^i} \times 100\% \tag{1.86}$$

$$Loss_{acoustic} = 1 - \text{Percentage Acoustic Transmission} \tag{1.87}$$

$$\mathrm{Re} = \frac{V_{aa}\, d_h}{\nu} \tag{1.88}$$

$$\xi_{ac} = \frac{\mathrm{V}_{aa}}{2\pi f} \tag{1.89}$$

$$\begin{aligned} St &= \frac{2\pi f \cdot ROC}{\mathrm{V}_{aa}} \\ &= \frac{ROC}{\xi_{aa}} \end{aligned} \tag{1.90}$$

$$St_{\,Dean} = \frac{2\pi f \cdot ROC}{\mathrm{V}_{aa}} \times \left[\frac{r_h}{ROC}\right]^{\frac{1}{2}} \tag{1.91}$$

$$\begin{aligned} f_{c,square} &= \frac{\mathrm{c}}{2d_h} \\ &\approx 3.8 \text{ kHz} \end{aligned} \tag{1.92}$$

$$\frac{\alpha^2}{De} = 0.655 \tag{1.93}$$

$$\frac{\alpha^2}{De} = 0.41 \tag{1.94}$$

$$\begin{aligned} \frac{\alpha^2}{De} &= \frac{St_{\,Dean}}{2} \\ &= \frac{\omega}{2 \cdot \mathrm{V}_{aa}} [r_h \times ROC]^{\frac{1}{2}} \end{aligned} \tag{1.95}$$

$$St_{\,0.5\,Dean} = \frac{St_{\,Dean}}{2} = \frac{\alpha^2}{De} \tag{1.96}$$

$$St_{\,0.5\,Dean,Nonlinear\ Onset} = -3.37\left[\frac{r_h}{ROC}\right] + 5.00 \tag{1.97}$$

$$Loss_{\,acoustic,Nonlinear} = -28\,St_{\,0.5\,Dean} - 92.17\left[\frac{r_h}{ROC}\right] + 140.12 \tag{1.98}$$

Symbol and abbreviation	*Description*	*Units*
I_{aa}	Acoustics Intensity	(kg s^{-3})
V_{aa}	Upstream Incident Velocity Component	(m s^{-1})
Re	Reynolds Number	(dimensionless)
d_h	Hydraulic diameter	(m)
ν	Kinematic viscousity	(m^2 s^{-1})
ξ_{ac}	Acoustic Particle Displacement	(m)
f	Frequency	(s^{-1})
St	Strouhal Number	(dimensionless)
ROC	Radius of Curvature of the Bend	(m)
$St_{\,Dean}$	Strouhal Dean number	(dimensionless)
r_h	Hydraulic Radius	(m)
$f_{c,square}$	Plane wave cut-off frequency for Square duct	(s^{-1})
c	Speed of sound	(m s^{-1})
α	Womersley Number	(dimensionless)
De	Dean Number	(dimensionless)
ω	Angular Frequency	(s^{-1})
$St_{\,0.5\,Dean}$	Strouhal Dean number x 0.5	(dimensionless)
$St_{\,0.5\,Dean,Nonlinear\ Onset}$	Strouhal Dean number for the onset of Non-linear losses	(dimensionless)
$Loss_{\,acoustic,Nonlinear}$	Estimation of the percentage transmission loss corresponding to the $St_{\,0.5\,Dean}$ in the Non-linear region	(dimensionless)

Chapter 1

Introduction

1.0 Introduction

The thermoacoustic process describes the cyclic interaction between a fluid and a solid thermodynamic medium that facilitates the interchangeable conversion between heat and acoustic wave energy. The process requires no moving component and operates optimally with noble gasses as its working fluid[1]. It is shown that the reversible travelling wave thermoacoustic process is capable of achieving up to 41% of the Carnot efficiency. These are desired characteristics for both heat engine and heat pump systems. The feasibility of adapting this phenomenon for developing new commercial systems has raised interest from both the scientific community as well as from the industry. It is noted however, that the high efficiencies of current thermoacoustic system are a result of system pressurisation (up to 30 bars) and the use of very large operating temperatures (≈725^{o}C). The introduction of thermoacoustic technologies at such niche operating condition would however face stiff competition from existing systems. Thermoacoustic systems are thus challenged to obtain more stable and reliable systems at higher efficiencies with lower operating requirements.

The SCORE project took an interesting approach towards the development of the thermoacoustic system in that it aims at optimising the efficiencies of low operating temperature systems. The operating temperature range in this case, corresponds to the heat generated from the burning of wood and other biomass materials (charcoal, grass, etc.). The SCORE project's objective is to develop a 100We electrical generating, wood fire stove for rural communities who still do not have

access to electricity. The SCORE-stove system is that of a travelling wave thermoacoustic heat engine integrated with an efficient wood fire burning stove. The engine utilises a linear alternator (reverse speaker) to convert the acoustic energy generated by the engine into electricity. The engine is designed to operate at relatively low frequencies which will allow the linear alternator to function optimally. In order to keep the operating frequencies low however, the axial length of the resonator has to be long (2-3m). Duct bends are used to coil the resonator such that the engine remains compact for practical domestic usage, while maintaining the axial length required for its low frequency operation.

The efficiency of a travelling wave thermoacoustic system is correlated to the maximum oscillating amplitude obtainable within the acoustic resonator loop for a fixed temperature difference between the ends of its regenerator. The temperature difference between the regenerator determines the amplification rate of the regenerator. The maximum oscillating amplitude occurs when the amplification rate is equivalent the rate of energy loss within the resonator system. It is thus of interest to minimise these loss mechanism within the resonator such that a larger maximum operating amplitude can be obtained. The net loss within the system is shown to be the independent sum of the discreet losses occurring in each constituent component of the resonator. It is shown that the most repeated component of the resonator is the duct elbow bends used to coil the resonator up. Previous investigations on this component were based on steady flow system through duct bends. The minor losses corresponding to the bends could be as high as 3% per bend. Literature has shown that acoustic propagation through bends shows different and varied behaviour based on the amplitude and wavelength of oscillation as compared to steady, uni-directional flow system. This could possibly lead to higher losses within the system. The duct bend was thus targeted to be optimised in this research.

The next subchapter 1.1 describes the thermoacoustic phenomena and gives a brief history of the development of thermoacoustic heat engine systems. This leads to the introduction of the SCORE-

project which is the basis for this research. Subchapter 1.2 also outlines the design and operation of the SCORE-stove system in addition to the challenges it faces. The literature review on acoustic propagation as well as oscillating flow through duct and curved bend systems are given in subchapter 1.3. The problem statement and research objectives are then stated in subchapter 1.4. In conclusion, the summary of thesis is outlined in subchapter 1.5.

1.1 Thermoacoustics

Acoustics as a science, encompasses the generation, transmission and reception of energy as waves in matter[2]. The vibrational waves described is often caused by external disturbance which while propagating through the matter causes the molecules in the matter to be temporally displaced from its original position and oscillate longitudinally about a mean. The oscillation of these molecules creates a successive pattern of compression and expansion which in turn generate a variation in temperature and pressure of the medium. The localised, cyclic adiabatic compressive heating and compressive cooling of the acoustic medium and its interaction with its solid boundaries, forms the basis between the field of acoustics and thermodynamics. Acousticians working with pressure oscillations[3] and acoustic wave propagation[4] in resonators have observed the formation of temperature gradient along sections of the length of the resonator. The magnitude and location of the temperature gradient formed within the resonator depends on the amplitude and wavelength of the acoustic wave respectively. This thermofluid relationship is also shown to be able to work both ways, in that acoustic wave can also be excited through the formation of a sufficiently large temperature gradient between two point in the acoustic medium under suitable conditions. The phenomena have been observed by traditional glass blowers where their blowing tubes vibrate violently whenever a hot molten bulb of glass is attached to its end[5]. Similarly, cryogenic researchers have also observed that their hollow stirrers vibrate violently when those tips are dipped in liquid nitrogen[6]. These phenomena are also known as the Sondhauss/Tarconis tubes and shows that it is the temperature gradient formed between the two points along the waveguide are the source of the acoustic excitation rather than the amount of

heat applied to the system. Rayleigh[7] was the first to qualitatively explain these acoustic thermofluid interactions:

> *"If heat is given to the air at the moment of greatest condensation (compression) or be taken from it at the moment of greatest rarefaction(expansion), then vibration is encouraged. On the other hand, if heat be given at the moment of greatest rarefaction, or abstracted at the moment of greatest condensation, the vibration is discouraged" –Rayleigh criterion(1896)*

Nearly a century later, Rott developed the mathematics of the linear wave and energy equations that quantitatively describes the linear wave and energy equations; that accurately describes the mechanism of the phenomena[8]. Fittingly, it was Rott who introduced the term "Thermoacoustics". Through Ceperley's understanding that acoustical energy is a fluctuating form of mechanical energy[9] and Gifford[3] and Merkli[4]'s discovery of the temperature gradient formed within their acoustic resonator systems, the thermoacoustic phenomena quickly attracted interest for technology development especially pertaining to engineering applications involving heat engines and heat pumps. In line with this research, this literature review will focus on the operation as well as the development of the thermoacoustic heat engine. There are two categories of thermoacoustic systems; the standing wave and travelling wave systems. Rayleigh's criterion holds true for the variation in operating mechanism of these thermoacoustic heat engines.

1.1.1 Standing Wave Thermoacoustic Systems

The Sondhauss tube is perhaps the most basic form of a standing wave prime mover. Since its discovery, the glass blowers pipe has been optimized to for acoustical generation. It was found that the oscillations are excited by the large temperature gradient between the ends of the long narrow tubes of the glass blowers. By choosing a material with higher thermal resistance while maintaining the diameter of the narrow tube, the same large temperature gradient can be maintained by shorter tubes. Since each of the shorter tubes acts as an acoustic generator when a sufficiently

large temperature gradient is maintained between its ends, acoustic output can be increased by bundling these shorter tubes together and placing them in a new resonator which has one end open and the other end closed. Heating no longer occurs at the end of the resonator but at the end of the bundle of tubes closest to the closed end. This new heating configuration allows for the removal of the buffer volume bulb. Tom Hofler proved that the bundle of tubes may be replaced by stacks of fibre glass plates placed parallel to the resonators length, as long as the separation between these plates are the same as the diameter of the tubes. Hofler also stuck shorter strips of copper to the each end of each plate in the stack to facilitate heat transfer[10]. These were the earliest known thermoacoustic heat exchangers and the term "stack" had evolved to encompass all standing wave "secondary thermodynamic medium" devices.

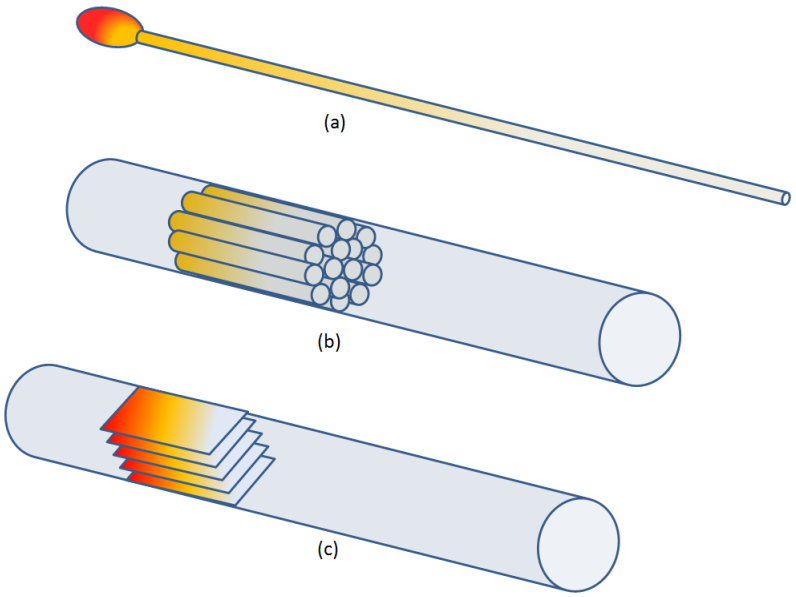

Figure 1-1: The evolution of the Sondhauss resonator: (a) The glass blower's pipe, one end stuck in hot molten glass bulb while the other open end left at atmospheric pressure. Steep temperature gradient is maintained through the length of the pipe. (b) Sondhauss resonator with bundle of low thermal conductivity tubes (similar temperature gradient as the glass blower's pipe maintained by shorter tubes). (c) Hofler resonator. The design of the "second thermoacoustic medium" can be varied as long as the separation of the channels with each other is equivalent to about 3 times the thermal penetration depth of the working fluid. The simplest configuration of the "second thermoacoustic medium" for standing wave is a "stack" as illustrated in (c). The term "Stack" eventually grew to encompass all standing wave "second thermoacoustic medium".

For the operation of Thermoacoustic standing wave system, Wheatley[11] states that there are 3 fundamental criteria which are required to be fulfilled. The first is the presence of 2 thermodynamic medium, namely the primary fluid acoustic medium and a secondary solid

thermodynamic medium (also known as the stack as described in Figure 1-1). The separation between the solid boundary of the secondary thermodynamic medium (known as the "stack" henceforth), is responsible for the second criterion in which a natural irreversible processes is produced, allowing for the correct phasing that facilitates thermoacoustic excitation. The third criterion involves the "breaking of the thermodynamic symmetry". Both the second and third criterion is better illustrated in Figure 1-2.

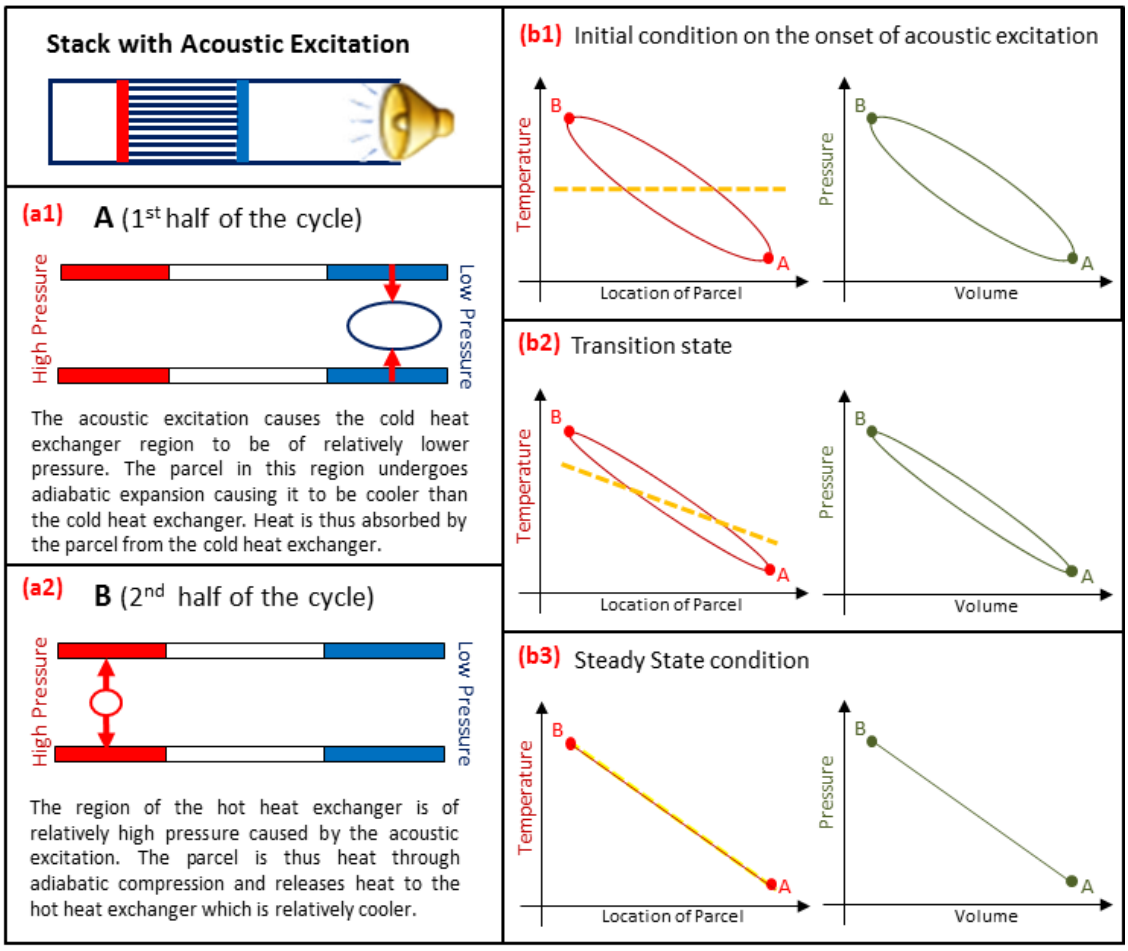

Figure 1-2: The operating principle of a quarter wavelength standing wave thermoacoustic heat pump. (a1) and (a2) show the snapshot of two halves of the thermoacoustic cycle. These properties of the parcel from these snapshots are represented by the dots A and B in (b1)-(b3). The yellow dotted line on other hand represents the temperature variation along the length of the stack. (b1) illustrates the initial onset of acoustic excitation in the resonator. The area encompassed by the PV diagram shows the work being done by the gas parcel in transferring heat from the cold heat exchanger to the hot heat exchanger ends of the stack. (b2) As time progresses the temperature gradient begins to form along the length of the stack. The eclipse of the PV diagram becomes thinner signifying less work is being done as a result of the formation of the temperature gradient. (b3) The maximum temperature gradient is reached. The temperature of the stack and the oscillating parcel are the same. No work is done although acoustic excitation is required to maintain this temperature gradient. The maximum temperature gradient is also known as the threshold/critical temperature gradient for the onset of acoustic excitation for thermoacoustic heat engines.

In the case of a standing wave refrigerator, the input acoustic energy is used as "work" to pump heat up a temperature gradient between the ends of the stacks(which are also known as heat exchangers in Figure 1-2). Although Figure 1-2(a1) and (a2) show that the velocity and pressure are 90^{o} out of phase (maximum and minimum pressures while velocity=0), this is not the case. In order for the standing wave thermoacoustic system to work, a deliberate imperfect thermal contact between both the parcel of gas and the stack has to exist in order to avoid this phasing. If perfect thermal contact exists, the PV diagram would show a reciprocal line as shown in Figure 1-2(b3) and no heat pumping work would exist. Imperfect thermal contact allows for a slight shift delay for both thermal expansion and contraction allowing for the elliptical PV cycle to exist. Thermal contact can be estimated by the thermal penetration depth which is the characteristic length of how far heat can diffuse laterally during a time interval of the order of the period of the oscillation divided by π [12].

$$\delta_{thermal\ penetration} = \sqrt{\frac{2k}{\omega \rho c_p}} \tag{1.1}$$

The separation between each stack plates has to be of the order of several $\delta_{thermal\ penetration}$, in order to achieve the required imperfect thermal contact. In fact, Garret[13] defines the secondary porous thermoacoustic medium, a "stack", when its Laucret number, $\mathrm{N}_L \geq 1$. The Laucret number is the ratio of the hydraulic radius of the stack to the secondary acoustic medium's thermal penetration depth.

$$\mathrm{N}_L = \frac{r_h}{\delta_{thermal\ penetration}} \tag{1.2}$$

The hydraulic radius, r_h, is given in *Equation (1.5).* In the case of Figure 1-1(c), the hydraulic radius is taken as half the separation length between each of the stack's plates. The pressure-velocity phase correction through imperfect thermal contact between both thermoacoustic medium causes the standing wave thermoacoustic cycle to be intrinsically irreversible (Wheatley's second criterion). The breaking of the thermodynamic symmetry is illustrated in Figure 1-2(b1) and (b2),

where the temperature of the secondary acoustic medium parcel differs from that of the stack. In the case of a standing wave thermoacoustic heat engine, the thermoacoustic symmetry has to be broken in that the temperature gradient generated between the ends of the stacks, ΔT, has to be larger than the critical temperature gradient, ΔT_{crit} described in Figure 1-2[12] . The breaking of the thermoacoustic symmetry allows for the excitation of acoustic waves as heat is converted into acoustic energy. The critical temperature gradient can be approximated by:

$$\Delta T_{crit} = \frac{\omega A p}{\rho_m c_p u} \tag{1.3}$$

Here, ω is the angular frequency, A,the cross sectional area, p, the acoustic pressure amplitude, ρ_m, the mean gas density, c_p, the gas thermal capacity and u, the acoustic velocity amplitude. It must be noted however, that the design of the hydraulic radius must be a compromise between being small enough to achieve the required thermal contact with the working fluid yet not so small as to cause undesired viscous losses. The viscosity is governed by the viscous penetration depth define as the characteristic length of how far momentum can diffuse laterally during a time interval of the order of the period of the oscillation divided by π.

Thus, for spontaneous acoustic oscillation to occur, the temperature gradient must also be sufficiently large such that the amplitude of the acoustic wave generated is able to overcome the dissipative mechanism of the stack itself[14]. The temperature difference, at which the excited acoustic oscillation is equal to the dissipative losses in the stack, is termed the onset temperature difference, ΔT_{onset}. Spontaneous acoustic oscillation would only occur if the temperature difference, ΔT:

$$\Delta T > \Delta T_{onset} > \Delta T_{crit} \tag{1.4}$$

Figure 1-3 illustrates the case in which heat is continuously supplied and removed from the hot and cold heat exchanger respectively, in order to maintain a steady state ΔT with $\Delta T > \Delta T_{onset}$. The optimisation parameter for the design stack involves obtaining the lowest possible ΔT_{onset} for the

operation of the engine. The onset temperature differences for the standing wave stack depend on two main parameters; the location of the stack along the length of the resonator, and its hydraulic radius. The stack's location for a standing wave resonator relates to the local acoustic impedance of the stack, while the hydraulic radius has to be a compromise between being sufficiently small in order to achieve the required thermal contact yet large enough to avoid unnessary viscous dissipation in the stack. Numerical simulation[15] and experimentation [16] have shown that the lowest onset temperature difference obtained thus far is with stack position at $5\lambda/32$ of the fundamental oscillation in the resonator and the hydraulic radius given in terms of the Laucet number as $\mathrm{N}_L = 1.3 - 1.5$.

Efforts have been made to utilize its oscillating working fluid to produce useful energy. In 1888, Carter proposed oscillating a polarized working fluid through a magnetic field in the tube in order to generate electricity[5]. It was not until 1988 that Migliori and Swift worked on this concept to produce a standing wave engine using liquid sodium as its working fluid to generate electricity via a magnetohydrodynamic (MHD) transducer[17]. The use of liquid sodium was an expansion on Malone's concept of liquid working fluids in heat engines[18]. There have been several other methods in harvesting the acoustic work to produce electricity. To date, the most efficient and commonly used technique for 'acoustic wave-electricity' conversion involves using linear alternator and its variation[19, 20] or using piezoelectric materials[21, 22]. Another popular application is the use of the standing wave heat engine in order to drive a thermoacoustic heat pump for refrigeration and even cryogenic purposes.

The irreversibility of the engine however caps the efficiency of the standing wave system. To date, the highest achieved thermal efficiency recorded in open literature stands is approximately 18% to 20%[23-25] for both standing wave heat engine and heat pump systems. Further increment of efficiencies and improvement of desired output would require development with thermoacoustic travelling wave devices which operates on reversible processes. Although travelling wave devices

has the upper hand in terms of higher achievable efficiencies, standing wave devices has the advantage in generally having much simpler design and less components (thus easier and more cost effective to manufacture) relative to travelling wave devices.

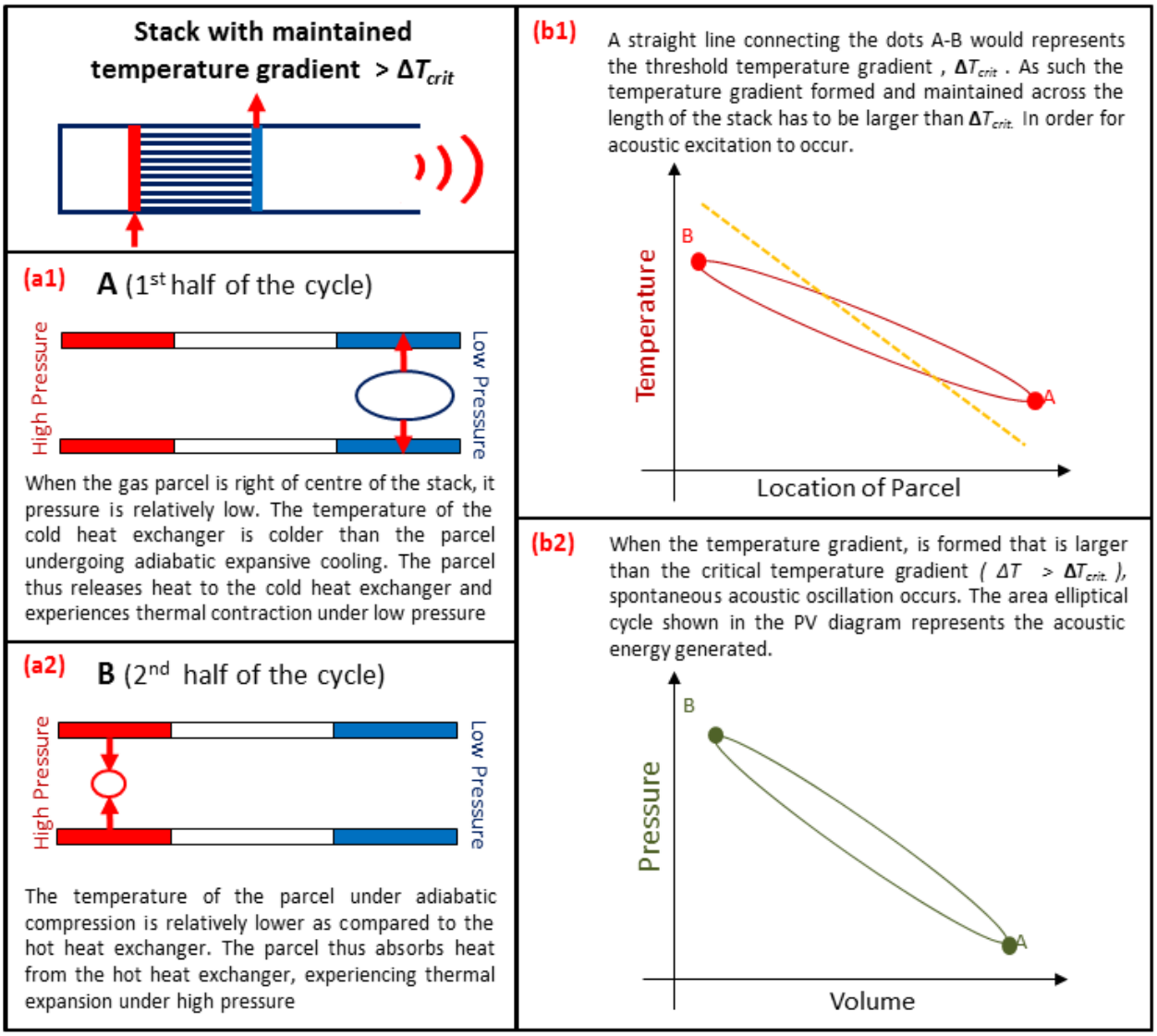

Figure 1-3: Standing wave Thermoacoustic Heat Engine

The fundamental excited frequency of the standing wave heat engine is greatly dependant on the axial length of the resonator. Thus far, development have been focused on low frequency (below 100Hz), high amplitude engines. In the spirit of developing more practical and commercially viable engines, interest have been sparked to develop more compact engine working at higher frequencies (300Hz)[26].

1.1.2 Travelling wave (Stirling) Thermoacoustic System

Thermoacoustic travelling wave systems can be seen as a progression from the Stirling systems. The Stirling systems depend on the piston-displacer crank mechanism in order to control the phasing of the working fluid in bring it through a thermodynamic cycle. The Stirling cycle is reversible which allows for high thermal efficiencies that could rival that of Internal Combustion engine systems[27]. The dependence on mechanical components of Stirling systems however, limits the efficiency and durability of the system. The largest challenge came from the sliding seals of its pistons where compromise between efficient sealing of the system versus the increased frictional losses caused by proper sealing. Thus the development of the Stirling technology was for fewer moving components as well as less complicated methods of sealing the working fluid in the engine [13, 28-31]. The development of Free Piston Stirling engine was an initial step towards reducing the complexity and the number of moving parts of the engine[32]. In 1984, the Fluidyne engine was developed. This engine uses oscillating liquid in columns to replace the displacer and/or the piston of the Stirling engine[33]. This indirectly solves the problem previously faced by moving seals. The system is however, limited to a low operating frequency because of its dependence on the liquid piston's momentum and inertia.

The big breakthrough came in 1989, when Ceperley realized that the phasing between the pressure and velocity oscillation in a travelling acoustic wave is similar to that of the working fluid in the Stirling cycle[9]. The cycle is shown to occur in the regenerator of the Stirling engine, where the engine's working fluid is nearly isothermal with the solid porous packing of the regenerator. This meant that the travelling acoustical wave is able to replace the Stirling engine's crank mechanism in bringing the working fluid through the thermodynamic cycle in order to produce work[34]. Figure 1-4 shows a comparison made between the phasing of a travelling acoustic wave with that of the working fluid in a Stirling engine regenerator. Unlike the Stirling engine where the regenerator is only a device to improve the engine's thermal efficiencies, it is important to note that the regenerator is the fundamental core for the operation of the travelling wave engine. It is also

crucial to understand that the regenerator acts only as a power amplifier in the travelling wave engine. To complete the thermodynamic process in the regenerator, acoustic power has to be supplied to the ambient end of the regenerator with a near travelling wave phasing. This can either be achieved by an external acoustic source[35, 36] or a feedback mechanism[25, 37, 38] designed to return acoustic power back to the ambient end of the regenerator.

In both, the Stirling cycle and an acoustic travelling wave, the pressure and acoustic velocity of the working fluid are in phase. This phasing is a result of the perfect thermal contact the working fluid has with the regenerator. The regenerator is more of a solid porous media rather than stacks of plates as in a standing wave system. The hydraulic radius is approximated as the ratio of the total volume of the working fluid in the regenerator to the area in which the working fluid comes into contact with:

$$r_h = \frac{V_{working\ fluid}}{A_{wetted}} \tag{1.5}$$

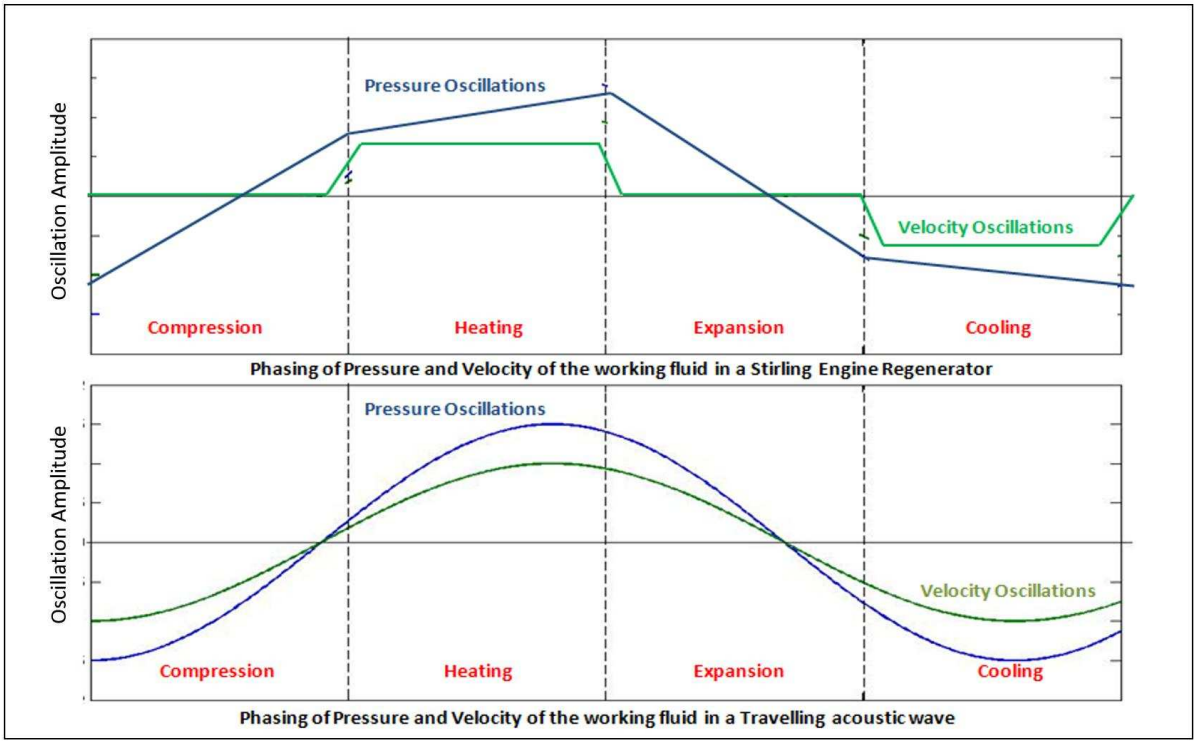

Figure 1-4: Comparison between the phasing of a Stirling cycle and a Travelling acoustic wave [39]

The size of the hydraulic radius for travelling wave thermoacoustic regenerator is several times smaller than the thermal penetration depth. Garret[13] defines a regenerator when its Laucret number is $N_L \ll 1$. This ensures that the working fluid is isothermal with the temperature gradient along the resonator allowing for the proper phasing for the thermoacoustic cycle as shown in Figure 1-4. However, the large surface to volume ratio of the working fluid in the regenerator causes severe viscous dissipation which must be suppressed in order for the engine to operate. Similar to standing wave devices, the optimisation parameter involves obtaining the lowest attainable ΔT_{onset}. Although the required thermal contact between the working fluid and regenerator limits the changeable length of the hydraulic radii, the length, porosity and position of the regenerator can still be optimised to give the optimum level and phasing of the acoustic impedance. The amplified acoustic wave from the regenerator is often not a pure travelling wave but has an Standint Wave Ratio (SWR) close to unity[38] (the SWR is defined in *Equation(2.2)*). Accordingly, the optimum position of the regenerator has been shown to be at the pressure antinode of the standing wave component of the wave[40]. It has also been shown that ΔT_{onset} may be significantly reduced by introducing a pressure disturbance into the system[41]. This can be in the form of pressurising or depressurising the closed loop resonator system, thus providing acoustical excitation through speaker or piston, etc.

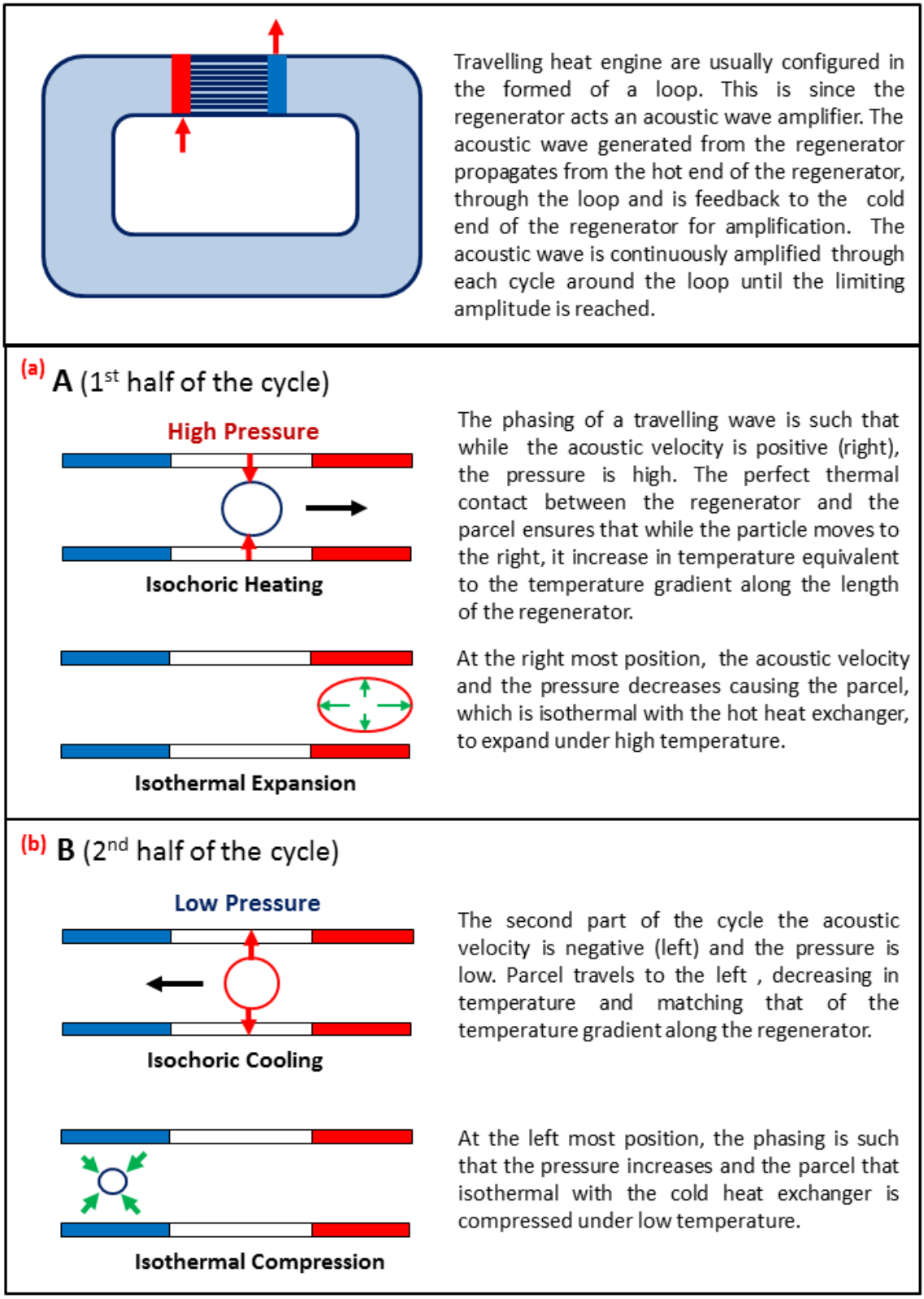

Figure 1-5: The thermoacoustic cycle of in the regenerator of a travelling wave heat engine.

Yazaki was the first to successfully build an operating thermoacoustic travelling wave loop engine[38]. The engine had a resonator loop length equivalent to an acoustic wavelength. While

this allows for an acceptable level of acoustic impedance, the system still suffered from low efficiencies due to the high viscous dissipation from both in the regenerator and along the long length of the resonator loop. Viscous dissipation is a function of the acoustic velocity squared. One solution to mitigate these viscous losses, is to keep the acoustic impedance, especially in the regenerator high. This allows for continued pressure wave amplification while supressing the viscous losses in the regenerator. For a pure travelling wave, the characteristic acoustic impedance is given as:

$$Z_{travelling\ wave} = \frac{p}{U} = \frac{\rho_m c}{A} \tag{1.6}$$

However, in order to sufficiently supress the viscous losses in the regenerator, the acoustic impedance needs to be 15 to 30 times larger than $Z_{travelling\ wave}$, while maintaining the zero phasing between pressure-velocity oscillations of the wave.

$$Z_{regenerator} = \frac{p}{U} \gg \frac{\rho_m c}{A} \tag{1.7}$$

The local impedance and pressure-velocity phasing of the wave are determined by the combination of the resistance, inertance and compliance, and can be adjusted based on the geometric changes made to the individual components of the resonator loop. Small Helmholtz resonators have also been shown to be effective acoustic pressure amplifiers and phase tuners when connected to different sections of the resonator loop[42]. Based on this principle, Backhaus and Swift[43] designed a compact feedback loop attached to a long resonator column (Figure 1-6c). The pathway of the compact loop contains an inertance tube and a large compliance bend that creates a positive feedback such that the acoustic wave channelled back to the cold end of the regenerator has a zero pressure-velocity phasing. This ensures optimal travelling wave amplification. The regenerator is placed in the feedback loop which has inherently high impedance due to its compact size. The long quarter wavelength resonator connected to the column acts as a Helmholtz resonator. While a pure travelling wave phasing is induced in the compact loop, the wave propagating in the resonator is that of the standing wave. The operating frequency is a function of the length of the resonator

column. As such, the resonator column is designed to be sufficiently long in order to keep the operating acoustic wavelength shorter than the axial length of the feedback loop. This further reduces the viscous dissipation of the travelling wave in the feedback loop. Luo et al[44] discovered the occurrences of shockwaves in constant cross section of the resonator column which limits the pressure ratio (ratio of the maximum pressure amplitude to the mean pressure). The formation of these shockwaves can be suppressed by tapering the resonator column along its length. The resonator column still has a large surface area for acoustic viscous dissipation. An alternate design is for the replacement of the long resonator column with a mechanical resonator[45]. Although this complicates the system by introducing mechanical moving parts in the engine, it helps to compact the entire system down. Backhaus et al replaced the mechanical resonator with a linear alternator that performs the resonator's function as well as extracts electrical energy. This concept was also adopted by Wu, who mounted a compact feedback loop engine on top of a solar concentrating disk that was able to produce 200We[46]. Thus far, the most efficient travelling wave thermoacoustic engine of this configuration (compact loop with quarter wavelength resonator) has a thermal efficiency of 30%[25] and the highest pressure ratio achieved is 1.4[47].

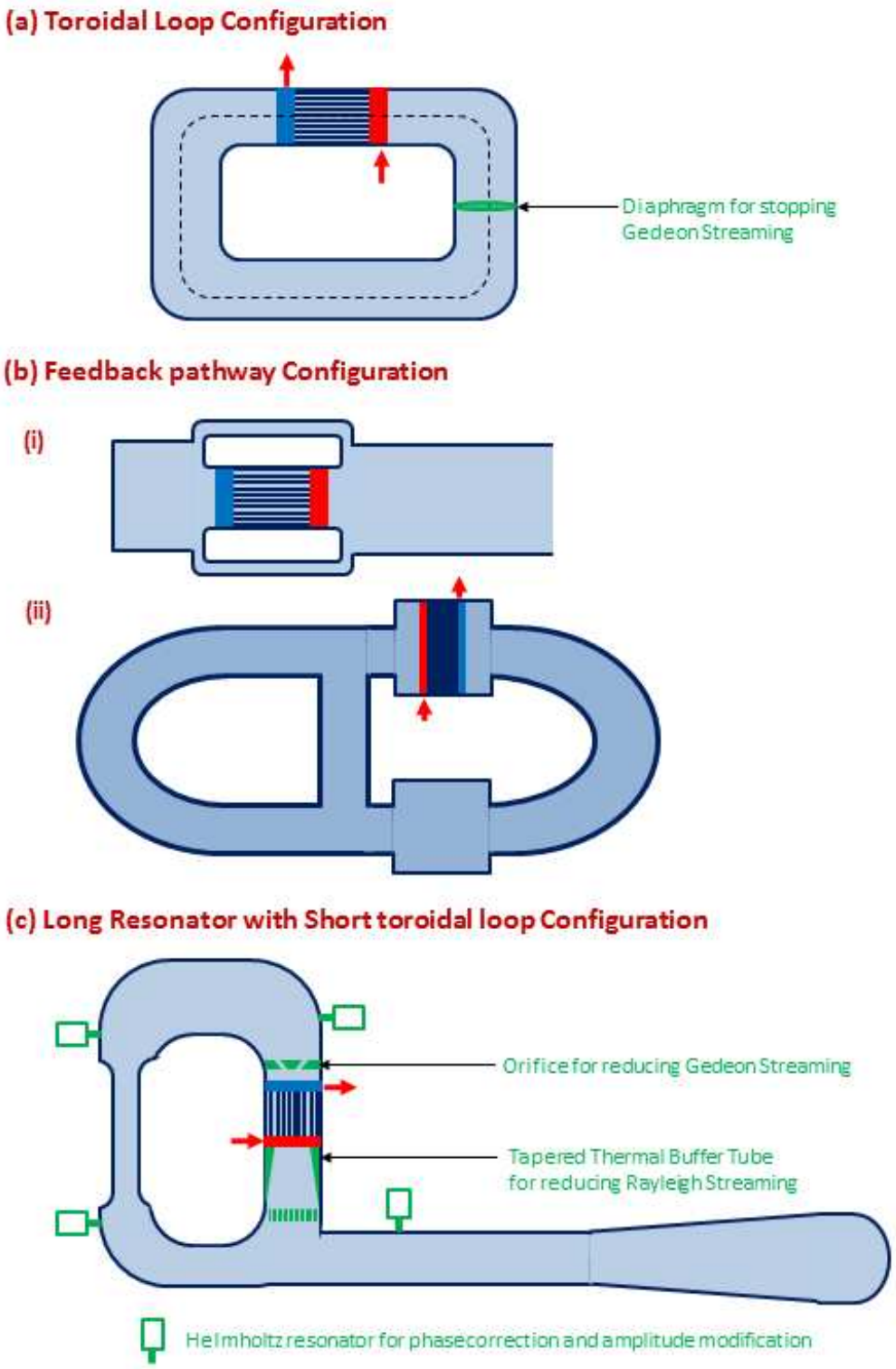

Figure 1-6: The configuration of the different form of travelling wave engines.

It must be noted however, that although the high local acoustic impedance increases the efficiency of the regenerator, it also increases the onset temperature difference required for operation. The Backhaus-Swift engine requires an onset temperature difference of approximately 1000K. This limits the application of such engines as most heat sources are unable to reach such high

temperature. Being so, a different approach was adopted by De Blok in order to develop efficient travelling wave systems with low onset temperature difference. De Blok's design was based on Yazaki's original toroidal loop with the adaptation of the inertance tube and compliance volume to control the pressure-velocity phasing of the wave. The design also introduces an additional feedback pathway into the system (Figure 1-6(b)) which is used to tune the impedance of the feedback loop such that it matches that of the local impedance at the cold end of the regenerator[48]. The match between these impedances allows for a travelling wave phasing throughout the system. The acoustic wave propagating out of the hot end of the regenerator is forced to split between the feedback pathways. This reduces the volumetric velocities of both separated acoustic flow which results in a general reduction of viscous losses around the double loop resonator system. The separated acoustic waves are then converged before being fed back to the cold end of the regenerator for amplification. The regenerator was specifically designed with a large cross sectional area such that it will have low local acoustic impedance. This configuration reduces the onset temperature difference to be as low as 65K[24]. De Blok has also tested using multiple regenerators in series with this configuration in order to obtain higher power density systems.

There is another challenge that threatens the efficiency of travelling wave systems. It has been found that travelling waves of sufficiently large amplitude propagating though a waveguide tend to induce a mean flow in the acoustic waveguide. This phenomenon is known as acoustic streaming. There are two forms of acoustic streaming which effect the performance of travelling wave systems: "Gedeon streaming" is the induced secondary mass DC flow in the direction of the propagating wave[49] and "Rayleigh streaming", the secondary mean flow in the form of vortex circulation. The resonator loop design allows for pathway for undesired heat and mass transfer from the hot heat exchanger of the regenerator through the feedback loop back to the cold heat exchanger. This reduces the ΔT in the regenerator and accounts for approximately 3% to 4% of the degradation of the systems' thermal efficiency. Backhaus proposed counteracting the Gedeon

streaming by using the hydrodynamic effect of placing an orifice in the resonator loop[25]. The acoustic wave propagating through the orifice will be tripped to turbulence hence reducing the velocity. This orifice has been shown to work for pressure ratio lower than 1.067[50]. For higher pressure ratios, an elastic diaphragm has been proven to be effective for eradicating DC flow while effectively transmitting acoustic energy. Rayleigh streaming are acoustic streaming caused by a large velocity gradient between the viscous boundary layer and the free stream of the oscillation. This causes the formation of a double vortex like circulation which dissipates heat from the hot end of the regenerator. It was found that the Rayleigh streaming phenomenon can also be suppressed by tapering the section the duct in which the circulation occurs[25]. This pipe section is known as the thermal buffer tube.

1.2 SCORE Project

The SCORE (**S**tove for **Co**oking **R**efrigeration and **E**lectricity) project, started in 2007, is an international collaborative research effort to develop an autonomous stove system that could provide electricity to rural communities that are not connected to the electrical power grid. The £2 million project funded by EPRSC is led by Paul Riley from the Department of Electrical and Electronic Engineering at The University of Nottingham. The project academic and research collaborators includes established Universities from the UK, China, Malaysia, Bangladesh, Nepal and India. The industrial collaborators include the charity organisation, Practical Action; Aster-Thermoacoustics, a commercial thermoacoustic technology development company and Alstom from the power generation sector.

The preliminary stage of the project involved a social study of these communities and their use of energy[51]. The study revealed that there are approximately 1.5 billion people worldwide still relying on biomass fires as their primary form of energy for heating, cooking and lighting. A majority of these communities rely on open fire and makeshift stove designed for cooking. Studies have shown that from these inefficient cooking configurations, approximately only 10% of the heat generated from the fire is actually used for cooking while the rest are dissipated into the

surroundings. SCORE members who went to live with these communities have also observed that a number of these communities have their cooking fire indoors with no proper ventilation for smoke emissions. Statistics have shown that nearly 3% of deaths around the world each year are due to carbon monoxide poisoning from smoke inhalation besides other countless health related issues. The criteria for the technology selection were based on these social study parameters. The choice of technology to develop should be flexible and operable on any form of heat source, improve the efficiencies of biomass combustion and maximise utilisation of its generated heat, reduce fire smoke emission, be affordable to these communities, robust and simple to maintain. Several technologies were considered -- thermoelectric systems, solar combine with stove, steam engines, Stirling engines and thermoacoustic systems. Thermoacoustic devices were chosen because of their flexibility of heat sources, high theoretical efficiencies, and minimal moving components, thus simplifying manufacturing and maintenance.

In Chapter 1.1.2, it was shown that the most efficient travelling wave engine thus far was that developed by Backhaus and Swift. Their compact loop, long resonator configuration however, requires a very large onset temperature difference which is unattainable by burning wood or other forms of biomass. As the Score-stove engine relies on the low onset temperature difference configuration, its design was similar to that proposed by de Blok where the cross sectional area of the regenerator is large while having a short length between its hot and cold ends. This lowers the local impedance of the regenerator and reduces the onset temperature difference. While adopting de Blok's design however, the second feedback bridge was not included. Instead the Helmholtz resonator stub were placed near the hot end of the regenerator in order to tune the amplitude as well as the pressure-velocity phasing of the wave that is being fed back to the regenerator. Thence, in order to increase the power density of this low onset temperature configuration, Ceperley proposed using multiple regenerators in a single feedback loop. Since the Score-stove configuration induces a travelling wave phasing throughout its system, there is a large "sweet spot" for the placement of additional regenerators in the system. The Score-stove uses a dual

regenerator configuration with Helmholtz tuning stubs near the hot end of both the regenerators. The hydraulic radius used for the feedback resonator loop was 44mm. This relatively large waveguide size is to allow for a larger volume to surface ratio in order to minimise viscous dissipation. A linear alternator is connected in series to the feedback loop and is situated near the cold end of one of the regenerators.

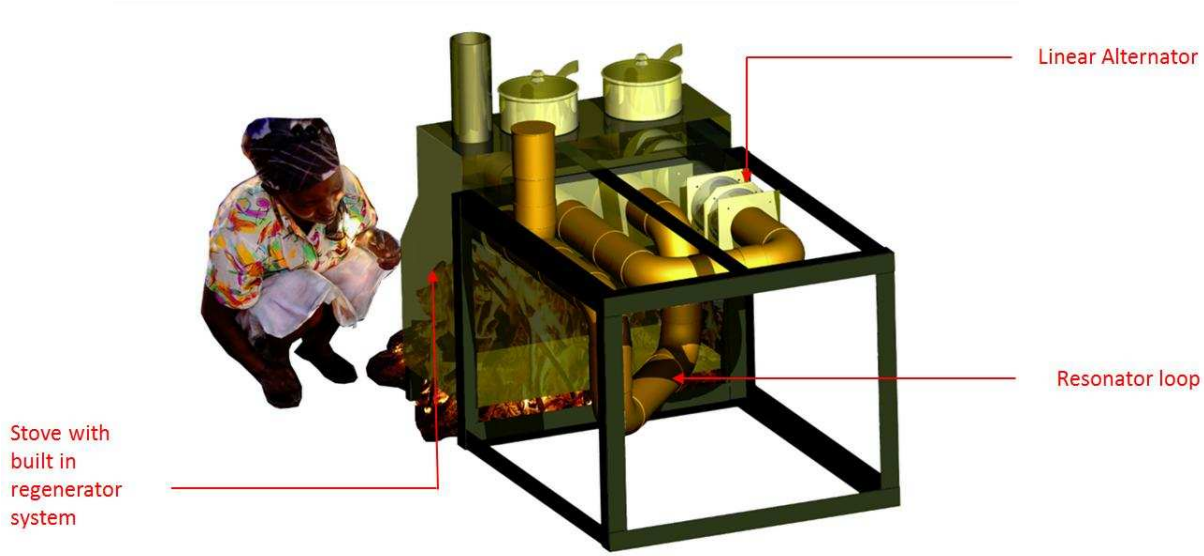

Figure 1-7: The Computer generated model of the SCORE-stove engine

The current and continuing objective of the SCORE project is to optimise the performance of the engine in order to increase the electrical output of the system. These correspond largely to the performance of both the thermoacoustic engine and the linear alternator. The linear alternators are essentially converted subwoofer speakers. As such, these linear alternators perform optimally in accordance to the speakers' operating frequency range (corresponding to 50Hz – 180Hz). This range of frequencies corresponds to the resonator axial length of 2m to 7m. The design of the SCORE-stove engine however, has to remain compact (approximately 1m x 1m x 1m) that would allow practical storage and usage within the target communities' homes. As such, in order to maintain the axial length of the engine's resonator that is required for the optimum operating frequency, while keeping the system compact, elbow bends were introduced to coil the resonators' ductings.

Miles[52] regards acoustic propagation through 90° sharp bends to be a "discontinuity" in his investigation using transmission line analysis. It has also been shown in countless publications that losses are incurred in flow through duct bend systems[53, 54]. Although the flow losses through these bend discontinuity have been considered to be minor, the cumulative losses of all the bends used in the coiled resonator would contribute to a non-negligible, percentage drop of the engine's overall efficiency. This is especially since the efficiency of the system is largely based on the maximum achievable travelling wave amplitude propagating through the resonator loop. It is thus important to investigate the alteration in the acoustic wave properties as it propagates through these discontinuities. This is not only with respect to the acoustic transmission losses through them, but also its impedance and pressure and velocity phasing and standing wave ratio as well. As previously mentioned, these are important parameters to consider in the design of a thermoacoustic engine's resonator and will determine the performance of the systems. The literature review of oscillating flow through bend discontinuities and curved duct systems is given in the following subchapter.

1.3 Flow Oscillation through Duct Bend systems

The propagation of acoustic oscillation through duct systems can be categorised as unsteady flows of a compressible fluid. In addition to this, these acoustic oscillations also have characteristics of a wave which allows it to be reflected, diffracted and distorted. There are two branches of literature which investigate oscillating flow systems through duct bend systems. The first is largely based on treating the acoustic oscillation as a wave. These investigations are largely based on the analytical modelling of acoustic wave propagation in ducts as transmission line systems. The empirical investigations are based on the analysis of the pressure measurements using signal processing techniques. These acoustic wave investigations are however, limited to the plane wave mode of propagation in waveguide systems. The second branch of literature concerns oscillating flow systems through curved ductings system. These investigation focus on the flow behaviour of the oscillation as it propagates through the curved sections of the ducting. These investigations involve

numerical investigation of the oscillating flow in both the axial and cross sectional plane of the curved ducting section. These numerical investigations have been verified with experimental flow visualisation and measurements. Both of these literatures are discussed in greater detail in the following subchapters.

1.3.1 Literature review on Acoustic wave propagating through Duct Bend systems

In 1945, Rayleigh[55] identified the difference in flow characteristics of acoustic wave propagating through a curved duct from that of straight one. This initial finding was based on the numerical analysis of the equation of motion. Parallel to the development of these numerical investigation was the development of analytical modelling used to investigate the acoustic wave transmission through duct bend systems [56]. Most notably of this was Miles' [57-59] proposal of using the transmission line model analogous to electrical systems in order to model the acoustic transmission in 90^{o} mitered bend duct systems. Lippert[60, 61] conducted experimental investigations on square cross section mitered bends for various angles. Lippert's results successfully verified Miles' transmission line theory for the single mode plane wave approximation. Furthermore, Lippert's results showed that introducing a curvature (equal to the width of the duct) to the outer wall of the mitered bend had significantly increased the acoustic transmission through the bend. Dequand et al[62] conducted both numerical and experimental analysis on wave transmission through 90 degree sharp bends for both circular and square cross sectional waveguide systems. Dequand used the four microphone Scattering Matrix technique to obtain acoustic transmission results similar to Lippert's. Dequand's results are shown in Figure 1-8. The investigated range of frequencies for the works conducted thus far corresponds to 0Hz to the plane wave mode of propagation cut off frequency (dependent on the hydraulic diameter of the duct ≈2000Hz). The summary of the acoustic transmission from literature is given in Figure 1-8. The dimensionless frequency is the ratio of the investigated frequency over the cut off frequency for the plane wave mode of propagation. The cut off frequency for waveguide systems are given by Equations (2.3) and (2.4). It

is thus shown that these investigations are made exclusively within the range of the plane wave mode of propagation..

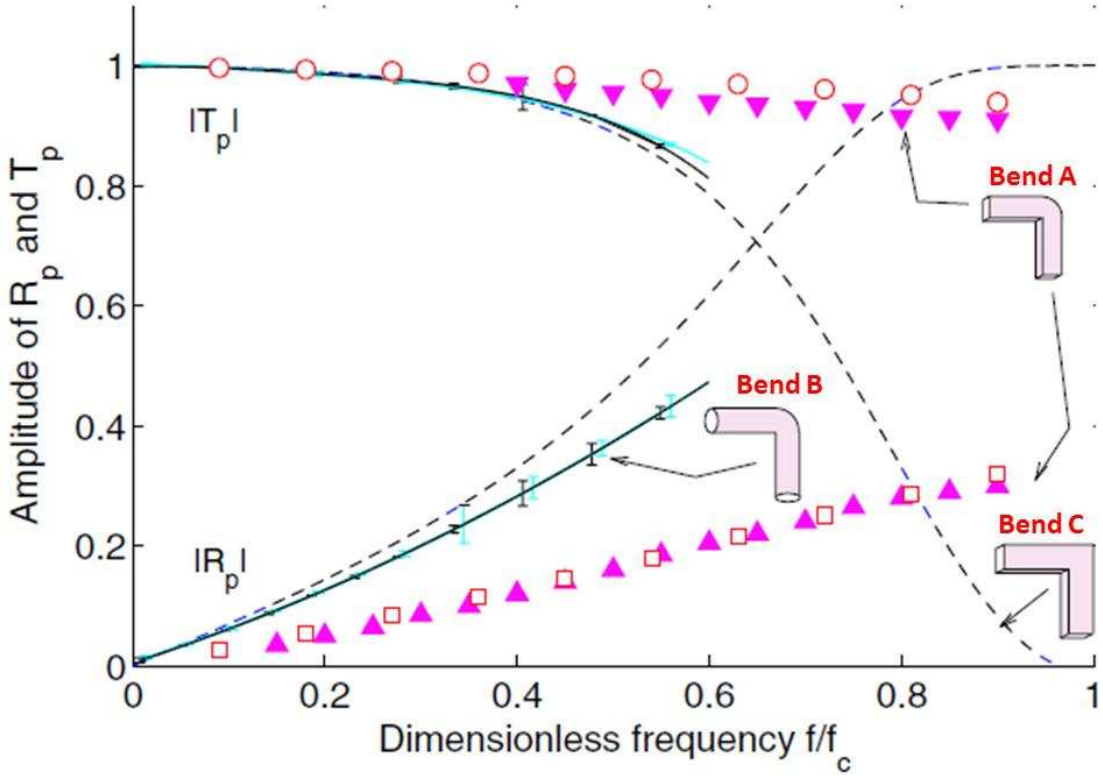

Figure 1-8: The acoustic transmission and reflection coefficients plotted against the dimensionless frequencies for the 3 types of investigated bends[63]. The cut-off frequency used in this investigation is 67 kHz. Lippert's results on Bend A are given by(∇, Δ). This is compared with the 2-D numerical data obtained by Dequand represented by ($\square, \circ$). Numerical investigated were also used to investigate transmission through Mitered bends. The results for Bend C are given by '- - -'lines. The solid lines represent the experimental result of the pressure wave decomposition (PWD) technique used to investigate Bend B.

Dequand's results show that the acoustic transmissions within the 3 bends are similar for acoustic oscillations below 1000Hz. The divergence in transmission behaviour is shown to occur at approximately 2,600Hz. At higher frequencies, it is shown that bends with curvatures have much higher transmitivity as compared to mitered bends.

There have also been investigations conducted on "long waves" propagating through curved duct bend systems. Rostafinski conducted a comprehensive study on the subject using both analytical modelling[56] and numerical techniques[64] in order to model acoustic transmission through two dimensional duct bend systems. His works were expanded upon and verified experimentally by several others, including Cummings[65], Cabelli[66], El Raheb and Wagner[67]. These works are

collocated in a monograph on the subject published by NASA [68]. The main points derived from these works are summarised in point form bellow:

1. The plane wave mode of propagation cannot be sustained within the curved section of the duct bend. Curved duct section causes a variation in pressure and velocity distribution in the cross section of the curvature. It is shown however, that the waves straighten back up into a plane wave after propagating through a distance equivalent to its hydraulic diameter in the straight duct section after the bend. This is shown in Figure 1-9

2. The acoustic wave propagating through a curved duct bend has a higher phase velocity as compared to that through a straight bend.

3. Low frequency acoustic oscillations have better transmitivity through duct bend systems. The longer waves cause less reflection in the bend and also have a lower rate of energy dissipation through convection in the duct bend.

4. As a long wave propagates through a duct bend, some of the wave's energy is "stored" within the duct bend section. This represents the energy convected for the formation of higher oscillation modes or acoustic streaming.

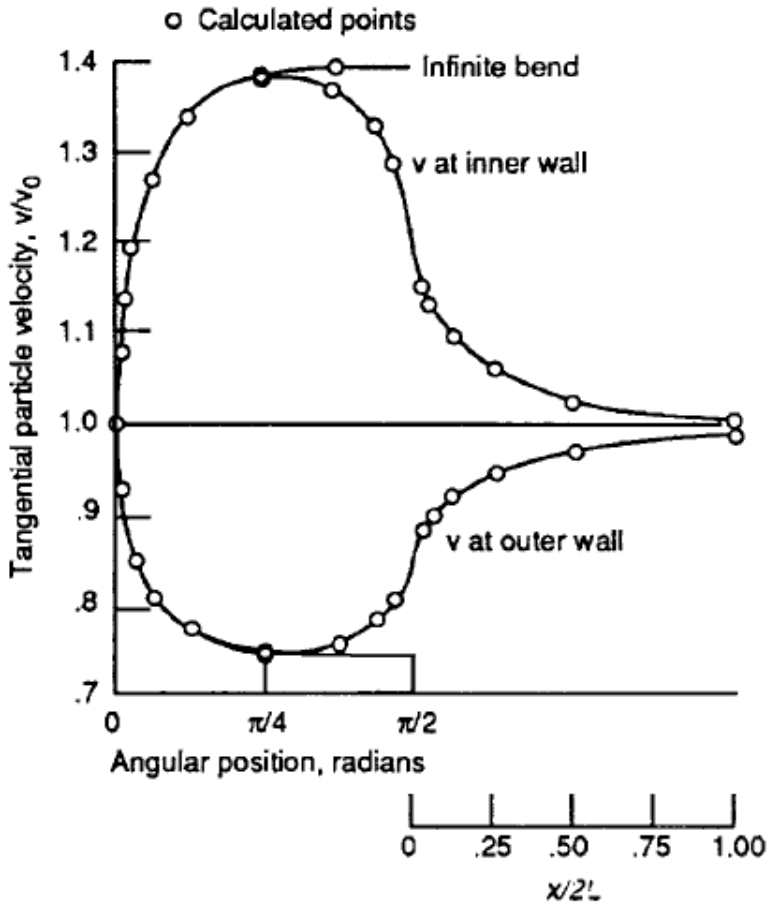

Figure 1-9: The plot of the tangential particle velocity against the axial length of the curved elbow duct bend. V_0 represents the tangential particle velocity at the 0 radian, angular position. The x represents the distance travelled by the wave through the straight duct section after the bend. It is shown that the velocity profile straightens back up into that of a plane wave mode of propagation after travelling the distance equal to the hydraulic radius of the duct[56].

1.3.2 Literature review on acoustic wave propagation through Curved duct systems

Studies on flow properties through curved ductings have been done as early as 1910. Eustice[69] studied energy flow losses in curved pipe by comparing the pressure change between fluid flowing down coiled spiral pipes to that of a fluid flowing down a straight slanted pipe from the same elevated height, with the same axial pipe length. Through numerical perturbation analysis, Dean[70] realised that these additional flow energy losses through curved ducts were caused by the convection of a portion of the primary axial flow energy into secondary flow circulations. The developments of these secondary flows are a result of the pressure gradient formed between the inner and outer cross section of the duct due to the centrifugal forces generated by the primary axial flow through the curved section of the ducting[71].

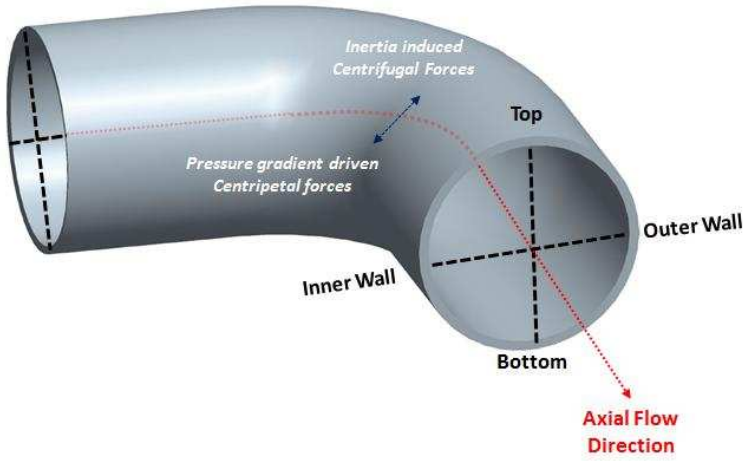

Figure 1-10: The illustration of the different forces generated for a flow through a duct bend system

The flow losses in curved ductings are thus mainly dependent on the magnitude of the generated centrifugal forces which is a function of the slender ratio (hydraulic radius to the radius of curvature of the duct) of the duct as well as the ratio between the inertia and viscous forces of the flow(Reynolds number). Based on this, Dean[72] found the relationship between the product of the square root of the slender with the Reynolds number to be able to accurately characterise the flow through curved duct and predict the energy losses in them[73, 74]. This non-dimensional parameter became known as the Dean Number.

$$\mathrm{De} = \left(\frac{ur}{\nu}\right)\left(\frac{r}{\mathrm{R}}\right)^{\frac{1}{2}} \tag{1.8}$$

Since Dean's reports in (1927 & 1928), numerous other researches had been made regarding steady flow through curved ducting systems. With the advancement of measurement technologies such as the hotwire, LDV and PIV systems, experimental measurement and flow visualisation investigations had also been made on the flow through curved duct. A large portion of these numerical simulation and experimental investigations of steady flow through curved ducts were summarised in Berger's comprehensive literature review on the subject[53]. A majority of these researches focused on the axial velocity profile of the flow as well as the cross sectional secondary flow circulation patterns in curved ductings in order to deduce the flow characteristics and the various forces controlling them. For low Dean number values, the viscous boundary layer thickness is close

to the hydraulic radius of the duct. In this case, the flow is viscous dominated, causing the flow to behave similar to a steady state flow through a straight duct, with an axial velocity profile similar to that of a Poiseuille type flow. Viscosities are the main causes of flow losses for this type of flows (Table 1-2 [Region A]). For larger Dean number values, the viscous boundary layer is restricted to the vicinity of the duct's wall causing the axial oscillating flow in the core region of the duct to be inviscid and inertia dominated. The tangential component of the inertia dominated inviscid axial flow causes the axial oscillating flow velocity profile to be skewed towards the outter wall of the curved duct which in turn forms a pressure gradient across the cross section of the curved duct. The pressure gradients generates the centrifugal effect which induce a pair of secondary counter rotating flow circulations which are symmetric in the top and bottom half of the cross section of the duct (Table 1-2 [Region B]). These pairs of secondary circulation pattern are known as the Dean type circulation as shown in Figure 1-11. The superposition of these secondary circulations with the primary axial flow causes the higher primary axial flow velocity to be concentrated towards the outer wall of the curved duct. The flow losses, in this case, are mainly due to convection. These numerical and experimental observations were mainly conducted with circular cross section curved ducts. It is, however, interesting to note that the same Dean type secondary flow circulation were observed for steady flow through square cross section curved ducting systems (with sufficiently large Dean Number)[75]. This suggests secondary flow circulations in curved ducts are, to a certain extent, independent of the curved duct's cross sectional shape.

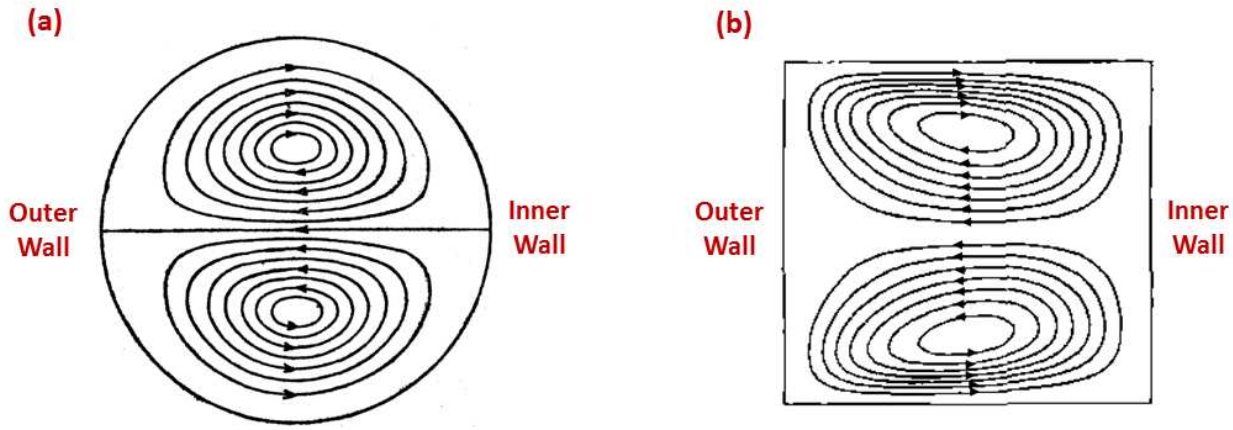

Figure 1-11: The Dean type secondary circulations in circular and square cross section ductings.

The flow through curved/coiled duct systems described thus far, are considered to be steady unidirectional flows (also known as “through” and “DC flows” in certain literatures). There has also been a great interest in the investigation of unsteady flow systems through curved ducting especially related to the circulatory systems in the biomedical field as well as other industrial applications. The investigation done on these unsteady systems may be categorised into oscillating and pulsating flow systems. Both oscillating and pulsating flow systems are periodic. For simplification purposes, the oscillating flows investigated by the majority of literature are sinusoidal with a zero mean. Pulsating flows systems are the superposition of an oscillating flow with a mean flow. Periodic unsteady flows are synonymous with the acoustic flow propagation through thermoacoustic resonator systems. Pulsating flow may represent acoustic propagation with the occurrence of acoustic streaming. This literature on unsteady flow through curved ducting thus forms the background for the understanding of the different acoustic propagation behaviours in curved resonators and their respective loss mechanism, plus offering some insight as of how to optimise these systems. The results from the experimental measurements and observations made will also be compared with these literatures.

In order to characterise the unsteady flow, another non-dimensional parameter is required in order to take into acoustic the periodicity of the unsteady flow. This frequency parameter was first introduced by Womersley[76] and was initially used as reference in order to maintain the “dynamic symmetry” of scaling up of blood vessel models for experimental investigations. The Womersley parameter is the ratio of the inertia contribution of the unsteady flow to its viscous component[77]. Incidentally, this also gives the length ratio of the hydraulic radius to the thickness of the viscous boundary layer.

$$\alpha = \frac{\sqrt{2}\ r}{\delta_{viscous\ penetration}} = \mathrm{r}\left(\frac{\omega}{\nu}\right)^{\frac{1}{2}} \tag{1.9}$$

Lyne[78] pioneered this area of research when he conducted numerical perturbation analysis (similar to that used by Dean) by using a low frequency, sinusoidal varying flow in order to study the behaviour of unsteady flow through the curved duct. Lyne's unsteady perturbation analysis revealed a different form of secondary flow pattern from those previously described by Dean. The illustration of these flow patterns are shown in Table 1-2. The secondary motion shows the formation of 2 pairs of counter rotating circulation. The first pair was confined to the viscous boundary region and showed motion similar to the Dean type circulation; the second pair was located in the central free stream region of the cross section with circulatory direction towards the inner wall of the curvature. This central inviscid secondary circulation pair shows the dominance of the centripetal effect for these flows. The superposition of the secondary flow with the primary unsteady axial flow resulted in the higher axial velocity being forced towards the inner wall of the curvature. This unsteady secondary flow pattern was named the "Lyne-type circulation" after its founder. The discovery of this centripetal dominant secondary circulation was further verified independently through numerical and experimental analysis by Zalosh et al[79], Munson[80], Mullin et al[81] and Eckmann et al[82]. Bertelsen[83] later used a suspension of tracer particle in the flow that allowed visual confirmation of the formation of these secondary "Lyne type vortices".

The existence of Lyne type circulation for unsteady flow through curved duct systems shows that there is a magnitude reversal of the pressure gradient between the inner and outer wall of the curvature that causes a transition of influence between the apparent centrifugal forces observed in steady flow to the centripetal forces in unsteady flow systems. The balance between centrifugal and centripetal components is determined by the unsteady inertia component of the flow as well as the flow viscosity which are represented in the simplified Navier Stokes equation in toroidal coordinate system, given as[84]:

$$\frac{\partial u}{\partial t} + u\frac{\partial u}{\partial r} + \frac{w}{r+R}\left(\frac{\partial w}{\partial \theta} - w\right) = -\frac{1}{\rho}\frac{\partial p}{\partial r} + \upsilon f_{\upsilon} \tag{1.10}$$

Table 1-1 The components of the Navier stokes equation

Navier Stokes Terms	Equations
Spatial Inertial force	$\rho u \frac{\partial u}{\partial r}$
Temporal Inertial force	$\frac{\partial u}{\rho \partial t}$
Centrifugal force	$\frac{w^2}{r+R}$
Pressure gradient	$\frac{\partial p}{\partial r}$

In the central free stream region of the duct, the flow may be assumed to be inviscid ($\upsilon f_\upsilon = 0$) and that $\frac{w}{r+R}\left(\frac{\partial w}{\partial \theta}\right)$ is smaller than $\frac{w^2}{r+R}$. The pressure gradient in the central region can thus be written as:

$$\frac{\partial u}{\partial t} + u\frac{\partial u}{\partial r} - \frac{w^2}{r+R} \approx -\frac{1}{\rho}\frac{\partial p}{\partial r} \tag{1.11}$$

From both (1.10) and (1.11), it can be deduced that the pressure gradient which determines the balance between the centrifugal and centripetal forces in the duct are dependent on the ratio of the unsteady inertia effect as well as its viscous forces. The geometric parameters and flow characteristics that influence this ratio is given by both the Dean and Womersley number. It was found that the previous research on Lyne type circulation in unsteady flow systems were mainly focused on low Dean and Womersley number. Yamane et al[85] extended this research by conducting further numerical and experimental analysis for a wider range of Dean and Womersley number. Yamane showed that by using these two parameters, the unsteady flow can be characterised into seven flow regions which consist of two distinct regions (centripetal and centrifugal dominated regions) and five step transitional regions[85]. Sudo expanded on this research by conducting flow visualisation analysis on oscillating flows for each of these regions[86].

Tada continued by conducting numerical analysis on pulsating flow systems for these regions[87]. The results from the analysis of these regions show a consistent match. The summary of the flow characteristics of the different regions are given in Table 1-2.

Table 1-2: The description of the characteristic regions of oscillating flow through curved waveguide systems [85, 86, 88]

[Region A] ***Poiseuille Type Flow***	***Viscous Dominated Region***
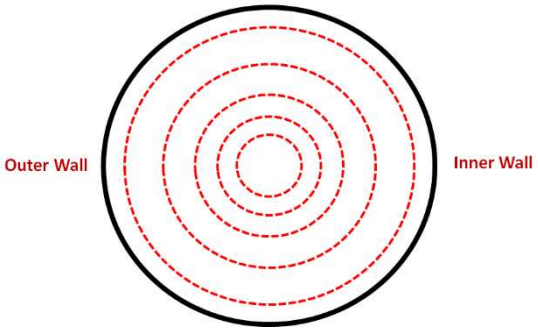	***Region Boundaries:*** *Low Dean Number & Low Womersley Number* $(De \leq 15 \quad \& \quad \alpha \leq 2)$ *For very low Dean and Womersley number, a large viscous boundary layer exists and that extends throughout the cross section of the duct. The oscillating flow exhibits an almost symmetrical Poiseuille axial velocity profile. This flow behaviour is analogous to a unidirectional steady laminar flow through a straight pipe[89].*
[Region B] ***Dean Type Vortices***	***Centrifugal Dominated Region***
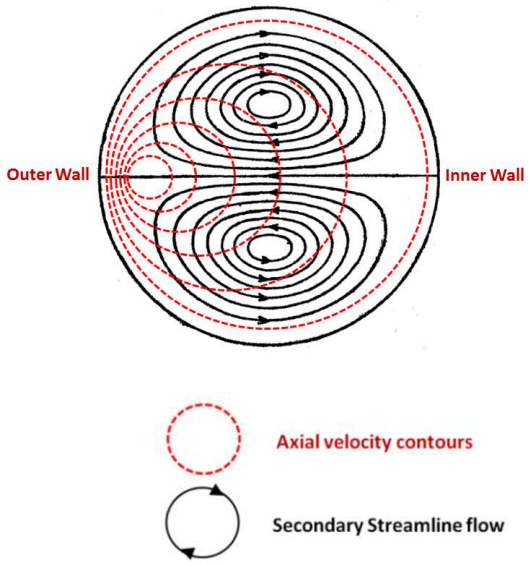	***Region Boundaries:*** *Low Dean Number* $(15 \leq De \quad \& \quad 2 \leq \alpha \leq 5.5)$ *High Dean Number* $(De \geq 200 \quad \& \quad \alpha \leq 5.5)$ *With a slight increase in Womersley number, the viscous boundary layer is still large but no longer extends throughout the entire cross section of the duct. However, it has a central inviscid core. The oscillating period is large as compared to the viscous diffusion rate. As such, the oscillating flow behaves as unidirectional flow through a curved duct. The increase in Dean number also meant that the central axial inviscid flow generates a dominant centrifugal force that builds a pressure gradient between the outer and inner wall of the curvature[80]. This induces a pair of secondary counter-rotating circulation that concentrates higher axial oscillating velocities towards the boundary layer of the outer wall of the curvature. These secondary circulations are known as Dean type Vortices. The large viscous boundary layer ensures that these Dean vortices remain in the central region of the duct.*
[Region C] ***Deformed Dean Type Vortices***	***Centrifugal balanced by Centripetal Pressure Gradient***
	Region Boundaries: *Low Dean Number* $(15 \leq De \leq 100 \quad \& \quad 5.5 \leq \alpha \leq 10)$ *High Dean Number* $(De \geq 200 \quad \& \quad 5.5 \leq \alpha \leq 10)$ *A further increase in the Womersley number would further reduce the thickness of the viscous boundary layer relative to the radius of the pipe. This allows for an inviscid central region in the duct for axial oscillating flow which increases the unsteady inertia effect in*

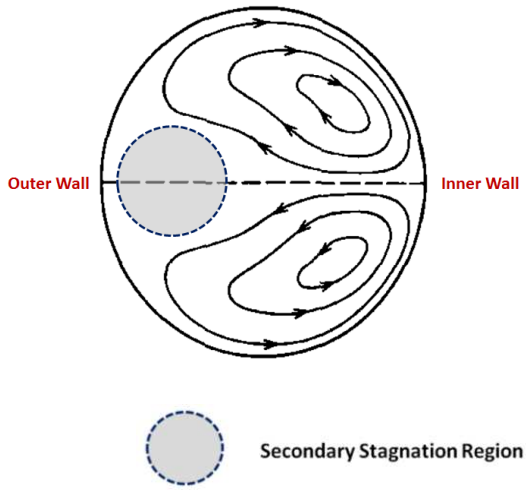	*this region. At this Womersley number, the inertia effect caused by the inviscid oscillation is a balance between centrifugal forces and the centripetal pressure gradient. This weakened the secondary flow towards the outer wall of the curvature and creates a secondary flow stagnation region in that area. This deforms and displaces the pair Dean vortices towards the inner wall of the curvature.*
[Region D] *Transitional type Vortices*	***Time Dependent Centripetal Pressure Gradient Dominance***
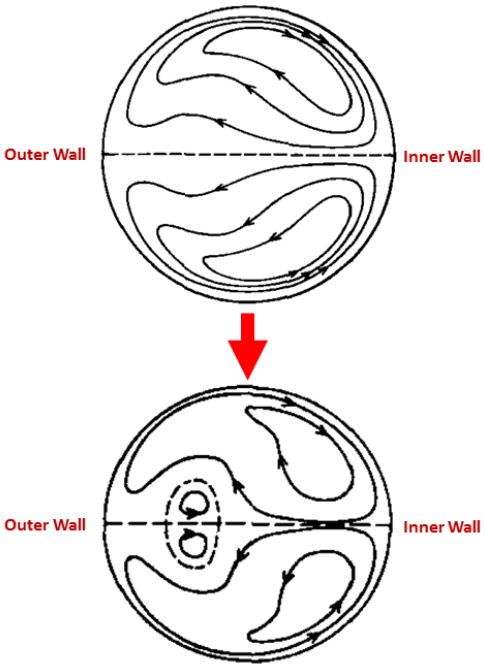	***Region Boundaries:*** *Low Dean Number* $(De \leq 100 \quad \& \quad 10 \leq \alpha \leq 14)$ *High Dean Number* $(De \geq 200 \quad \& \quad 10 \leq \alpha \leq 16)$ *The Transitional type secondary circulation behaviour is interesting because for the first half of the oscillating period, it behaves as the Deformed Dean type circulation, and the next half, it behaves as the Deformed Lyne type circulation.* *An increase in Womersley number causes a greater inertia effect as compared to the viscosity. This in turn produces a large centripetal pressure gradient that dominates over the centrifugal forces. This causes the fluid in the secondary stagnant region to move towards the inner wall of the curvature through the central region. The combination of this secondary flow with the deformed Dean circulation causes the formation of an additional two counter-rotating circulations near the outer wall of the curvature. These are preliminary stages of the Lyne type secondary circulation.* *The second half of the period the centripetal pressure gradient is reduced to the same level as the centrifugal forces, and the deformed Dean type circulation is reformed.*
[Region E] *Deformed Lyne type Vortices*	***Large Centripetal Pressure Gradient***
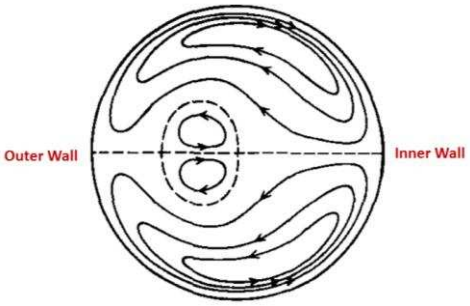	***Region Boundaries:*** *Low Dean Number* $(De \leq 100 \quad \& \quad 10 \leq \alpha \leq 17)$ *High Dean Number* $(De \geq 200 \quad \& \quad 10 \leq \alpha \leq 18)$ *Increasing the Womersley number causes the centripetal pressure gradient forces to be larger than the centrifugal forces throughout the oscillating period. The Lyne type circulations become more defined and move closer to the central region of the duct.*
[Region F] *Lyne type Vortices*	***Centripetal Pressure Gradient Dominated Region***

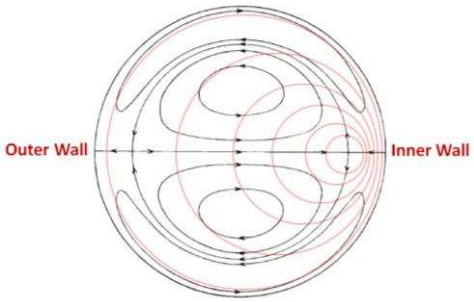	***Region Boundaries:*** *Low Dean Number* $(De \leq 100 \quad \& \quad \alpha \geq 17)$ *High Dean Number* $(De \geq 200 \quad \& \quad \alpha \geq 18)$ *With large Womersley number the viscous boundary layer is now confined to a thin layer near the duct walls. The centripetal pressure gradient greatly dominates the inviscid axial central flow. Thus the Lyne type vortices are shown to be large and at the centre of the duct. The Dean type circulation are displaced towards the upper and bottom boundary layer of the duct. The centripetal pressure forces the higher axial velocity towards the inner wall of the curvature.*

1.4 Problem Statement and Research Objectives

This research investigates the acoustic wave transmission through curved duct bend systems with the objective of optimising the SCORE-stove travelling wave thermoacoustic system. The investigation was conducted using particle image velocimetry and involves:

- Qualitatively understanding the change in oscillating flow behaviour in the duct bend and how it leads to the various acoustic energy loss mechanisms in the system.
- Quantitatively measuring the acoustic transmission through curved duct bend system

1.4.1 Problem Statement

The optimum operating frequency for the SCORE-stove linear alternator falls within the range of 50Hz to 200Hz. These frequencies correspond to the lower end of the investigated range for acoustic transmission through duct bend literature. The results obtained for this range of frequency were mostly obtained through numerical investigation, analytical modelling and extrapolation of empirical results. Direct experimental measurement within this range of frequency has proven to be difficult. The techniques used to measure the acoustic transmission relies on the cross correlation between two measured points, separated at short distance along the axial length of the investigated waveguide system. The challenge largely lies in finding the appropriate measuring instruments that has sufficient resolution to accurately measure the change in

amplitude and phasing between these two measured points for long wavelength oscillations. In addition, the amplitude of the acoustic wave propagating through the thermoacoustic resonator is large. As such, the measuring instrument is required to be able to measure large amplitudes and at the same time have a very good measurement resolution. It is generally observed that the resolution of an instrument is inversely proportional to its amplitude range. The measurements are often made using pressure transducers that are flush mounted onto duct which allows for a non-intrusive measurement of the wave. This technique assumes that the wave propagates only in the plane wave mode of propagation. The hydraulic radius of the SCORE-stove resonator however is relatively large in size. The large oscillating amplitude and hydraulic radius may results in the distortion of the plane wave mode of propagation within the straight section of duct itself. This will undoubtedly cause complication with the measurements. Therein lays the advantage of using PIV for this investigation. PIV allows for the confirmation of the plane wave mode of propagation before measurements are made. The adaptive correlation technique used to process PIV images ensures that the most suitable interrogation window size is used to compute each velocity vector in the measured plane. This improves the accuracy of the measured velocity vectors as well as the resolution of the measurement as a whole.

In addition to measuring the acoustic transmission, this research also aims at understanding the acoustic energy loss mechanism of an acoustic wave propagating through a curved duct elbow bend system. There is a detailed literature regarding the investigation of oscillating flow behaviour in the cross sectional plane of curved ducting systems. The duct curvature causes a variation in the velocity profile of the oscillating flow propagating thought it. The plane wave of propagation is thus skewed to the inner or outer wall of the bend depending on the frequency and amplitude of oscillation. This leads to the formation of secondary flow circulations in the cross sectional plane of the curved duct section. These secondary circulations are predicted to be three dimensional in nature and should also be observed in the axial cross sectional plane of the duct bend. The investigations of oscillating flow through the duct bend in the axial plane are however limited and

have not been compared with the behaviour observed in the cross sectional plane. The author hypothesises that correlations exist between these secondary circulation structures and the acoustic transmission of the system. It is noted however, that there has yet to be any work bridging the literature of acoustic transmission in duct bend systems with that of the investigation of oscillating flow behaviour in curved duct bend systems.

1.4.2 Research Objectives

a) Develop a new technique for quantatively analysing the acoustic transmission through duct bend system from PIV measurements.

b) Identify the various oscillating flow loss mechanisms that contribute to the net acoustic transmission loss of the system.

c) Find a unifying non-dimensional parameter that will help identify the acoustic transmission behaviour of acoustic waves based on the geometric properties of the duct bend as well as the properties of the acoustic wave.

d) Find the optimum acoustic transmission condition based on the identified non-dimensional parameter.

1.5 Thesis Outline

The technique previously used to empirically measure the acoustic transmission through duct bend systems are reviewed in Chapter 2. These techniques are largely based on one dimensional signal processing methods in order to generate inputs for analytical transmission line models. The experimental investigation using the pressure wave decomposition technique is also given in this chapter. It is shown here that the pressure transducer does not have sufficient resolution to give accurate results for the investigated range of frequencies. As such, the research proceeds with PIV investigations on the duct bend system.

Chapter 3 introduces the particle image velocimetry technology and describes in detail the PIV system used in this investigation. This chapter also discuss the experimental setup of the PIV

system for acoustic wave measurements. This includes the investigation of suitable seeding techniques for acoustic oscillations, the methods to reduce reflection and glare and the PIV image recording techniques. Chapter 4 describes the development of the Velocity based Wave Decomposition (VWD) technique based on the PWD describes in Chapter 2.0. The VWD technique was developed to analyse the PIV measurements. PIV measurements allow for the reconstruction of the oscillating wave's amplitude profile along its axial length for each measured timestep. This allow for a more precise measurement of the difference in oscillating amplitude between the two cross correlated points that would improve the accuracy of the wave decomposition technique.

The experimental setup for PIV investigation on acoustic wave propagating through duct bends systems is given in detail in Chapter 5. This chapter also discusses the preliminary observations made from the raw PIV velocity vector results as well as the as the mean flow circulation pattern observed in the axial plane. The mean flow component would be used to verify the identified secondary flow circulation in later chapters. This chapter concludes with a detailed description of the Proper Orthogonal Decomposition (POD) which was further used to analyse the PIV results.

The results for the Proper Orthogonal Decomposition technique are discussed in Chapter 6. The Proper Orthogonal Decomposition technique shows that the first two Proper Orthogonal Modes (POMs) correspond to the acoustic wave propagating though duct bend system. The third and higher modes correspond to the acoustic energy convected to the formation of secondary circulations. The energy cascade loss mechanism has also been identified using the POD technique.

The POD technique also allows for the quantitative measurement of the kinetic energy available in each POM. As such, the percentage acoustic energy transmitted through the bend can be computed from the POD results. Chapter 7 describes the development of a unifying non-dimensional parameter for the prediction of acoustic transmission through the duct bend systems. The acoustic transmission results were also compared with extrapolated results found in literature. It is shown that the acoustic transmission can be divided into 3 distinct regions based on the

different dominating loss mechanisms. The non-dimensional number which fits the acoustic transmission behaviour within duct bend systems corresponds to the ratio of the square of the Womersley number to the Dean number. This parameter is named the Strouhal Dean number. It is shown that an optimum transmission value exists for this parameter.

Chapter 9 discusses the application of this research for the optimisation of Thermoacoustic heat engine systems. Chapter 10 then summarises and concludes this thesis.

Chapter 2

Investigation Techniques for Acoustic Waveguide System

2.0 Investigation Techniques for Acoustic Waveguide systems

The acoustic wave propagation in the resonator loop of the Thermoacoustic engine can be modelled using lumped element analysis[90] as shown in the previous chapter. The lumped component model simplifies the description of the spatial behaviour of acoustic waves into 1-D transmission line approximation. This means that each component of the resonator loop has their respective transmission characteristics determined by their respective complex impedance. This research focusses on the acoustic transmission through elbow bend which gives the resonator its characteristic feedback loop behaviour.

In order to study the propagation and transmission behaviour of waves, two distinct criteria are required. The first, is the ability to generate a wide range of different forms of acoustic wave for experimental investigation. The second, is that the different forms of acoustic wave can be accurately generated repeatedly. Based on these two criteria, subwoofers were chosen to be used as the acoustic source for the investigations instead of the Thermoacoustic engine loop itself. This is because the Thermoacoustic acoustic generation is susceptible to fluctuation due to a variety of parameters which are difficult to control[91]. This also removes the complexity of the start-up time required for the engine as well as the tedium of changing the resonator components in order to get the different acoustic waves. The use of a function generator and a power amplifier allows a more accurate control of the acoustic wave produced by the subwoofer and also allows the generation of a wide range of different acoustic waves such as those usually found in the engine loop. This

chapter describes the measurement and analytical techniques used for acoustic wave measurement and analysis. It also describes the experimental setups and the development of the experimental techniques which are expounded in later chapters.

2.1 Acoustic Wave Measurement and Analytical Techniques

Acoustic transmission is an important parameter for the optimisation of waveguide system whether to promote or suppress acoustics waves. The Noise Pollution and Abatement Act of 1972[92] regulates the noise level acceptable for both the aerospace and automotive industry. Similarly, for most engineering purposes, aeroacoustics and thermoacoustic generation from pipe flows, jet flow, combustion, etc. are perceived as detrimental. Acoustic transmission plays an important role in the material and design selection for exhaust muffler and silencer systems[93]. There are also studies being done to promote better acoustic transmission through waveguide systems. These include studies on musical instruments, particularly pertaining to wind instruments where the acoustic transmission through the instruments' curved or loop resonators are essential[94, 95]. Similarly, the same measurements and analytical techniques will be applied to analyse the acoustic transmission through the bends used in the thermoacoustic feedback resonator loop.

The field of acoustic studies is based on two main measureable properties of an acoustic wave, its pressure and its velocity. Both of these properties are related by a third property known as the acoustic impedance. The acoustic impedance is the measure of the level of sound pressure generated by the vibration of the acoustic medium at a particular frequency. It is given by the ratio of the acoustic pressure to the flow volume (velocity x cross sectional area), U:

$$Z = \frac{p}{U} \tag{2.1}$$

In waveguides, the acoustic impedance of the system is determined by the physical and geometric characteristics of the waveguide, its termination and the frequencies of the wave propagating

though it. The acoustic impedance, in this case, can also be thought of as the complex resistance the acoustic wave encounters propagating through the section of the waveguide. If the impedance of the waveguide matches that of the termination and that of the acoustic wave, the incident acoustic wave is allowed to propagate through the waveguide without having any reflections. In this case, the incident acoustic wave is termed as a pure travelling wave and the pressure and velocity measurement made by any position along the wavelength of the wave would yield the same amplitude. The pressure and velocity oscillation would also be in phase. In this case, the acoustic transmission can be measured using just 2 pressure transducers.

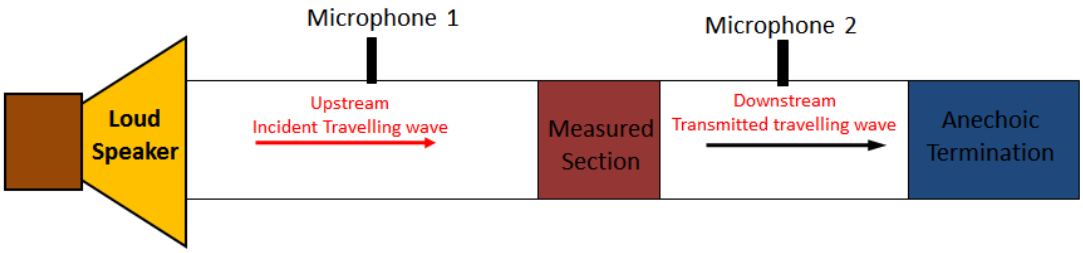

Figure 2-1: Ideal case in which the acoustic impedance of the waveguide ducting, the measured section and the termination are a match. Since both upstream and downstream wave are pure travelling waves, only one pressure measurement is required for each section. The acoustic transmission would thus be the amplitude of the transmitted wave over that of the incident travelling wave.

In most cases however, the waveguide and termination impedance are a mismatch. The change in impedance at the termination of the waveguide causes reflection to occur. The amplitude of the reflected wave is proportional to the degree of mismatch between waveguide and termination impedance. The termination also determines the phase in which the wave is reflected at. The reflected wave is superimposed on the incident travelling wave to form what is known as a standing wave. The ratio between amplitudes of the incident and reflected waves is known as the Standing Wave Ratio (SWR) and is given by *Equation (2.2)*, where A and B are the incident and reflected wave's amplitude respectively.

$$SWR = \frac{A + B}{A - B} \tag{2.2}$$

In the case where the SWR is not equal to unity, the pressure and velocity measurements made at different positions along the wavelength of the wave would yield different amplitudes. The acoustic transmission measurement technique shown in Figure 2-1 is no longer applicable and analytical techniques are first required to compute the acoustic impedance of the system before the acoustic transmission. The acoustic impedance is the ratio of the acoustic pressure to the volumetric velocity of the medium. The traditional method of measuring the acoustic impedance in waveguide system is shown in Figure 2-2. A microphone was used to measure the amplitude of the wave in accordance to the axially traversed distance of the pipe[96]. By measuring the amplitude change with respect to the traverse position of the microphone, the phasing of the wave can be found. This allows the computation of the impedance of the investigated section and thus the acoustic transmission. This technique has been used to measure acoustic absorption[97] of materials and acoustic transmission losses in pipe bends[98]. This technique is known as the Standing Wave Ratio (SWR) technique.

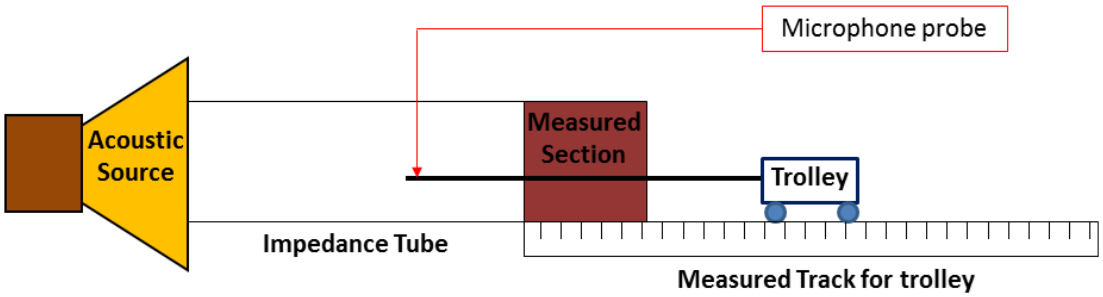

Figure 2-2: Experimental Setup for the Standing wave Ratio Impedance measurement technique. A microphone probe is used to measure the pressure transversely along the axial length of the pipe. The standing wave ratio found from the pressure measurements are used to compute the impedance of the system.

The Standing Wave Ratio method however, proved tedious and is an intrusive method of measurement which may affect the pressure readings. In order to overcome the complexity of the transverse microphone method, more convenient techniques have been developed which only requires fixed point measurements to be made. Figure 2-3 shows an example of the setup for such techniques. These fixed point measurement techniques are restricted to measuring the surface pressure on the inner wall of the duct. This limits the techniques to analysing only the acoustic

wave which propagates in the first mode plane wave mode of propagation. This condition is met if the wave frequencies investigated is below that of the cut-off frequency, f_c, for the first order mode of propagation which is given by:

For circular duct:
$$f_c = \zeta_0 \frac{c}{\pi d} \tag{2.3}$$

For square duct:
$$f_c = \frac{c}{2d} \tag{2.4}$$

The cut of frequency is a function of the speed of sound, c, the zero of the ordinary Bessel function of the first kind, ζ_0, and the duct's hydraulic diameter. It must also be noted that a plane wave propagating through any form of discontinuity and back into a constant cross sectional duct, will straighten itself back into a plane wave from any distortion after propagating through the axial distance equivalent to the waveguide's hydraulic diameter[99].

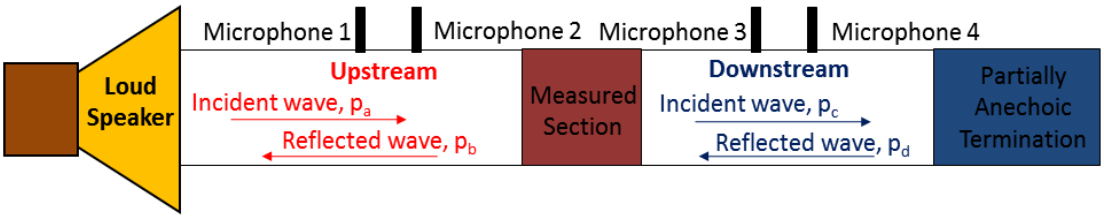

Figure 2-3: Fixed point pressure measurement techniques, a minimum of four pressure transducers are flush mounted onto the duct; two before the investigated section and two after the investigated sections. The separations between the microphones are known.

Given that the separation distances between the measured points are known, these techniques rely on the comparison between the amplitude and phasing between the measured points in order to determine the characteristics of the acoustic wave propagating through the duct.

There are two separate techniques for computing the acoustic transmission of the system utilising these measurement techniques; the first involves using the measured independent state variables to solve a matrix equation through which the matrix coefficient yields the transmission and reflected coefficient of the waves; the second involves using a transfer function in order to decompose the wave into its constituent incident and reflected components in order to analyse the

acoustic impedance. The first is known as the Two Port technique and the second the Wave Decomposition technique.

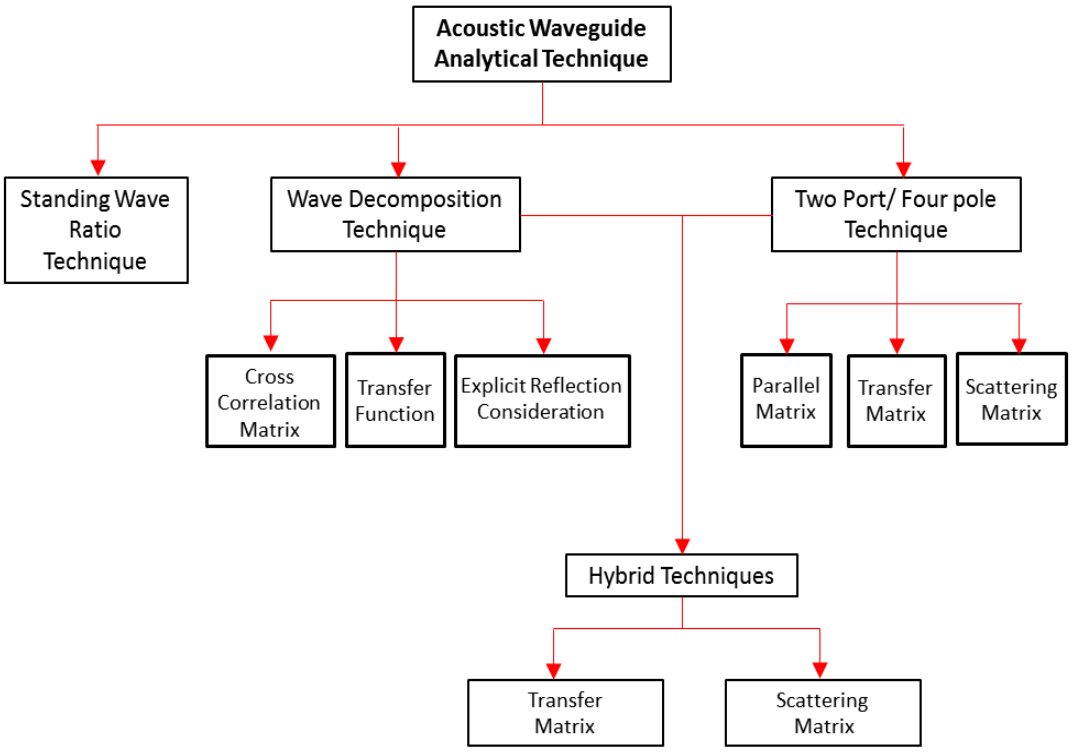

Figure 2-4: Summary of existing acoustic waveguide analytical techniques[93, 100-108].

2.1.1 Two Port/Four Pole Technique

The Two Port is an electrical analogy for modelling the linear transmission through a black box network system which is only accessible by its four terminals (quadrupole/four poles) which are paired to form the input and output ports[109]. The same system can be used to model linear plane wave acoustic transmission in duct systems. The two port system is described using two independent state variables at its pair of terminals as shown in Figure 2-5.

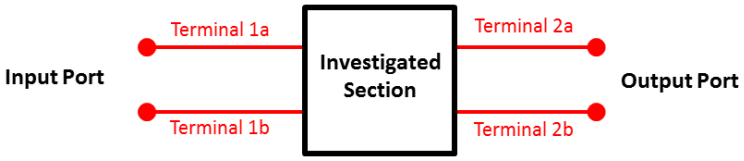

Figure 2-5: The Two Port Analysis system

In electrical circuits, voltage and current are commonly chosen as the pair of independent state variables. In acoustical analogy, the voltage is replaced by the pressure and the current by the volumetric velocity. The pair of independent state variables at the input and output terminals are related through a [2x2] matrix. The variation in position of the independent variables in the matrix equation determines the form of Two Port techniques that is used and the [2x2] matrix that is to be solved. There are generally 3 forms of Two Port Matrix techniques, namely, The Transfer Matrix, The Mobility Matrix and the Scattering Matrix, each of which has their respective advantage for analysing their particular systems.

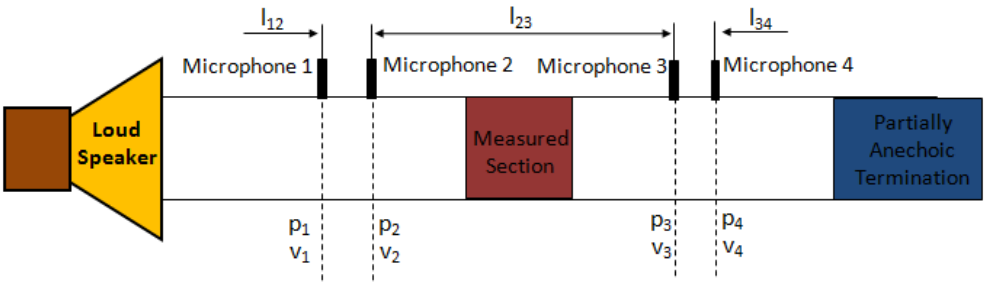

Figure 2-6: Two Port Transfer Matrix Setup

The Transfer Matrix Two Port method has the both the independent variables (pressure and volumetric velocity) on the terminals of the same port. This configuration is suitable for measuring transmission of networks which are coupled in cascade[100] such as the design of muffler and silencers systems[97, 110]. The Transfer Matrix equation is written generally as:

$$\begin{bmatrix} p_{output} \\ U_{output} \end{bmatrix} = \begin{bmatrix} T_{11} & T_{12} \\ T_{21} & T_{22} \end{bmatrix} \begin{bmatrix} p_{input} \\ U_{input} \end{bmatrix} \tag{2.5}$$

The Mobility Matrix Two Port method is one which has the set of same independent variables at the terminals of the same port[111]. This form of the Two Port analysis is also known as the Impedance parameter (Z-parameter)[112] since the solution to the Mobility Matrix is the ratio of the pressure to the volumetric velocity. The Mobility Matrix is suitable for networks which are coupled in parallel.

$$\begin{bmatrix} p_{input} \\ p_{output} \end{bmatrix} = \begin{bmatrix} Z_{11} & Z_{12} \\ Z_{21} & Z_{22} \end{bmatrix} \begin{bmatrix} U_{input} \\ U_{output} \end{bmatrix} \tag{2.6}$$

The Scattering Matrix technique is a combination between the Two Port Matrix and the Wave Decomposition analysis techniques. The technique uses the incident and reflected component of the measured waves in its input and output terminals of only one variable (either pressure or volumetric velocity).

$$\begin{bmatrix} p_{incident,downstream} \\ p_{reflected,upstream} \end{bmatrix} = \begin{bmatrix} T_i & R_r \\ R_i & T_r \end{bmatrix} \begin{bmatrix} p_{incident,upstream} \\ p_{reflected,downstream} \end{bmatrix} \tag{2.7}$$

The upstream and downstream annotation refers to the wave decomposition analysis done before the investigated section (upstream) and after the investigated section (downstream). The wave decomposition technique will be discussed in greater detail in the next Sub-Chapter 2.1.2.

Equation (2.5) and (2.7) are underdetermined systems. The matrices have four unknown coefficients, with only 2 equations. In order to solve these Matrices, a second set of measurement is required with a slight change in experimental parameters. There are two established method to obtain the second set of equation. The first is to change the complex termination impedance of the system, by changing the termination load of the system[93, 113]. This is known as the two load method. The difference in acoustic impedance between the two terminations has to be sufficiently large in order to avoid the matrix from becoming singular. The second technique method is to swap the position between the acoustic source and termination. This technique is known as the two source method and will only work if the measured system is not symmetric between source and termination[106]

.

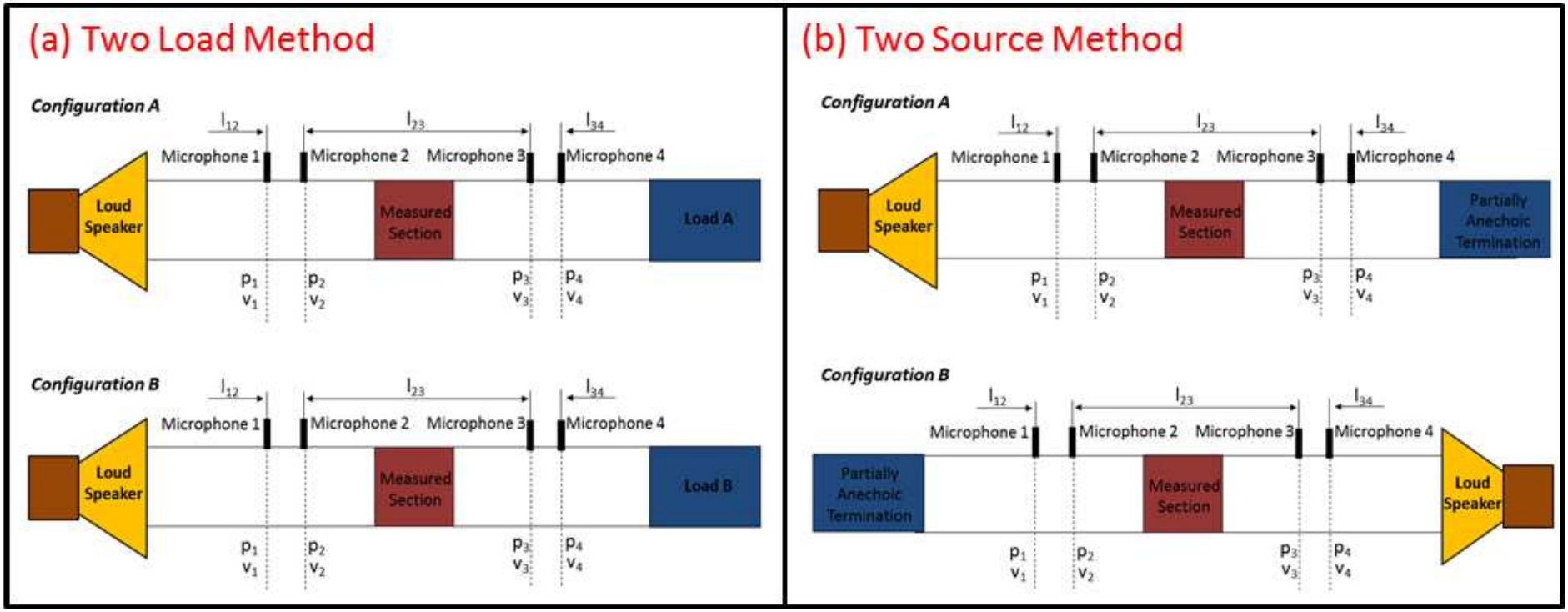

Figure 2-7: The two established method used to solve the underdetermined system of the Two Port method. (a) The termination impedance is changed in order to obtain the second set of equations. (b) The position of the source and termination are swapped in order to obtain the second set of equations.

2.1.2 Pressure based Wave Decomposition (PWD) Technique

An acoustic travelling wave emitted from a source propagating through a waveguide system is constrained to propagate only in the direction parallel to the axial length of the acoustic waveguide[114]. If the acoustic wave is propagating below the cut-off frequency, f_c, the wave can be assumed to be a plane wave and the acoustic transmission through the waveguide system may be simplified to a 1-dimensional transmission line model, analogous to that of an AC electrical circuit. The pressure measurement at any point along the axial length of the waveguide duct would thus yield the result of the superposition between the incidents and reflected travelling wave components at that point. Seybert and Ross[115, 116] first introduced the Wave Decomposition(WD) technique which would allow the measured wave to be analysed down to its constituent incident and reflected travelling wave components through the use of cross correlation techniques. Chung and Blaser[102, 117] simplified the technique by replacing the cross correlation techniques with transfer functions which made the computation of the WD technique much less intensive. Ho et al[103] derived another form of the wave decomposition technique which explicitly takes into account the reflected components of the waves. Salissou and Panneton[107] improved on this method by evaluating the reflective coefficient for all the reflected surfaces (the excitation source, the entrance face and the exit face of the measured section and the absorbing termination). These newer explicit reflection consideration techniques are underdetermined systems that require the experiment to be repeated under two different settings, much like the Two Port techniques.

The WD technique selected for this research was that developed by Seybert[115, 118]. Although it is more computationally intensive, it is gives the full spectrum of the incident and reflected travelling wave components. This allows the investigation of different wave forms, acoustic wave with multiple frequencies and also harmonic formation.

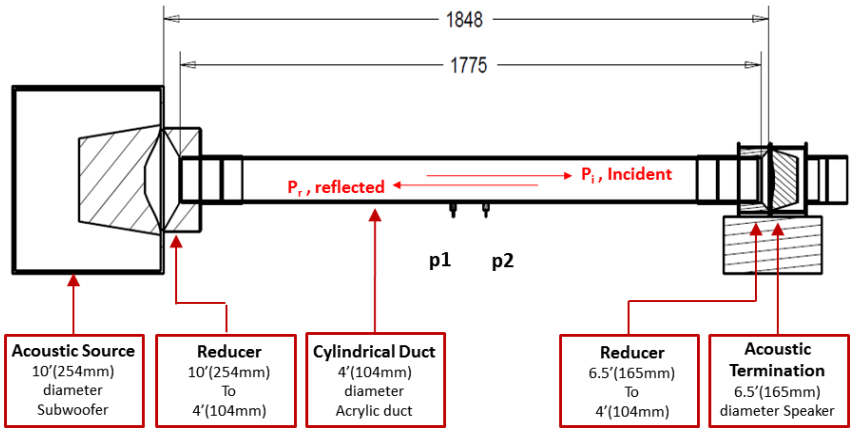

Figure 2-8: Pressure based Wave Decomposition Technique

Seybert and Ross[115] introduced the Wave Decomposition technique as an improvement to the Standing wave Ratio(SWR) measurement technique. The new technique requires a minimum of two point pressure measurements, separated at a known distance from each other along the axial length of the duct, as shown in Figure 2-8.

$$\widetilde{p_1}(x_1,t) = \tilde{a}(t)e^{i(\omega t - k_i x_1)} + \tilde{b}(t)e^{i(\omega t + k_r x_1)} \tag{2.8}$$

$$\widetilde{p_2}(x_1,t) = \tilde{a}(t)e^{i(\omega t - k_i x_2)} + \tilde{b}(t)e^{i(\omega t + k_r x_2)} \tag{2.9}$$

Each of the pressure transducer measures the amplitude of the superposition values of the incident and reflected wave components as given by (2.8) and Equation (2.9). Here the incident wave's amplitude is denoted by $\tilde{a}$ and the reflected wave's by $\tilde{b}$. The wave decomposition technique utilises a transfer matrix and the correlation of the cross spectral densities between the pressure measurements in order to analyse the wave into its constituent amplitudes. The WD transfer matrix is given as:

$$\begin{bmatrix} S_{PAA} \\ S_{PBB} \\ C_{PAB} \\ Q_{PAB} \end{bmatrix} = [TM_P]^{-1} \begin{bmatrix} S_{P11} \\ S_{P22} \\ C_{P12} \\ Q_{P12} \end{bmatrix} \tag{2.10}$$

Here, S_{AA} and S_{BB} are the incident and reflected power spectral densities respectively. The Cross Spectral Density, S_{AB}, is represented in terms of its real and imaginary components, C_{AB} and Q_{AB}.

$$S_{AB}(f) = C_{AB}(f) + j\, Q_{AB}(f) \tag{2.11}$$

$$S_{12}(f) = C_{12}(f) + j\, Q_{12}(f) \tag{2.12}$$

S_{11} and S_{22} are the auto spectral density measurements from microphone 1 and 2 respectively. Similarly C_{12} and Q_{12} is the real and imaginary component of the cross spectral density; S12, between pressure measurement from microphone 1 and 2. The Transfer Matrix's coefficient, $[TM_P]^{-1}$,is given by:

$$\delta \begin{bmatrix} 1 & 1 & -2\cos k_r(x_1 - x_2) & 2\sin k_r(x_1 - x_2) \\ 1 & 1 & -2\cos k_i(x_1 - x_2) & -2\sin k_i(x_1 - x_2) \\ -\cos(k_i + k_r)x_2 & -\cos(k_i + k_r)x_1 & \cos(k_r x_1 + k_i x_2) + \cos(k_i x_1 + k_r x_2) & \sin(k_i x_1 + k_r x_2) - \sin(k_r x_1 + k_i x_2) \\ -\sin(k_i + k_r)\, x_2 & -\sin(k_i + k_r)\, x_1 & \sin(k_r x_1 + k_i x_2) + \sin(k_i x_1 + k_r x_2) & \cos(k_r x_1 + k_i x_2) - \cos(k_i x_1 + k_r x_2) \end{bmatrix}$$

With its determinant δ given by:

$$\delta = \frac{1}{4}\sin^2\left[\frac{1}{2}(k_i + k_r)(x_1 - x_2)\right] \tag{2.13}$$

The wave numbers are written as:

$$k_i = \frac{2\pi f}{c(1+M)} \quad \text{and} \quad k_r = \frac{2\pi f}{c(1-M)} \tag{2.14}$$

Seybert[118] modified the setup of the Decomposition technique to include a third microphone as shown in Figure 2-9. This setup was used to investigate the acoustic transmission through a measured section which was located between microphone 2 and 3. This experimental setup requires that the end termination of the duct to be perfectly anechoic such that the measured pressure from microphone 3 is only that of the transmitted wave. In this case, the acoustic transmission is ratio between the transmitted wave p_T and the incident wave p_a.

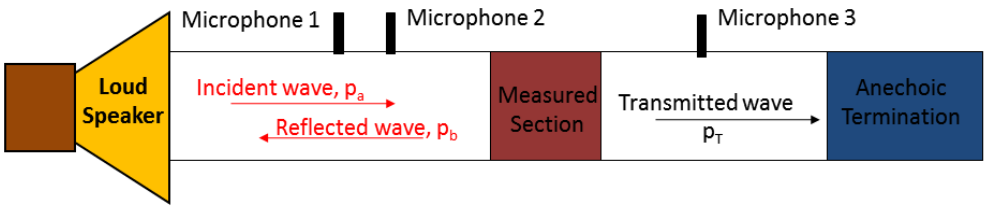

Figure 2-9: Ideal transmission investigation setup with perfect anechoic termination

An anechoic termination is hard to achieve, an imperfect anechoic termination will cause reflections downstream of the measured section thus leading to errors in the transmission measurements. The subsequent sub-chapters will discuss the development of an adjustable acoustic termination that will allow the suppression of the downstream reflected wave component.

2.1.3 Passive Reflection Cancellation (PRC) Method

An anechoic termination is typically a very long tapered pipe packed with varying density of acoustic absorbing material. This setup allows the smooth dissipation of the acoustic wave's energy as it propagates through the termination. Such a termination is difficult and costly to manufacture and only works for a limited range of frequency in which it was designed for. The thermoacoustic resonator loop however, requires that a large range of frequency to be investigated. As such, in order to work within the research budget and requirements, new techniques have been developed in order to create a suitable acoustic absorbing termination for the experiments. The initial concept was to develop a flexible termination such as a diaphragm that would allow the absorption and dissipation of the wave energy through its elasticity. It was found that each diaphragm had a limited effective frequency range due to the inherent characteristic of the diaphragm's stiffness. Thus, in order to develop an effective acoustic absorptive termination, a diaphragm with variable stiffness is required. The development of the linear alternator showed that the mechanical resistance towards the speakers suspension is govern by the equation[119]:

$$R_{mech} = \frac{m\omega_n}{Q_{mech}} \tag{2.15}$$

Here, the mechanical quality property of the speaker, Q_{mech}, is proportional to the square root of the electrical resistance of the speakers coil. The stiffness of the speaker's suspension, R_{mech}, is thus also proportional to the speaker's coil electrical resistance. Additional electrical resistances can be added by connecting the speaker to an external load box with variable resistance. The ability to tune the amount of electrical resistance, added to speakers coil, gives some control over

the stiffness of the speaker's diaphragm. This in essence allows the tuning of the termination impedance to more closely match that of the waveguide system in order to reduce reflections. This technique does not require the input of energy into the termination speaker and merely relies on the passive acoustic absorbing qualities based on the stiffness of the diaphragm. As such, this technique is named as the Passive Reflection Cancellation (PRC) technique. The experimental setup of this technique is shown in Figure 2-10.

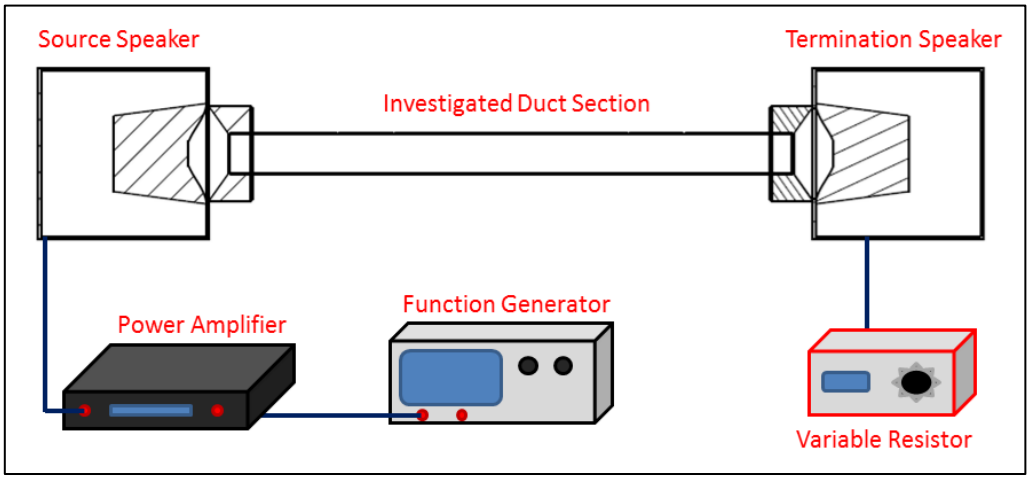

Figure 2-10: The setup configuration for the Passive Reflection Cancellation (PRC) technique.

In order to calibrate the PRC technique, the added resistive load was varied between the maximum and minimum that the load box could provide. Using the Wave Decomposition (WD) technique discussed in the previous chapter, the Standing wave Ratio (SWR) was computed for each investigated frequency at each resistive load interval. The results from this are plotted in Figure 2-11. The resistive values in which the lowest SWR values are obtained are within 0 to 10 Ohms. As such, experimental runs were conducted with every 1ohm increment in this region. A polynomial fit was then used to approximate the lowest attainable SWR value with its corresponding resistive load value. It is shown that the PRC technique is able to obtain SWR values of less than 1.5 for the range of investigated frequencies.

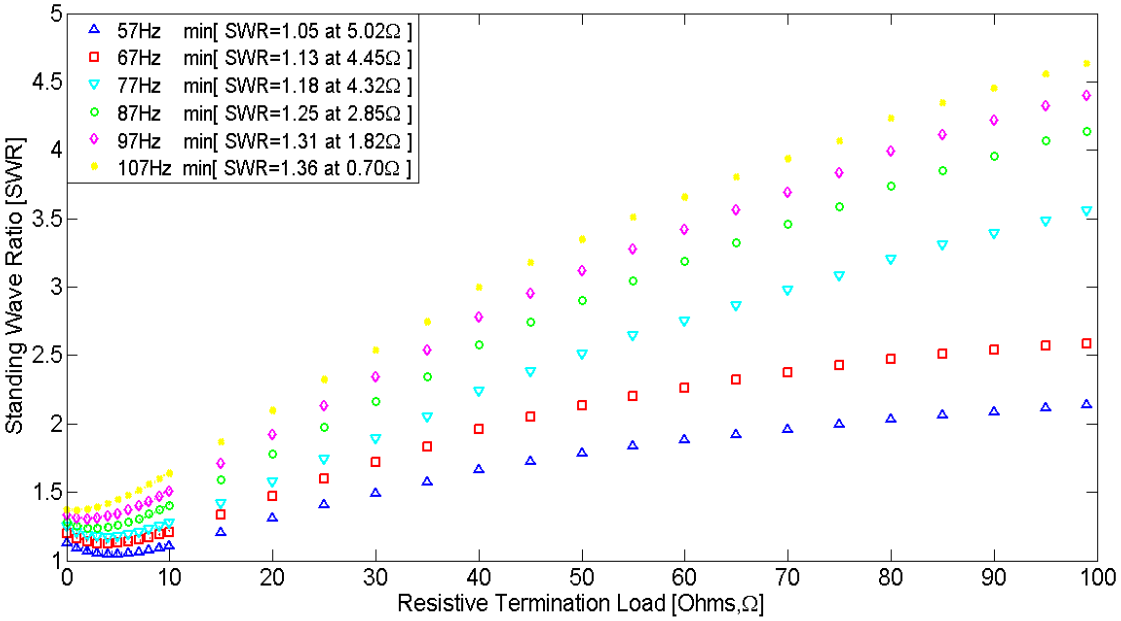

Figure 2-11: **PRC Calibration technique. The variable load box was varied between its maximum and minimum for 6 different frequencies. A polynomial fit was used to approximate the region between 0-10 Ohms. Based on the polynomial fit, the lowest attainable SWR values as well as the corresponding resistive load that has been added to the speakers coil are obtained.**

The relationship between the added resistive load value which gave the lowest SWR values and the frequency shows a squared relationship which matches that of Equation (2.10). The polynomial approximation shown by the dotted line in Figure 2-12 is given as:

$$\Omega_{min} = -0.0011f^2 + 0.0933f + 3.3021 \tag{2.16}$$

Equation (2.16) is then used to compute the required Ω_{min}, that would give the lowest SWR value for the investigated frequencies within the calibrated range.

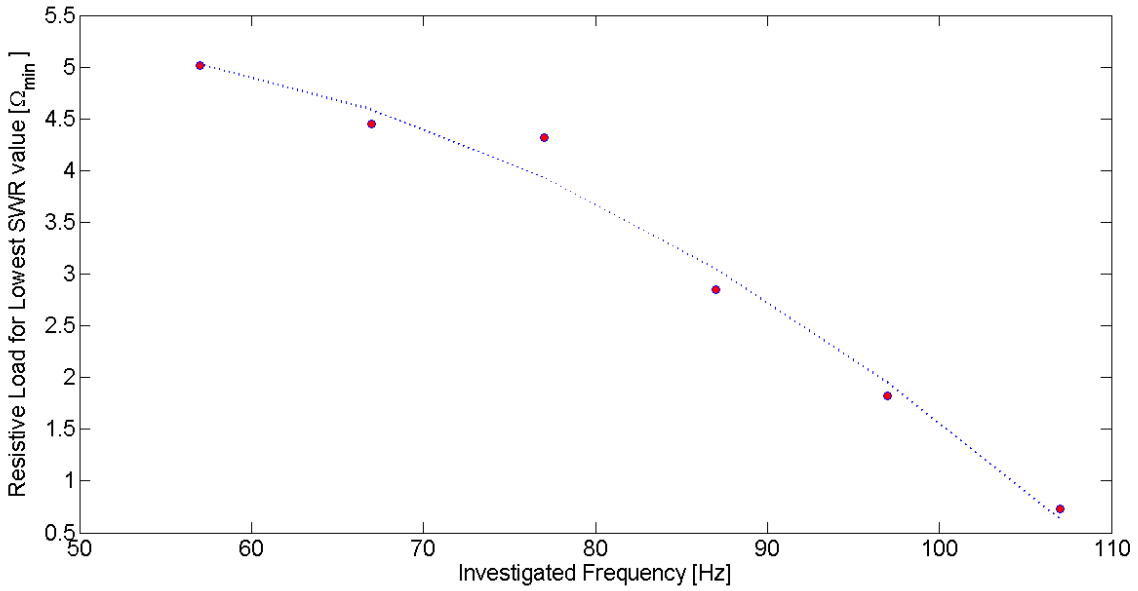

Figure 2-12: The added Resistive Load plotted against the calibrated frequency range. A squared polynomial fit (shown by the dotted line) is used to approximate the trend of the plot.

Termination speaker used is shown to be more effective as an acoustic wave absorber for lower acoustic wave frequencies. Figure 2-13 shows that the lowest attainable SWR values increases proportionally to the increase in the waves frequency. This linear relationship is given by:

$$\mathrm{SWR} = 0.0063f + 0.6941 \tag{2.17}$$

Equation (2.17) can be used to estimate the expected SWR value from the investigated frequency values.

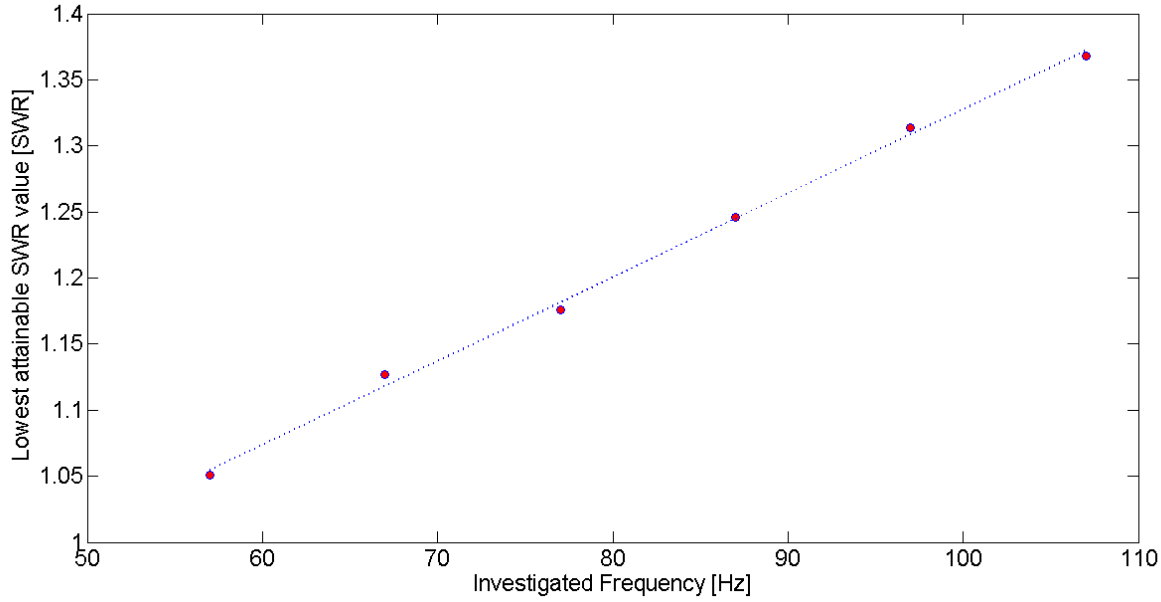

Figure 2-13: The lowest attainable SWR value using the PRC technique vs. the Investigate Frequency.

2.1.4 Active Reflection Cancellation (ARC) Method

The PRC setup has been shown to be an effective technique for developing an acoustic absorptive termination. The PRC technique is however limited in its ability to provide a pure travelling wave required for accurate acoustic transmission measurement. Thus, a new "active" reflection cancellation (ARC) technique was developed as an improvement to the PRC technique. This technique is termed "active" since energy is supplied to the termination in order to actively nullify the energy from the acoustic incident wave approaching it. The ARC experimental setup is shown in Figure 2-14. The Wave Decomposition setup for the ARC technique is the same as shown in Figure 2-3 where the WD technique is applied upstream before the investigated section and downstream after the investigated section. For the ARC technique, it is of interest only to obtain a pure travelling wave downstream of the investigated section as shown in Figure 2-9.

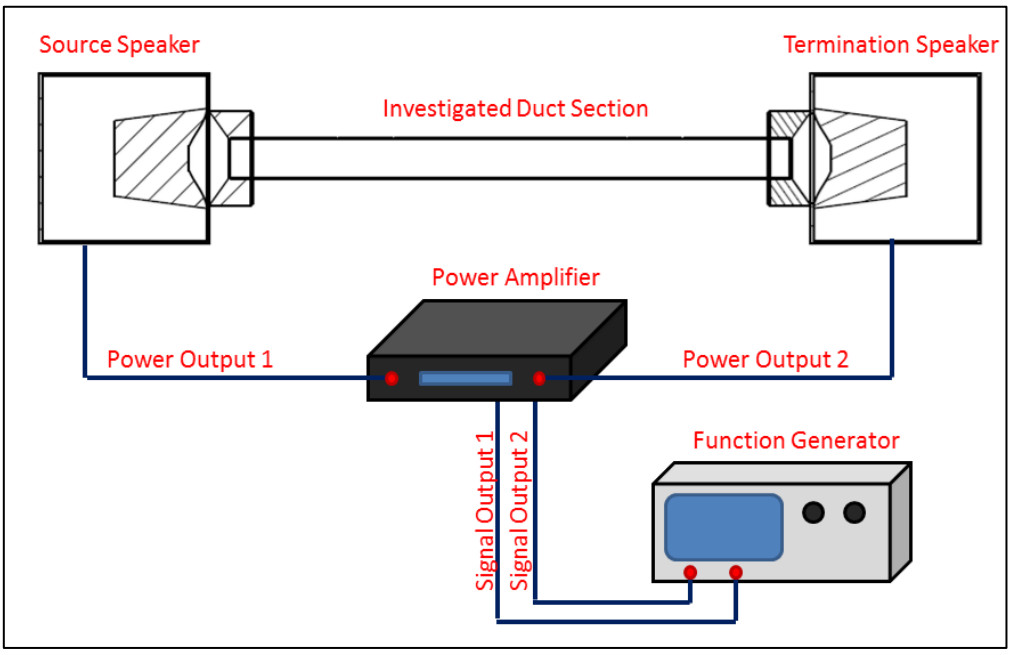

Figure 2-14: The experimental setup for the Active Reflection Cancellation technique

The ARC technique relies on using a dual signal output function generator that is capable of regulating the phase between its two signal outputs. The first signal output would be for the intended generated acoustic wave form to be fed to the source speaker. The second signal output would be of the same signal but of a different phasing from the first. The phase difference, ϕ, between the first and the second signal is the phase time it takes for the wave to travel from the

source to the termination, τ , plus π , such that the waves generated at the termination are at antiphase.

$$\phi = \tau + \pi \tag{2.18}$$

The calibration of the ARC technique is shown in Figure 2-15 where the phase difference, Φ, is plotted against the range of the investigated frequencies. Based on the linear approximation of the trend observed in Figure 2-15, the phase difference for this setup configuration may be approximated using Equation (2.19):

$$\phi = -9.01f + 792.48 \tag{2.19}$$

The amplitude of the wave generated from the termination speaker must also be tuned to match that of the incident wave downstream. The amplitudes of the waves are controlled from the power amplifier. A Labview VI program has been written such that the WD analysis is continuously computed using the live measurements, in order to give reference that will enable the tuning of both the phasing as well as the amplitude of the wave generated by the termination speaker, so as to completely eliminate the downstream reflected wave component. The ARC technique is capable of obtaining an SWR value of 1.02 throughout the range of investigated frequencies.

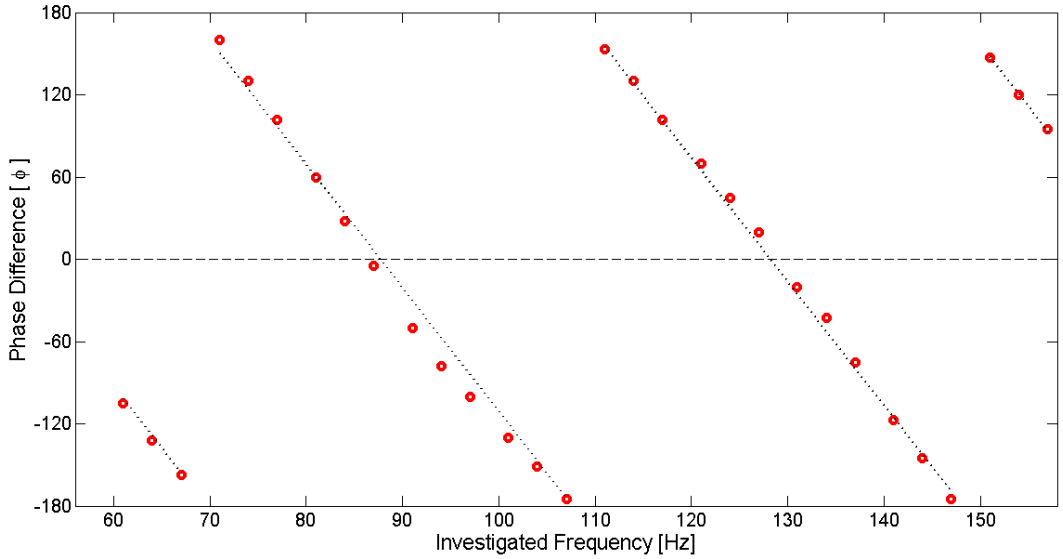

Figure 2-15: The phase difference between the signal given to the source and termination speakers plotted against the investigated frequencies.

The ARC technique was several advantageous over the PRC technique:

1. It is able to obtain an SWR value of 1 for almost any investigated frequency as well as for different waveforms.
2. Capable of generating SWR values between 1 and ∞ which will allow further acoustic transmission investigation.

The cost of the function generator that is capable of phase regulation as well as dual signal output is almost 4 times more expensive than that for single output function generator. This makes the ARC technique very costly.

2.2 Acoustic Transmission Measurement

Both the Passive Reflection Cancellation (PRC) as well as the Active Reflection Cancellation (ARC) techniques was developed to produce an effective anechoic termination for the experimental waveguide setup. This is to ensure that only a pure travelling propagates through the waveguide ducting from the source to the termination speaker. In order to measure the transmission through a waveguide component (such as bends, expansion, constriction, stubs, etc.), the investigated waveguide component is placed in the midsection of the acoustic waveguide system, with 2 pressure transducers to measure the Wave Decomposition (WD) upstream, before the investigated component, and 2 more pressure transducers to measure the WD downstream, from the investigated section, as shown in Figure 2-3.

Often, the investigated waveguide component will have a different impedance than that of the waveguide ducting. This will cause reflection to occur and the WD upstream will yield an SWR value of more than 1. This will not matter if the waveguide termination downstream is anechoic. For such cases, the acoustic transmission coefficient for the measured section would simply be the ratio of the transmitted wave, downstream to the incident wave, upstream:

$$T_c = \frac{p_T}{p_a} \tag{2.20}$$

It has been discussed however, in previous sub-chapters, that an anechoic termination is difficult to obtain. The ARC technique is capable of obtaining an SWR value of 1 based on the WD technique. The PRC technique is limited in its ability to obtain a pure travelling wave. As such, reflection still occurs downstream of the investigated component. It is important to note that the incident wave downstream, p_c, is not the same as the transmitted wave, p_T. The reflected wave downstream must be taken into consideration. As such, it is important to adopt a transmission measuring technique that is able to accurately measure transmission in the absences of an anechoic termination for the experimental waveguide system. M. Abom[100, 120] suggested applying the two port electrical analogy of the Scattering Matrix as an accurate means of measuring transmission through acoustic waveguide systems. The Scattering Matrix is essentially a hybrid technique between the WD and Two Port technique. This is since the 4 poles of the Two Port technique consists of the WD computed incident and reflected components from both upstream and downstream. The Scattering Matrix is given by:

$$\begin{bmatrix} p_c \\ p_b \end{bmatrix} = \begin{bmatrix} T_f & R_b \\ R_f & T_b \end{bmatrix} \begin{bmatrix} p_a \\ p_d \end{bmatrix} \tag{2.21}$$

Here, p_a and p_b represent the incident and reflected component upstream; p_c and p_d, the incident and reflected component downstream. T_f and R_f represent the forward transmission and reflected coefficient when the acoustic termination is anechoic ($p_d = 0$). Similarly, T_b and R_b are the backward transmission and reflected coefficient when the acoustic source is anechoic. The Scattering Matrix has been primarily used to measure acoustic transmission in aeroacoustic waveguide systems such as in ductings and automotive muffler systems[121]. For aeroacoustic systems, the Scattering Matrix is shown to be an underdetermined system with 4 unknown

coefficients and only 2 equations. However, Dequand [62, 122] has shown that for a pure acoustic system, in the absence of a mean flow, the Scattering Matrix is symmetric.

$$T_f = T_b = T = |T|e^{i\Phi_T}$$

$$R_f = R_b = R = |R|e^{i\Phi_R} \tag{2.22}$$

As such, only one experimental run is required to provide the two equations with which to solve the transmission and reflected coefficient T and R.

2.3 Experimental Investigation

The acoustic transmission technique discussed in the previous chapter was used together with the PWD technique to investigate experimentally the acoustic transmission in curved duct bend systems. The objective of this experiment is to investigate the possibility of using the discussed pressure wave acoustic transmission measurement technique. The experimental setup is shown in Figure 2-16. The material used for the experimental setup are standard PVC fittings used for underground drainage piping and are of the same materials used to construct the waveguide of the thermoacoustic engine's resonator loop. These are circular cross section pipes that have a hydraulic radius of 50mm.

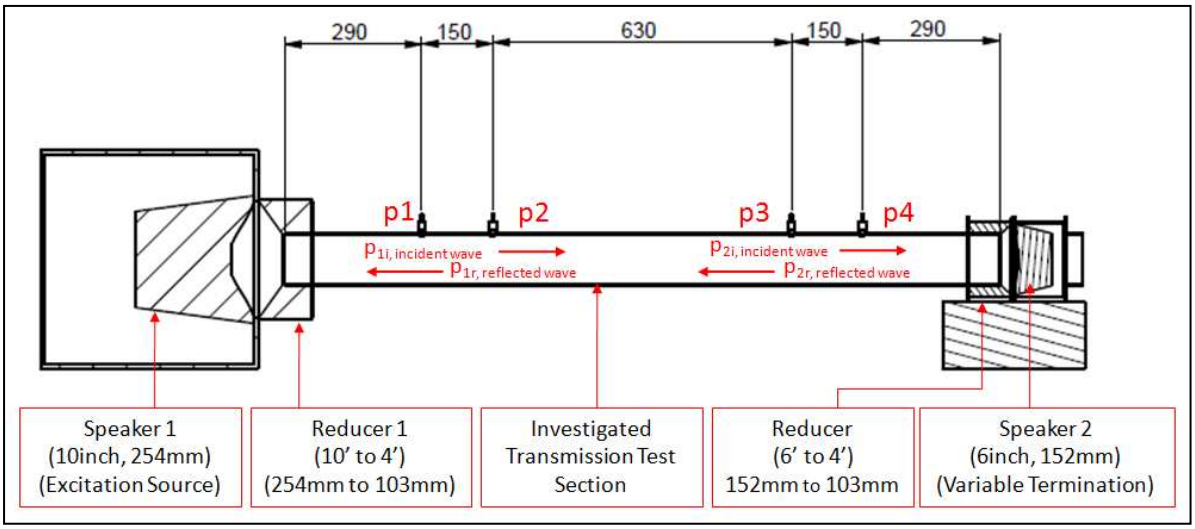

Figure 2-16: Experimental Setup (all dimensions are given in mm). A function generator connected to an amplifier system is used to control the acoustic excitation produced by Speaker 1. The PRC technique is used to keep the SWR ratio as close as possible to unity. The calibration for the PRC technique is shown in Figure 2-12.

The acoustic transmissions are measured through three 90° bends with the same hydraulic radius but with different radius of curvature as shown in Figure 2-17. These correspond to the actual pipe bends used to construct the SCORE stove's resonator. The frequencies investigated are between the range of 50Hz to 220Hz corresponding to the operating frequency of the SCORE-stove.

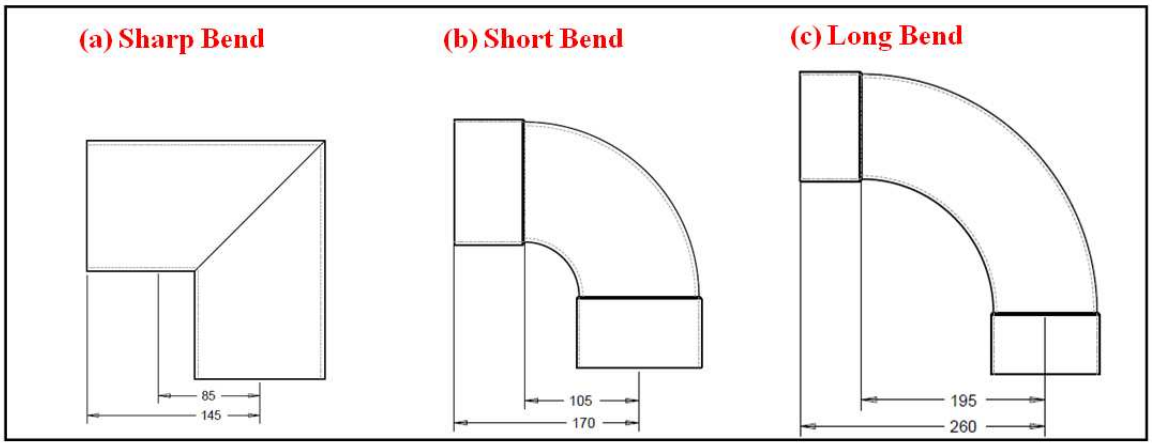

Figure 2-17: The dimensions of the 3 investigated duct bends. All dimensions are given in mm. The Short Bend has a radius of curvature (ROC=105mm) and the Long Bend has a ROC=195mm.

Four pressure transducers are used for this experiment; two pressure transducers, p1 and p2 as shown in Figure 2-16, are located upstream near to the excitation source. The test section (elbow bends) is located between pressure transducers, p2 and p3. The axial distance, corresponding to the centreline of the pipe between pressure transducers p2 and p3, is maintained as 630mm for each of bend tested. Pressure transducers, p3 and p4, are located after the test section downstream near to the termination Speaker 2. The pressure transducers used in this investigation were the Impress IMR-LR low range pressure transmitter. Amplitude of the acoustic wave investigated in the experiment corresponds to 20Pa-25Pa. This is due to the fluctuation in the subwoofer due to the heating of its solenoid coils. The acoustic transmission was computed using Equation (2.22) and the amplitude of the incident acoustic wave was computed using the PWD technique from pressure transducer p1 and p2.

The plot of the acoustic transmission loss vs. the acoustic particle displacement is shown in Figure 2-18. The acoustic particle displacement is given by the ratio of the upstream incident pressure

wave amplitude to the product of the angular frequency and the characteristic impedance of the wave:

$$\xi_{ac} = \frac{\mathrm{P}_a}{2\pi f \cdot \rho c} \tag{2.23}$$

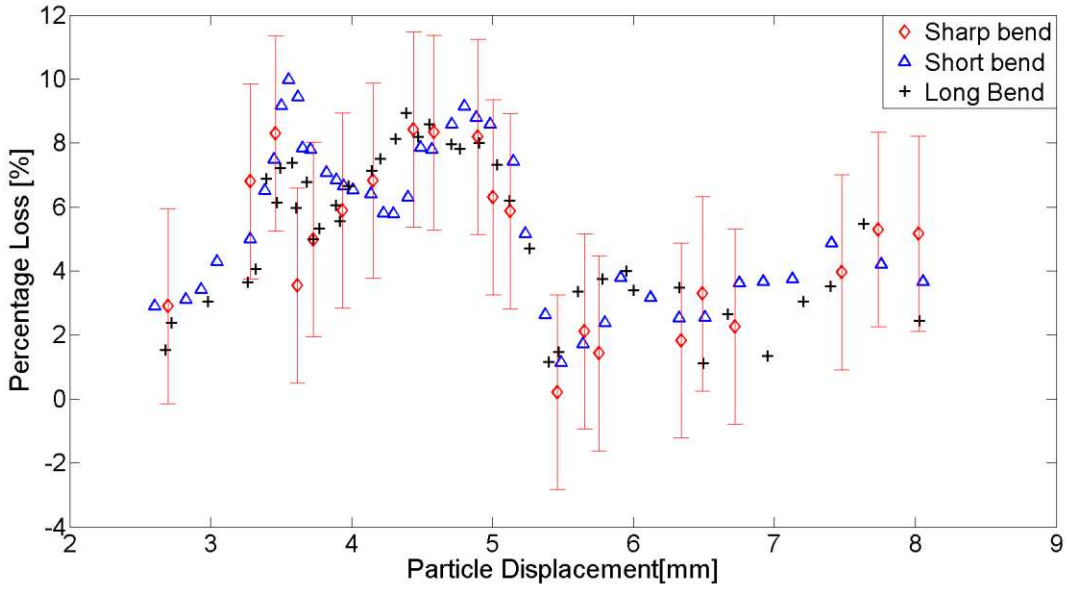

Figure 2-18: The mean particle displacement plotted against the Percentage transmission Loss. The error bars are included for the sharp bends to indicate the level of result uncertainty.

The results obtained from the measurements are within 10% of those obtained by Dequand[62, 122] (as previously discussed in Chapter 1.3.1). The standard deviations of each of the measured runs are plotted together with the results of the sharp bend in the form of error bars. It is noted that the standard deviation for all 3 bends are within the same range of approximately ±3% of the percentage acoustic transmission loss. The standard deviation is shown to be larger than the difference between mean percentage transmission losses of the 3 investigated elbow bends. The same is shown for the percentage acoustic transmission loss vs. the Strouhal number given in Figure 2-19. The difference in acoustic transmission performance between the 3 bends is thus inconclusive.

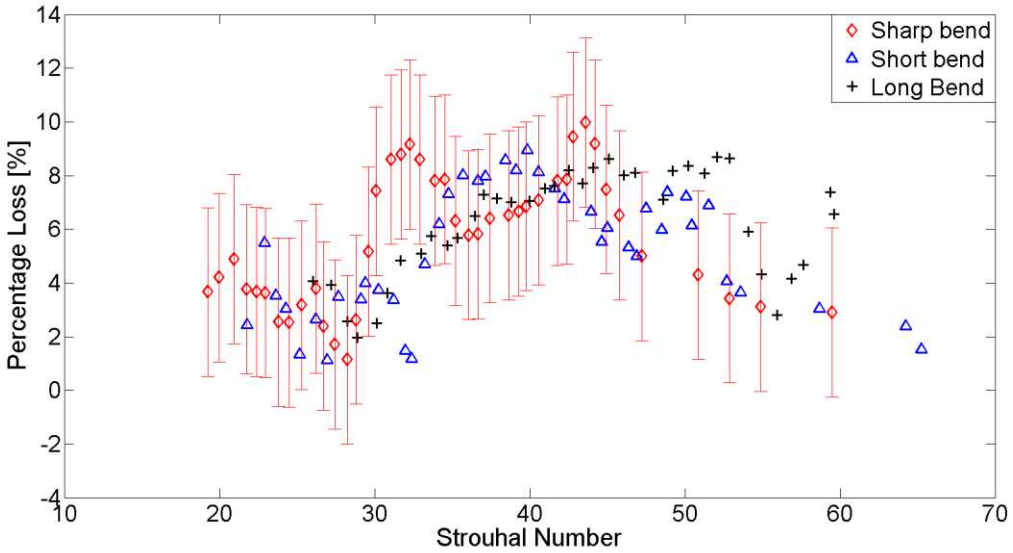

Figure 2-19: The Strouhal number plotted against the Percentage transmission loss

It is shown that the pressure transducer used in this investigation has insufficient resolution in order to differentiate the acoustic transmission difference between the 3 investigated bends. The pressure transducer used a measurement range of 0-50mbar and an accuracy of ±0.1% FS (BFSL). This corresponds to a pressure measurement accuracy of ±5Pa. It is also noted that each of the pressure transducers have their respective transducer output curve. The accuracy of each of the pressure transducers are thus not the same. The PWD technique and the Scattering matrix technique are computed using the independent measurement of the 4 pressure transducers. This adds to the error in the measurement. Pressure transducers with higher resolution are thus required for this investigation. It is noted however, that the resolution of the transducers are usually inversely proportional to their measurement amplitude range. The range of acoustic amplitude used in this investigation is between 1000-1200Pa. This amplitude range corresponds to the sustainable amplitude limit of the subwoofer system used. Efficient thermoacoustic systems are expected to have much higher amplitudes than this.

The errors in the results are not entirely based on the resolution of the pressure transducers alone. The PWD technique and the flush mounted pressure transducer measurement technique are based on the one-dimensional propagation of the acoustic wave. Although Equation (2.3) indicates that

for the range of investigated frequencies, the acoustic wave should only propagate in the plane wave mode of propagation, it is possible for non-linearity to occur within the Stokes oscillating boundary layer.

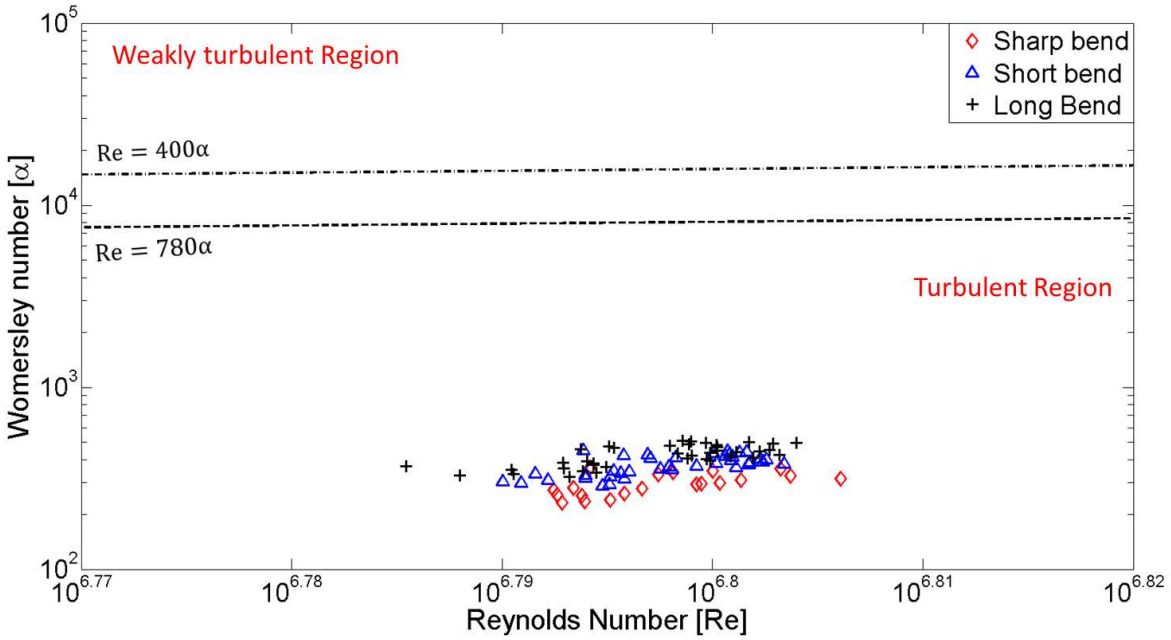

Figure 2-20: The Womersley number vs. Reynolds number chart for flow regime characterisation

When the results of the experiments are plotted in the Reynolds Number vs. Womersley number chart, it is shown that this investigated oscillation range corresponds to the turbulent oscillating flow regime. In this regime, the formation of streamwise vortices causes fluctuation within the boundary layer of the oscillation. The formations of these non-linear fluctuations are due to the bursting processes which will be further discussed in Chapter 6.0. These fluctuations will definitely distort the pressure measurements made by the flush mounted pressure transducers. The acoustic wave may still be propagating in the plane wave mode of propagation outside the boundary layer and in the free stream region of the oscillation. As such, it is proposed that the amplitude measurements of the wave be taken from the free stream of the oscillation. Such measurement would be similar to the technique shown in Figure 2-2. This would however prove to be an intrusive measurement technique which will also cause distortion in the oscillation.

The acoustic transmission investigation must be improved in order to obtained meaningful results. This can be accomplished by using a higher amplitude resolution measuring instrument that is capable of measuring the free stream oscillation through non-intrusive techniques. Particle Image Velocimetry was thus chosen as the investigation.

2.4 Chapter conclusion

This chapter has discussed the various pressure measurement and analytical techniques for investigating acoustic transmission through waveguide systems. These techniques are largely based on the one-dimensional transmission line analytical models. Based on the PWD technique, an active and passive technique has been developed in order to generate an anechoic termination for the range of investigated frequencies. The reviews on these experimental and analytical techniques serve as a basis for the experimental setup which will be shown in subsequent chapters.

The acoustic transmission was experimentally investigated using the PWD and Scattering matrix techniques. The results were inconclusive. In order to accurately measure the acoustic transmission through these curved duct bend system, several issues need to be address:

1. The large uncertainty of the results is a result of the use of 4 independent measuring instruments. Although these instruments have the same specification but their transducer output curves may not be the same. As such, there will be an offset between each of the instrument's BFSL. The uncertainty of the PWD technique will thus be proportional to the product of the maximum deviation from the BFSL of both pressure transducers. This form of error can be reduced by using a single measuring instrument that is able to measure the pressure differential between the four points (p1, p2, p3 and p4). The uncertainty of the 4 measurements will thus have the same bias error. The PWD technique operates only on pressure differentials and as such, the bias error may be negligible.

2. The acoustic transmission measurement technique discussed in this chapter assumes that the wave propagation is one dimensional. As such, the flush mounted pressure transducer measurement techniques will only work if the investigated wave is propagating in the plane wave mode of propagation. This has to be verified before the analysis is conducted.

3. The range of acoustic frequency and amplitude corresponds to the turbulent oscillation regime. In this oscillating flow regime, random fluctuation occurs within the boundary layer region of the oscillation due to the formation of streamwise vortices. Measurements made within this boundary layer will be affected by these fluctuations. It is possible that these random fluctuations are confined within the boundary layer region and that the plane wave mode of propagation still exist in the free stream region of the oscillation. Hence, measurements from the free stream oscillation should yield more accurate results.

The points discussed above can be resolved by using Particle Image Velocimetry. PIV allows for the qualitative flow visualisation of the acoustic wave as well as the quantitative measurement of the amplitude of oscillation. As such, PIV will be used in place of the pressure measurement technique for this research. The next chapter explains the development and operation of PIV technology.

Chapter 3

Particle Image Velocimetry

3.0 Particle Image Velocimetry (PIV)

In order to gain a deeper understanding on the acoustic transmission through bends in duct systems, it is of interest to not only measure the acoustic transmission but also to study the acoustic flow behaviour which influences the acoustic energy losses through these bends. The study of the interaction between acoustic flow behaviour and its solid boundaries was conducted experimentally using Particle Image Velocimetry (PIV) [123]. This technique uses a suspension of seeding particles dispersed in the fluid medium in order to observe and measure the flow[124]. The basis of this technique consists of 3 fundamental components:

1. **Tracing particles.** These are the particles that allow the visualisation of the flow. Ideal tracer particles should be sufficiently small in size and have densities similar to that of the fluid to be able to follow the flow smoothly without influencing the flow or changing the properties of the fluid medium. It is also important that the tracing particle has better light scattering properties than the fluid it is tracing[125].

2. **Source of illumination.** The tracer particles require sufficient lighting for it to be visible and also be detected and recorded by the visual recording device used. The illumination of the flow is usually conducted via a thin light sheet of the investigated plane of flow. This gives better contrast which will allow better visualisation of the particles in the investigated plane. Illumination sources vary from high intensity lighting to pulse laser systems[126].

3. **Visual recording devices.** This includes high speed cameras and video recorders. The images or the videos capture can then be used for further analysis of the flow. Quantitative measurement can be made from the flow recordings.

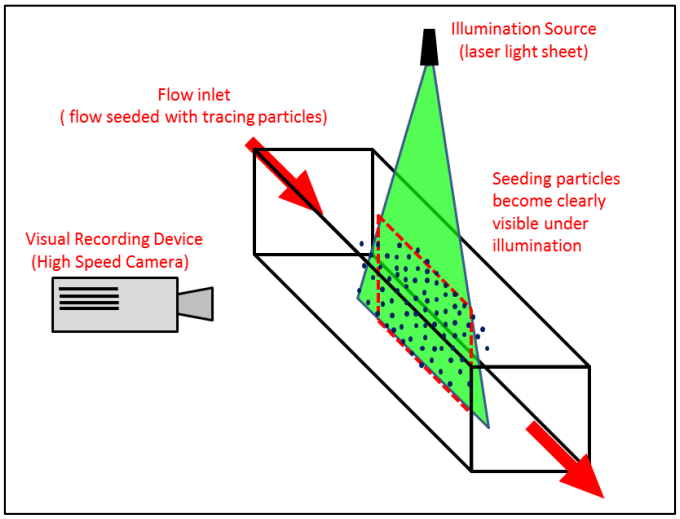

Figure 3-1: Flow visualisation techniques leading to Particle Image Velocimetry. The illumination source is a pulse laser system which is synchronised with the high speed camera. Pulse lasers are chosen because of their ability to provide high power illumination within the short duration of a pulse. The system is set such that the camera shutter is open just prior to the laser pulse and close after. The synchronisation ensures that sufficient light is provided for the illumination of the tracer particles for the duration of the recording period.

The computation of the flow velocities involves measuring the tracer particles' displacement from the flow recordings and dividing that with the separation time between the recordings. That meant that the velocity measurement is highly dependent on the camera's frame rate as well as the laser system's pulse repetition rate and the amount of power each pulse can provide at that rate for illumination. A summary of the techniques used for PIV is given in Figure 3-2

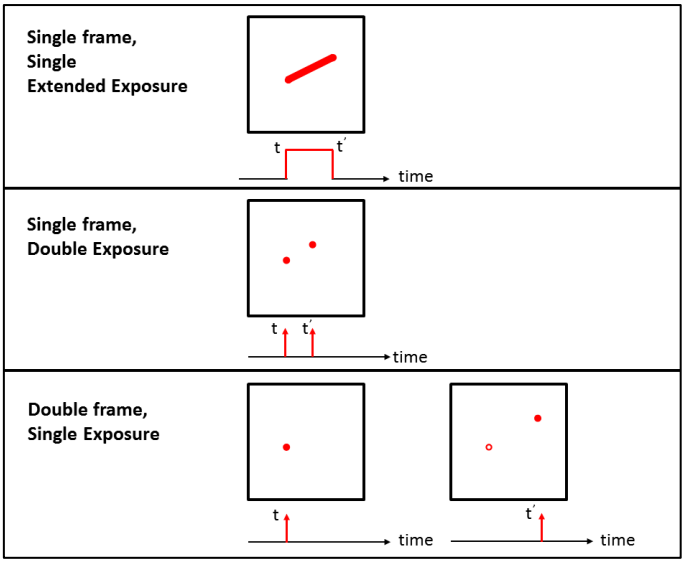

Figure 3-2: A summary of PIV techniques for measuring particle velocity for one time step. The red arrowed line represents the shutter opening time of the camera. The red dots red lines represents the image taken by the camera. For an extended exposure time, the particle appears as a streak in the image taken. Length of the streaks represents the distance travelled by the particle in the time t-t´. For the double frame technique, the red circle represents the particle which appears in the previous frame. For all techniques, the particle velocity is measured by the displacement of the particle over t-t´ [127, 128].

The single frame PIV techniques were mainly used prior to the availability high speed digital cameras systems. The tracer particles velocities were computed through statistical autocorrelation of the recorded frame[129]. Image shifting was used to determine the flow direction of the particle. The development of CCD and CMOS chip in the last two decades have made high frame rate digital camera more available for such measurement techniques[130]. Digital cameras now have high spatial and temporal resolution with frame rate that could go up to a million frames per second. As a result, almost all PIV systems now employ the double frame, single exposure technique or an improved variant of it. The double frame, single exposure requires that the camera shutter be opened twice with nanoseconds interval between the two frames for each recorded time step. The shutter timing has also to be synchronised with the pulsing of the laser system. As such, there is set time between the shutter interval in between the pair of recorded images that is based on the sampling frequency used for recording. This is the preferred technique as this preserves the temporal order of the particle images[131]. The velocities of the tracer particles are found using statistical cross-correlation between the two captured frames. The advantages of using

the multiple frames, single exposure as compared to the single frame, multiple exposures are that it:

- Solves directional ambiguity
- Allows the use of a wider range of pulse separation time
- Gives a higher signal to noise ratios in the correlation plane is available at the same interrogation window size. This allows smaller interrogation windows and therefore increasing the spatial resolution at the same resolution of the recording.

3.1 Computation of Particle displacement based on statistical techniques

The objective of Particle Image Velocimetry is the conversion of the recorded images of particles displacements in flow into velocity vector maps. With the use of PIV to measure more complex flow and the use of heavy seeding for better resolution of the flow, the computation of velocity vectors based on the displacement of these seeding particles will have to rely on computational techniques[132]. The PIV system used in this investigation uses the double frame, single exposure recording technique; hence this literature will concentrate only on the interrogation methods used for this recording technique. The analytical interrogation technique is computed by deconvoluting the pair of images. This is done by dividing the Fourier Transform of each respective image with each other[133]. The accuracy of this analytical technique however, is very sensitive to the noise level between the recorded images. As it is difficult to control the noise level of the recorded images, the more robust statistical approach is preferred. Adrian[134] introduced the basis for statistical computation of the particle displacement through the use of the autocorrelation function of the single frame, doubly exposed recorded flow images. The technique was later improved upon to allow the computation of single frame multiple exposure recorded measurements. The introduction of digital cameras into PIV systems allowed for the preferred double frame single exposure technique to be used more readily. In-line with the technological development, Willert

and Gharib[135] developed new techniques for computing particle displacement based on the digitisation of the recorded images[136]. In 1993, Keane and Adrian[137] introduced the cross-correlation analytical technique for computing particle displacement for the double frame, single exposure technique. Westerweel[138] improved on the technique by introducing the sub-pixel interpolation for a more accurate computation of velocity vectors. The cross correlation technique and its improved variant, the adaptive correlation technique which has been used for this acoustic flow investigation, will be described in more detail in the next subsection.

3.1.1 Image Pre-processing and Cross Correlation Interrogation Technique

The PIV image cross correlation is a statistical technique developed for computing the average particle displacement for the investigated pair of recorded images. The analysis of the recorded image starts with the division of the recorded image into smaller sections of equal sizes. Each of these sections is known as "interrogation" areas. Each interrogation area from the first time step image measurement ($t = t_0$) is cross correlated with its corresponding counterpart in the second time step image measurement ($t = t_0 + \Delta t$). Each interrogation area would thus yield a velocity vector corresponding to the average spatial particle displacement in its area. The digitally recorded image of the measured flow can be represented in a two dimensional signal field[139]. In this case, the functions, $f(m,n)$ and $g(m,n)$, correspond to the light intensity within the interrogation area for the pair of recorded images (t_0 and $t_0 + \Delta t$). The symbols (m,n) are representative of the Cartesian co-ordinates measured in pixels for the recorded image.

The image correlation works most accurately when there is a clear and distinct contrast between the seeding particles and a uniform dark background. Such ideal conditions are rare, and most of the time the image background is not perfectly dark due to the illumination from laser reflection, etc. In some case, the images would also contain stationary objects in its background and/or laser flares, which would yield false peaks in the image correlation. In addition, the recorded digital images from the high speed camera are affected by a variety of noise causing factors such as pixel

irregularities, the mechanism of the camera, and the artefacts of digitisation of the image themselves. The pre-processing step before the cross correlation is to try to filter out as much noise as possible without corrupting the image as well as to get rid of the objects which would give false peaks. The recorded image will also yield particle images of different intensity due to a variety of reasons, such as irregularity of particle size and shape, the difference in intensity between the two laser pulse light sheets, out of plane movement of the particles, etc. These variations will cause a bias correlation signal as the correlation peak will tend towards the brighter particles images. For this reason, it is important that the pre-processing not only enhances the contrast of the particles but also standardises the intensity level of each particles as well.

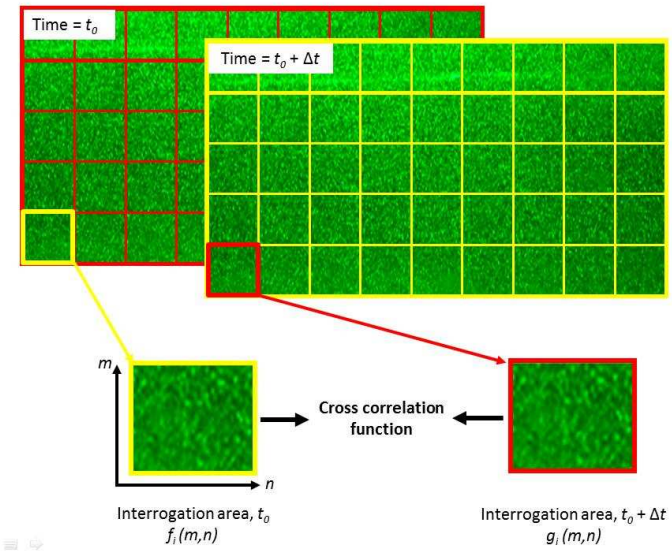

Figure 3-3: Example of the two frame single exposure pair of recorded images. Both images are subdivided into a set of interrogation areas. The corresponding spatial interrogation areas from the pair of images are cross correlated to give the spatial average particle displacement

The first step in image pre-processing is the application of an image mask to the recorded images. This is the manual elimination of areas outside the flow region in the recorded image. This process will reduce the computation time as well as help reduce false peaks caused by stationary objects and laser flares which are outside the investigated flow region. In order to improve the contrast as well as homogenise the intensity of the seeding particles in the images, Westerweel[140] proposed using the min-max filter technique used in image processing. The technique computes normalised intensity value for each pixel based on a determined kernel size. The size of the kernel should be 2

to 3 times larger than the particle diameter, so that spatial variation in the background around the particle may be eliminated[141].

The next step in image pre-processing is the filtering done in the frequency domain of the image functions. This is in-line with the digitisation of particle image velocimetry where the cross correlation is also computed in the Fourier domain[135]. The Fourier transforms of the image functions, $f(m,n)$ and $g(m,n)$, is represented by their capitalisation, $F(u,v)$ and $G(u,v)$ respectively. It must be noted that the frequencies domain of these function describes the spatial variation and not time. The most basic of these filter function is the DC filter. This is similar to subtraction of the image mean, where the value at the origin (0,0) is replaced with zero. The DC filter is ideal for reducing background noise, low frequency distortions and may help recover regions affected by laser flare. The low pass filter is used to remove the other source of high frequency noise due to the camera and effects of digitisation. The simple form of the low pass filter is to set all intensity values above a certain threshold frequency to zero. It is, however, hard to determine the threshold frequency which separates the noise without the loss of data. As such, the Gaussian weighted function employed such that priority is given to the low frequencies and dampens out higher frequencies. Not all noises are contained in the high frequencies however, variation in the background of the image are often contained in the lower frequencies. In this case, the band pass filter is used. This filter attenuates noise from high and low frequencies leaving the median frequencies unchanged. The Gaussian weighted function can also be used to smoothen out the attenuation for the band pass filter. It must be noted that the Gaussian function has effect of blurring the image which will cause the correlation peak to be wider. This is in essence good for avoiding peak locking for smaller seeding particles. (Peak locking is described on pg.79).

Table 3-1: Image Filter Weighing Function types[142]

Filter Type	Filter Weighing Function
DC Filter (Subtraction of Background)	$W(u,v) = \begin{cases} 0 & for\ (u,v) = (0,0) \\ 1 & otherwise \end{cases}$
Low pass filter (Gaussian Weighted)	$W(u,v) = \begin{cases} 0 & for\ (u,v) = (0,0) \\ e^{\left(-\frac{u^2+v^2}{U \times V}\right)} & otherwise \end{cases}$ (U,V) is the size of the investigated frequency domain which is related to the size of the interrogation area.
Band pass filter	$W(u,v) = \begin{cases} 0 & for \quad r > 1 \\ 1 & for \quad {}^1/_4 < r \leq {}^3/_4 \\ 4r & for \quad r \leq {}^1/_4 \\ 4 - 4r & for \quad {}^3/_4 < r \leq 1 \end{cases}$ Where, $r = \sqrt{\left(\frac{2u}{U}\right)^2 + \left(\frac{2v}{V}\right)^2}$

The average spatial particle displacement can be modelled using a linear digital signal processing model shown in Figure 3-4.

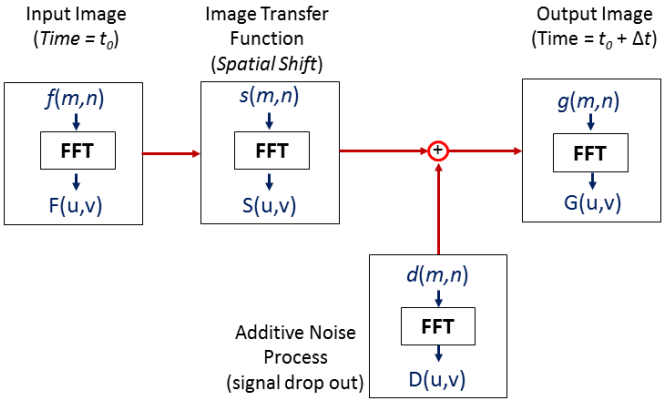

Figure 3-4: Modelling the Particle displacement function

Here, the capitalised $F(u,v), G(u,v), S(u,v)$ and $D(u,v)$ represent the Fourier transform of the functions in the spatial frequency domain. The two main components of interest of the model are:

1. The system's impulse response, $s(m,n)$, which the transfer function that dictates the average spatial particle displacement. This transfer function is related to the measured flow as well as the time separation between the two recorded image pair.
2. The additive noise process, $d(m,n)$. The noise function is related to the number of seeding particles that have moved in and out of the interrogation area during the time interval between the two recorded images. This is also known as 'signal drop out' or 'loss of pairs' and will contribute to a decrease in SNR since either initial or final position of the particle is lost.

The output image function, $g(m,n)$, is given as the spatial convolution of the input image function with the transfer function with noise.

$$g(m,n) = [f(m,n) * s(m,n)] + d(m,n) \tag{3.1}$$

The spatial cross-correlation technique is applied in order to compute the transfer function, $s(m,n)$. Here the cross correlation function between the two recorded images is given as:

$$\phi_{fg}(m,n) = E[f(m,n)\,, g(m,n)] \tag{3.2}$$

By substituting Equation (3.1) of the output image function, $g(m,n)$, into Equation (3.2), the cross correlation function becomes:

$$\phi_{fg}(m,n) = E[f(m,n)\,, [f(m,n) * s(m,n)] + d(m,n)] \tag{3.3}$$

If the effects of noise, if assume to be insignificant, the noise function, $d(m,n)$, may be negated.

$$\begin{aligned} \phi_{fg}{}'(m,n) &= E[f(m,n)\,, f(m,n) * s(m,n)] \\ &= \phi_{ff(m,n)} * s(m,n) \end{aligned} \tag{3.4}$$

The cross correlation function is computed in the spatial frequency domain since this has been found to be computationally less intensive[135]. This is part of the optimisation process for digital PIV systems, allowing for a much faster yield of results.

$$\Phi'(u,v) = F(u,v) \cdot G(u,v) \tag{3.5}$$

The inverse Fourier transform is then applied to the spatial frequency cross correlation function in order to obtain $\phi'(m,n)$. The physical interpretation of this cross correlation function is shown in Figure 3-5.

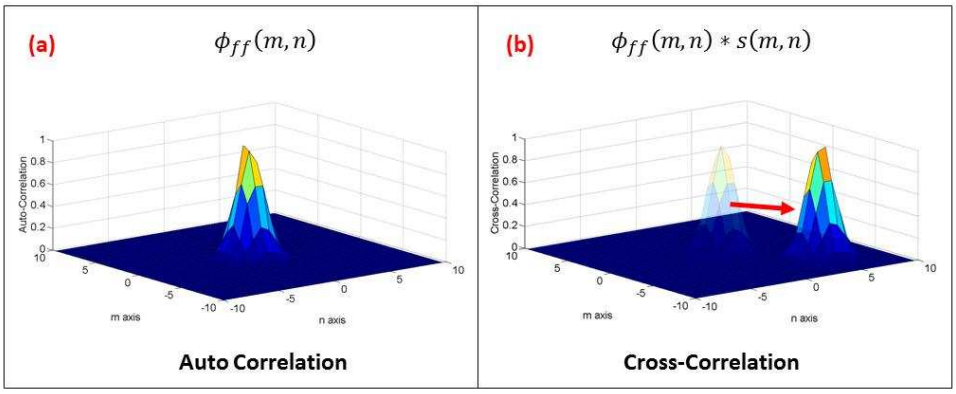

Figure 3-5: Illustration of the Spatial Cross-Correlation function between the two recorded images.

The autocorrelation of the input image, $\phi_{ff}(m,n)$, is akin to conducting the cross correlation of stationary images. This will results in a large correlation peak at the origin. The cross correlation of the image is essentially the convolution of the autocorrelation of the input image with that of the transfer function as shown in Equation

(3.4). The transfer function is shown to give the spatial shift of the autocorrelation peak. This spatial shift of the autocorrelation peak is the statistical representation of the average spatial particle displacement (in pixels) for the investigated interrogation area. The average spatial displacement in SI unit measurement can be obtained by multiplying the cross correlation result with the conversion function $h(x,y)$.

$$f'(x,y) = \phi'(m,n) \cdot h(x,y) \tag{3.6}$$

The conversion function is obtained through the calibration of the high speed camera of the PIV prior to the measurement. $h(x, y)$ simply gives the measurement length in SI units for each measured pixel in the *x* and *y* axis corresponding to the Cartesian co-ordinate of the investigated plane.

3.1.2 Adaptive Correlation and other Improved Interrogation Techniques

The Cross correlation technique described in Section 3.1.1 is a Single pass interrogative correlation technique. There are several improved interrogative techniques to obtain a more accurate displacement correlation of the recorded images; either by:

a. adaptively shifting[143] and/or

b. adaptively changing the size of the interrogation area[144].

These are iterative interrogative techniques whose initial pass is the same as the cross correlation described in Section 3.1.1. The adaptive shifting technique involves shifting the interrogation area of the second recorded image in the direction and magnitude equal to the average spatial displacement found using the initial cross correlation technique. It is hoped that the newly shifted interrogation area in the second image would contain more of the same particles from the first interrogation area and hence reduces the number of signal dropouts. This would greatly improve the signal to noise ratio of the correlation. The second interrogation area is again shifted, with respect to the newly obtained average particle displacement, and the process is repeated until the average displacement converges to within an acceptable threshold (typically 1-2 pixels). This technique is also known as the "forward difference interrogation algorithm". A further improvement to this technique is the "central difference interrogation algorithm". This technique involves shifting the interrogation area of both the first and second recorded images. The interrogation area of the first image is shifted by half the length of the initial computed average displacement length, in the opposite direction. The interrogation area of the second image is shifted half the length of the average displacement in the same direction. This central shifting

algorithm takes into account the number of particles moving in and out of the interrogation area in its original position and thus further reducing the amount of signal dropout. This technique is seen to be a second order algorithm which improves the accuracy of the forward displacement interrogation technique without much additional computational requirements[145].

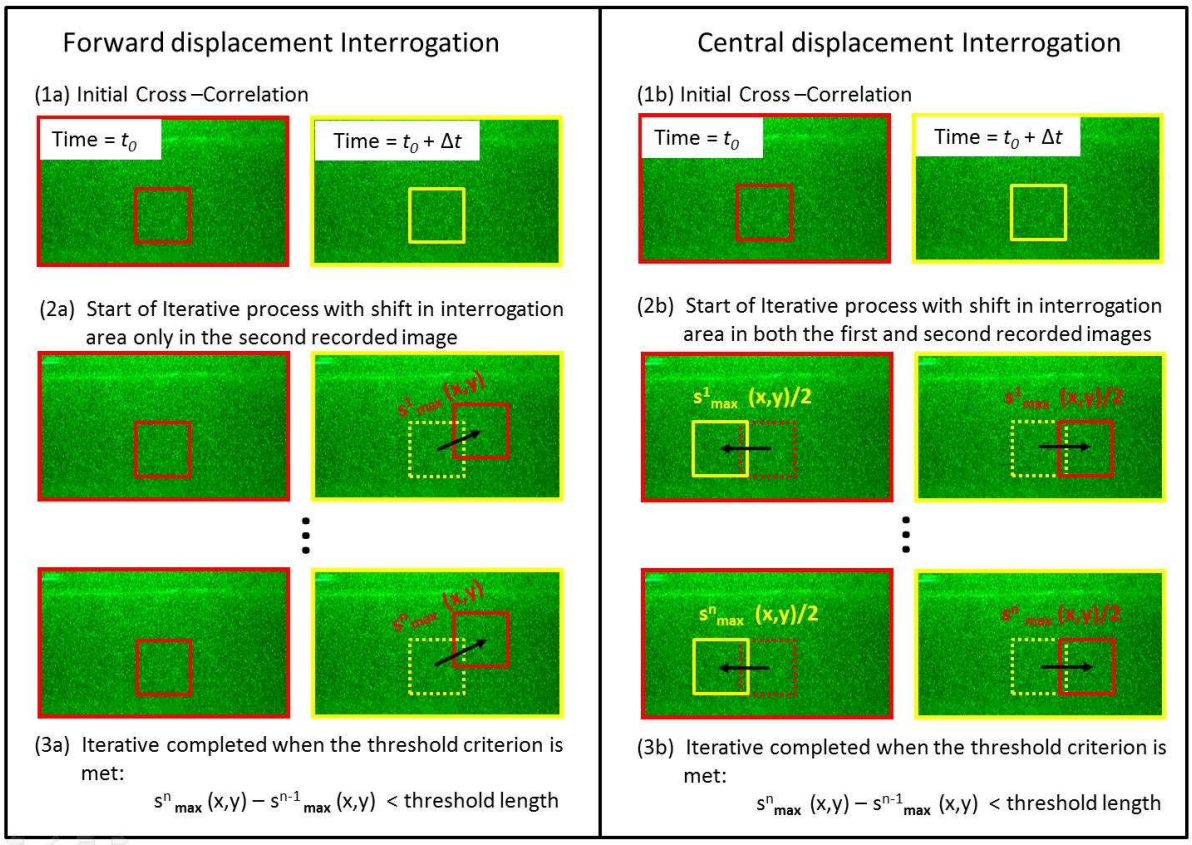

Figure 3-6: The illustration of the Forward and Central Displacement Interrogation techniques.

There is an added advantage in the use of the central displacement interrogation technique. The shifting of both the interrogated area of the first and second image also allows the measurement of particle displacements which are larger than the length of the interrogation area itself. This means that finer interrogation area size may be used, thus increasing the resolution of the velocity vector map[146]. This technique involves the progressive refinement in interrogation area size until the required resolution is achieved[147]. The initial step of this technique involves conducting the original cross correlation. Based on the average displacement obtained from this initial computation, the grid is refined to the next level, and the average displacement is used to estimate

the spatial shift for both the newly sized interrogation area for the first and second image. This step is continuously repeated until the desired velocity vector resolution is obtained.

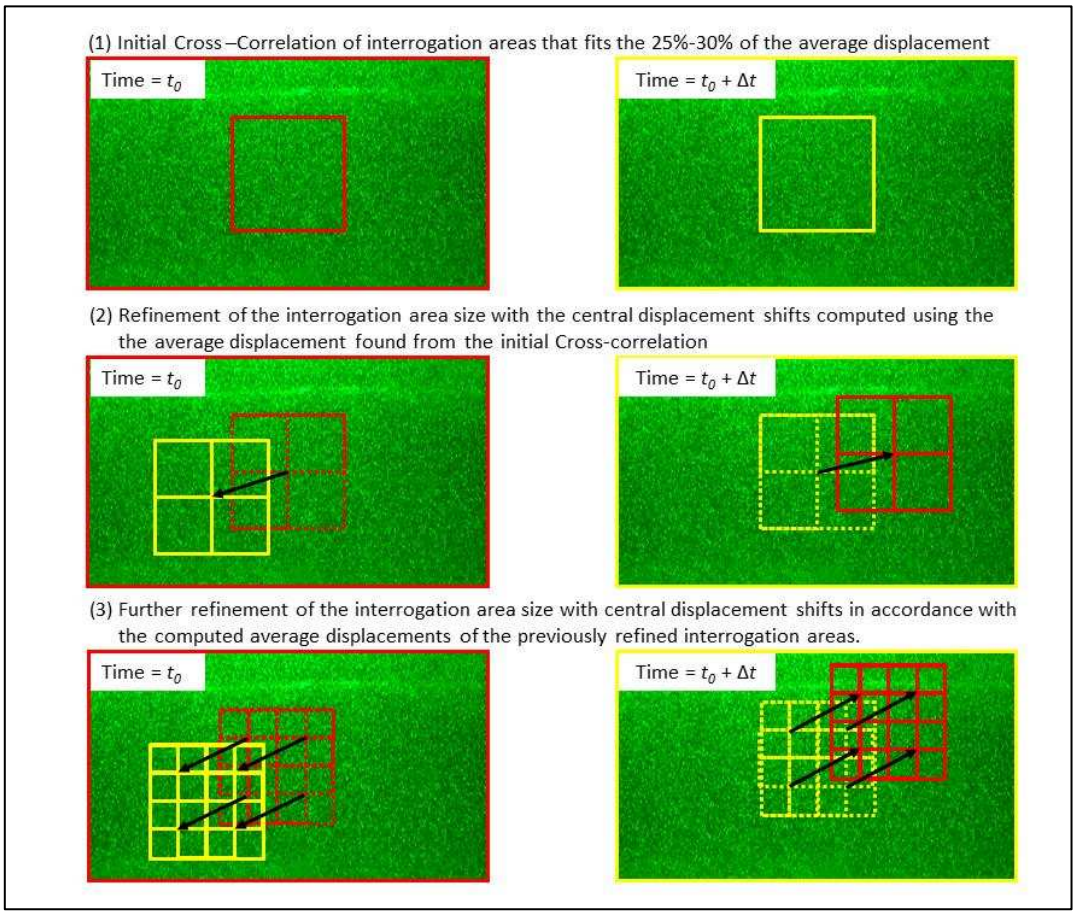

Figure 3-7: The Interrogation area refinement technique for obtaining higher resolution velocity vector maps.

It must be noted however, that the interrogation area refinement technique assumes that the average particle displacement of the initial correlation is a good representative of all the particles in the interrogation area. If there is a large variance in particle displacement within the interrogation area (also known as velocity gradient), the central displacement shift of the refined interrogation areas would be inaccurate causing more signal dropout or loss of signal entirely. As such, the initial size of interrogation area has to be selected with care in accordance the investigated flow behaviour.

3.1.3 Peak Detection and Sub pixel interpolation

In real PIV measurements, the results of the cross correlation may not always yield a single peak as previously shown in Figure 3-5. Those other peaks are a result of the correlation of the seeding

particles with other particles other than themselves. The effects of signal drop out, as discussed in the previous subsection, significantly contributes to the correlation of such lower peaks. Accordingly, these peaks are also a function of the noise, $d(m,n)$. Since it is assumed that the signal would be much larger than the noise level, the average displacement would thus correspond to the largest peak found in the correlation function[148]. The Dynamic Studio 3.0 software is programmed to detect the four largest correlation peaks for each measured interrogation area. The largest peak is determined to be the average particle displacement for the interrogation area. The second peak would correspond to the highest noise level. An iterative method is used to check the accuracy of this initial assumption through which the displacement of the interrogated area is compared to the displacements obtained from neighbouring interrogative areas. This is part of the post processing.

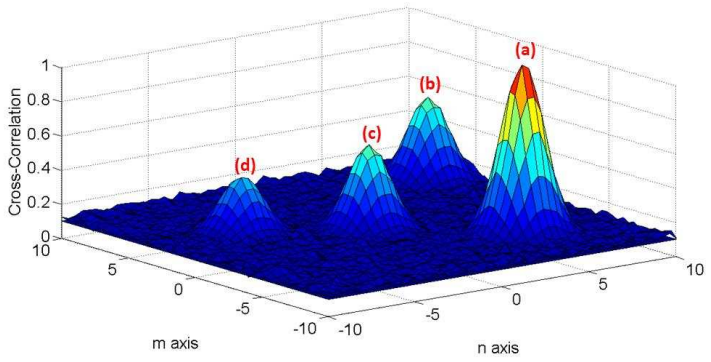

Figure 3-8: Multiple peak detection

The determination of the average spatial displacement is greatly dependent on the amplitude of each of the correlated peaks; it is important to get an accurate measurement of each peak. The spatial resolution of correlation function peaks may span one or more pixels. This resolution level is not accurate enough for many applications[138]. As such, in order to obtain better particle displacement resolution of the correlation peak, interpolation techniques are used. These interpolation techniques are able to improve particle displacement measurements up to sub pixel levels (typically up to $\frac{1}{20^{th}}$ of a pixel for an interrogation area of 32 x 32pixles[131]) and are thus

termed “sub-pixel interpolation” techniques. The most commonly used functions for the sub-pixel interpolation techniques are the Centroid, Parabolic and Gaussian peak detection methods.

The curve fitting technique requires a minimum of 3 adjacent points for the computation of the interpolation peak. These 3 main points correspond to the investigated coIrrelation maximum and its immediate neighbouring values which are above the noise floor level. The location of the sub-pixel interpolated peak should be between the correlation maximum and its direct adjacent value. Figure 3-9 illustrates the example of the identification of the 3 interpolation points. This also shows that the peak can be identified independently in the x and y direction.

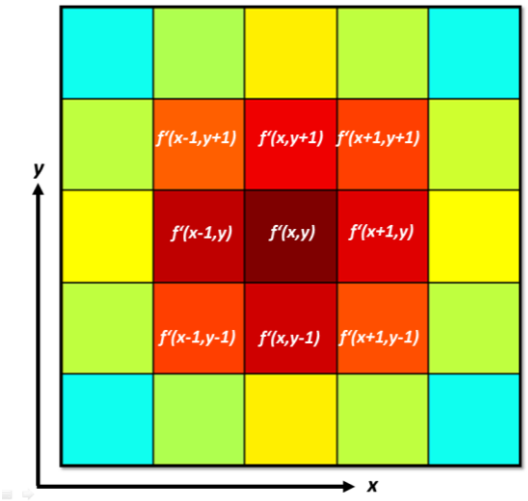

Figure 3-9: General identification of the neighbouring minima beside the interpolated peak

The most basic interpolation technique is the centroid technique. The centroid interpolation assumes the peak to be the centroid of the area between two minima (that are above set threshold percentage of the noise floor level)[149]. This centroid peak is equivalent to the ratio of the first moment to the zeroth order moment. The centroid technique thus prefer a broader correlation peak as it will allow more adjacent values to be used to estimate the centroid fitting. The drawback of the centroid technique however, is that the centroid peak is biassed towards pixel integer values[150]. This phenomenon is known as “peak locking”.

A more comprehensive technique is by fitting a function through the correlation peaks and its neighbouring values. The two most commonly used functions are the Gaussian and Parabolic

fittings. The Gaussian function is the preferred technique as it gives a good approximation of the Airy intensity patterns found in the recorded images[151]. The Gaussian function is also able to give accurate peak detection based on using only the minimum 3 point sample which makes it good for estimating narrow correlation peaks.

Table 3-2: The curve fitting functions used to estimate the peak of the cross correlation function[127, 152]

Function	Equation for Discrete function
Centroid $f(x,y) = \frac{first\ order\ moment}{zeroth\ order\ moment}$	$x_{max} = \frac{(x-1)f'_{(x-1,y)} + xf'_{(x,y)} + (x+1)f'_{(x+1,y)}}{f'_{(x-1,y)} + f'_{(x,y)} + f'_{(x+1,y)}}$ $y_{max} = \frac{(y-1)f'_{(x,y-1)} + yf'_{(x,y)} + (y+1)f'_{(x,y+1)}}{f'_{(x,y-1)} + f'_{(x,y)} + f'_{(x,y+1)}}$
Parabolic Fitting $f(x) = Ax^2 + Bx + C$	$x_{max} = x + \frac{f'_{(x-1,y)} - f'_{(x+1,y)}}{2f'_{(x-1,y)} - 4f'_{(x,y)} + 2f'_{(x+1,y)}}$ $y_{max} = y + \frac{f'_{(x,y-1)} - f'_{(x,y+1)}}{2f'_{(x,y-1)} - 4f'_{(x,y)} + 2f'_{(x,y+1)}}$
Gaussian Fitting $f(x,y) = C\,e^{\frac{-(x_{max}-x)^2}{k}}$	$x_{max} = x + \frac{\ln\left[f'_{(x-1,y)}\right] - \ln\left[f'_{(x+1,y)}\right]}{2\ln\left[f'_{(x-1,y)}\right] - 4\ln\left[f'_{(x,y)}\right] + 2\ln\left[f'_{(x+1,y)}\right]}$ $y_{max} = y + \frac{\ln\left[f'_{(x,y-1)}\right] - \ln\left[f'_{(x,y+1)}\right]}{2\ln\left[f'_{(x,y-1)}\right] - 4\ln\left[f'_{(x,y)}\right] + 2\ln\left[f'_{(x,y+1)}\right]}$

3.1.4 Post Processing – Replacement of Spurious Velocity Vectors

The computation of the velocity vector field using the statistical interrogation technique would often yield a number of "spurious" vectors in the measured plane even after careful experimental and interrogation technique setup. "Spurious" vectors are those that deviate largely in both magnitude and direction from their neighbouring vectors[153]. These are probably due to correlation between images of insufficient particle pairs or the use of false or wrong correlation

peaks for determination of particle displacement[154]. If the number of "spurious" vector is small as compared to the number of valid velocity vector in the measured plane (approximately 5%), these spurious vectors can still be recovered by replacing them with a bilinear interpolation computed using the vector's four neighbouring valid vectors[155]. Another method of spurious vector correction without interpolation is through looking at the other top four sub-pixels interpolated peaks of the correlation. If any of these peaks coincides with the average displacement of its valid neighbouring interrogation areas' displacement, that peak is used as a replacement for determination of the velocity vector[142].

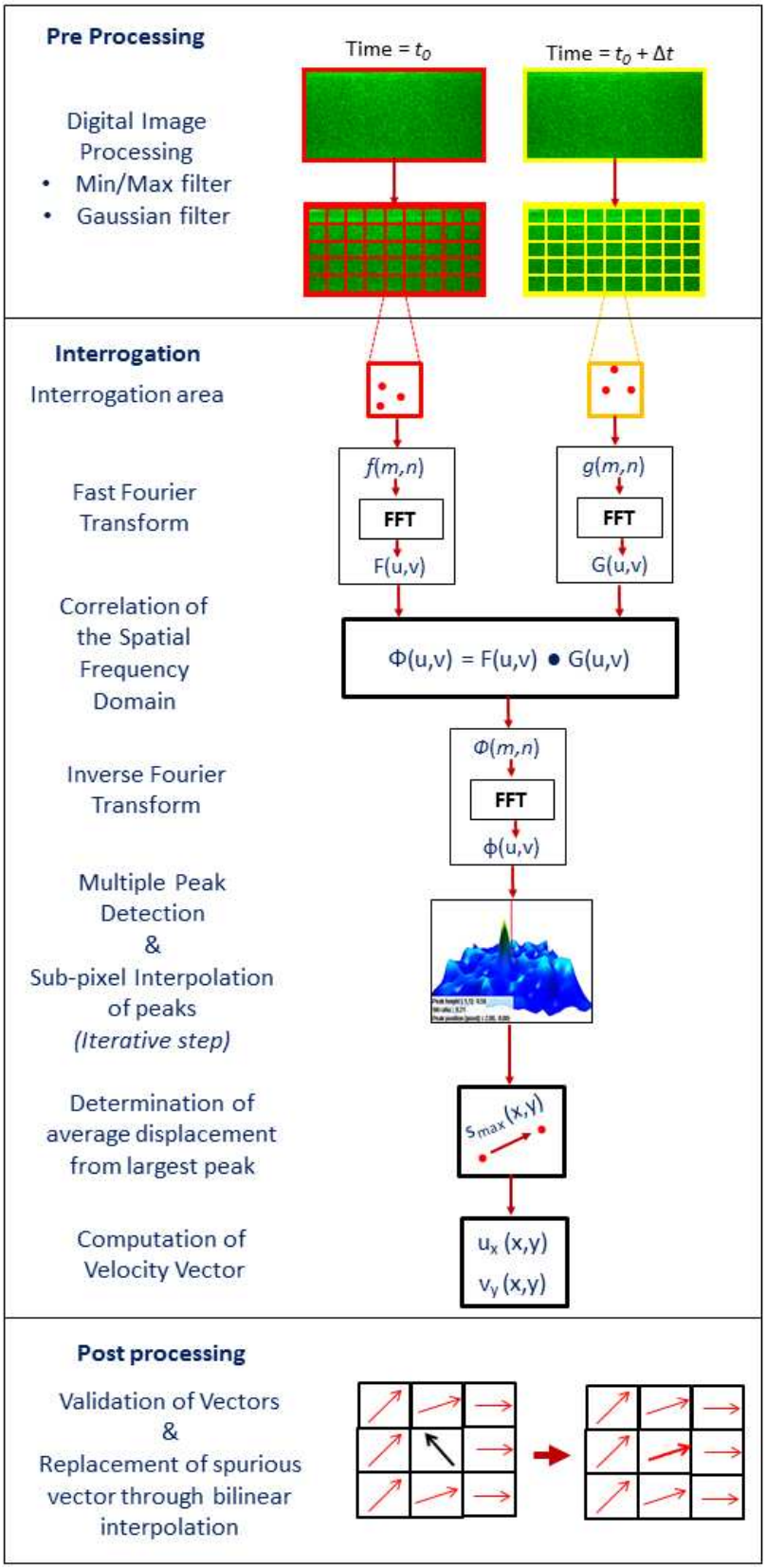

Figure 3-10: Summary of the interrogation process

3.2 PIV System used

The time resolved Particle Image Velocimetry (TR-PIV) system used for this research is the DANTEC Dynamics, Dual Power 15-1000 series. The laser unit used for this PIV system was developed by Litron and is a double pulse, 534nm wavelength, 15mJ, Nd:YLF system. The light sheet produced by the laser is approximately 1.5mm thick. The system is capable of firing up 10 kHz with nanoseconds intervals between the pair of pulses. The system utilises a Phantom CMOS High Speed Camera which has a resolution of 12 bit with a 1280x800 sensor. The camera is capable of capturing up to 1 million frame rates per second (fps) depending on the number of active sensor pixels used.

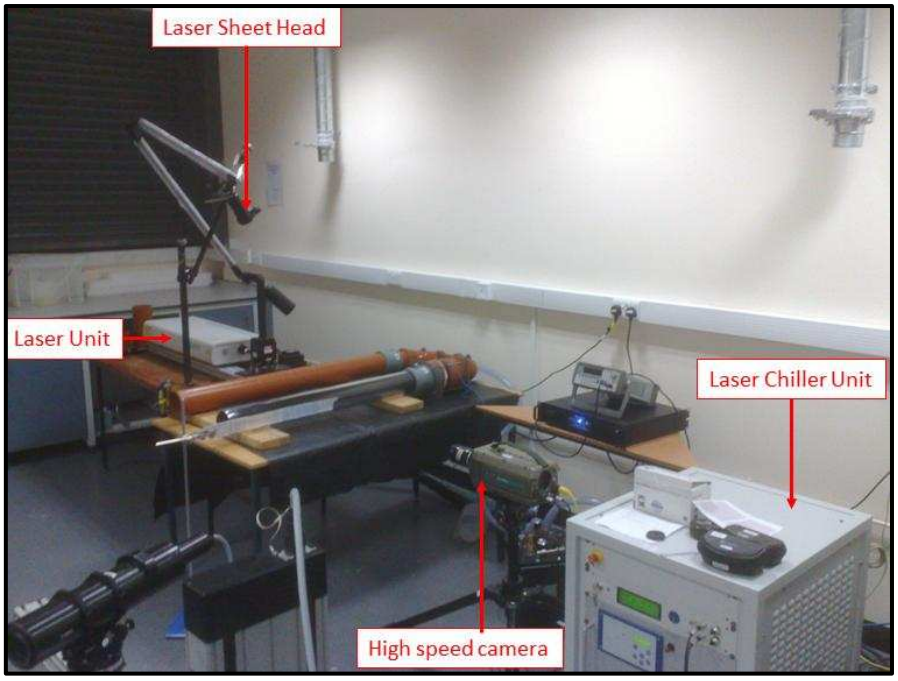

Figure 3-11: Layout of the DANTEC dynamic: TR-PIV system

The TR-PIV system comes with the Dynamic Studio 3.0 software package developed by DANTEC dynamics for analysing and computing the velocity vectors of the measured images. The investigation of pure acoustic flow using PIV is rare. Hence, some preliminary investigation is required for the setup of the acoustic flow experiment. These include finding suitable seeding particles and methods of seeding. The investigation was also carried out using a circular cylinder; there are however complications with light reflections due to the concave geometry of the circular duct system.

3.3 PIV Seeding Techniques

The tracer/seeding particles are those that allow the visualisation and measurement of the flow. It must be noted that PIV measures the seeding particles velocity as an estimate to the actual flow velocity. In order to minimise the discrepancies between particle and flow velocity, careful consideration is required regarding the choice of seeding particle, especially pertaining to its physical properties. The main considerations include:

1. The seeding particle must be sufficiently small that is able to follow all velocity fluctuations that occur in the flow.
2. The seeding particles should have good light scattering properties in order to be observed and recorded[152].
3. The density and thermodynamic properties of the seeding particles should ideally be the same as the fluid medium it is tracing, such that the property of the suspensions does not deviate too much from the fluid medium.
4. The duration in which the seeding particles is available for flow observation and measurement after being dispersed into the fluid medium. This is known as the seeding "residence time".

It is seen that the first and second parameters are a contradictory. While smaller seeding particles allow for better flow resolution and tracing, the sizes of the particles are proportional to their light scatter. As such, the smaller the particle, the harder it is to be observed and recorded for analysis. Finding a good compromise between these two considerations is important especially when flow medium is gaseous such as for this acoustic flow investigation. This is since gaseous medium used as thermoacoustic working fluid have density which are relatively much lower than that of seeding particles. The particle sizes have to be kept small enough such that the gravitational force does not influence the flow trajectory of the seeding particles. The comparison between size and density of each of the investigated seeding particles, as well as their light scattering properties are shown in

Table 3-3.

In thermoacoustics, the thermal interaction between the working fluid and its solid boundaries are the basis of the phenomena. As such, a good choice of seeding particle would be one that has similar or better thermodynamic properties as compared to the working fluid. In this case, the general desired properties for a thermoacoustic working fluid are:

- Low Prandtl number (viscous diffusion rate over thermal diffusion rate)[156].
- High ratio of specific heats[157].

Consideration as has also to be taken regarding the flash point and auto ignition temperature of the seeding particle with respect to the temperature of the hot heat exchange of the thermoacoustic engines' regenerator. In order to avoid such complications and to get a better control of the experiment, loudspeakers were used as the acoustic source and termination for this investigation. As such, the investigation can be treated as purely acoustic experiment without the complications of heat transfer. The thermodynamic properties thus become secondary for the selection of seeding particles. The comparisons of thermodynamic properties are included in

Table 3-3.

Most seeding particles have a limited time duration in which it is equally dispersed in the flow medium and is of optimum density for flow visualisation. There a several dispersion mechanisms which limit the residence time of the seeding particle. These include natural dispersion, agglomeration leading to deposition, deposition, sedimentation and evaporation (for fluid based seeding particles). The residence time is thus strongly dependent on the velocity as well as the turbulence of the flow. The reciprocal, high velocity, oscillating flow caused by acoustic excitation will enhance the dispersion mechanism and hence limit the residence time of the flow. It is thus important to find the right seeding particles that have sufficient residence time for the oscillation flow to become steady and maintain constant seeding density throughout the flow recording

period. The seeding particles are also predicted to enhance the probability of acoustic streaming. This can cause the unwanted DC flow of particles around the acoustic circuit.

Table 3-3: Comparison between the thermoacoustic working fluid properties with that of the seeding particles used

Thermoacoustic working fluids	Size(microns)	Density(kg/m^3)	Ratio of heat capacity (kJ/kg.K)	Prandlt Number
Air	-	1.207	1.4	0.713
Helium	-	0.164	1.66	0.261
Seeding Particle				
Water	0.5 – 1.0	995	1.33	7.01
Ethylene Glycol	0.5 – 1.5	1000	2.42	203
Sunflower Oil	0.5 – 1.5	1000	2.00	100-800
Smoke	0.5 - 3	1000-1500		3

The experiment was carried out with glycol water seeding mixture. Glycol-water mixture was chosen as the seeding liquid because:

1. Smaller particle size with reasonable density
2. It is less flammable compared to vegetable oils
3. The solubility of glycol also allows the volumetric percentage of glycol concentration to be varied in water
4. Glycol is water soluble making it easier to clean the surface of the measured section as compared to oils.
5. Glycol has relatively good light scattering properties.

The experiment was carried out to qualitatively test the effects of volumetric glycol concentration on the seeding properties of the glycol-water seeding mixture. The experiment was conducted with 10%, 20% and 30% volumetric glycol-water mixture. Distilled water was used as control for the experiment. Sunflower oil, which has the best light scattering property, was also used for comparison.

Two different techniques were investigated for the generation of these fluid based seeding particles. These include the ultrasonic transducer used for mist generation, and the second is the

high pressure Laskin Nozzle technique. The ultrasonic produces seeding particles through 2 separate mechanisms[158]. This first, is in accordance to the Taylor instability series in which the transducer exerts a downward force larger than the nominal gravitational acceleration on the crests of the surface capillary waves causing atomisation as the fluid particles are torn away from the bulk of the fluid[159, 160]. The second mechanism, the cavitation hypothesis, suggests that when the liquid is sonicated, small cavitation bubble forms at the surface of the liquid film. The implosive collapse of these cavities causes intense hydraulic shock which disintegrate the liquid film causing atomised liquid droplets to be ejected out from the liquids surface[161]. The sizes of the particles produced from the ultrasonic transducer tend to be more random in size because of the two separate atomisation mechanisms. The seeding particle sizes are proportional to the seeding's liquid viscosity as well as the ultrasonic excitation frequency. The mean seeding particle size can be predicted using[161]:

$$d_p = 0.34\left(\frac{8\pi\sigma}{\rho f^2}\right)^{\frac{1}{3}} \tag{3.7}$$

Where, d_p is the particle size diameter, σ (N/m) and ρ (kg/m^3) are the surface tension (determined by the viscosity) and the density of the seeding liquid. From experimentation it was found that the ultrasonic transducer is unable to produce seeding particles of sufficient density for direct seeding into the rig. As such, the seeding particles are allowed to accumulate in closed container as shown in Figure 3-12(c) before being slowly pumped into the investigated rig. This slow seeding technique is advantageous in that it requires less time for the seeding particle to be "settled" and be equally dispersed in the investigated rig. The seeding particles are considered settled when they are only executing random Brownian motion and void of the influence of the pumping. This technique requires that the seeding particles have long residence time with low deposition rate.

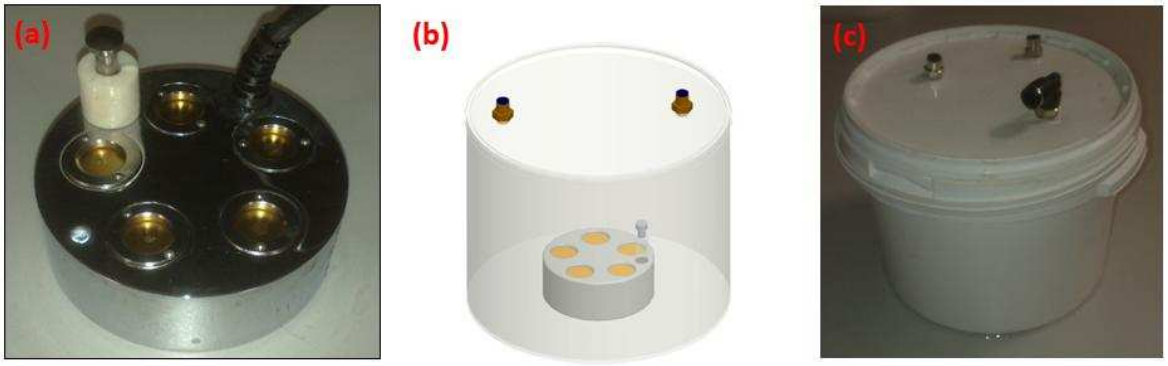

Figure 3-12: The ultrasonic transducer used in the PIV investigation. (a) The ultrasonic transducer, the sonication is produced from the 5 gold transducers seen on the housing. The stub protruding out from the housing is the liquid level sensor. (b) The transducer is immersed in the seeding liquid which has a depth 2cm higher than the transducers liquid level sensor. The transducer is allowed to generate sufficient seeding mist before pressurised air is used to pump the miss into the PIV investigated rig. (c) The ultrasonic seeding rig used in experimentations

The high pressure Laskin nozzle technique is capable of producing large volume of seeding particles rapidly and is usually used for seeding open systems. A schematic of the operating principle of this seeder is shown in Figure 3-13. The pressurized air inlet piping is divided into 2; the first runs past the impactor plate into the seeding liquid with a Laskin nozzle at its end. The other pressurized pipe is flush connected to the top of the pressure vessel. The Laskin Nozzle is nothing more than a small circular opening (of around 1mm in diameter) at the end of the pipe. Although the schematic only shows one pipe dipped into the liquid, the actual seeder may have several and each of these pipes usually has 4 Laskin Nozzles[162]. Pressurized air forced through the Laskin Nozzle generates tiny sonic jets whose shear stress causes small droplets to be formed and carried to the liquid surface in bubbles form. The impactor plate acts as a filter for these particles. The impactor plate is essentially a wide horizontal circular plate which has a very small gap between the walls of the pressure vessel. Small droplets formed by the Laskin Nozzle are allowed to escape through the impactor Plate's gap while larger particles are retained below. The smaller particles which escape are pressurized by the second pressure pipe and blown out of the seeder through the aerosol outlet.

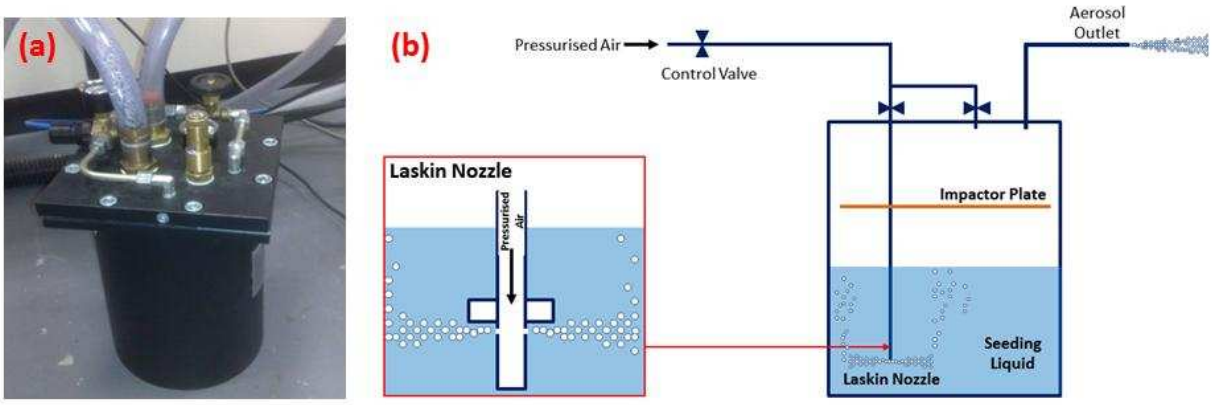

Figure 3-13: (a) Laskin Nozzle Seeding Rig. (b) Schematic layout of the Laskin Nozzle seeding rig

Because of its design and operating principle, Laskin nozzle is only suitable for fast seeding technique. This technique is advantageous for open systems such as wind tunnels where the residence time is not an issue. In closed system, the fast seeding technique ensure that there is quick equal dispersion of seeding particles in the investigated rig; however a longer settling time is required for the seeding after its insertion.

It was observed from experimentation, that fluid based seeding particles have a high deposition rate and thus low residence time for both fast and slow seeding techniques. The seeding showed relatively consistent density during the settling period after being pumped into the investigated rig. However, as soon as acoustic excitation is given, seeding density drops rapidly due to agglomeration and deposition. The deposition of the fluid seeding caused the investigated section to "fog up". As such, the investigated section had to be cleaned in between each experimental runs. This proved tedious and the rapid decaying density of the seeding during PIV measurement is a concern on the accuracy of the results. In order to get an improvement of the residence time of the seeding, solid seeding particles were considered. The best compromise between the seeding particles density and air was smoke particles. Smoke was generated by coiling a thin rope, which has been dipped in oil, around a cartridge heating element.

The smoke generated from slowly burning the rope was allowed to accumulate in a container until sufficient density is reached before pumping it into the investigated rig. This is a slow seeding

technique similar to the ultrasonic transducer seeder. The smoke seeding particles gave very good residence time which could last up to an hour, and could maintain consistent density through acoustic excitation. A summary of the experimented seeding particles and technique are shown in Table 3-4.

Table 3-4: Qualitative Results for Seeding Particles Tested for Acoustic PIV measurements

Tracing Particle	Seeding Technique	Qualitative results
Water Seeding	Laskin Nozzle & Ultrasonic Mist Generator	Advantages: • Gives good resolution • Does not fog up the test cross section easily • Easy to clean up the test cross section Disadvantages: • Poor residence time due to poor buoyancy (4-7 seconds)
Water-Glycol seeding mixture 10% Volumetric Glycol concentration	Laskin Nozzle & Ultrasonic Mist Generator	Advantages: • Better resolution than water seeding • Better residence time compared to water seeding (20 seconds to 50seconds) Disadvantages: • In sufficient particle density • Quick to fog up the test cross section
Water-Glycol seeding mixture 20% Volumetric Glycol concentration	Laskin Nozzle & Ultrasonic Mist Generator	Advantages: • Same resolution as 10% water glycol mixture • Same residence time compared to 10% water glycol mixture (1minute to 3 minute) • Sufficient particle density Disadvantages: • Fogs up the test cross section much faster than 10% water glycol mixture. • Difficult to clean test cross section
Water-Glycol seeding mixture 30% Volumetric Glycol concentration	Laskin Nozzle Ultrasonic Mist Generator	Advantages: • Better residence time compared to 20% water glycol mixture (3- 5 minutes before fogging of test section) Disadvantages: • Poorer resolution as compared to 20% water glycol mixture due to over density of particles • Fogs up the test cross section much faster than 10% water glycol mixture. • More difficult to clean test cross section
Sunflower Oil	Laskin Nozzle Ultrasonic Mist Generator	Advantages: • Gives very good resolution • Better residence time (5-7 minutes) Disadvantages: • Fogs up the test cross section • Much more difficult to clean test cross section
Smoke	Heating element assembly	Advantages: • Excellent Residence time (45vminutes – 1 hour) • Low deposition rate, does not fog up (1-2 hours) Disadvantages: • Fogs up the test cross section

It must be noted that the seeding particles tested here was solely to be used for acoustic flow measurement purposes.

3.4 PIV Illumination Technique

The illumination for the PIV investigation was provided via a laser light sheet. The laser light sheet is able to penetrate through the walls of transparent ducting sections made out of materials manufactured from glass, acrylic and sapphire in order to illuminate the flow within. The use of circular cross sectional ducting has always posed a problem for PIV measurements, mainly because of the light scattering properties of its curved surfaces. It is of interest however, to investigate an acoustic wave propagating through circular duct section, which is being used for the thermoacoustic engines resonators. Thus, several techniques were investigated in order to reduce the glare and reflection caused by the circular geometry of the ducting, as to obtained good PIV measurements. Figure 3-14 shows the main region in which light is scattered when the Laser Sheet is shone in the middle of the circular cross section of the tube, parallel to its length. Region (a) and (d) refer to the top and bottom region of light scatter for the outer curved surface of the tube. Although the light reflections of these regions are scattered away from the tubing, care must be taken that this stray reflections are not re-reflected on the tubing or onto the lenses of the camera.

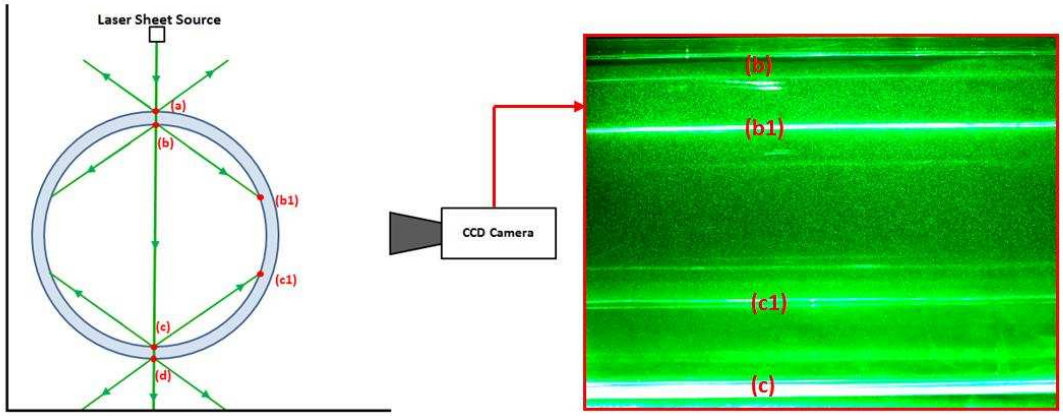

Figure 3-14: The main region of light scatter for a Laser Sheet shone parallel along the length of a circular cross section tube.

The light scatter of region (b) and (c) pose more of a concern as the light is scattered within the tube which may cause unwanted “flare” in the recorded image, such as shown by (b1) and (c1) in

Figure 3-14. The laser reflection "flares" may be reduced by strategic placement of light absorbing materials to absorb stray reflections which causes the "flares". Several methods were tested using black paper as the light absorbing material in this experiment.

- Using black paper as the backdrop of the cylinder (Figure 3-14)
- Covering the half of the outer surface of the cylinder with black paper (Figure 3-15)
- Coating the inner half of the cylinder with black paper (Figure 3-16)

Black paper was chosen because of its low cost and its flexibility in usage (easy to be cut to the shape and size required and also able to some extend follow the shape of the object it covers). The black paper was used as the backdrop of the measured cylinder. This was done to absorb the stray reflections such as from region (a) and (d) as shown in Figure 3-14. The black background also gave better seeding particle contrast for the PIV measurements. The reflected "flares" corresponding to region (b) and (c) of Figure 3-14 still pose a major disturbance to the image captured.

When the black paper is used to coat the outer surface of the cylinder as shown in Figure 3-15, the image captured of the particles has an even better contrast. Although the flares from region (b1) and (c1) are still present, the intensity of the flare seemed to have been reduced. This may be due to the small portion of the reflection being absorbed by the black paper coating.

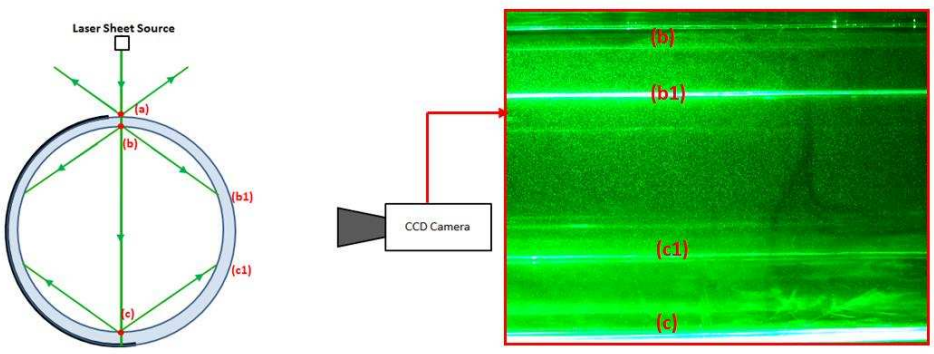

Figure 3-15: Result of Laser Sheet Light Dispersion with Black Paper Covering Half of the Outside surface of the tube (corresponding flares regions are marked both on the layout as well as the sample image)

Based on the results in Figure 3-15, the next step to furtherance to reduce the reflection flares would be to coat the inner surface of the tube with black paper as shown in Figure 3-16. As such,

the flare from region (c1) of Figure 3-15 can be completely eliminated. This is shown in Figure 3-16, the effects of the flare of region (b1) has also been reduced to an extent that it no longer affects the image captured.

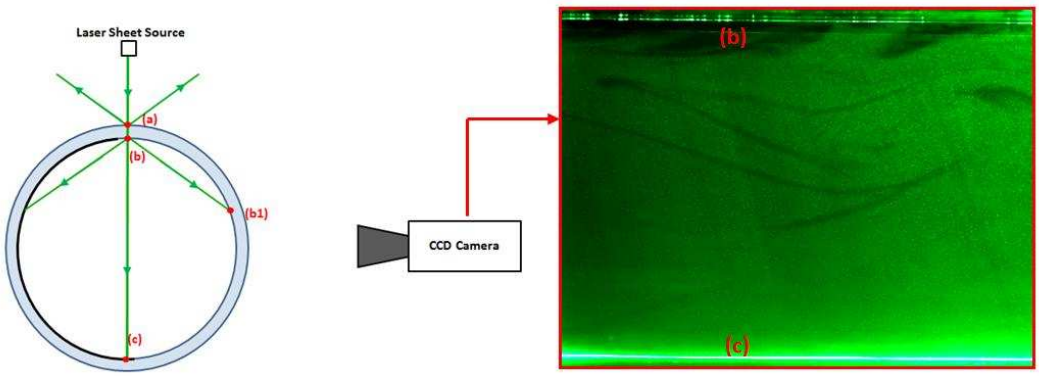

Figure 3-16: Result of Laser Sheet Light Dispersion with Black Paper Covering Half of the Inner surface of the tube (corresponding flares regions are marked both on the layout as well as the sample image)

It must be noted however, that while method 1 and 2 are both non-intrusive, method 3 is. Having the coating on the inner surface of the cylinder will have an effect on the flow due to several factors:

- The black paper would have a different surface roughness as compared to the transparent tube.
- The diameter of the section coated with the black paper will be minutely smaller as compared to the section of the tube not coated.
- There is a small step between the paper coating and the transparent tube.

PIV measurement however shows that the effect of the inner coating on the acoustic flow is minimal and that the velocity vector measurements with or without the black paper inner coating is the same. By minimising flare and allowing only the scattered light from the seeding particles in the laser illuminated plane to reach the camera, the PIV image appears more planar allowing for more accurate velocity field measurement. PIV calibration was conducted using both a calibration grid as well as a fixed checker box calibration sheet shown in Figure 3-17. The image distortion due to the curved surface of the circular duct was shown to be negligible.

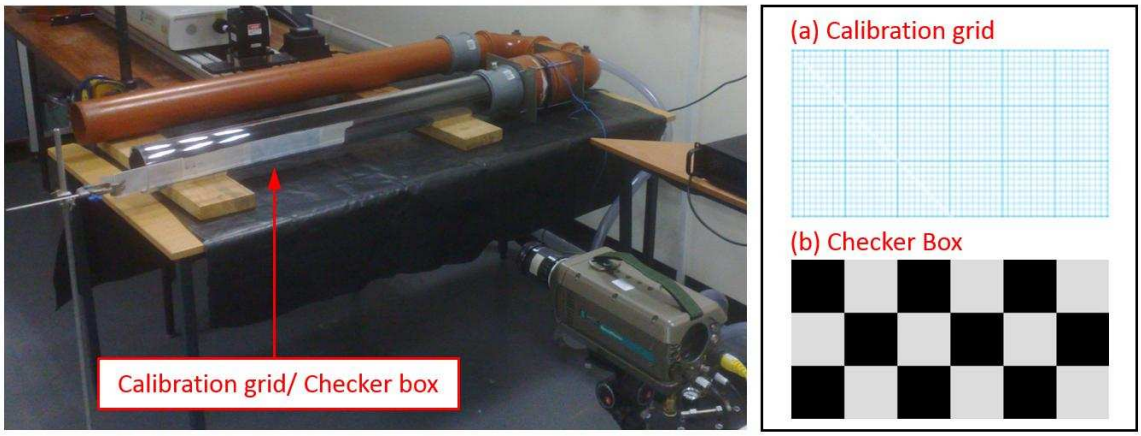

Figure 3-17: Result of Laser Sheet Light Dispersion with Black Paper Covering Half of the Inner surface of the tube (corresponding flares regions are marked both on the layout as well as the sample image)

Based on Snell's law on refraction and reflection, it can be stipulated that the position and angle of the laser head can determine the direction of the light reflection. Traditionally, PIV measurements were done with the laser head positioned perpendicular to the horizontal surface of transparent tube. This was done so that the overlap of intensities between the pulses of both the laser sheets are the same for the flow visualization section. Because of the difference in density between the transparent acrylic duct test section and the air, reflection and refraction is unavoidable. This is even more apparent when the acrylic ducting has a circular cross section.

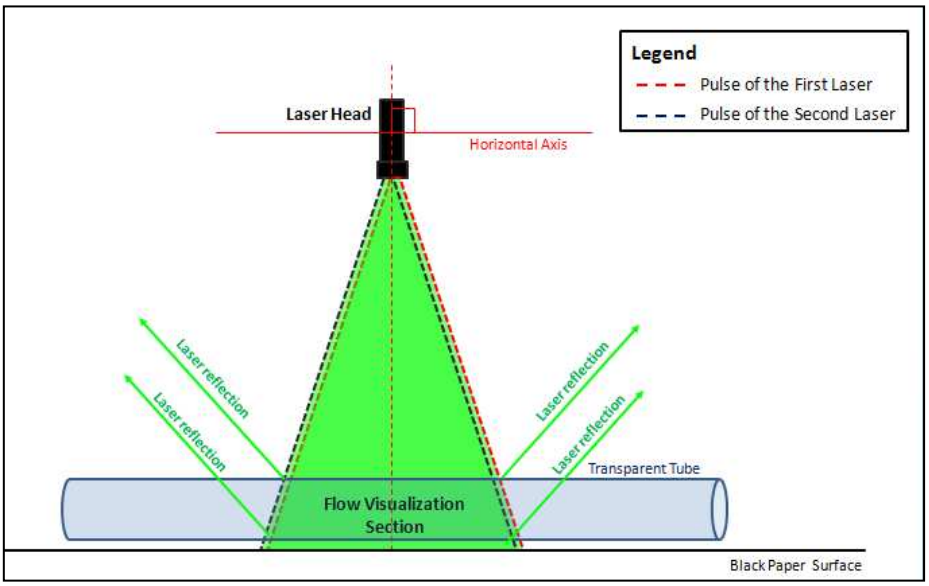

Figure 3-18: Layout of the experiment with the Laser Head perpendicular to the horizontal transparent tube

The vertical configuration of the laser however gave a lot of undesired laser light reflections, majority of which are directed in the axis of the camera (out of the page direction for Figure 3-18) causing glares in the image captured. It was found that adjusting the angle of the laser head, as shown in Figure 3-19,had allowed for a majority of the laser reflection to be deflected away from the camera and plane of measurement.

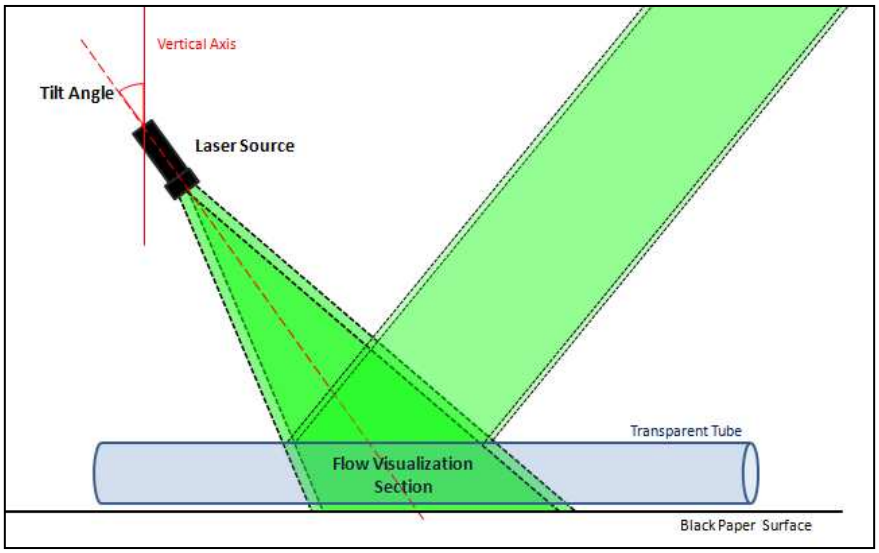

Figure 3-19: Layout of the experiment showing the Laser Head tilted at an angle and the reflection deflected away from the flow visualization section

The image captured using the PIV software showed a larger reduction in glare corresponding for this method. There is however an optimal angle for the tilt of the laser head. If the tilt angle was too low, the reflection would not be deflected away sufficiently resulting in residual glare in the recorded image. Too large a–tilt angle however causes the laser sheet to be spread out over a larger area, thus reducing the intensity of the illumination over the length of the test section. The optimum tilt angle was found to be approximate 30^{o} from the vertical for this experiment where the laser head was approximately 50cm above the measured section. The tilting of the laser head however requires the laser head to be slightly further from the flow visualisation section causing the laser sheet to be spread over a larger area and reducing the overlap of intensity in the image plane. The laser power (kWe) was increased by 15% in order to overcome this problem.

Chapter 4

Velocity based Wave Decomposition Technique

4.0 Development of the Velocity based Decomposition Technique

The acoustic wave analytical techniques described in the previous chapter are based on pressure measurements. The pressure based analytical techniques are constricted within the conditions for plane wave mode of propagation and assumes that the wave behaves linearly. This is because these pressure techniques rely on point pressure measurements made using pressure transducers that are flush mounted onto the investigated section of the waveguide in order to analyse the wave in the system. The development high speed cameras and laser technologies in the last decade, has made acoustic field measurements possible using particle image Velocimetry (PIV) [163, 164]. These relatively new optical measurement techniques can also be used to study acoustic propagation in waveguide system such as in the Thermoacoustic engine resonator. PIV allows both the flow visualisation of the acoustic field through the axial cross sectional plane of the waveguide as well as measurement of the acoustic velocity vector field of the same investigated plane. Flow visualisation makes it easy to determine the mode of propagation of the wave and if any non-linear acoustic behaviour is occurring. The analysis of the velocity vector field will reveal the characteristics of the investigate wave in greater detail. It is however, to the best of the authors knowledge, that the acoustic wave decomposition technique described in Chapter 2.0 is limited to pressure measurements and as yet, no effort has been made for analysing acoustic wave through its decomposition via using its velocity measurement. It is therefore of vital importance for the

development of such a technique considering the continuous improvement of PIV systems and the added advantages it can offer in the measurement and analysis of acoustic waves.

This chapter describes the development of a new comprehensive Velocity based Wave Decomposition (VWD) technique that is to be used with PIV measurements for the analysis of acoustic wave propagating through waveguide systems. It must be noted that the VWD technique can also be used with other acoustic velocity measurement techniques, such as hotwire anemometry and Laser Doppler Anemometry (LDA), but will not yield such a comprehensive analysis as when used with PIV measurements. The development of the VWD technique is based on the adaptation of the already established Pressure based Wave Decomposition technique(PWD)[165]. This requires that the technique be traced back to its fundamentals in order to be reworked for use with velocity measurements.

As discussed earlier in Chapter 2.1, Chung[117] and Seybert[115] were pioneers of the wave Decomposition technique. Although both their techniques are essentially the same, Seybert's technique was chosen for adaptation even though it is slightly more computationally intensive. This is because it can provide the power spectrum of the constituent wave components which allows for the analysis of the wave's harmonics in addition to its fundamental frequency. The spectrum will also show the energy distribution as well as the Signal to noise ratio which is important to determine the level of confidence of the analysis. The mathematical derivation of the VWD technique is given in detail in sub-chapter 4.1.

A MATLAB programme was used to simulate a 2D synthetic plane wave, one that would resemble the velocity vector plane result from PIV measurements. The simulation was also made to generate pressure plane fields complimentary to the velocity vector planes, such that the VWD results can be compared with that of the results using the proven PWD technique. This would also allow for a two tier verification of the VWD technique; the first being the VWD results compared with that of the simulated values, and the second of which being that the VWD compared with the PWD technique.

Simulation was then used to verify the velocity based decomposition (VWD) technique throughout its development stage. The validation of the VWD technique via the simulation is described and discussed in sub-chapter 4.3.

The VWD technique was also verified experimentally using simultaneous velocity and pressure measurements. Time resolved Particle Image Velocimetry (TR-PIV) and pressure transducers were used to measure the same section of the waveguide so that the comparison between the established PWD techniques can be compared with that of the newly developed VWD. The experimental verification is single tiered since there is no base value in which to compare the VWD results with besides the PWD results. The experimentation however provides real acoustic propagation conditions which were not included in the simulation. The experimental phase was important to prove that the VWD technique is functional in real measurement conditions. The details of the experiment are given in sub-chapter 4.3. Figure 4-1 shows the summary of the development and verification of the VWD.

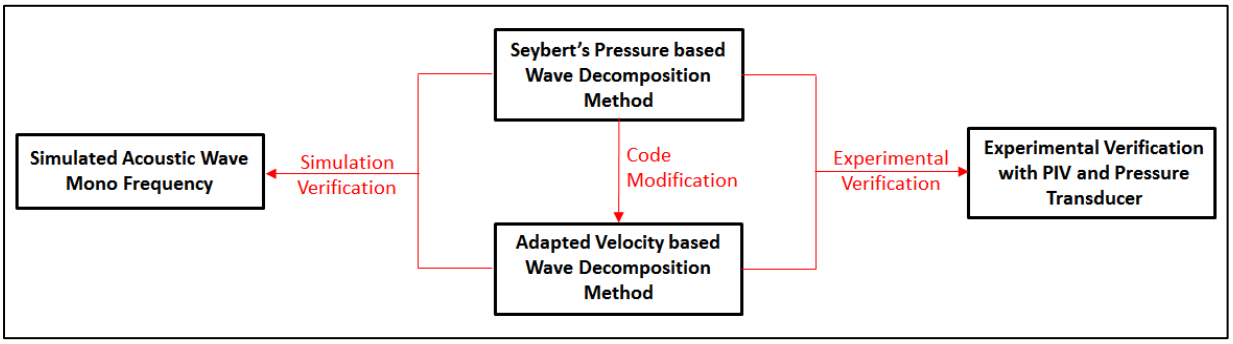

Figure 4-1: VWD development flow chart. Simulation was used to generate the pressure and velocity components of synthetic acoustic waves in order that the results of the VWD technique maybe benchmarked against the established PWD technique results. The VWD is thus verified through simulation and experiments by comparison between known theoretical results and PWD results.

4.1 Mathematical Derivation of the VWD technique

The field of acoustic studies is based on two main measureable properties of an acoustic wave: its pressure and velocity. The measurement of either property in a free acoustic field yields the resultant superposition value of its constituent travelling wave components at the point of measurement. For a waveguide with rigid walls, these constituent travelling wave components are

continuously reflected off from the waveguide's wall, such that the wave propagation is confined to the direction parallel to the axial length of the waveguide, allowing only incident and reflected wave components to propagate[114]. The reflections, caused by the constituent travelling wave components which are not parallel to the waveguide's axial length, give rise to the formation of harmonics which in turn result in the formation of different modes of propagation in the waveguide[113]. This occurs only when the oscillation's wavelength is much larger than the hydraulic diameter of the waveguide. The wave's mode of propagation is dependent on the cross sectional size of the waveguide as well as the frequency range it propagates in. An acoustic wave propagating below the threshold known as the cut-off frequency, fc, of the zeroth order mode of propagation, can be assumed to be a plane wave[166]

An acoustic plane wave propagating in a duct is the superposition of its constituent incident and reflected travelling wave components (denoted by the subscript *i* and *r* respectively). Being a scalar quantity, the pressure measured at any point along a resonator ducting would be the sum of the wave's constituent travelling wave components given by the equation:

$$\tilde{p}(x,t) = \tilde{p_i}(x,t) + \tilde{p_r}(x,t) \tag{4.1}$$

The adaptation of the velocity based Decomposition technique begins with the velocity being a vector quantity. The analogy used in this paper is that the incident direction is indicated as positive and the reflected as negative. The velocity measured at any point along the resonator duct is thus given as:

$$\tilde{\boldsymbol{v}}(x,t) = \tilde{\boldsymbol{v_i}}(x,t) - \tilde{\boldsymbol{v_r}}(x,t) \tag{4.2}$$

The Wave Decomposition technique utilises the phase and amplitude relationship between the two point measurement made at a known separation along the duct in order to decompose the wave into its respective incident and reflected component.

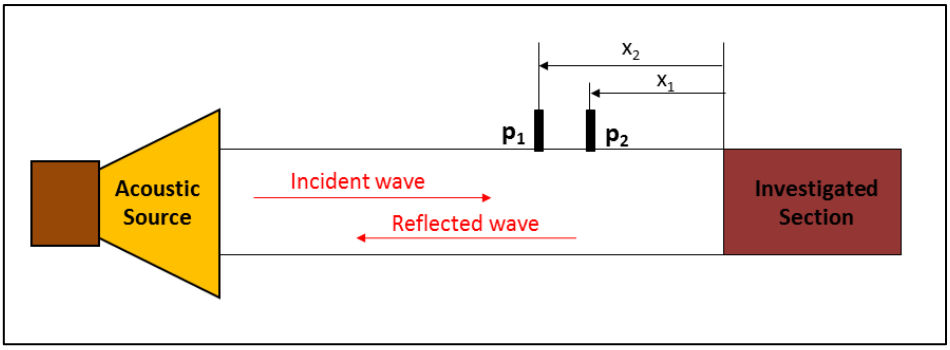

Figure 4-2: Pressure based Wave Decomposition experimental setup

The incident and reflected travelling wave components can be written in terms of its one dimensional Euler wave solution representation shown in Equation (4.3)

$$\widetilde{v_i}(x,t) = \tilde{a}(t)e^{i\omega t - ik_i x} \tag{4.3}$$

$$\widetilde{v_r}(x,t) = \tilde{b}(t)e^{i\omega t + ik_r x} \tag{4.4}$$

The measured velocity from point 1 and point 2 can be written in terms of their Auto Spectral Density form as S_{V11} and S_{V22}. The cross correlation between the velocity measured from point 1 and pont 2 can be written in terms of its real C_{V12} and imaginary Q_{V12} components. These are related to their corresponding Incident (S_{VAA}) and Reflected (S_{VBB}) auto spectral densities and cross spectral density (C_{VAB} and Q_{VAB}) by a transfer matrix given by Equation

(4.5).

$$\begin{bmatrix} S_{V11} \\ S_{V22} \\ C_{V12} \\ Q_{V12} \end{bmatrix} = [TM_v] \begin{bmatrix} S_{VAA} \\ S_{VBB} \\ C_{VAB} \\ Q_{VAB} \end{bmatrix} \tag{4.5}$$

The derivation of the velocity based Decomposition transfer matrix $[TM_v]$ is shown in [118]; The $[TM_v]$ is given as:

$$\begin{bmatrix} 1 & 1 & -2\cos[(k_i+k_r)x_1] & -2\sin[(k_i+k_r)x_1] \\ 1 & 1 & -2\cos[(k_i+k_r)x_2] & -2\sin[(k_i+k_r)x_2] \\ \cos[k_i(x_1-x_2)] & \cos[k_r(x_1-x_2)] & -\cos[k_ix_1+k_rx_2]-\cos[k_rx_1+k_ix_2] & -\sin(k_ix_2+k_rx_1)-\sin(k_rx_2+k_ix_1) \\ \sin[k_i(x_1-x_2)] & \sin\left(k_r(x_1-x_2)\right) & -\sin(k_ix_1+k_rx_2)+\sin(k_rx_1+k_ix_2) & -\cos[k_rx_1+k_ix_2]+\cos[k_ix_1+k_rx_2] \end{bmatrix} \quad (4.6)$$

The spectral density components for the velocity wave components are thus given as:

$$S_{VAA} = \frac{S_{V11} + S_{V22} - 2C_{V12}\cos k(x_1-x_2) + 2Q_{V12}\sin k(x_1-x_2)}{4\sin^2 k(x_1-x_2)} \quad (4.7)$$

$$S_{VBB} = \frac{S_{V11} + S_{V22} - 2C_{V12}\cos k(x_1-x_2) - 2Q_{V12}\sin k(x_1-x_2)}{4\sin^2 k(x_1-x_2)} \quad (4.8)$$

$$C_{VAB} = \frac{S_{V11}\cos 2kx_2 + S_{V22}\cos 2kx_1 - 2C_{V12}\cos k(x_1+x_2)}{4\sin^2 k(x_1-x_2)} \quad (4.9)$$

$$Q_{VAB} = \frac{S_{V11}\sin 2kx_2 + S_{V22}\sin 2kx_1 - 2C_{V12}\sin k(x_1+x_2)}{4\sin^2 k(x_1-x_2)} \quad (4.10)$$

The respective auto and cross spectral densities of the resultant incident and reflected component from Equation

(4.5) can be used to compute the pressure and velocity Cross Spectral Density, S_{PU}, and the velocity auto spectral density, S_{UU}, such as shown in Equation (4.6) and (4.11):

$$S_{PU}(f,x) = \rho c[S_{AA}(f) - S_{BB}(f) - 2iQ_{AB}(f)] \quad (4.11)$$

$$S_{UU}(f,x) = S_{AA}(f) + S_{BB}(f) - 2C_{AB}(f) \quad (4.12)$$

The Complex Acoustic Impedance in the frequency domain is the ratio of the cross spectral density and the velocity auto spectral density, given as:

$$\frac{Z(f,x)}{\rho c} = \frac{S_{PU}(f,x)}{S_{UU}(f,x)} = \frac{S_{AA}(f) - S_{BB}(f)}{S_{AA}(f) + S_{BB}(f) - 2C_{AB}(f)} + i\frac{-2\,Q_{AB}(f)}{S_{AA}(f) + S_{BB}(f) - 2C_{AB}(f)} \quad (4.13)$$

The absolute value of the complex acoustic impedance, $|Z(f,x)|$, gives the amplitude relation between pressure and velocity components of the acoustic wave. The arctangential ratio of the imaginary to the real component of the complex impedance gives the phase difference between the pressure and velocity component. In turn, the phase difference between the incident and reflected component of the wave is given by the arctangential ratio of the imaginary, Q_{AB}, to the real, C_{AB}, component of the Cross Spectral density, S_{AB}:

$$\theta_{AB} = \tan^{-1}\left(\frac{Q_{AB}}{C_{AB}}\right) \tag{4.14}$$

4.2 Simulation Verification of the VWD technique

Simulation of synthetic waves is an ideal method with which the fundamental function of the VWD analytical technique can be verified. The type of synthetic wave generated is controlled by the input parameters for the simulation. By varying the input parameters, a whole range of different acoustic waves can be generated. The verification of the technique is based on the VWD analysis of the generated synthetic wave to match that of the simulation input parameters. A MATLAB code was written in order to simulate results of the 2-D velocity vector plane obtained from PIV measurements. In addition to this complimentary 2-D plane pressure field, the simulated velocity vector plane was also generated. This is used as a second tier validification wherein the synthetic waves are used as a control for the verification between both the VWD results and the PWD results.

In order to verify the fundamental function of the VWD technique, the synthetic waves were programed as one dimensional, linear, inviscid, non-dissipative plane waves as given by Equation (4.15) and (4.16) for the pressure and velocity components respectively. Here the amplitude *A(t)* and *B(t)* denotes the incident and reflected travelling wave components.

$$\tilde{p}(x,t) = \left[A_1 e^{i\omega_1 t - ikx} + B_1 e^{i\omega_1 t + ikx}\right] + \left[A_2 e^{i\omega_2 t - ikx} + B_2 e^{i\omega_2 t + ikx}\right] \tag{4.15}$$

$$\tilde{v}(x,t) = \frac{1}{\rho c}\left(\left[A_1 e^{i\omega_1 t - ikx} - B_1 e^{i\omega_1 t + ikx}\right] + \left[A_2 e^{i\omega_2 t - ikx} + B_2 e^{i\omega_2 t + ikx}\right]\right) \tag{4.16}$$

The time, *t,* is related to the sampling frequency over the number of samples taken. ω_h, is the angular frequency, the subscript, h, denoting the harmonics with 1, being the fundamental harmonic, 2, the secondary harmonic and so on. k, is the wave number given as the ratio of the angular frequency to the speed of sound. The simulation was set for 2000 time steps which is equivalent to the number of experimentally PIV recorded samples. As the wave Decomposition technique works only with the plane wave mode of propagation, the fundamental frequency of the simulated wave are kept below the zeroth order cut-off frequency[166] which, for a circular cross sectional duct, is given by:

$$f_c = \frac{j_0' c_0}{2\pi r} \tag{4.17}$$

Here, $j_0' \approx 1.84118$, is the first non-negative zero of the ordinary Bessel function of the first kind. The pipe diameter used in the experiment is, $2r=0.1m$. This corresponds to a cut-off frequency of, $f_c \approx 975.8Hz$. This is well above the frequency used in the investigation and hence assumed to only propagate in the plane wave mode. The Standing wave ratio is a good measure of the strength of the standing wave to the travelling wave component of the wave in interest. The Standing wave ratio (SWR) is given as the ratio between the pressure antinode to the pressure node of the measured wave. This can be written in terms of the amplitude of the incident and reflected wave component as shown in Equation (4.18).

$$SWR = \frac{A + B}{A - B} \tag{4.18}$$

In order to verify the technique and the resolution of the developed wave Decomposition technique, the technique would have to be tested with a pure travelling wave (SWR=1), a pure standing wave (SWR=∞) and as many points between them. The simulation was used to generate 1,000 different forms synthetics waves of SWR from 1 to ∞. This was accomplished by varying the amplitude of the incident wave component from 2,000Pa to 1,000Pa over 1,000 samples while simultaneously increasing the amplitude of the reflected component from 0Pa to 1,000Pa. The

formation of the 1,000 sample is better illustrated in Figure 4-3. The established PWD technique was used to compute the wave Decomposition using the pressure component of the synthetic wave and the VWD for the velocity component respectively.

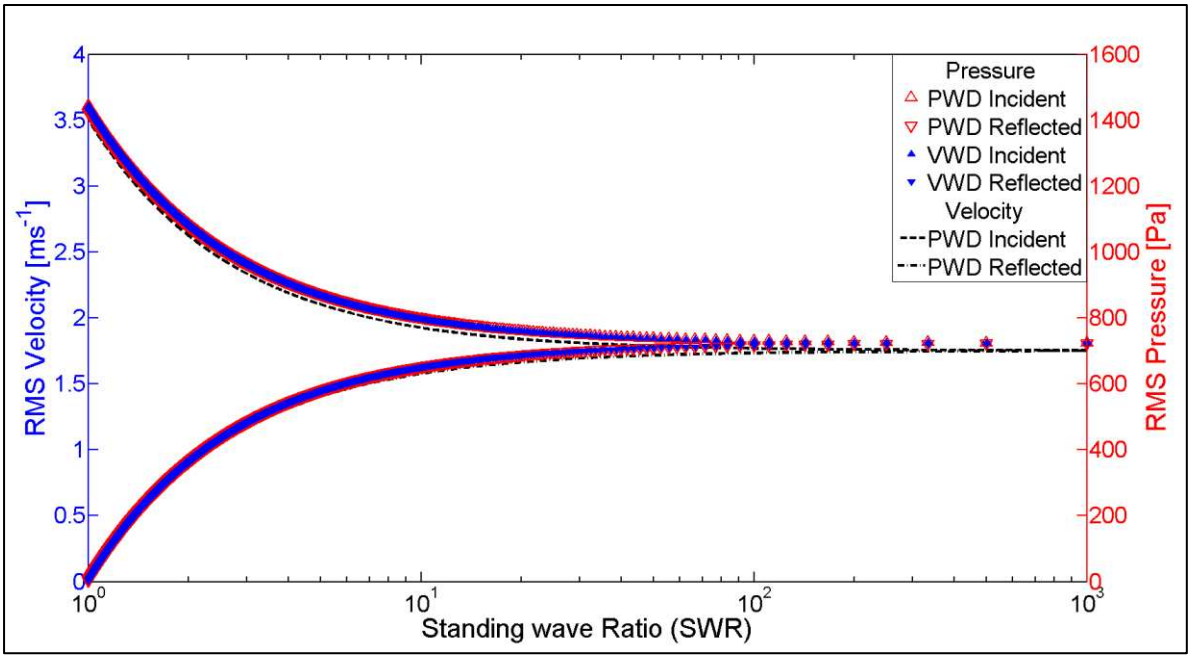

Figure 4-3: The Amplitude of the Incident and Reflected component plotted against their respective Standing wave Ratios. The Incident and Reflected component were computed using the PWD and VWD techniques from the ideal, lossless synthetic acoustic wave with no noise. The results for the PWD and VWD are a complete overlap and matches well with the actual values of the synthetic waves.

The results from the VWD and PWD analysis show a complete overlap between the incident and reflected components from both techniques as seen in Figure 4-3. There is an over prediction of about 0.5% between the wave Decomposition results and the simulated values for all runs. This can be attributed to the spectral resolution of power spectral density and converting its peak values into time domain amplitudes. The simulation results also show that the wave Decomposition technique has a resolution of at least 1Pa. The auto spectral density of the incident and reflected component from the respective VWD and PWD techniques are used to compute the complex acoustic impedance of the waves as in accordance to Equation (4.13). The complex impedance also shows a complete match between that obtained using VWD and that from PWD. The profile of the resistive (real) and reactive (Imaginary) component of the complex acoustic impedance corresponding to respective SWR are shown in Figure 4-4. The pure travelling wave corresponding

to SWR=1, is shown to be purely resistive while a pure standing wave, SWR= ∞, is purely reactive, which is in accordance with theory.

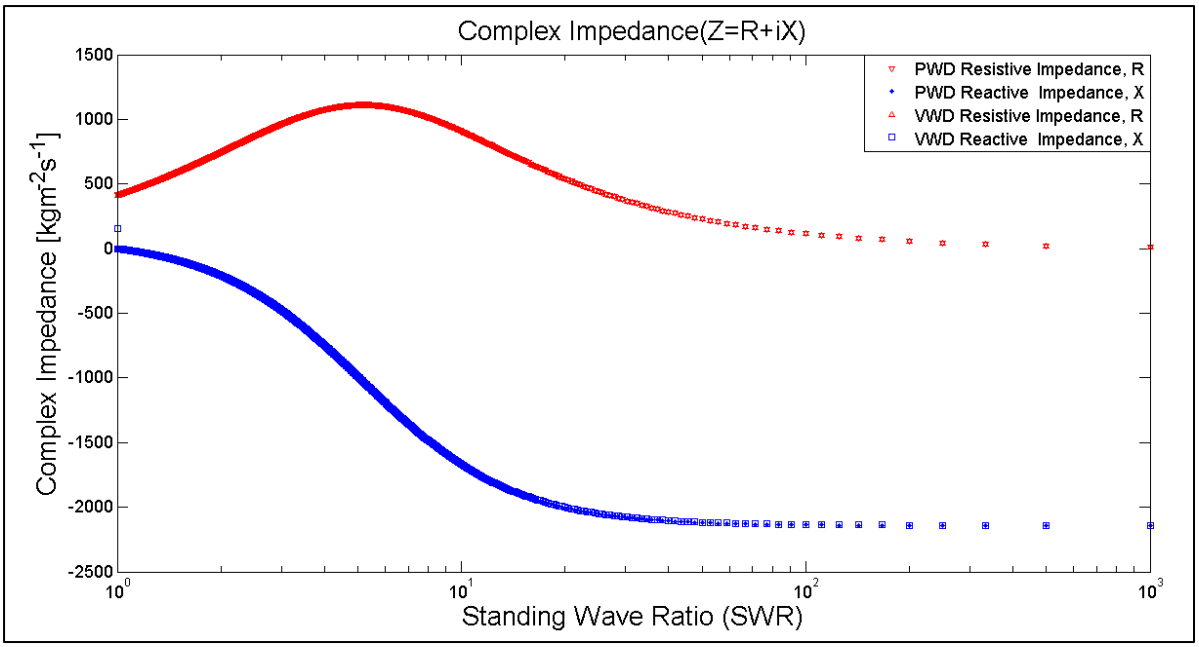

Figure 4-4: The Complex Impedance computed using the VWD and PWD techniques plotted against their respective Standing wave Ratio. The results from the VWD and PWD are again a complete overlap. The results of the Complex Impedance curves matches that in theory where a pure travelling wave (SWR=1) the Complex Impedance is purely resistive and for a pure standing wave (SWR = ∞) the Complex Impedance is purely reactive.

The angle between the reactive and resistive component of the complex impedance is the phase relation between the pressure and velocity component of the wave. Similarly the phase relations between the incident and reflected wave component are related by their cross power spectrum as given by Equation (4.14). The results from the phase relation between the pressure and velocities as well as that of the incident and reflected component from both the VWD and PWD are shown in Figure 4-5. As in accordance with the results of the complex impedance, the phasing between the pressure and velocity for both techniques are also a match. The results are in accordance with theory where the velocity and pressure component for a pure resistive wave are in phase and is 90^{o} out of phase with each other when the wave is purely reactive.

Figure 4-5 also shows the phase between the incident and reflected component for the different SWR waves. It is shown that as the SWR approaches a pure resistive wave, the VWD shows that the

phasing between the incident and reflected component increases, whereas the phasing for the PWD decreases. This is due to the difference in the pressure and velocity sign convention as shown in Equations

(4.1) and (4.2).

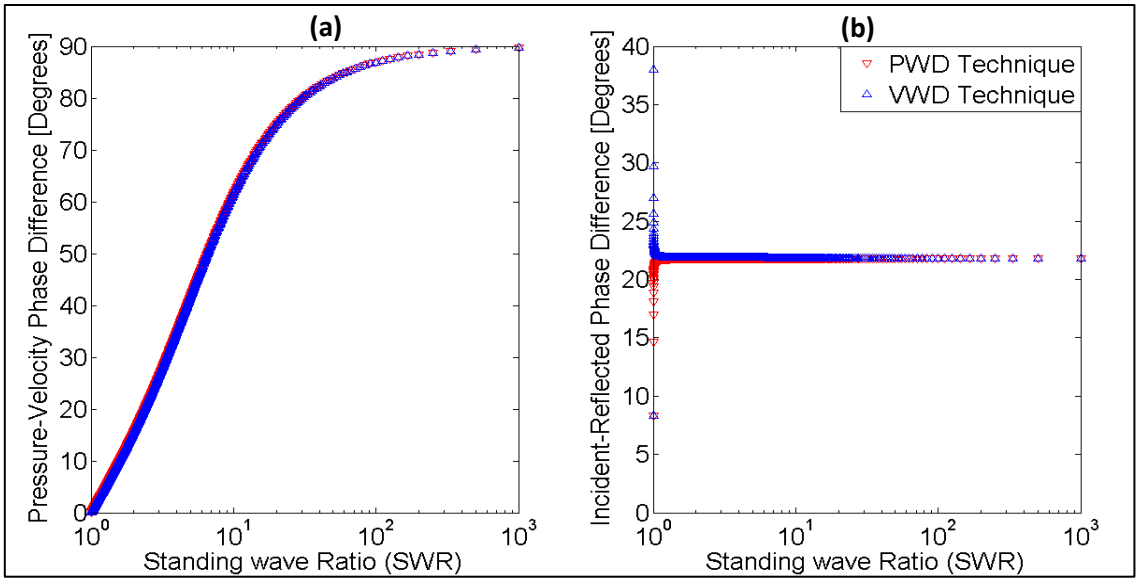

Figure 4-5: The Phase Angle corresponding to the Standing wave Ratio of the Simulation. (a) Phasing between the Pressure and Velocity component of the wave. (b) Phasing between the incident and reflected components of the wave.

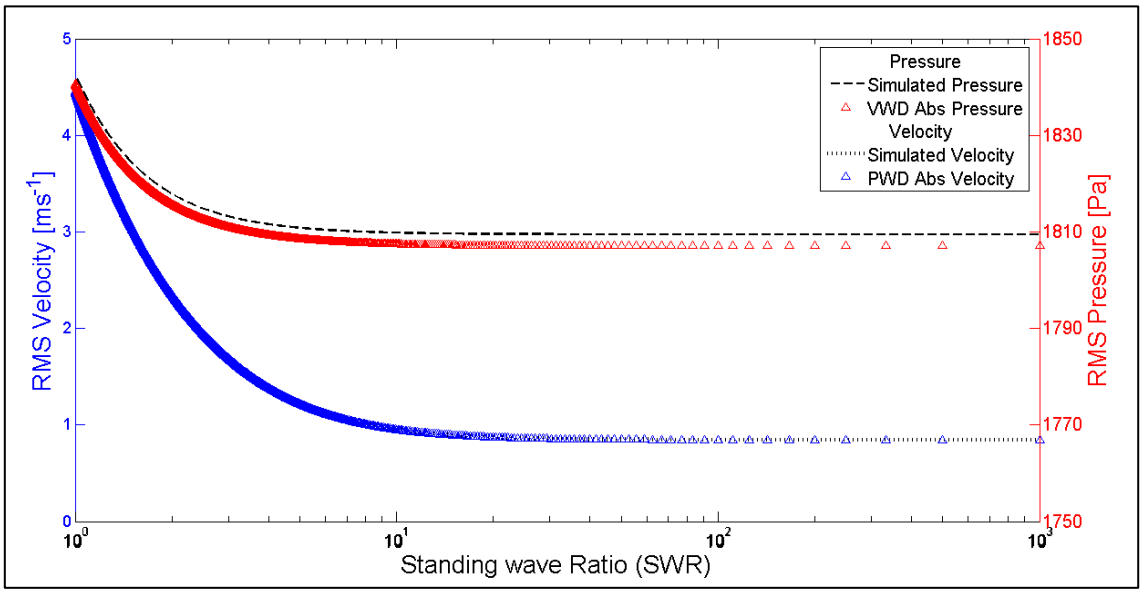

Figure 4-6: Comparison between the simulated Pressure and Velocity value and that obtained from the Wave Decomposition technique

The computation of the complex acoustic impedance also allows the direct conversion of a measured velocity at a point to be converted into pressure measurements. The results from the point computation of the complex acoustic impedance as shown in Figure 4-4 was used to convert the pressure and velocity component at the same point into their respective inversion. The result of the conversion from velocity to pressure using the VWD technique and pressure to velocity using the PWD technique are shown in Figure 4-6. There is a small difference between the simulated pressure and velocity values from that computed using the wave Decomposition technique. The Decomposition technique yields a lower value of 0.5% for both pressure and velocity values as compared to the simulation. The discrepancies are again attributed to the insufficient spectral resolution of the computed power spectral densities. This may be resolved by interpolating the spectrum points corresponding to the investigated frequency/ies. This however, was not done in order to simulate the real acoustic wave analysis where investigated frequency/ies are to be determined from the VWD analysis itself. The spectral resolution can be improved by taking a larger sample of the investigated wave. Based on the control simulated synthetic wave, it is shown that the newly develop VWD technique is able to perform the same analysis equally well as the established PWD.

4.3 Experimental Validation

The simulation proved that the VWD technique performs effectively for acoustic wave propagation under ideal, non-viscous and linear condition only. Acoustic wave propagation is sensitive towards small geometrical changes and even the slightest defect in waveguide system. For this reason, acoustic wave propagation is often not ideal as it has some element of dissipation and nonlinearity in it. It is thus important that the VWD technique is tested experimentally in order to verify its functionality as well as its sensitivity in real experimental conditions. The experimental verification procedure is summarised in the flow chart in Figure 4-7.

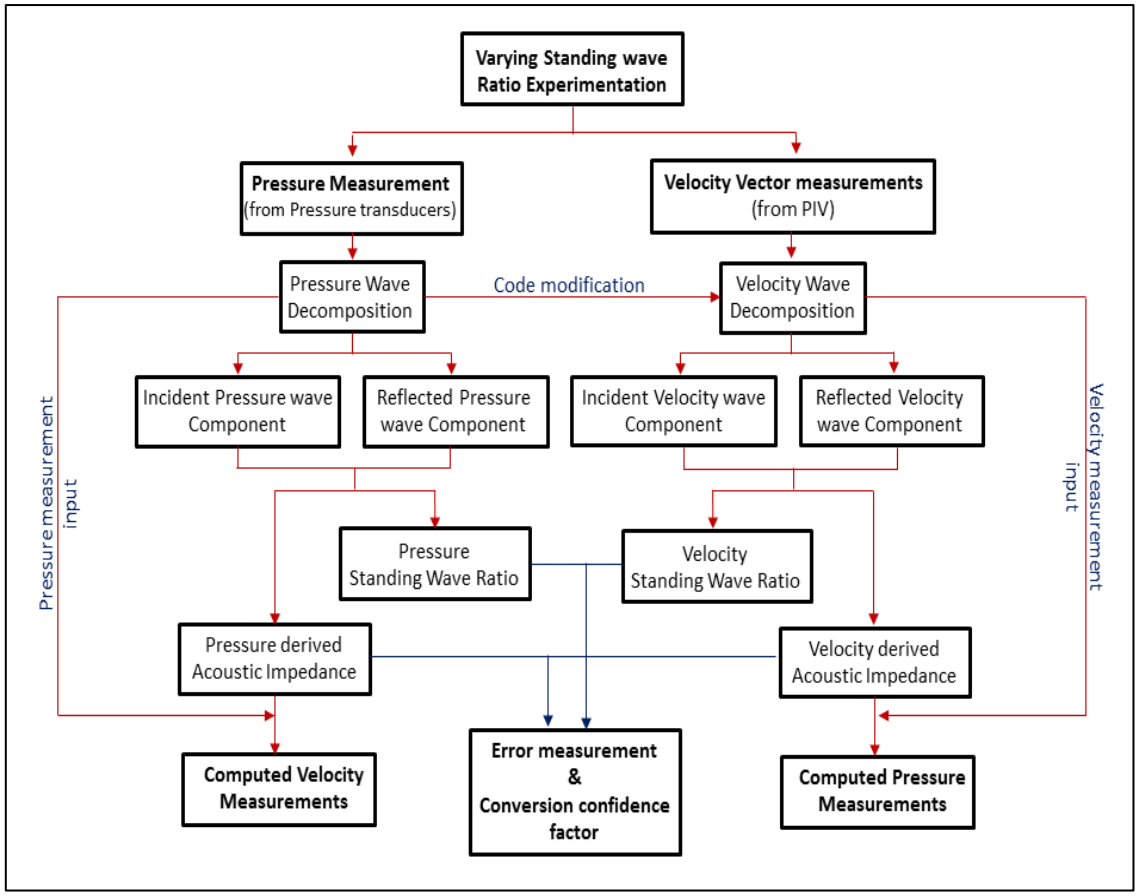

Figure 4-7: Flow chart of the experimental procedure

The experimentation was conducted using speakers instead of the Thermoacoustic engine itself. The experimental setup is shown in Figure 4-8. Speakers were chosen because these allow control of the type of acoustic wave propagating through the waveguide system. The Passive Reflection Cancellation (PRC) technique, described in Chapter 2.1.3, was used to change the termination impedance of the system, hence facilitating for a range of acoustic SWR to be tested with this setup. Pressure and velocity measurements were taken simultaneously from the same section of the waveguide duct by using flush mounted pressure transducers and PIV respectively. The pressure transducer system used has a minimum sampling rate of 2000Hz. In order to obtain a fair comparison between the results from both PIV and pressure measurements, only 5,122 numbers of samples from the pressure transducer measurements were used to compute the PWD analysis. This is to reconcile the number of sampled periods used for analysis between both instruments. The system was used with a sampling rate 10 times that of the fundamental frequency under study.

A Smoke generator was used to provide the seeding which was injected into the pipe and allowed to settle until only Brownian motion is observed, before any experimental runs and measurements were made. In acoustic PIV measurement, it is important to verify that the particle is able to trace the reciprocal motion of the acoustic flow. This is necessary owing to the difference in density between particle and the acoustic medium (air). The particle response time, t_{res}, was computed using[167]:

$$t_{res} = \frac{(\varepsilon - 1){d_p}^2}{18\upsilon} \tag{4.19}$$

Here, ε is given as the ratio between the particle and fluid density ($\varepsilon \approx 892.89$), d_p is the average seeding particle diameter ($d_p \approx 5\mu m$) and υ, the viscosity of the acoustic medium. The time response was calculated to be, $t_{res} = 79\,\mu s$, which is more than 1/100 times the period of the highest investigated frequency. Such a short response time ensures that the particle is sufficiently able to trace the investigated acoustic flow. The close match between PWD results obtained from pressure transducer (without seeding) and the VWD results from PIV measurement, which will be shown later, is evidence that the choice of seeding particle was optimal. The PIV system utilises the double frame, single exposure measurement system. The image pairs captured with this technique were analysed using an adaptive correlation technique[142]. The final interrogation area size was 32x32 with 50% window overlap and the vector maps were validated between each iterations.

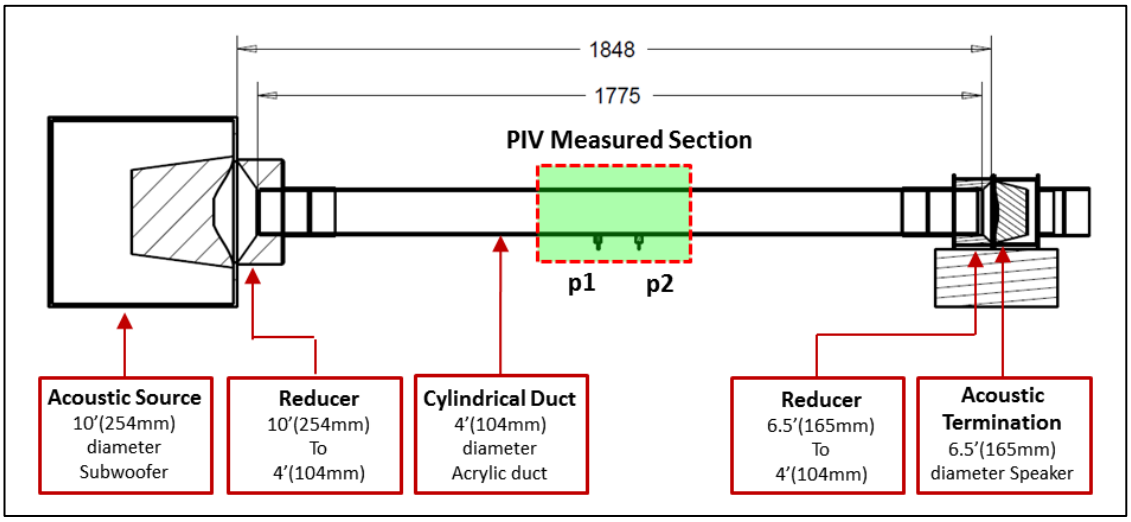

Figure 4-8: Diagram of the experimental setup (all dimensions in mm).p1 and p2 are the flush mounted pressure transducers used for pressure measurement in the experiment. PIV was used to measure velocity vectors across the entire axial cross sectional plane indicated by the dotted box region

The input power to the source speaker was kept at 100We for each of the runs. The calibration results for the PRC technique are shown in Figure 2-10. Both the PWD and VWD results from the pressure transducers and PIV measurements respectively, show that the lowest attainable SWR ≈1.7 corresponding to the added resistive load of 2Ohms. The maximum SWR≈6.2 was obtained when the added resistive load was at its maximum, 99 Ohms. The PRC technique allowed the experimental verification to be conducted over the stated SWR range.

The simulation shown in sub-chapter 4.2 assumed a single frequency acoustic wave propagating through a rigid duct with negligible losses. In the experiment, the separation distance between the two measured points is assumed to be small enough such that acoustic dissipation between the two points is negligible. It is shown that the variable termination was not tuneable to match the exact impedance of the system. As such, reflection due to the difference in the impedance will always occur. The reflection in turn will lead to the formation of harmonics from the fundamental 77Hz in the tube. It is for this reason, as previously discussed in sub-chapter 4.0, that the wave Decomposition technique that allowed the analysis of the spectrum of the incident and reflected component was selected. This has allowed for an overview of the amplitude relation between the harmonics of the incident and reflected components. The spectral components for the lowest attainable SWR=1.6 and the highest attainable SWR=6.2 are shown in Figure 4-9 and Figure 4-10 respectively.

The mis-match in impedance will result in reflection along the duct giving rise to harmonics in the duct. As the duct system's acoustic impedance is tuned further away from the incident wave's impedance, the harmonic is shown to increase proportionally. The greater the mis-match in impedance between wave and duct system, the higher the probability for reflection to occur. These reflected waves are not confined to the fundamental frequency but leak out as secondary harmonics as well. It is observed that the harmonic generation within the system prefers the 3rd

harmonic (231Hz) as compared to the 2nd harmonic (154Hz) since the amplitude of the 3rd harmonic is always larger than the 2nd harmonic. The PWD technique shows that for SWR=1.6, the incident pressure amplitude ratio between the fundamental frequency and its 3rd harmonic is approximately 22. For SWR=6.2, this ratio is only 12.

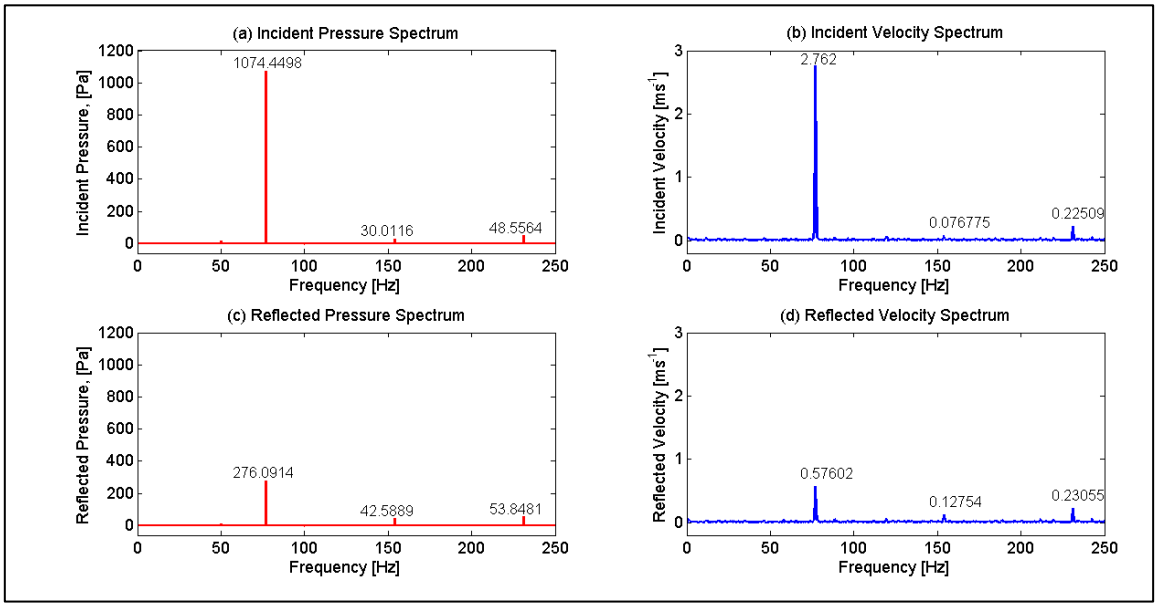

Figure 4-9: Resultant Spectral from PWD and VWD analysis for 2Ohm (SWR=1.6). Shown are the (a) Incident and (b) reflected pressure spectra and the (c) Incident and (d) reflected Velocity spectra.

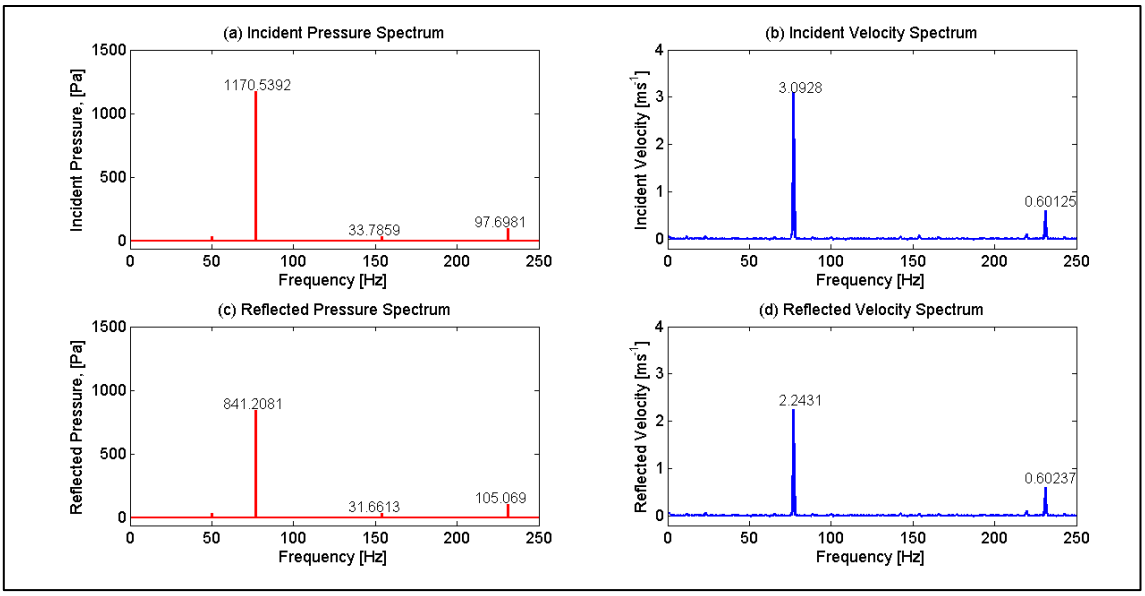

Figure 4-10: Resultant Spectrums from PWD and VWD analysis for 99.9Ohms (SWR=6.2). Shown are the (a) Incident and (b) reflected pressure spectra and the (c) Incident and (d) reflected Velocity spectra.

The acoustic power of the excitation speaker was kept constant; it is thus expected that the incident component of the wave remains constant throughout the different SWR runs. This is

shown in Figure 4-11 where the incident component has the velocity amplitude of approximately 2ms^{-1} and pressure amplitude of approximately 840Pa for the fundamental frequency. The amplitude of the reflected wave shows an increase with SWR as in accordance with the theory. The results show that there is fixed difference between the PWD and VWD computed incident component for all SWRs. The deviation between the PWD and VWD result values for the reflected component is seen to be increasing with the SWR values.

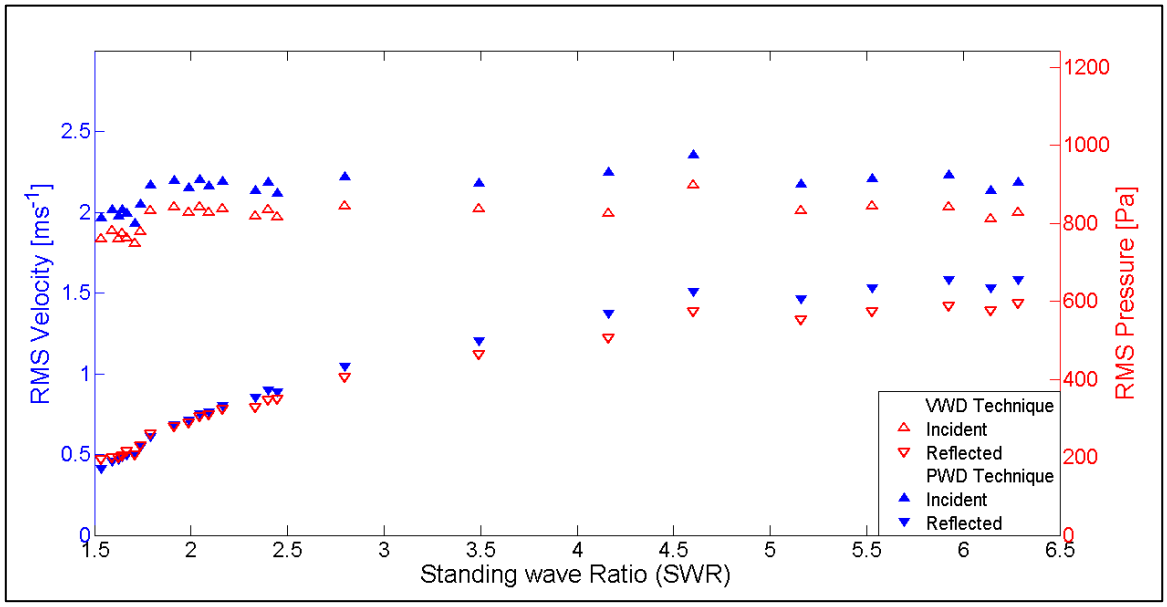

Figure 4-11: The experimental VWD and PWD results of the Incident and Reflected components plotted against their respective Standing wave Ratio. The maximum amplitude difference between the results of the VWD and PWD is approximately 5%. This difference may be attributed to the fact that the velocity measurements were taken at the centre of the tube (free stream velocity) while the pressure measurements were taken by pressure transducers flush mounted to the wall of the ducts (in the boundary layer).

The spectral density of the incident and reflected component are used to compute the complex acoustic impedance of each run and also the phasing between pressure and velocity as well as incident and reflected wave components. The results of the complex impedance plotted in terms of its resistive and reactive component against the respective SWR is shown in Figure 4-12.

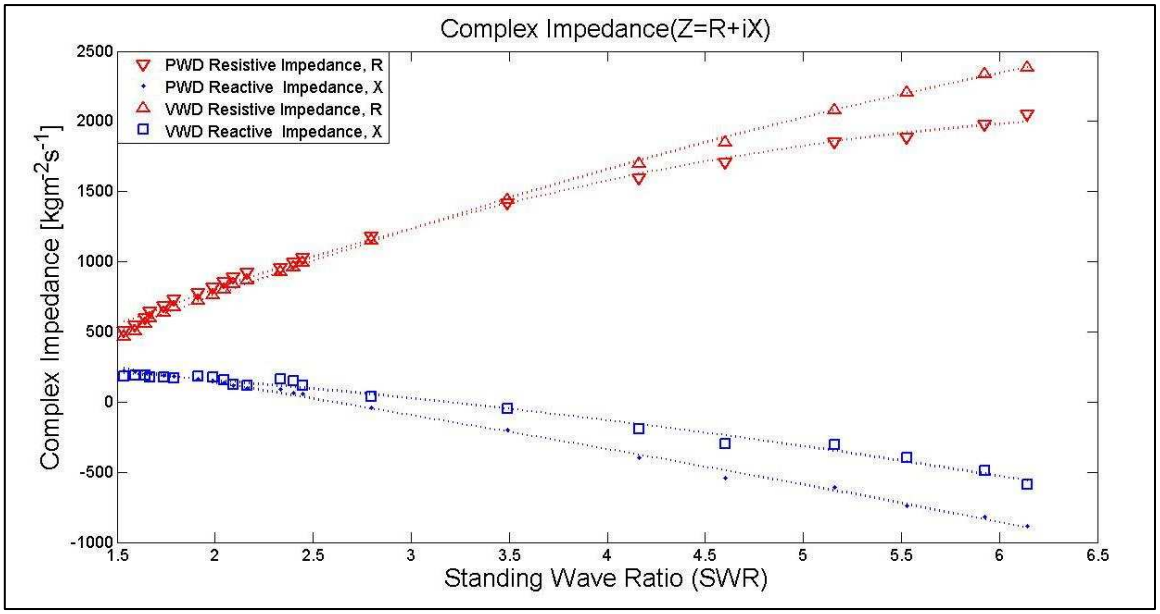

Figure 4-12: Complex Impedance from both the VWD and PWD based on measurements from both the PIV and Pressure Transducers respectively for the fundamental frequency component. The dotted lines were added to give a clearer trend to the behaviour of the Complex Impedance with increasing SWR

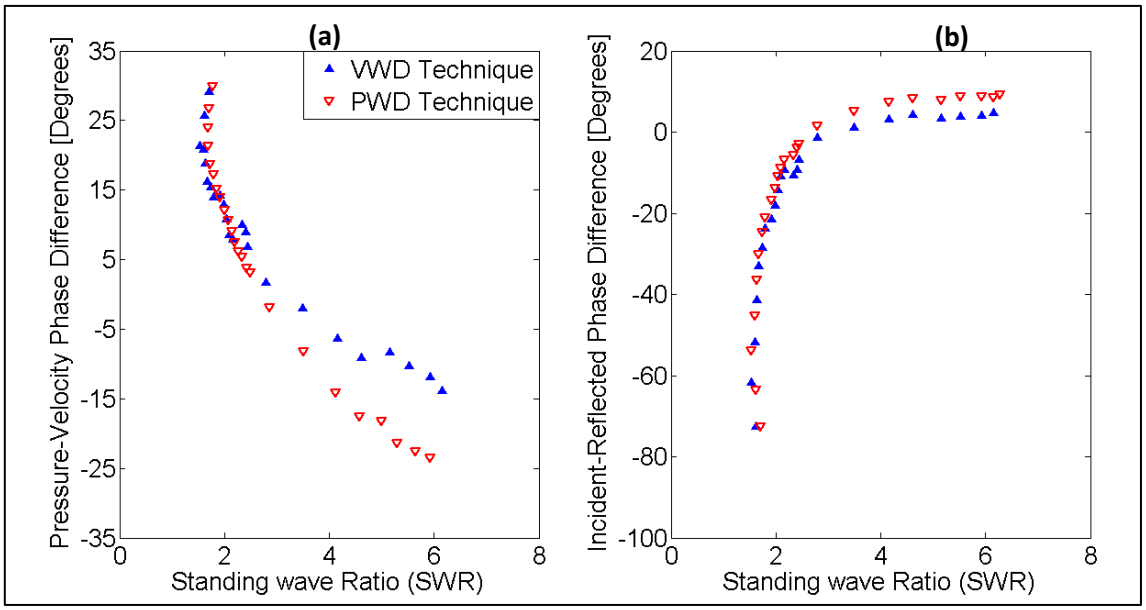

Figure 4-13: The Phase Angle corresponding to the Standing wave Ratio of the Simulation for the fundamental frequency component. (a) Phasing between the Pressure and Velocity component of the wave. (b) Phasing between the incident and reflected wave components.

The phase relation between pressure-velocity as well as incident and reflected component are shown together in Figure 4-13. The results for the acoustic impedance also show that there is an increasing deviation in the VWD and PWD results as the SWR increase pass 3.5. This discrepancy can be traced back to the growing deviation between the wave Decomposition techniques for the reflect values as shown in Figure 4-11, as both of these values have been computed from the same

auto spectra of the reflected wave component. This deviation will also be reflected in the computation of phasing between pressure and velocity component which is computed from the angle of the complex acoustic impedance components. Figure 4-13 shows that the maximum deviation between the computed phasing is approximately by 11^{o}. The phasing between the incident and reflected component which is dependent on their cross spectral density is less affected and only have a maximum deviation of 4^{o}. It should be noted that in Figure 4-13, the reactive component of the complex impedance does not tend to zero as would be expected in a perfect acoustical experiment. This is due to problems in generation and termination of the experiment, and not due to issues with the measurement technique. This is confirmed by the fact that both the new VWD and the more established PWD technique demonstrate the same behaviour and confirm that the VWD technique is identifying the salient features of the acoustic field present. In the next sub-chapter, the differences between the simulated and experimental wave decomposition results are discussed.

4.4 Comparison between Experimental and Simulated Wave Decomposition Results

The simulation verification showed that both the VWD and PWD analytical techniques are functional and accurate under ideal, non-dissipative, linear acoustic propagation conditions. The experimental verification also demonstrates that both VWD and PWD techniques shows results as a good match with an acceptable margin of errors. It is of interest to compare and match the simulation and experimental verification technique in order to fully verify the VWD technique. In order to compare the VWD results from the simulation with that from the experiment, the incident and reflected amplitude results from Figure 4-11 was used as the input parameter to simulate the new sets of synthetic waves. Figure 4-14 shows the VWD and PWD Complex Impedance results from analysing the new sets of synthetic waves.

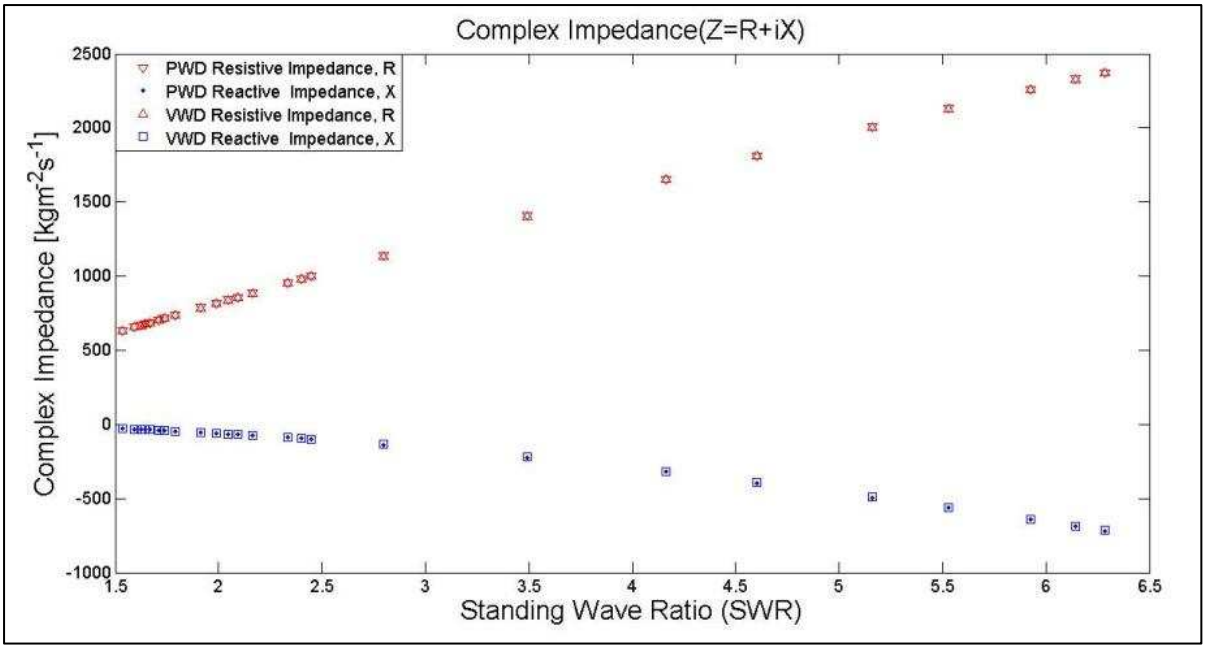

Figure 4-14: The VWD and PWD Complex Impedance result obtained from synthetic waves that were simulated using the Incident and Reflected amplitudes obtained from Figure 4-11.

Comparison between the ideal simulated results and that from the experiment, shows that the resistive impedance curve has shifted down by approximately 100kgm^{-2}s^{-1} while the reactive curve has shifted up by approximately -250kgm^{-2}s^{-1} for the lower standing wave ratio results (SWR=1.2 to 4). The shift in impedance curve found in the experimental results as compared to the ideal case simulation indicates that there are phase shifts between the pressure and velocity component of the experimental wave. The deviation in experimental impedance also implicitly suggests that a phase shift has occurred between the incident and reflected component of the wave. The speaker used as the acoustic waveguide termination in the experiment is complex impedance termination which may be represented using a simplified AC circuit analogy impedance equation as:

$$Z = R + i\omega L - \frac{1}{i\omega C} \tag{4.20}$$

Here, R, represents the real resistive component of the termination speaker, which is due to mechanical resistance, R_m, and the electrical resistance, R_e. The imaginary reactive component of the speaker consists of the inductance and capacitance component which are both frequency dependent. The inductance of the speaker is mainly due to the mass of the diaphragm and its

connected components, while the capacitance is due to the resonance volume of the speaker enclosure. Since the same frequency and speaker setup was used throughout the experiment, the reactive impedance component can be assumed to be constant. The tuning of the variable load box in order to get the various standing wave ratios, changes the resistive impedance of the system. The complex termination impedance determines both the amplitude and phasing of the reflected wave component. Since the amplitude of both the incident and reflected component was replicated through simulation, it may be concluded that, it is the phase difference between the incident and reflected component that needs to be matched in order to obtained the same complex impedance curves for the simulation as for the experimentation. The phasing between the incident and reflected wave component is given by the ratio between the complex and real component of their cross spectral density, S_{12}. The incident-reflected phasing information obtained from the experimental results was then used in the simulation. The result of this is shown in Figure 4-15 and it shows that the new simulation now replicates the acoustic situation more accurately. It is now possible to look at other issues to mimic the behaviour of the experimental results.

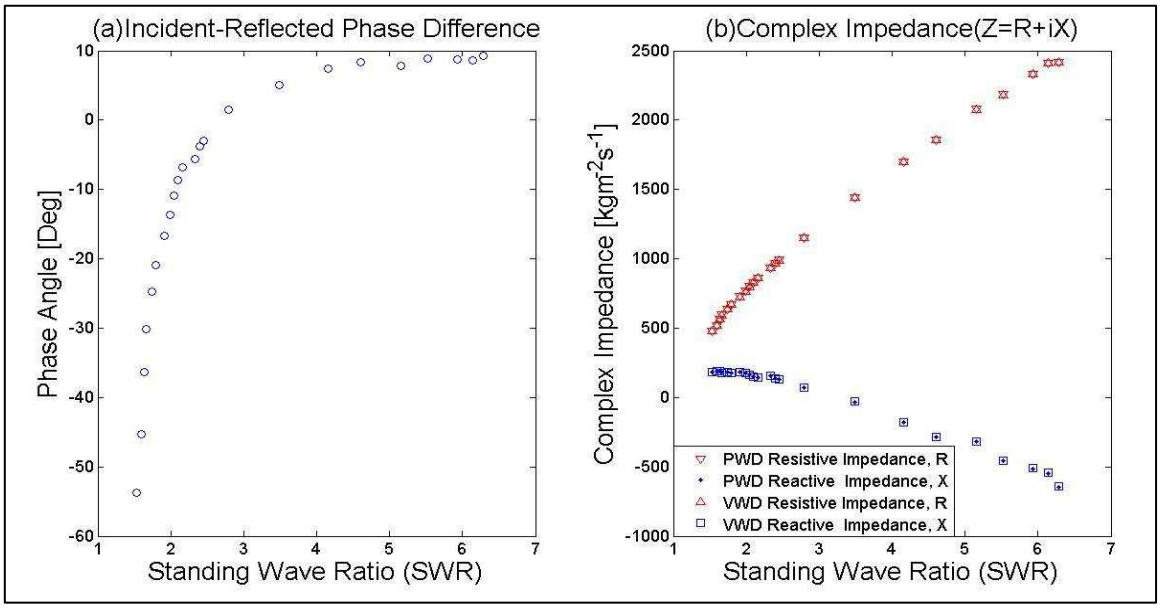

Figure 4-15: (a) The phase angle between the Incident and Reflected wave component used for the respective Standing wave Ratio. (b) The resultant complex impedance from using the phasing shown in (a).

4.4.1 Acoustic Attenuation

The wave decomposition technique functions by comparing the amplitude change between the two measured points. The assumption is made that the separation distance between the two measured points is sufficiently small such that the wave attenuation between the points are negligible. The separation between the two points also has to be sufficiently large, such that the change in amplitude corresponding to the wave length of the measured wave is detectable in accordance to the resolution of the measuring instrument. In this experiment, the chosen compromise for the separation distance is 100mm. In air, the attenuation across this distance is estimated to be approximately 0.1% of the wave's amplitude. However, it is known that the seeding used for PIV measurement has an effect on promoting viscous dissipation. An investigation was thus carried out to investigate the effects on attenuation on the VWD results using simulation. In this investigation, the varying parameter was the attenuation coefficient, α. The simulation was done from a range of α=0.01 to α=0.5. Simulation results from the run of attenuation coefficient, α=0.05, shows the closes resemblance to the experimental results. The attenuation effects for α=0.05 on the wave's amplitude and complex impedance are shown in Figure 4-16 and Figure 4-17.

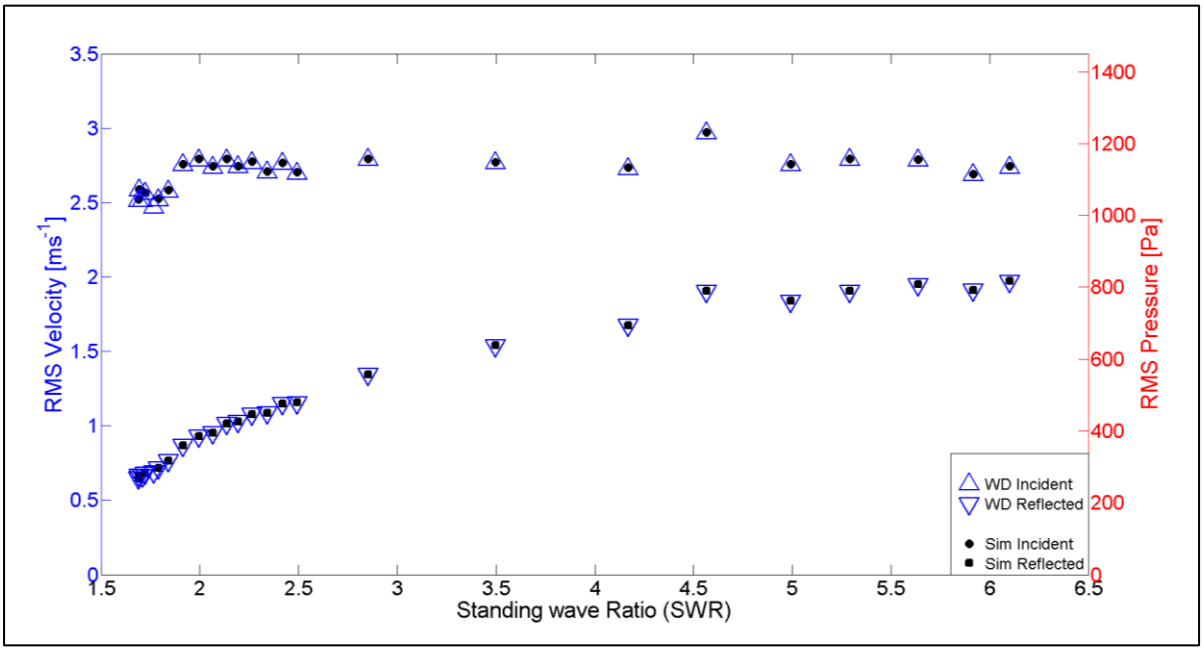

Figure 4-16: The Incident and Reflected wave component VWD results computed from simulated measurements with an attenuation coefficient of α=0.05. The amplitude of the Incident and Reflected VWD results shows only a minor deviation from the actual values for this level of attenuation.

The effect of attenuation on the VWD amplitude results shows minor deviation from the actual values with the largest deviation being only 0.34%. Although the effects on the amplitude are minor, there is a noticeable change associated with the complex impedance curves (Figure 4-18 to Figure 4-20). The attenuation causes the PWD impedance curve to be tilted slightly in the clockwise direction and the VWD in the anti-clock wise direction. The tilt of the impedance curves is shown to maintain the magnitude of the impedance $|Z|$ while changing its phase. The deviation in impedance phasing will cause error in determining the amplitude and phase relationship between the pressure and velocity component of the wave.

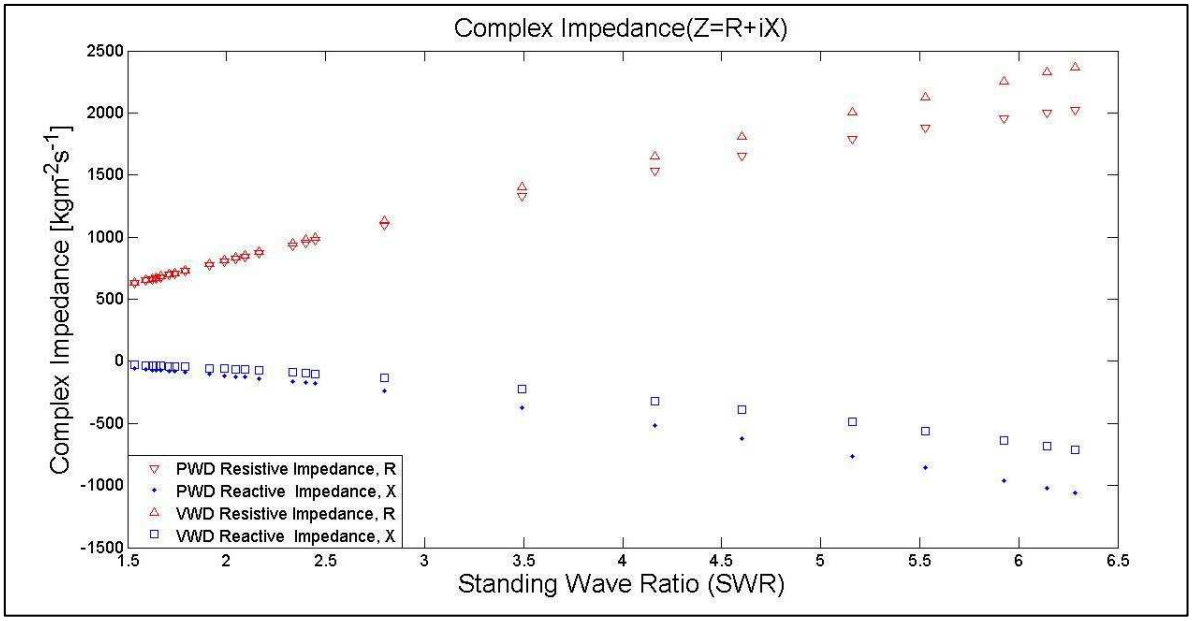

Figure 4-17: **The Complex Impedance results from the PWD and VWD technique computed from simulated measurements with an attenuation coefficient of α =0.05, plotted against its respective Standing wave Ratio. The results show that the wave attenuation causes the PWD complex impedance curves to be slightly tilted in down (in a clockwise direction) and the VWD complex impedance curves to be tilted up slightly (in an anticlockwise direction)**

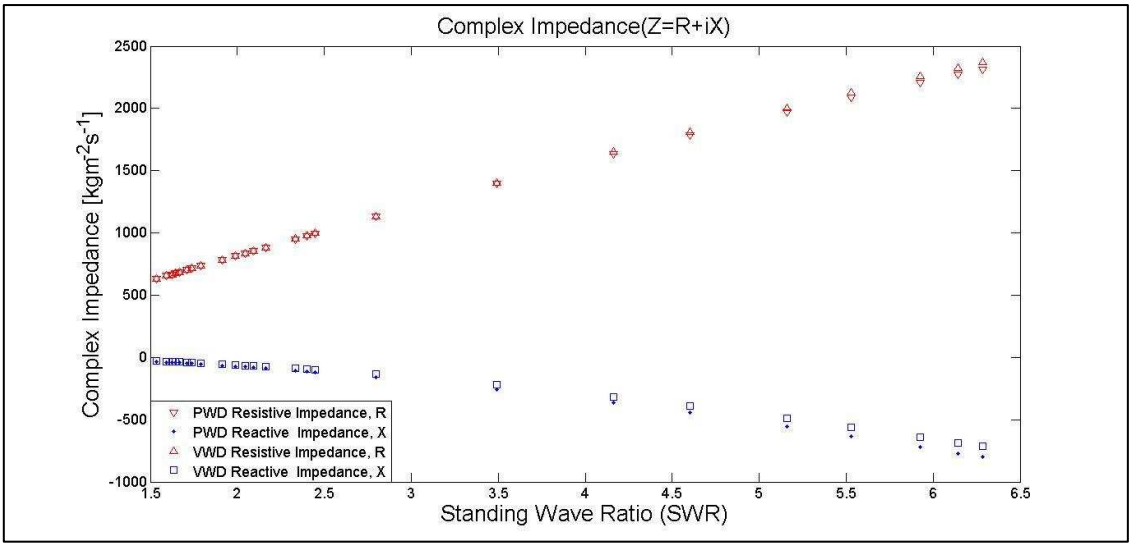

Figure 4-18: Attenuation Coefficient α=0.01

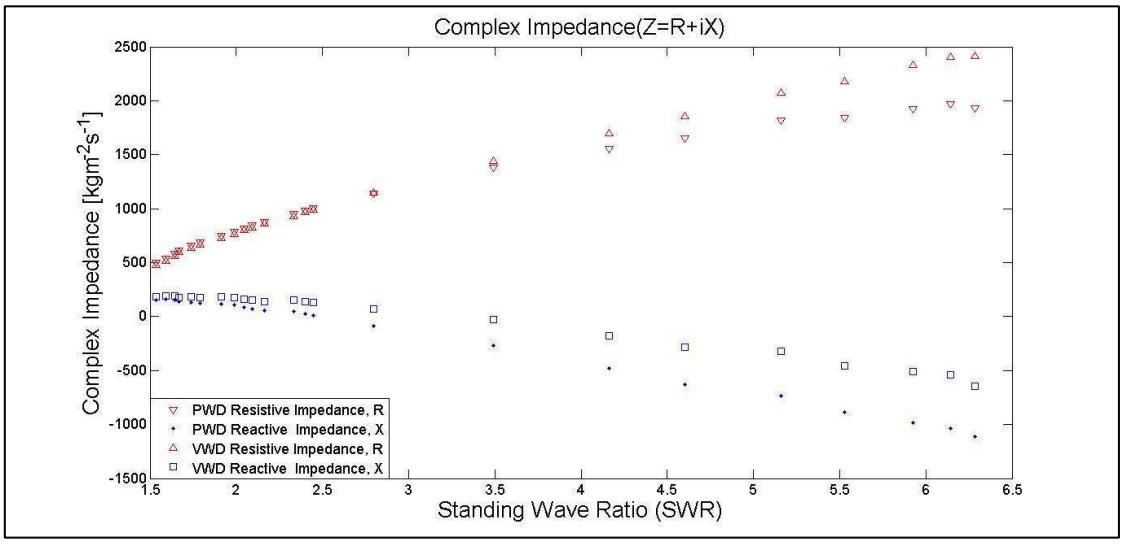

Figure 4-19: Attenuation Coefficient α=0.07

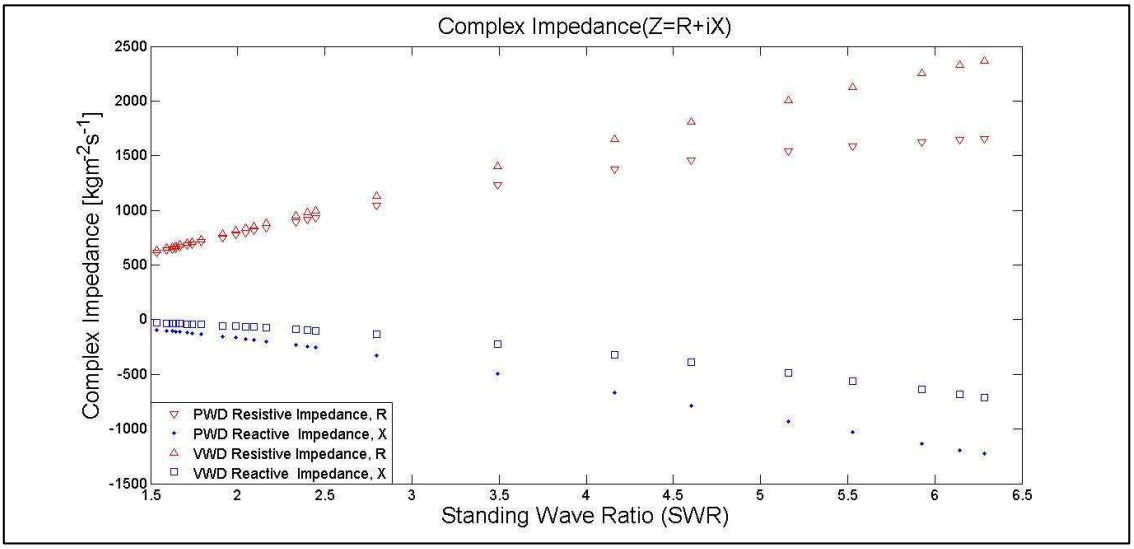

Figure 4-20: Attenuation Coefficient α=0.1

The effects of attenuation are shown in Figure 4-18, Figure 4-19 and Figure 4-20. These effects however, can be compensated. The attenuation coefficient, α_{approx}, can be approximated using the equation for acoustic viscous losses due to inhomogeneous suspension of an acoustic medium[2]:

$$\alpha_{approx} = \frac{1}{2}\left[\frac{r_m\, k\, \omega\ t_{res}}{1 + (\omega\, t_{res})^2}\right] \tag{4.21}$$

Here, r_m, is given as the ratio between the total mass of the seeding particles per unit volume of the acoustic medium (air) to that of the density of the acoustic medium. k and ω are the wavenumber and the angular frequency respectively. For this investigation, the approximated attenuation coefficient was found to be $\alpha_{approx} = 0.051$ which matches that found via simulation. This shows that Equation (4.21) is able to give an accurate approximation of the attenuation caused by particle suspension. The estimated attenuation coefficient can then be applied to the wave equation used in the VWD technique in order to compensate for the wave attenuation before the VWD analysis computed:

$$\tilde{v}(x,t) = \frac{1}{\rho c}\left(\left[A_1 e^{i\omega_1 t - ikx} - B_1 e^{i\omega_1 t + ikx}\right] \times \left[e^{-\alpha_{approx}\, x}\right]\right) \tag{4.22}$$

4.4.2 Effects of Noise on the VWD Technique

One of the challenges of using the PIV system is the inherent noise in its measurement system[168] It is thus important to quantify the errors associated with noise level from PIV measurements on the results of the VWD technique in order to determine the level of confidence of the analysis. The investigation on the effects of noise was conducted via simulation techniques. The MATLAB software was used to introduce Gaussian white noise into the simulated measured results. The varying parameter in this investigation is the signal to noise ratio(S/N). The same simulation done in sub-chapter 4.2 was repeated each time with a different noise level (S/N between 2 to 100). The results of 3 of the runs are shown in Figure 4-22, Figure 4-23 and Figure 4-24. For each of the S/N runs, the percentage maximum deviation of the VWD result from the actual value was recorded.

The maximum deviation for each noise level was then plotted against the respective S/N (Figure 4-21). It is shown that the percentage of maximum deviation does not increase by much above the S/N of 40. As the noise level increases pass this value however, the increase in percentage maximum deviation becomes exponential. Figure 4-8 and 4-9 show the results of the full simulation run for VWD incident and reflected amplitude at S/N=14 and 40 respectively.

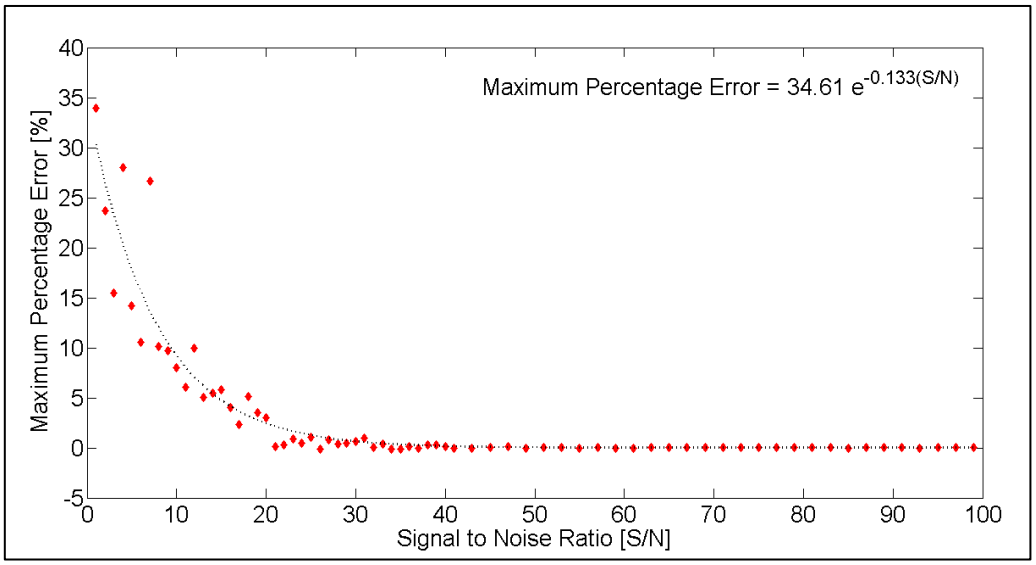

Figure 4-21: The maximum percentage error obtained from comparing the inputted value and that obtained from the VWD analysis, plotted against the Signal to Noise ratio (S/N).

An equation has been developed based on the trend observed in Figure 4-21 that would allow an estimate of the error levels associated with the VWD technique based on the signal to noise ratio of the measurement:

$$Max\ Percentage\ Error = 34.61 \times e^{-0.133(S/N)} \tag{4.23}$$

The level of noise can be reduced by taking larger sample sizes for each measurement run. In this experiment, the sample size for the PIV measurement was restricted to 2000 because of the time it took to transfer the captured images into the storage unit between each run and the time constraint the author had for doing the experiment. This will be addressed in further experimentation.

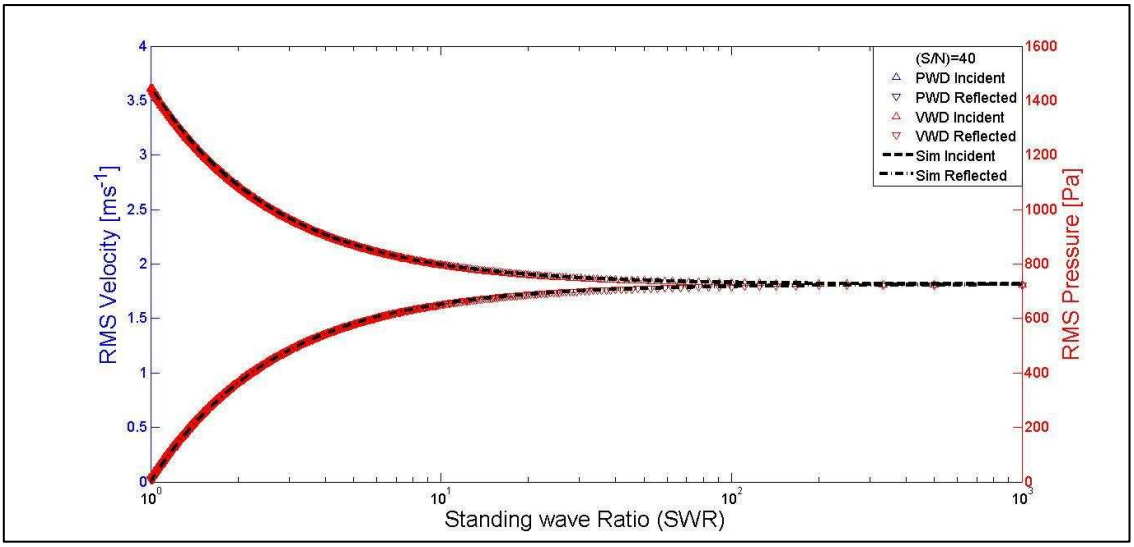

Figure 4-22: Amplitude of the Incident and Reflected wave component for (S/N) = 40

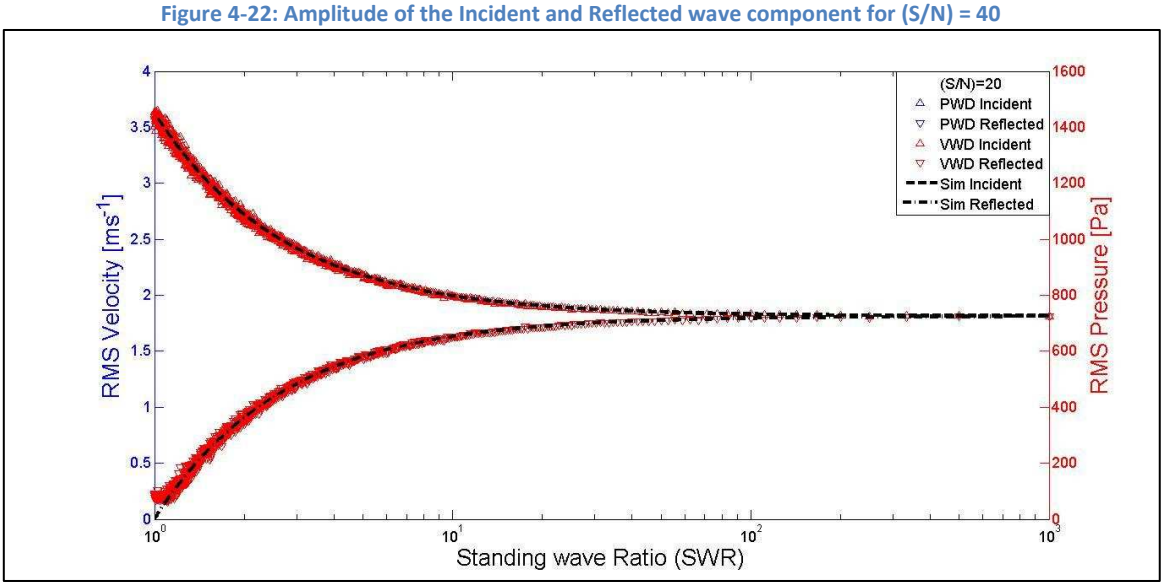

Figure 4-23: Amplitude of the Incident and Reflected wave component for (S/N) = 20

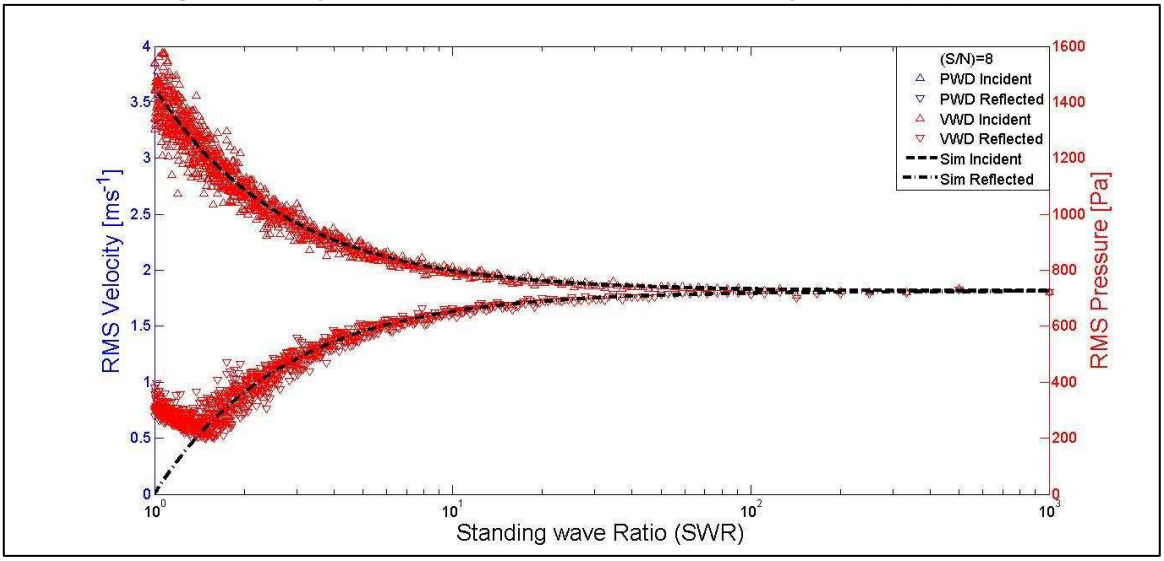

Figure 4-24: Amplitude of the Incident and Reflected wave component for (S/N) = 8

4.4.3 Matching the Simulation and Experimental Results

The combined effects of both the attenuation as well as the corrected phasing between the incident and reflected components give the simulation result of the complex impedance curves (Figure 4-25) which matches that of the experiment (Figure 4-15). Figure 4-25 shows a good match between the complex impedance curves. This proves that the main source of error in the experimentation results comes from the effect of attenuation of the wave between the two measured points. The effects of wave attenuation are more prominent in the computation of the Complex Impedance as shown in the results of Section 4.4.1 as compared to the amplitude of Incident and Reflected wave components as shown in Figure 4-16. For a complete and accurate use of the VWD technique, the attenuation coefficient α_{approx} must be found in order to compensate for the error of acoustic attenuation. This completes the verification of the VWD technique.

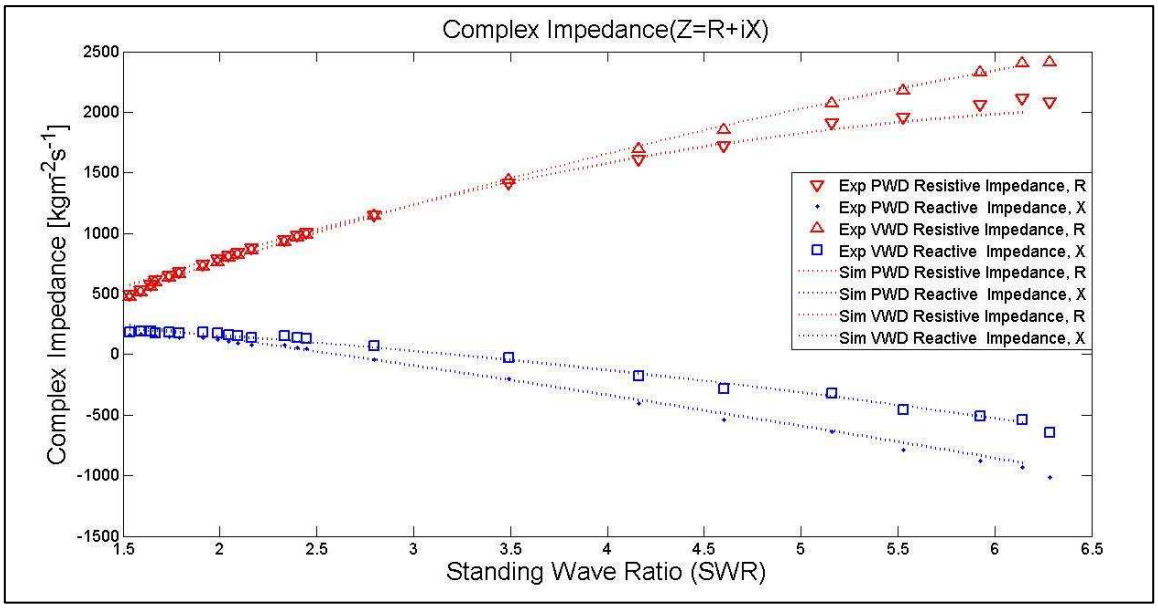

Figure 4-25: The comparison between the experimental Complex Impedance results and the Simulation based VWD results with phase shift shown in Figure 4-15(a) and an attenuation of α=0.05.

4.5 Measurement of multiple frequency waveforms and Categorising random noise

The previous validation methods showed that the VWD technique is efficient in decomposing mono-frequency wave component. The VWD however, is also capable of detecting and analysing more complex waveforms as well as mixed frequency acoustic waves associated with turbulent generated noise and other forms of aeroacoustic noise generation. Acoustic waves with different waveforms and of multiple frequencies were tested using simulation as described in Section sub-chapter 4.2. Figure 4-26 demonstrates the VWD technique's capability in handling different acoustic waveforms and acoustic wave consisting of multiple frequencies. The results of the VWD are a perfect match to the input simulated wave parameters. This serves to show that the VWD technique is a robust technique capable of analysing complex acoustic wave measurements particularly pertaining to aeroacoustics, thermoacoustics and other forms of noise generation and transmission in duct systems.

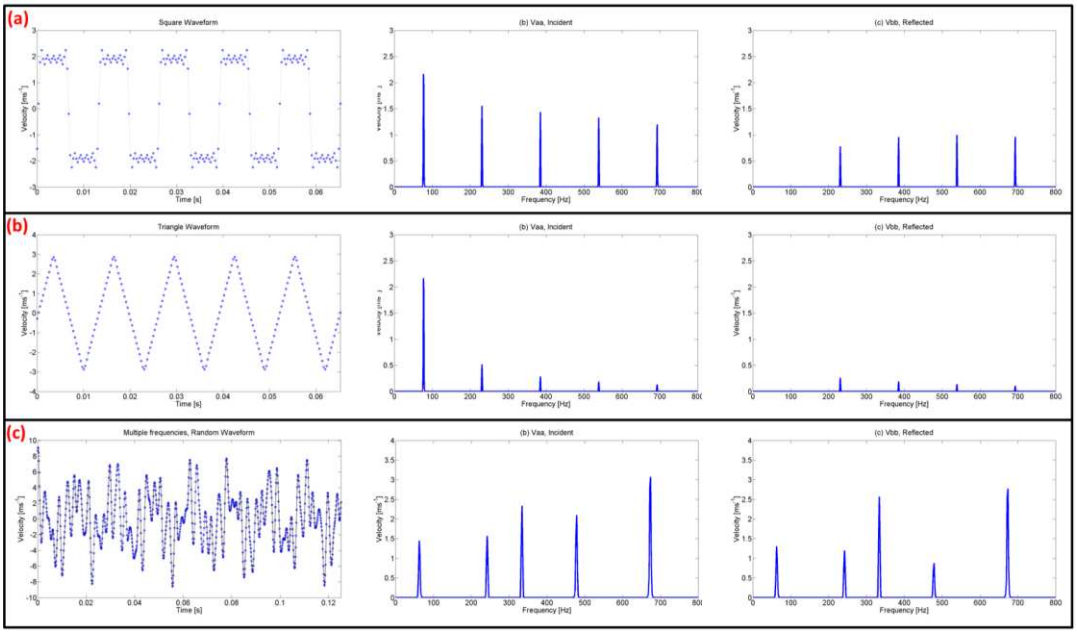

Figure 4-26: The VWD results on (a) Square waveform acoustic wave, (b) Triangular waveform acoustic wave, (c) A multiple frequency acoustic wave.

4.6 Conversion of Plane Velocity Vector Field into Plane Pressure Field Measurements

The added advantage of using the VWD technique with PIV measurement is that by analysing the complex acoustic impedance at each interrogation area of the PIV measurement, the entire velocity vector plane for each time step can be converted into plane pressure field measurement. The conversion of PIV measured velocity vector field into pressure field measurement is not new. Iterative techniques, used in CFD analysis, have been applied to solve the Poisson equation with different boundary conditions in order to convert PIV velocity vector measurements into pressure field measurements. Figure 4-27 shows a summary of the techniques that have been developed to solve the Pressure Poisson Equation for the purpose of velocity-pressure conversion.

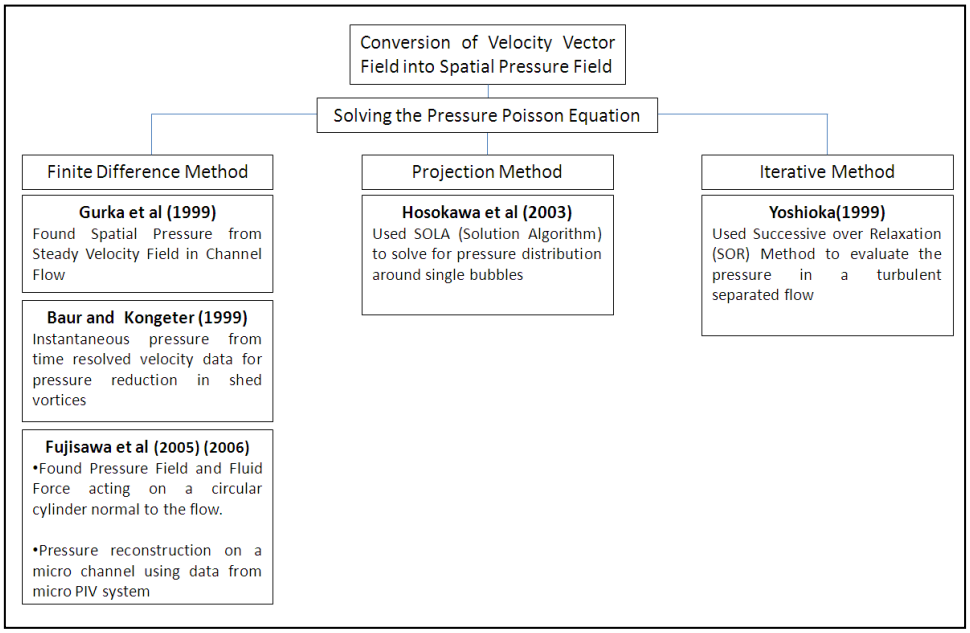

Figure 4-27: Summary of Velocity Field PIV data conversion into Spatial Pressure Field [169-174]

These techniques are accurate and can be applied to a wide variety of PIV flow measurements, but are very computationally intensive. This is since every PIV measured velocity vector corresponding to their respective interrogation area has to be individually iterated through each time step in order to get the pressure measurement at that point in time. The VWD techniques offer a faster, less computationally intensive method of converting the PIV measured velocity vector field into

pressure field for acoustic field measurements. This is done by finding the complex acoustic impedance at each interrogation area of the measured velocity vector plane. The product of a velocity vector and the corresponding complex impedance in the same interrogation area yields the pressure measurement at that point. This is computationally less intensive as the complex impedance is only found once and no iterative technique is required to convert the entire time step plane velocity measurement into pressure measurement.

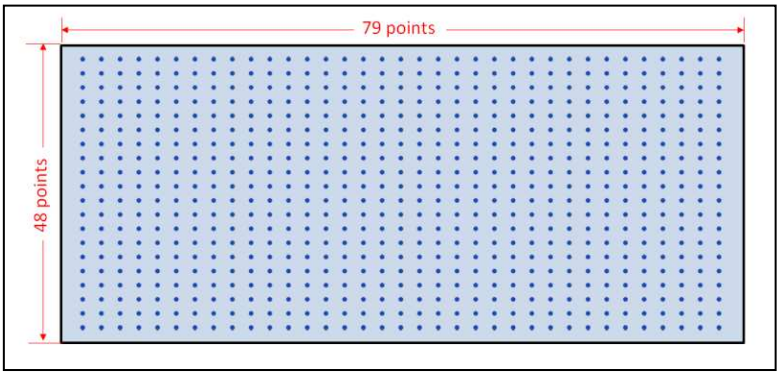

Figure 4-28: An example of PIV measured plane. Each of the dots corresponds to an interrogation area from which a single velocity vector measurement is produced for each time step. This investigate plane contains 48 rows and 79 columns of interrogation area which will give 3792 velocity vectors for each measured time step (Resolution = 48 x 79).

The conversion of the velocity vector field into pressure field is done point by point. The Velocity field plane has 49x79 velocity vector points measured simultaneously over time. The VWD technique requires the uses of two separate points on the same horizontal axis in order to compute the complex acoustic impedance of a third point on that axis. By systematically shifting these 3 points along the entire plane, the complex acoustic impedance was computed for all the 3871 velocity vector points.

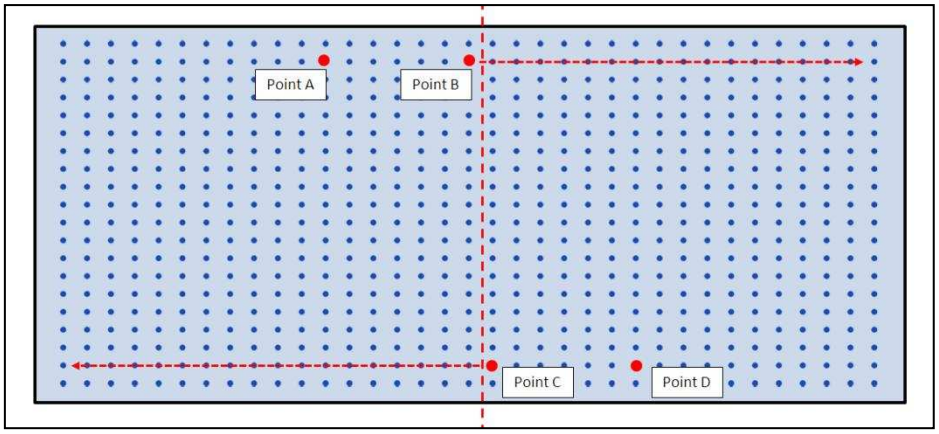

Figure 4-29: The systematic computation of Complex Acoustic Impedance via the VWD technique for each interrogation area of the PIV measured plane.

The velocity spectrum for each of the velocity vector points was multiplied with the corresponding computed acoustic impedance in order to obtain the pressure spectrum. The inverse Fourier transform is then used to convert the pressure spectrum into the resultant time domain pressure field. A sample of the conversion is shown for the experimental measured wave of both SWR=1.6 and SWR=6.2. These are shown respectively in Figure 4-30 and Figure 4-31

The contour plots p1-p4 and v1-v4 on both Figure 4-30 and Figure 4-31 show the phasing between pressure and velocity. These are more clearly represented by the pressure-velocity vs. time plot at the bottom of both figures. Both are in accordance with theory. The advantage of measuring the pressure field can be seen in these two examples, particularly Figure 4-30 which shows that the pressure wave does not propagate as a plane wave, but has a transverse pressure profile, possibly induced by the higher harmonics of the speaker. However, this is less clear in Figure 4-31.

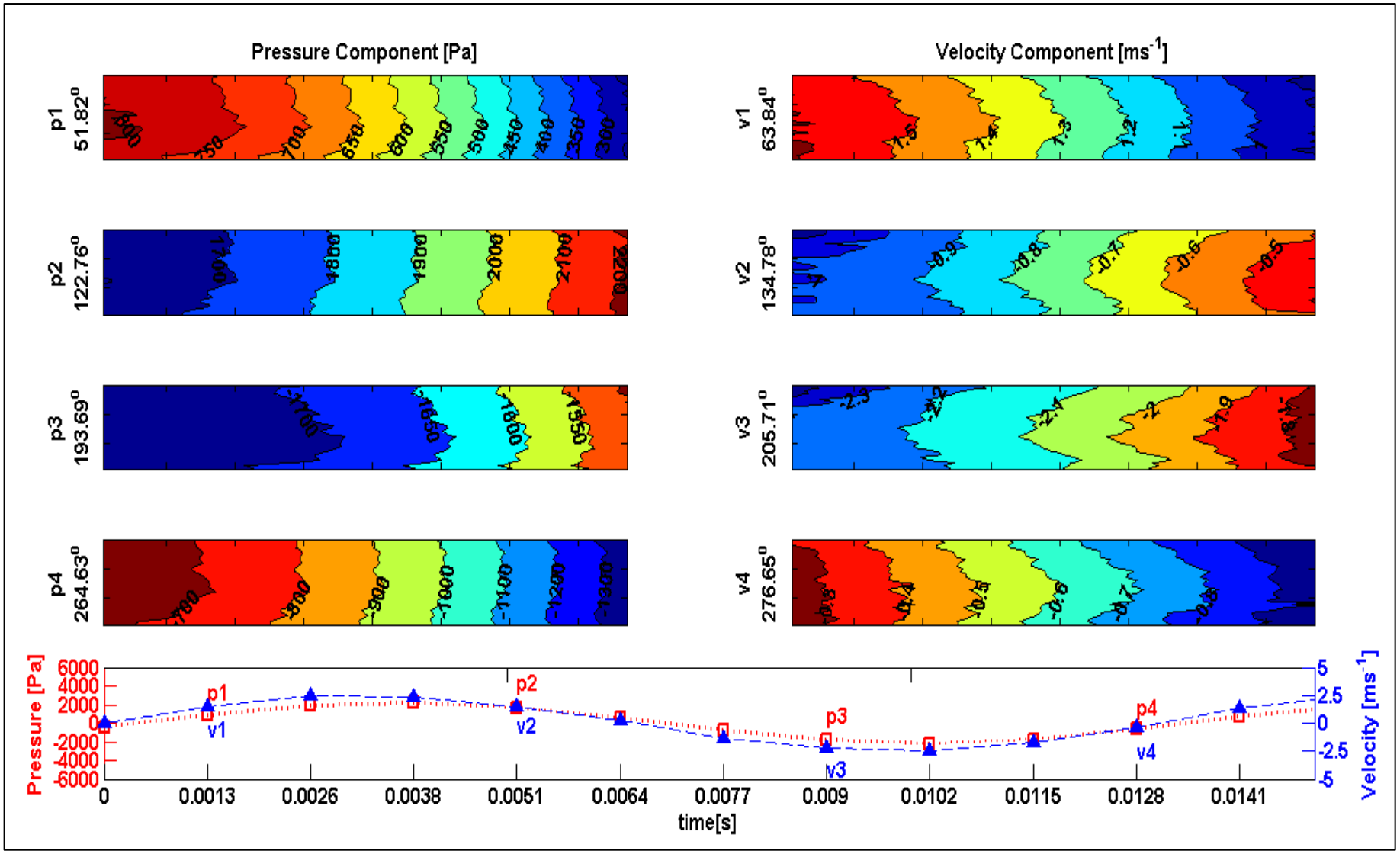

Figure 4-30: Pressure and Velocity field contours corresponding to SWR=1.6 [2ohm termination speaker resistance]. The pressure-velocity vs. time plot at the bottom shows the phasing between the pressure and velocity and also the phase at which the contours p1-p4 and v1-v4 represent.

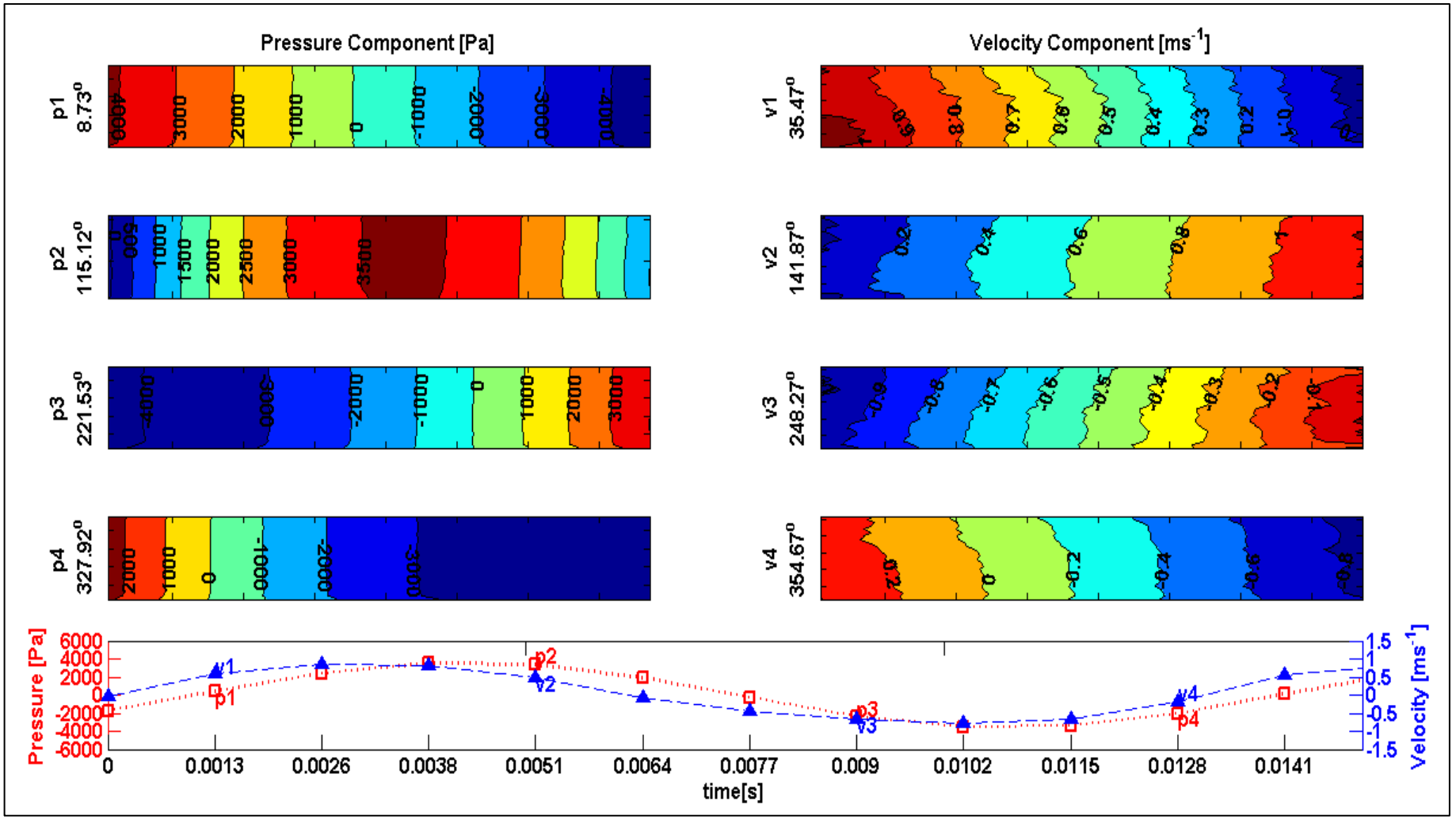

Figure 4-31: Pressure and Velocity field contours corresponding to SWR=6.2 [99 ohm termination speaker resistance]. The pressure-velocity vs. time plot at the bottom shows the phasing between the pressure and velocity and also the phase at which the contours p1-p4 and v1-v4 represent.

4.7 VWD Technique Conclusion

The Velocity based Wave Decomposition (VWD) technique has been developed for the analysis of acoustic wave propagating through waveguide systems. The technique has previously been verified using lossless simulated synthetic waves with no noise. The VWD technique was then tested experimentally and compared with the established PWD technique. The results between the VWD and the PWD techniques match well with a maximum deviation of approximately 5%. There was however, a discrepancy between the experimental and simulation results for the complex impedance curve, although the amplitudes used for both experiment and simulation were the same. This sub-chapter investigated the cause measurement error that might have led to this deviation. The complex impedance termination of the simulated acoustic wave was first corrected by matching the phasing between the incident and reflected component with that of the experiment. It was then clear that the main source of error was from acoustic attenuation that had occurred between the two points of measurement. Through simulation, the attenuation coefficient was found to be approximately $\alpha=0.05$. With the application of the attenuation coefficient value, the simulation results show almost a complete match to that of the experimentation. The very minor deviation between the curves may be associated with noise. This clearly indicates that the VWD requires compensation for the attenuation that takes place between the two points in order to produce accurate results. The compensation technique has been discussed in Section 4.4.1. Equation (4.23) allow the estimation of the level of confidence of the VWD technique has been worked out based on the Signal to noise ratio of the measurement. This concludes that the VWD is an effective accurate technique for acoustic waveguide analysis. For the validation against PWD, it was necessary to use a larger separation. For general use of the VWD technique, it will be possible to use adjacent velocity values for calculation. If the separation of the points is decreased, then the influence of the attenuation will be negligible. .

Chapter 5

PIV Investigation of Acoustic Propagation through 90^{0} Curved Duct Bends

5.0 PIV Experimental Investigation of Acoustic Propagation through 90^{o} Curved Duct Bends

In the continuing effort to measure and characterise acoustic wave transmission through duct bend systems, the more comprehensive Particle Image Velocimetry was employed. There are 3 main objectives for conducting these PIV investigations on duct bends: To

1. Conduct a more accurate acoustic transmission analysis using the developed VWD technique based on the multiple velocity measured points in the measured plane.
2. Conduct the acoustic wave energy transmission based on the Proper Orthogonal Decomposition (POD) technique
3. Observe and study the acoustic oscillation flow behaviour through the duct bends in an attempt to find and characterise the different loss mechanism involved in the system.

The experimental setup is shown in Figure 5-1. The experimental setup consists of two speakers, two straight ducts with constant cross sectional area and the 5 investigated bends with different radius of curvature. The straight ductings and elbow bend used in this investigation has a constant square cross section of (88mm x 88mm). Five bends with different radius of curvature (ranging from 55mm to 155mm) with equal axial length were used. The radius of curvature of each of the investigated bends was measured from the centre axial line of the duct. An Orion, 10' (1000W) subwoofer was used as the acoustic excitation source for the investigation. A function generator and an amplifier were used to control the frequency, waveform and amplitude of the acoustic wave

produced by the source speaker. The investigated amplitude was based on the input electrical power into the source speaker. In this investigation, the two investigated amplitudes were used: 200We and 50We. The Passive Reflection Cancelation (PRC) technique discussed in Chapter 2.0 was employed to ensure that the wave propagating through the system is predominantly a travelling wave with an SWR of less than 2. The PRC calibrations used for the termination speaker are shown in Figure 2-11.

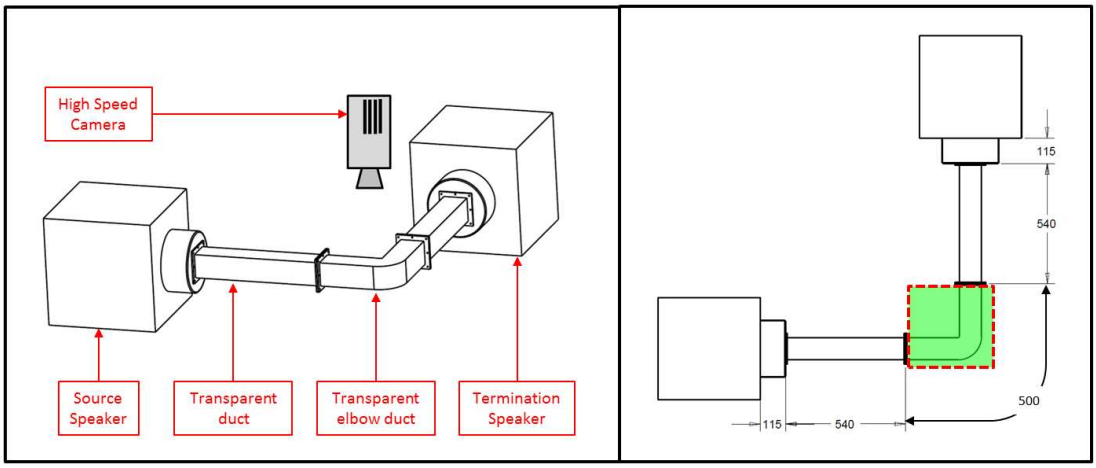

Figure 5-1: Layout of Experimental Setup. The source speaker is an Orion 10' 1000W subwoofer that provides the acoustic excitation for the system. The source speaker produces a travelling wave down propagating through the duct system and is absorbed by the termination speaker such that minimal acoustic wave reflection is incurred. All dimensions are given in mm.

The straight duct sections before the investigated duct section are to ensure that the travelling acoustic wave propagating into the bend is that of a plane wave[56, 166]. The bend section is connected to the straight ducts by using flange and an appropriate gasket seal. This allows the inter changeability between the 5 investigated bends. Special care is taken such that the ducts are properly aligned with each other during the experimental setup. The dimensions of the 5 investigated bends are given in Figure 5-2. The difference in axial length for each of the bends are compensated for using flanges with the appropriate thickness such that the axial distance between source and termination speaker is kept constant (1580mm) allowing the PRC technique to function optimally.

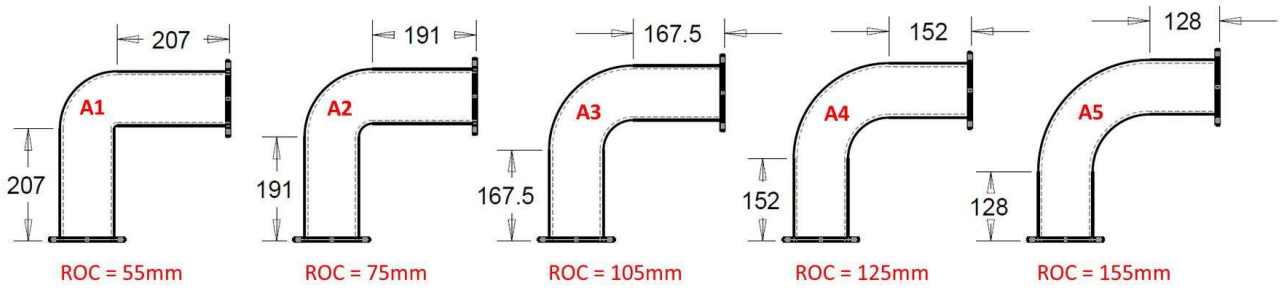

Figure 5-2: The dimension of the five investigated duct bends with different radius of curvatures. The axial length (500mm) and cross sectional area (88mm x88mm) is kept constant for each bend. All dimensions are given in mm.

Although the reduction of glare and reflection in PIV measurements for circular cross section ductings has been discussed in detail in Chapter 3.4, square cross sectional ductings were eventually chosen for this investigation. This was due to the difficulty and high cost of constructing a constant circular cross section bend with an accurate radius of curvature. As such, in working within the experiment's budget and time constraint, square cross sectional ducting (that has the same cross sectional area as the circular ducts used in the engine's resonator) were used. Literature (discussed in Chapter 1.3) has shown that the cross sectional shape has minimal effect on the acoustic transmission behaviour for the range of investigated acoustic properties. This indirectly has allowed for more accurate PIV measurements as the issue of impending complications such as particle absorption spectra, reflection and glare from circular sections was eliminated.

Table 5-1: The PRC calibration used for the termination speaker for the range of investigated frequencies. This calibration works for the input power range of 50We to 250We into the source speaker.

Investigated Frequency (Hz)	Resistive Load (Ω)	Lowest SWR value
67	4.5	1.13
87	2.8	1.25
107	0.7	1.36
127	0.4	1.62
157	0.1	1.85

The flow visualisation and velocity measurements for this investigation were conducted using the DANTEC Dynamic Time Resolve Particle Image Velocimetry (TR-PIV) system described in Chapter 3.2. The measured velocity vector field has 49 x 79 vectors corresponding to interrogation areas of 32 x 32 pixel resolution. The velocity vectors was computed using the adaptive cross correlation technique with the central displacement of 50% interrogation area overlap through the Dynamic Studio 3.0 analytical software. The cartridge heater smoke generating technique used in Chapter 4

was again employed here. The seeding has a residence time (approximately 15-20 minutes) while maintaining constant density under acoustic excitation. The transparent ducts and bends were washed thoroughly after each run before reseeding was conducted in order to avoid errors from seeding particle deposition.

The PIV measurements were made along the axial cross section of the duct as shown in Figure 5-1. This plane of measurement was chosen to allow the use of the VWD and POD acoustic transmission analysis techniques. Previous PIV experimental works have concentrated on the ducts transverse cross section in an effort to understand the different forces that control the balance between centrifugal and centripetal components in an acoustic flow through curved duct systems. To the best of the author's knowledge, this PIV investigation on the axial cross sectional plane of an acoustic flow through curve duct systems has never been done before and represents a fresh approach to investigating acoustic transmission through duct bend systems. Acoustic propagation in square section duct systems is 3 dimensional in nature and hence by investigating the acoustic propagation from a different plane may help verify and contribute to a more holistic understanding of the acoustic wave behaviour as it propagates through such a system.

5.1 Observation from raw PIV velocity vector map measurements

The post processing analysis of the velocity vector maps were done using MATLAB. Figure 5-3 shows the raw velocity vector maps for each time step of in a period as the acoustic wave propagates through the A1-Bend. The position of the node is clearly shown to be shifting in the direction of propagation of the wave. This shows that the investigated wave has a predominant characteristic of travelling wave oscillation. The almost uniform axial velocity across the cross section of the duct shows that the acoustic wave propagates in the plane wave mode in the straight section of the duct. This axial velocity profile becomes progressively skewed as the wave propagates into the bend and is shown to be most skewed in the mid-section of the bend (at approximately 45° bend angle). The velocity profile shows that the faster oscillating velocities tend to favour the region

nearer to the inner wall of the bend implying a strong influence of centripetal effect on the wave propagation through bend's radius of curvature. This is in agreement with literature[53] in which, unlike unidirectional flows which exhibits centrifugal effects (reflected by skewed axial velocity profile with the larger velocities near the outer wall of the curvature), oscillating flow through a curved duct system shows a shift from the centrifugal effect to a more dominant centripetal effect (reflected by skewed axial velocity profile with the larger velocities near the inner wall of the curvature). The shift in dominance between the centrifugal and centripetal effect have been discussed in Table 1-2.

The skewed velocity profile and the concentration of the higher oscillating velocities on the inner wall are of the same flow characteristics of which the secondary Lyne circulations were discovered[78, 86]. This is a strong suggestion that a secondary flow may exist within the measured PIV data. It is of interest to study these secondary flow systems as it may offer insights into the formation of these oscillating flow patterns as well as to the understanding of the oscillating flow loss mechanism. The measured PIV data sets contain both the qualitative and quantitative information of these secondary flow systems, but they must first be extracted effectively in order to yield useful information. The techniques used to extract the secondary flow systems are discussed in the following sub-chapters.

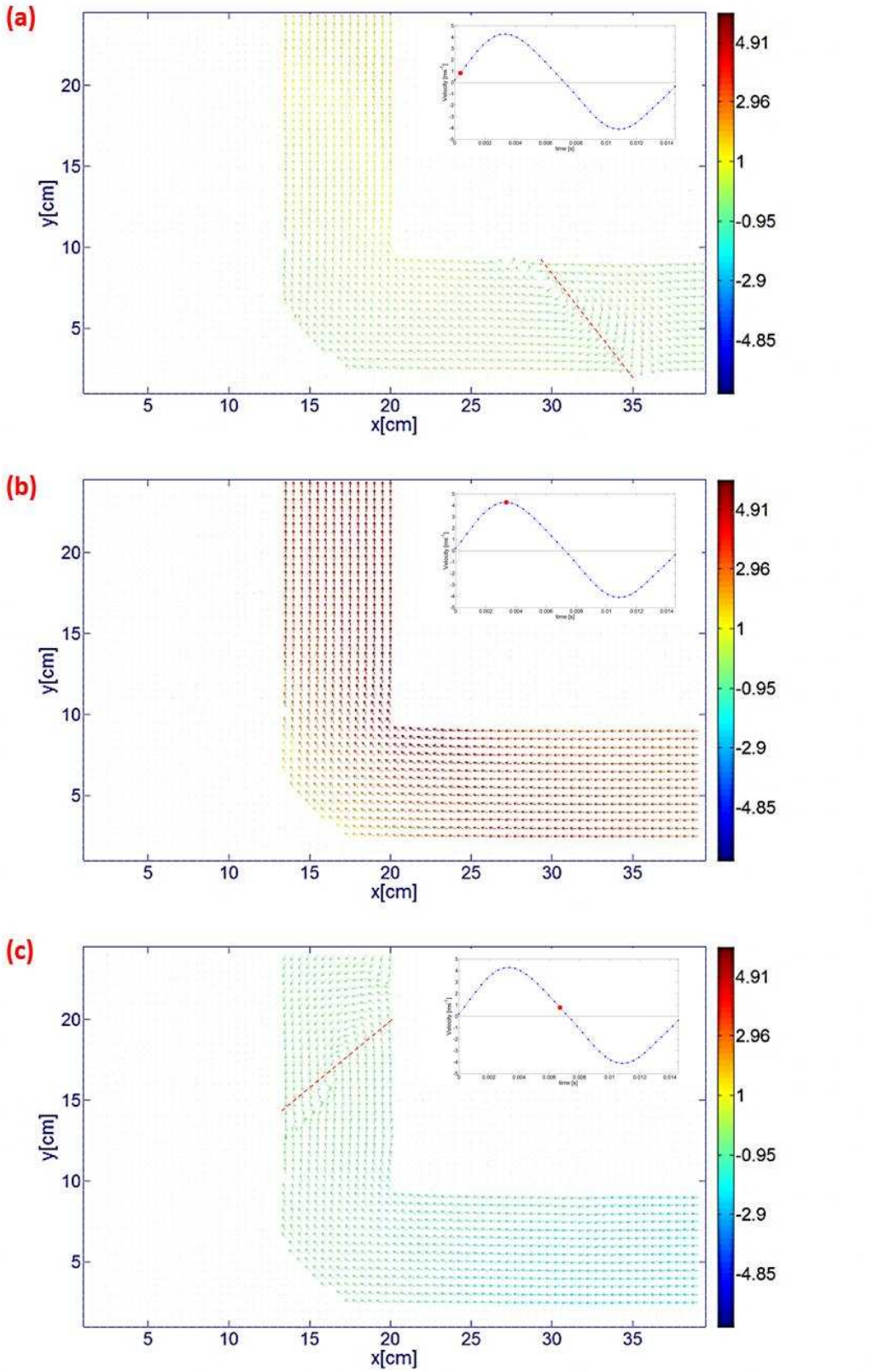

Figure 5-3 [*(a)-(c)*]: For caption see pg.139

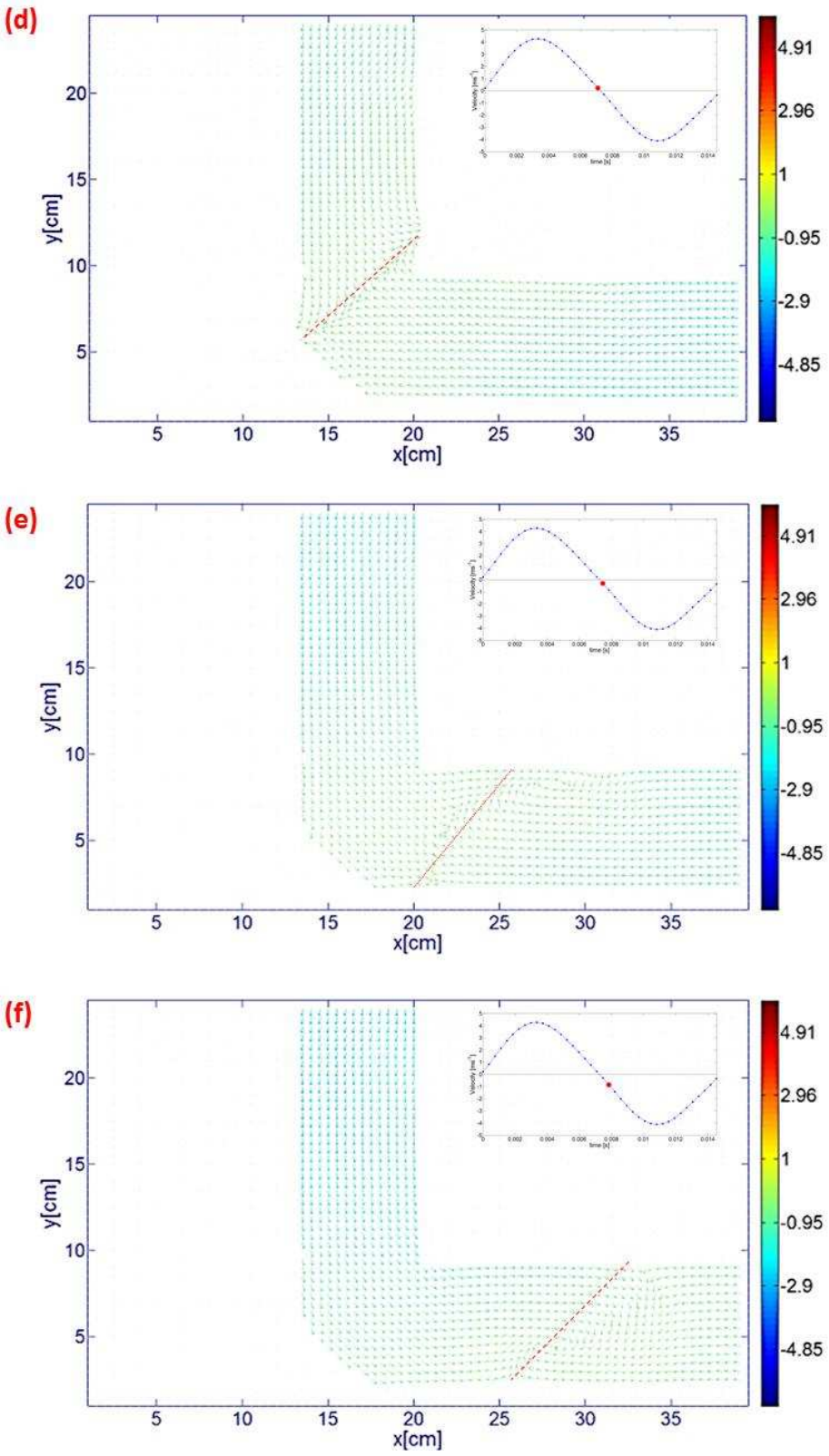

Figure 5-3 [*(d)-(f)*]: For caption see pg.139

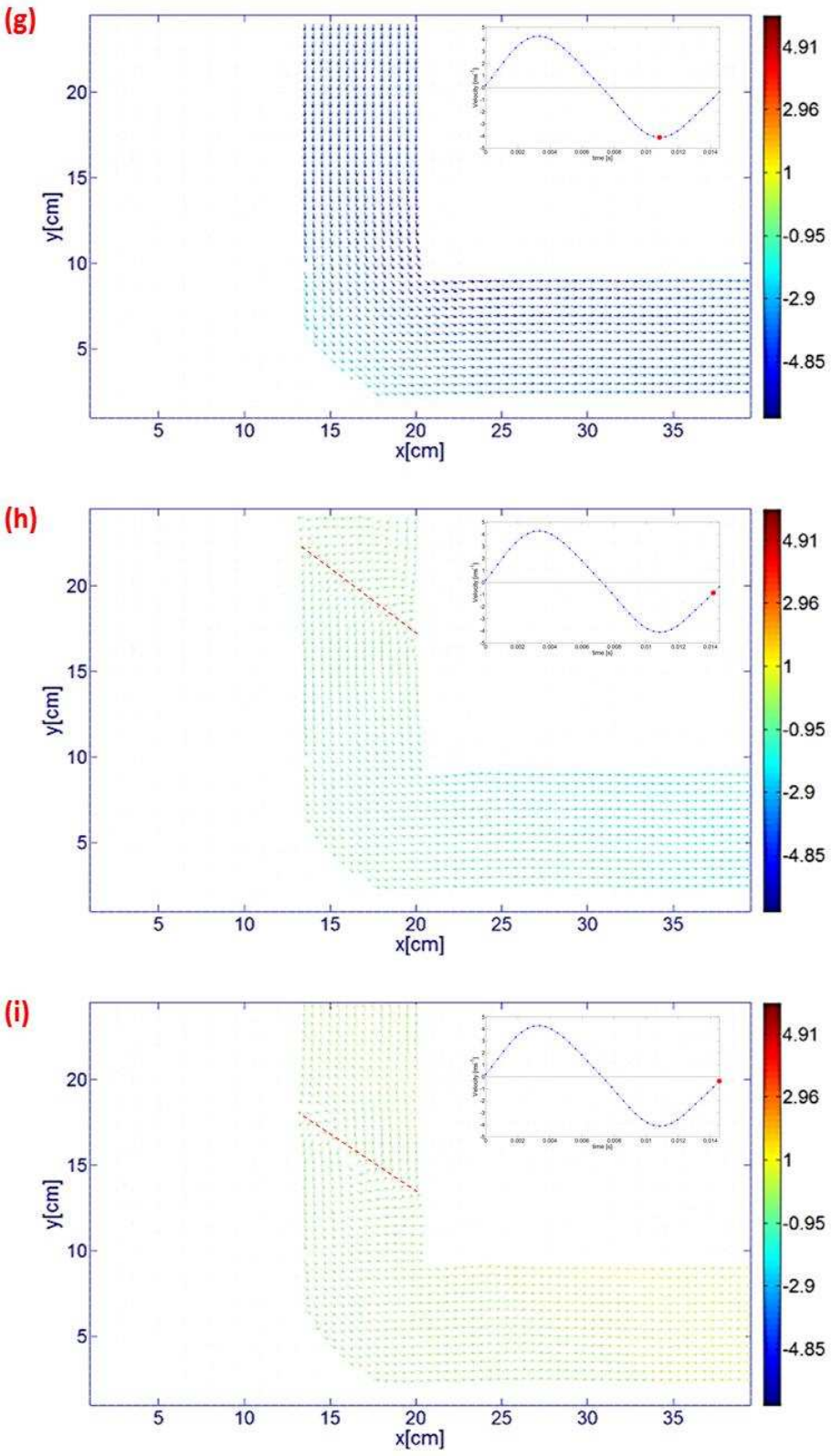

Figure 5-3[*(g)-(i)*]: The snapshots of the averaged phases for an oscillating period of the 200We, 67Hz Acoustic wave propagation through the elbow bend. The velocity amplitude of the vectors are represented by colours indicated by the colour scale. The phases of each snapshot are indicated by the red dot on the (mini time vs. amplitude) graph. The red dashed line (---) represents the position of the acoustic wave node.

5.2 Detection of Turbulence, Coherent Structures and Acoustic Streaming

The range of PIV investigated oscillating flow propagating through the five different radius of curvature duct bends, all revealed the skewed axial velocity profile in which the higher oscillating velocities are concentrated on the inner wall of the duct's curvature (Figure 5-3). Although this is the first time PIV investigation have been conducted for acoustic propagation through curved duct systems in the axial plane, there has been a large number of preceding literature investigating acoustic propagation in curved duct systems in the cross sectional plane. These literature reveal the existence of secondary flow systems in the cross sectional plane that takes the form of a pair of "coherent" counter rotating vortices whose circulation act to reinforce the skewed axial velocity profile towards the inner wall of the curvature. The similarity in oscillating flow characteristics between literature and the investigated range suggest that these secondary flow systems also exist within the measured PIV data. It is of interest to study these secondary flow systems in order to:

1. Gain an understanding of the formation of these secondary flow structures in the axial plane as compared to literature's cross sectional plane. This may reveal a more holistic understanding of the secondary circulation's 3D structure.
2. Investigate the oscillating flow loss mechanism which is theorised to stem from these "coherent" secondary circulations for oscillating flow systems.

The investigation of these secondary flow systems are similar to the analysis of turbulent flow systems. Turbulent flow systems are often regarded as chaotic, indeterministic processes. These random flow systems, however, are not entirely without order. Reoccurring flow patterns, in the form of counter rotating pair of vortices, have been observed in turbulent wakes[175]. Some of the more well-known occurrences of these structures are: the Von Karman vortex behind bluff bodies[176]; the Horseshoe vortices found in turbulent boundary layer systems[177]; and the Filament vortices structure in homogeneous flow systems[178]. Due to its seemingly organised spatial features and its cyclic temporal behaviour, these vortices have also became known as

coherent structures[179]. Coherent structures are taken to represents the preliminary convection of energy away from the primary flow component of a turbulent flow system. In accordance to the cascade energy dissipation mechanism[180] in turbulence, energy is first convected from the primary mean flow component into these large coherent structures. The kinetic energy in these coherent structures, are then cascaded down into progressively smaller scale circulating structures, until it reaches the micro-Kolmogorov scale, in which kinetic energy is finally dissipated as heat through viscous friction[181]. The total kinetic energy dissipation is thus mainly dependent on the energy convected from the primary flow component into these cyclic coherent structures[182]. Coherent structures have become one of the cornerstones in the study of turbulent flow systems, so much so that the special term 'eduction' has been introduced to describe the 'extraction of coherent structures' from experimental turbulent flow systems.

Similar vortical structures have also been found in acoustic wave propagation through duct systems[183]. These vortical flow structures however, appear to be steady with time and usually have amplitudes which are much lower than the primary oscillating component. As such, these flow structures are also known as 'secondary flow components' and usually correspond to the mean flow component of the oscillation. In acoustic systems however, the formation of these vortical, steady state component may be caused by adverse pressure gradient in the Stokes layer, causing mass streaming to occur in the boundary layer, thence leading on to flow circulation in the free stream oscillation. This is also known as acoustic streaming. Alternatively, it could be caused by the flow separation that occurs due to a sudden change in geometry of the waveguide system at a discontinuity.

In either case, it is theorised that the energy for the formation of these "quasi-steady" secondary circulating structures corresponds to kinetic energy dissipated away from the primary oscillating flow systems. It is hoped that by studying these structures and investigating their origins, a better understanding of the loss mechanism in oscillating flow systems can be made. The acoustic wave in

this investigation are purely oscillatory in nature, as such, if these secondary circulations are steady in nature, the eduction of these secondary flow system can be made by taking the mean component of the PIV measured oscillating flow systems. If the these secondary circulations are semi-steady in nature, a technique involving the use of phase aliasing can be used. Both of these eduction techniques are further explored in the next two sub-chapters.

5.3 Results from Mean Flow Analysis

The mean flow velocity vector field of the measurement is computed by taking the root mean square of the x- and y-axis velocity component for each interrogation area of the measured plane. The mean flow is particularly effective in identifying steady secondary flow circulation, within the pure oscillating flow systems. It must be noted however, that there are several forms of secondary flow systems and that their magnitude may vary from each system. These systems include the various forms of acoustic streaming, the secondary flow circulation generated by flow separation, the different scales of turbulence circulation, etc. The mean flow analysis would only be effective in educing the predominant secondary flow system. The results show that a pair of counter-rotating vortex circulation exists just upstream and downstream, before and after, the curved section of each of the bend. It is shown that these pairs of vortical structures are more prominent in bends with a sharper radius of curvature but very weak for large ROC such as in the A5-Bend. The circulation of these secondary flow vortices encourages flow towards the inner wall of the bends' curvature. This same characteristic is observed throughout the range of investigated frequencies for all the 5 different radius of curvature bend as shown in Figure 5-4 and Figure 5-5.

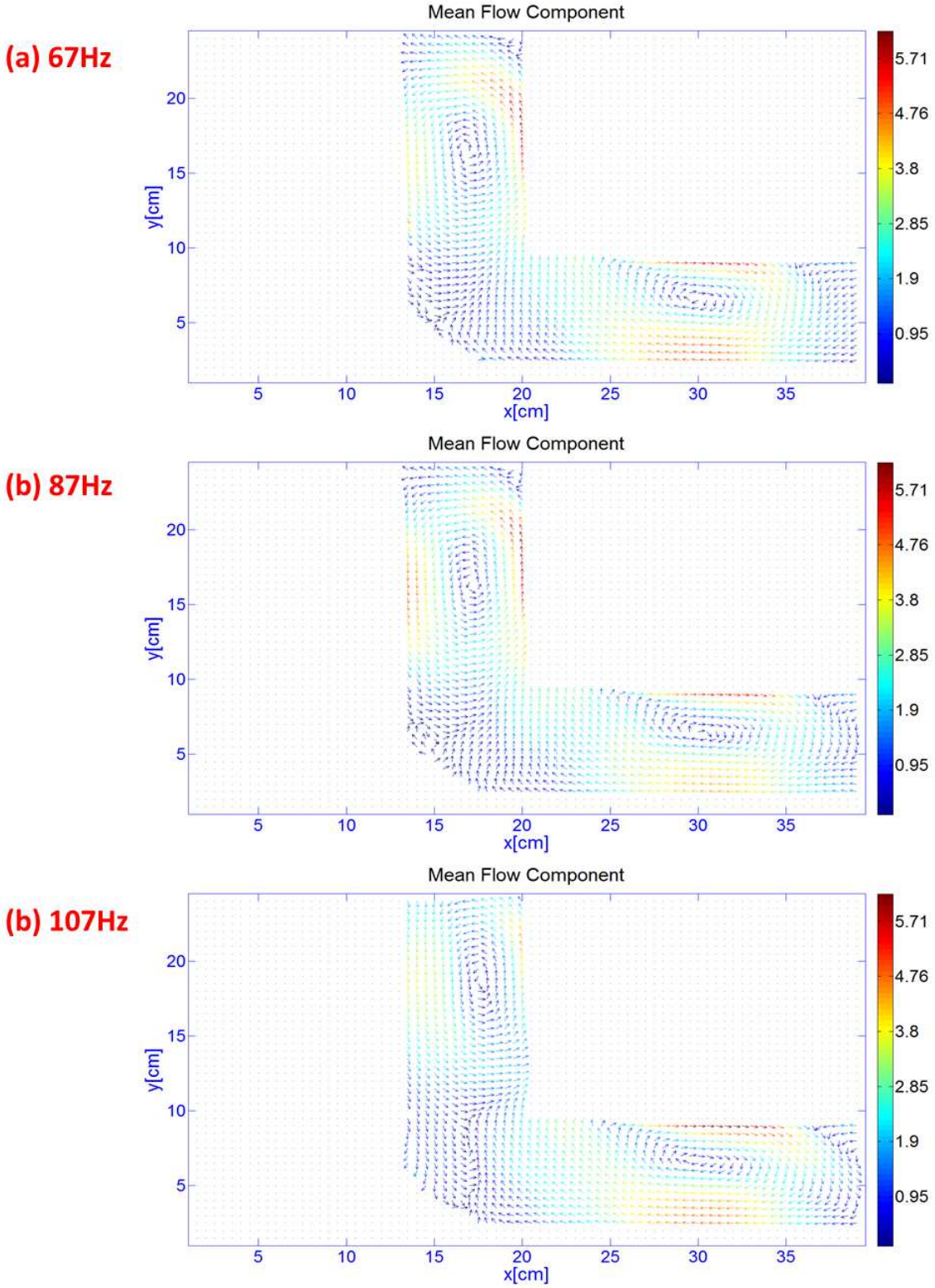

Figure 5-4[*(a)-(c)*]: For caption see pg.144

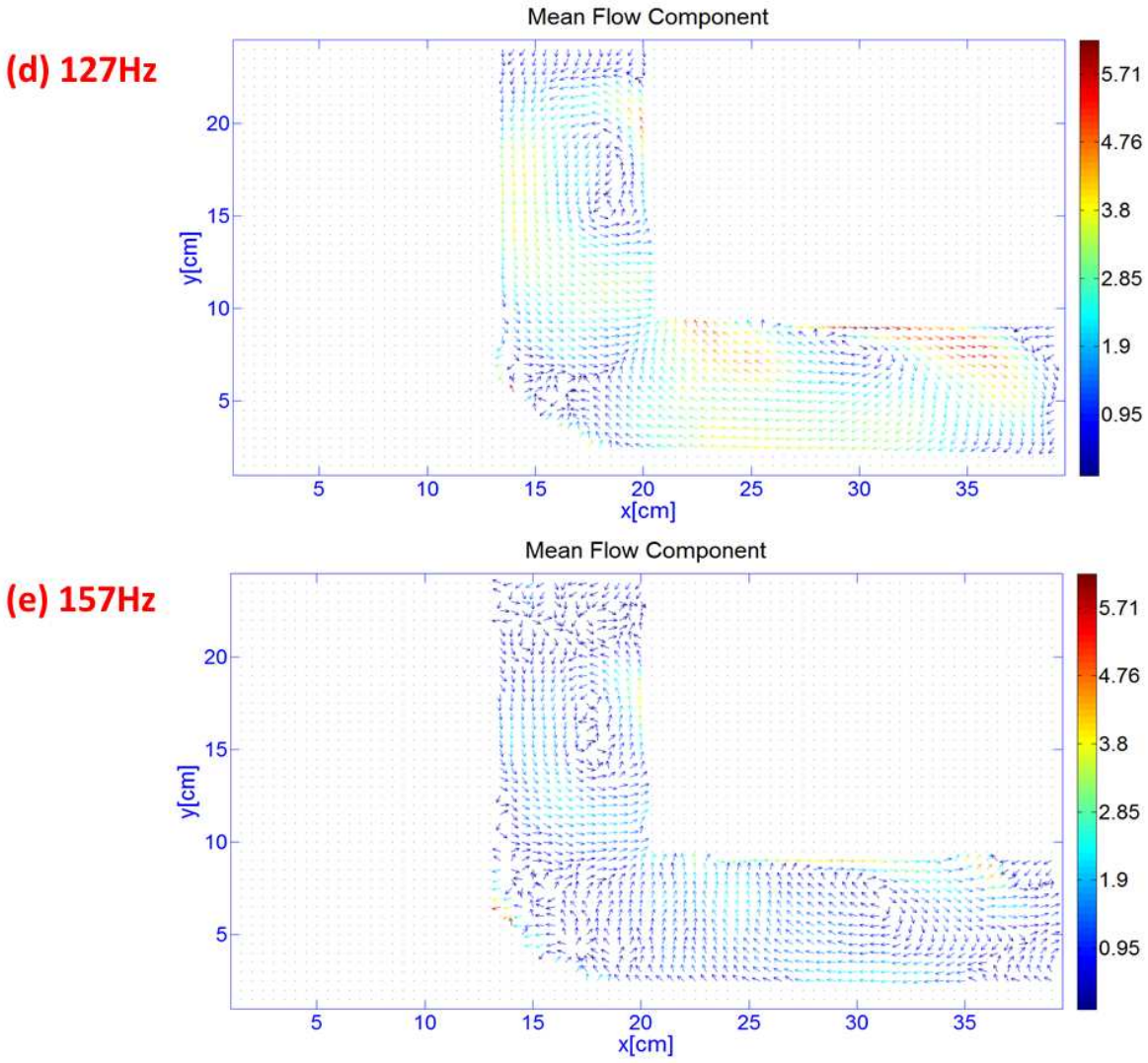

Figure 5-4: The A1 Bend Mean flow components for the range of investigated frequencies (67Hz- 157Hz) at 200We input power. The velocity amplitude of the vectors are represented by colours indicated by the colour scale (velocities given in ms^{-1}). The mean flow for all investigated frequencies is shown to form a pair of counter-rotating vortices just upstream and down stream of the curved section of the bend. These vortices are shown to encourage motion towards the inner wall of the curved duct bend. The intensity of these vortices are also shown to be proportional to the wavelength of the acoustic wave propagating through it.

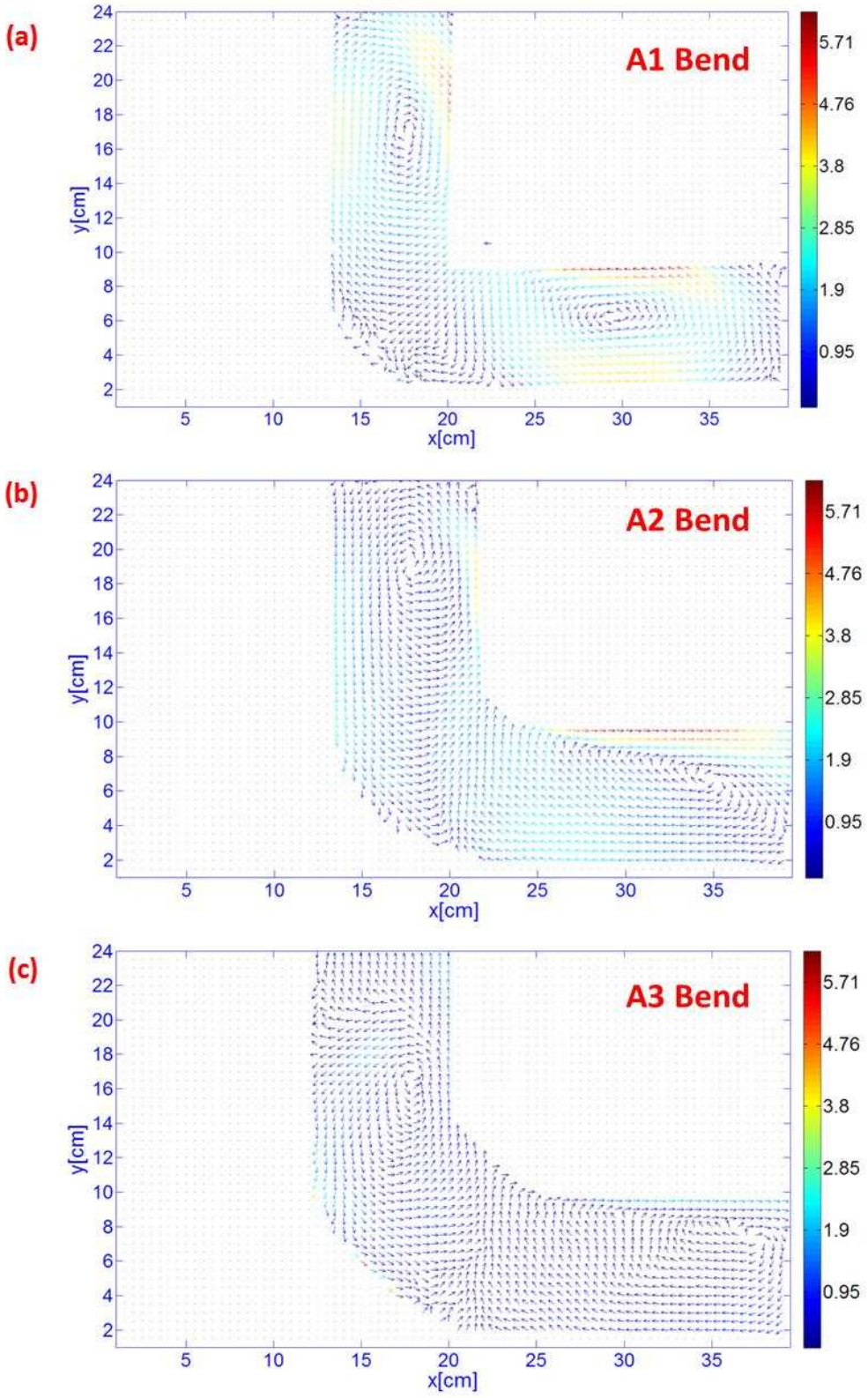

Figure 5-5[*(a)-(c)*]: For caption see pg.146

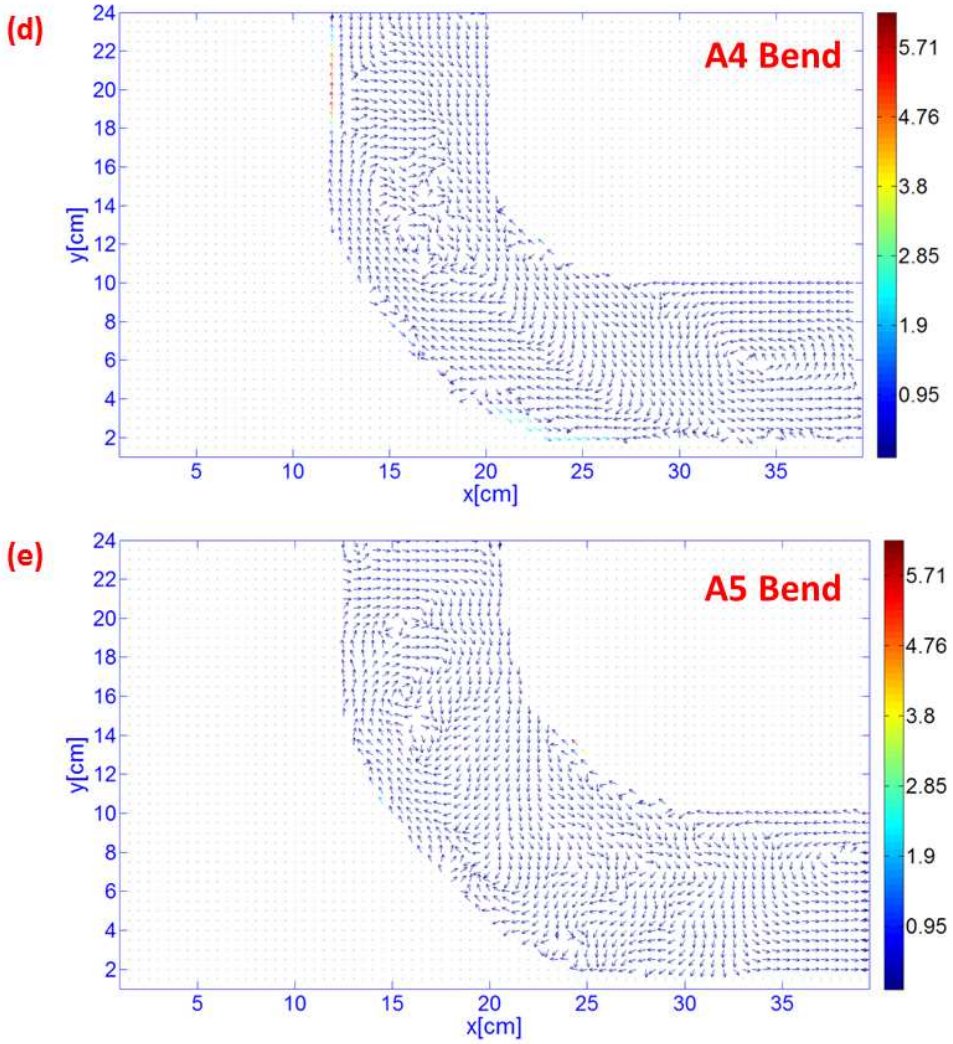

Figure 5-5: The result of the mean flow components for the 67Hz oscillting flow at 200We input power through curved duct bend A1-A5. The velocity amplitude of the vectors are represented by colours indicated by the colour scale (velocities given in ms^{-1}).

The results from Figure 5-4 shows the formation of the mean secondary circulation in the A1 Bend for oscillating flow of the same acoustic energy content but with different wavelengths. The results reveal oscillating flow with the longer wavelength (67Hz to 107Hz) tend to form stronger more well defined pair of secondary circulations. As the oscillating wavelength is increased, the pair of secondary circulation becomes progressively weaker and the secondary circulation structure becomes less defined.

The results from Figure 5-5 show that the secondary flow circulation formed in the sharper duct bends (A1 –A2) have both a larger circulation velocity as well as a more defined circulation structure.

As the radius of curvature of the bend increases, the prominences of these secondary circulation begin to dimish. The mean component of the A1 Bend(Figure 5-5) shows 2 distinct pair of strong circulatory structures. As the radius of curvature is increased, these pair of circulating structures are shown to be stretched and become progressively weaker as shown in A2 –A3 Bend (Figure 5-5). As the radius of curvature is further increased, the pair of stretched circulations are finally shown to divide into smaller circulations with less distinct circulations structures as shown in the A4 – A5 Bends (Figure 5-5).

Both observations from Figure 5-4 and Figure 5-5 suggest that the flow seperation has a larger influence in the formation of these secondary circulations as compared to the genertion of the adverse presssure gradient due to the oscillation through the curvature. The sharper radius of curvature for A1-A2 Bends has only one tangential point that allows for flow seperation to occur. The secondary circulation for these bends are thus strong and defined. As the radius of curvature is increased, the number of tangential point along the curvature for flow seperation to occur increases. Hence the number of secondary circulation increases, each with decreasing strength as shown in Figure 5-5. It is also noted that for oscillating flow of the same acoustic energy content, the oscillating displacement is proportional to the oscillating wavelength. Oscillations with larger oscillating displacement would have a higher probability for flow seperation to occur at these tangential points. The results from Figure 5-4 is in agreement with this theory. Further investigation will be discussed in the following chapters regarding this.

5.4 Results from Phased Aliasing Technique

The phase aliasing technique is a manual technique for educing secondary flow components from acoustic flow field measurements. This technique is based on captured images using the PIV phase locking recording technique described in Chapter 3.0. In this case, the cross correlation computation of the secondary flow velocity vector is done using two images from the same phase of the oscillation, one or more periods apart. The technique is illustrated in **Error! Reference source not found.**.

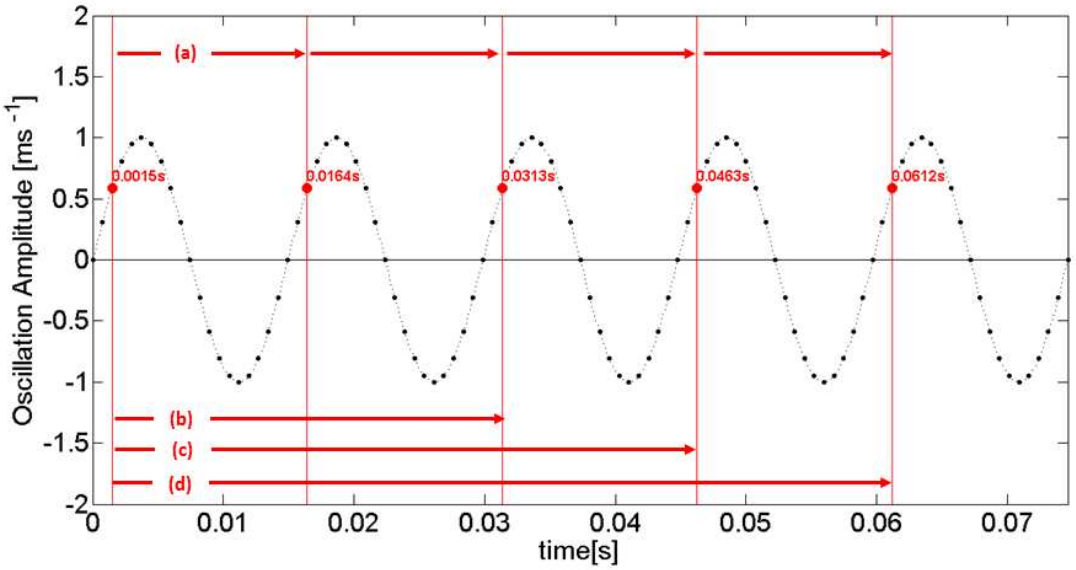

Figure 5-6: This technique is similar to phase locking, where flow recording is made at the same phase for every cycle such as shown in (a). Here the red dot and line represents the time of the recorded snapshot of the oscillating flow. Depending on the magnitude of the secondary flow, measurements may also be made for the same phase every 2 or more cycles apart such as shown in (b), (c) and (d).

In order for the technique to work however, prior knowledge of the oscillation, such as its waveform, oscillating frequency/ies and initial phasing, are required. This requires a preliminary analysis of the wave before the recordings are made. Since the number of periods separating the two images is initially unknown, a large sample size is required while ensuring that the investigated acoustic oscillation remains steady and repeatable throughout the recording period. The number of periods between the two images with which to compute the velocity vectors is determined empirically. It is hoped that by investigating each secondary flow characteristics obtained through the step incrementation of the number of period between the phased locked images, the secondary

flow corresponding to each stage of the Kolmogorov cascading energy dissipation mechanism may be obtained. The technique can then be repeated for all of the recorded locked phases in order to obtain the cyclic temporal behaviour of the secondary flow for a complete oscillating period.

The phase aliaing technique was conducted for each of the measured PIV data by varying the number of periods seperating the phased locked PIV images within the range of 1-50 periods. The phase aliasing technique was only able to educe the predominant secondary circulation featuring the same pair of counter-rotating vortices found in the mean secondary circulation discussed in the previous sub-chapter. This was the same for all the investigated runs. This suggest that the smaller cascade secondary circulation are much weaker (requiring a larger number of seperation period between images) or that these secondary circulation are not steady with time. The results of the predominant secondary circulations are shown in Figure 5-7 and Figure 5-8.

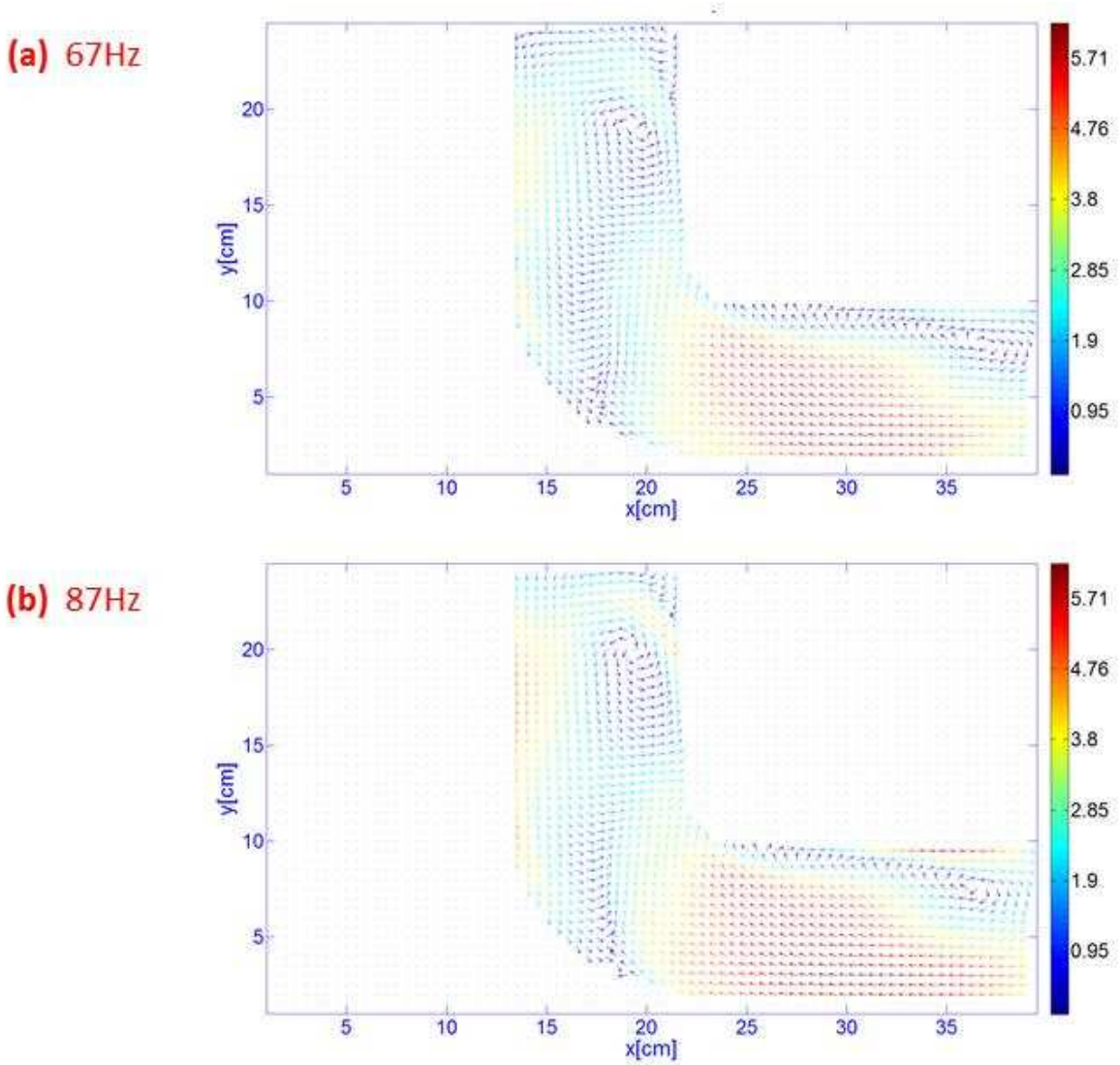

Figure 5-7 [*(a)-(b)*]: For caption see pg.150.

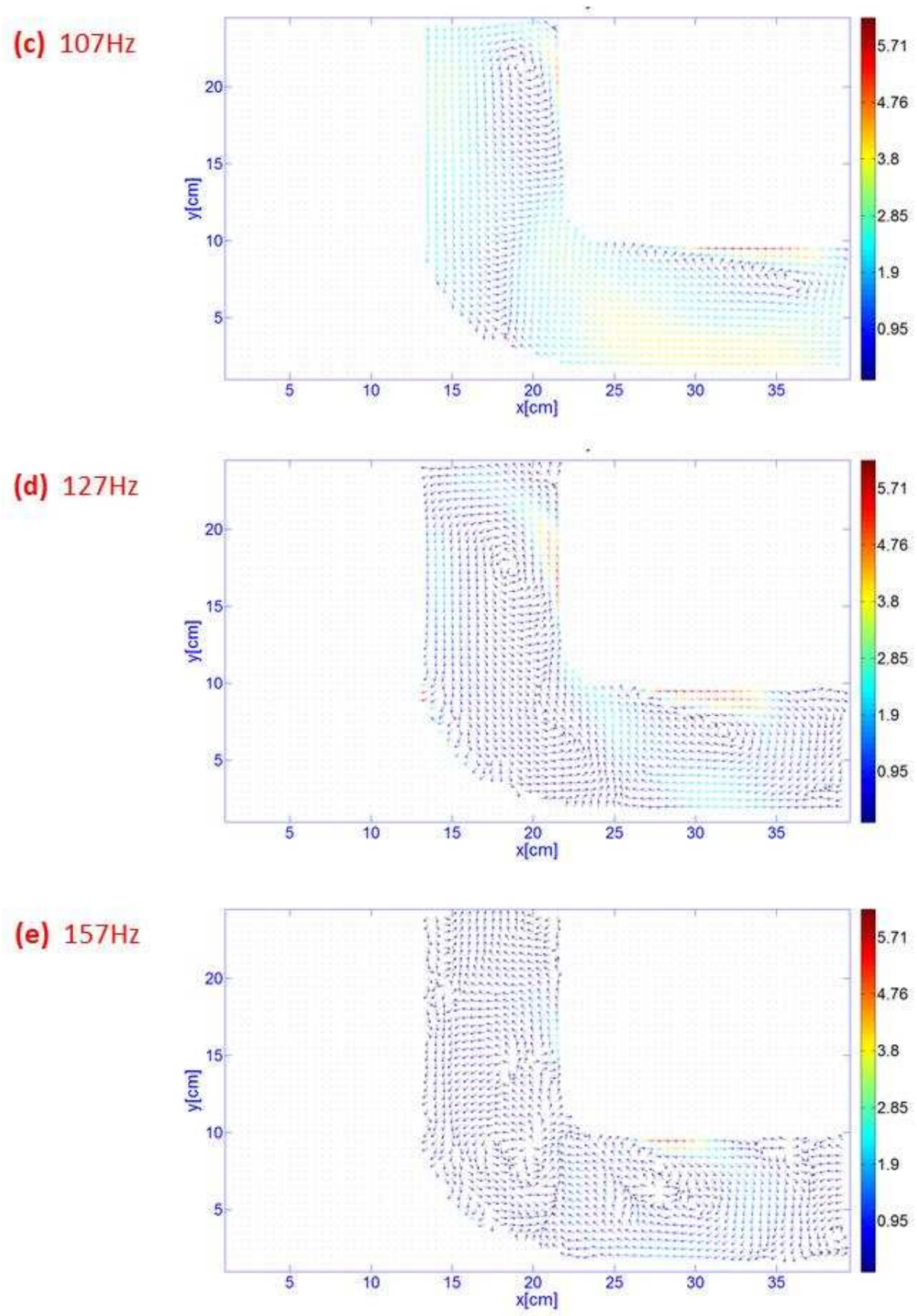

Figure 5-7: The secondary flow component for the A1 Bendrange over the investigated range of frequencies which was obtained from using the phase aliasing technique. The velocity amplitude of the vectors are represented by colours indicated by the colour scale (velocities given in ms^{-1}).

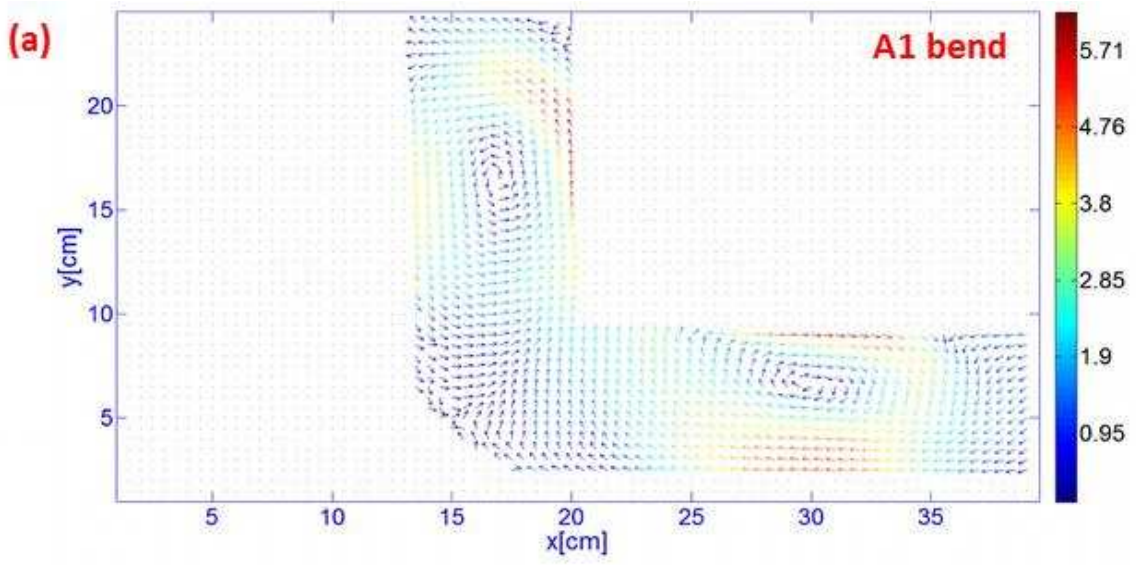
(a)
A1 bend
y[cm]
x[cm]
5.71
4.76
3.8
2.85
1.9
0.95

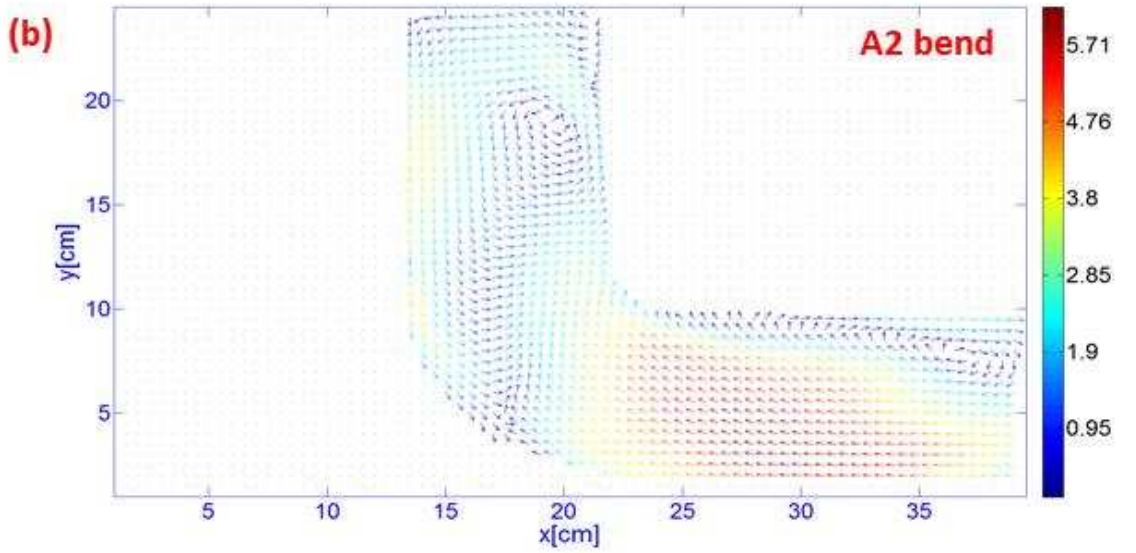
(b)
A2 bend
y[cm]
x[cm]
5.71
4.76
3.8
2.85
1.9
0.95

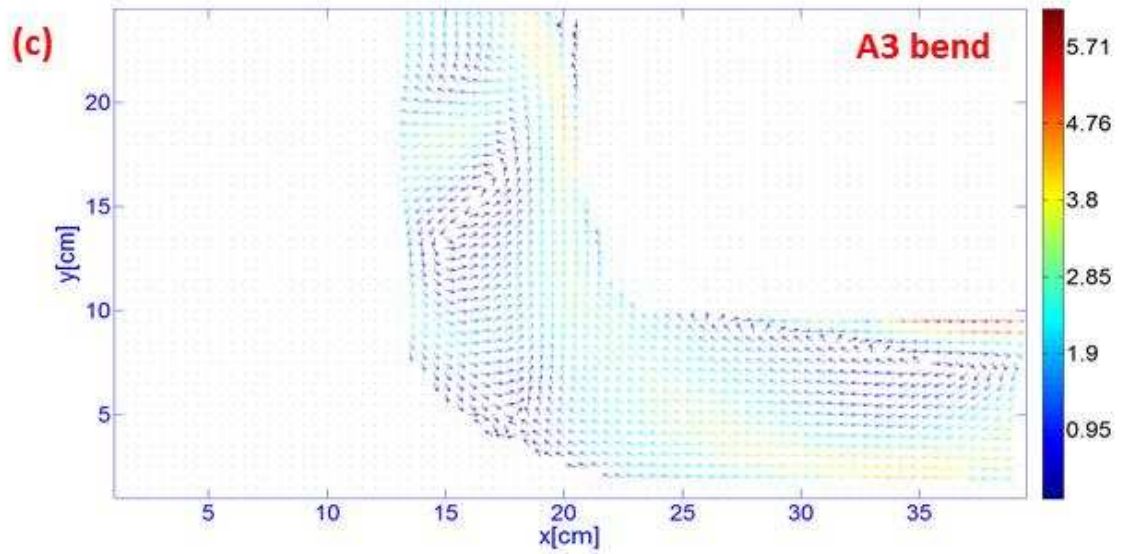
(c)
A3 bend
y[cm]
x[cm]
5.71
4.76
3.8
2.85
1.9
0.95

Figure 5-8[*(a)-(c)*]: For caption see pg.152.

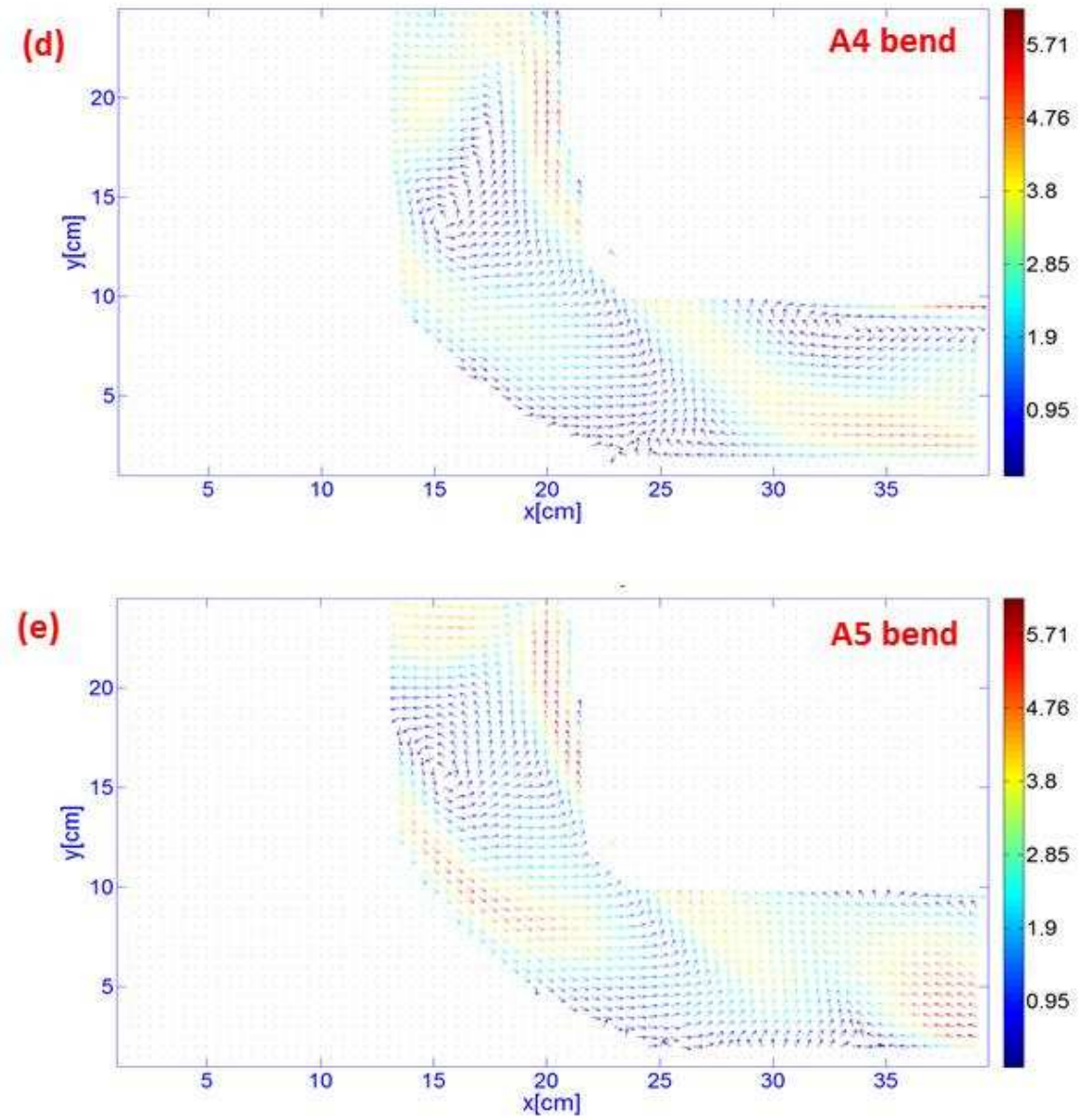

Figure 5-8: **The secondary flow component obtained using the phase aliasing measurement techniques for bends A1 to A5 for acoustic wave propagation of 200We at 67Hz. The velocity amplitude of the vectors are represented by colours indicated by the colour scale (velocities given in ms^{-1}).**

The secondary circulations results obtained from the phase aliasing technique shows the same secondary circulation characteristics as the mean flow secondary circulation investigation. Figure 5-7 shows that the strength of the counter-rotating pair secondary circulaton is proportional to the wavelength of the oscillation. Interestingly, Figure 5-7(e), shows the formation of smaller circulations in addition to the predominant pair of counter-rotating vortices. The oscillating displacement of the

157Hz wavelength oscillation is relatively shorter, hence the flow separation may have occurred at other tangential points rather than only at the mid tangential point of the curvature. Figure 5-8 shows the stretching of the pair of counter-rotating secondary circulation as the radius of curvature of the bend is increased progressively. These match in secondary circulation flow profile between Figure 5-4 and Figure 5-7 as well as between Figure 5-5 and Figure 5-8 shows that the predominant secondary circulation is almost steady with time. The inability of the phase aliasing technique to educe the smaller scale cascade secondary circulation after using the number of separation period between phase locked PIV images of up to 50 (other than Figure 5-7(e)), implies that the strength and energy content of these smaller scale secondary circulations are minimal. The predominant secondary circulation obtained using both the mean and phase aliasing technique can thus be taken to be the main source of acoustic energy dissipation away from the oscillating flow. It can also be inferred that these acoustic losses are largely due to oscillation flow separation at tangential points in the bend.

Both the phase aliasing and mean flow analytical technique successfully identified the predominant secondary circulation formed within the primary oscillating flow as it propagates through the curvature. A more comprehensive and qualitative form of analysis is required in order to fully investigated. This would involve the use of the Proper Orthorgonal Decompostion(POD) technique. The results from the phase aliasing and mean flow technique can be used as a basis for verification against the results obtained using the POD technique which will be discussed in the following sub-chapter.

5.5 Proper Orthogonal Decomposition technique

The Proper Orthogonal Decomposition (POD) is the name given by Lumley[184] to describe the empirical orthogonal decomposition technique used for the analysis of turbulence in the field of fluid dynamics. The orthogonal decomposition is a pattern recognition technique for signal and data processing. The technique is believed to have been introduced independently by several different researchers including Hotelling[185], Kosambi[186], Loève[187] and Karhunen[188], each in their respective field of research. As such, the technique is also known as the Karhunen- Loève Decomposition (KLD), Principal Component Analysis (PCA), and Singular Value Decomposition (SVD)[189, 190]. POD, PCA, KLD and SVD represent different routes by which to compute the same orthogonal decomposition of the investigated data set. The technique is also used for data reduction and compression through lower dimensional approximation of the orthogonal modes. As such, the technique has also been widely used in signal and data analysis, image processing, facial recognition algorithms, control optimization and fluid dynamics related fields[152]. Since the technique is primarily used for acoustic flow analysis in this research, it shall here on be referred to as the "POD" as in accordance with Lumley's terminology.

Turbulent flow is believed to be a superposition of the primary flow with other components, such as coherent structures and secondary flow components, that causes the random fluctuation in the flow. Each of these flow components would have their distinct flow pattern and behaviour with their respective amplitudes. As such, each of these flow components would have different energy level content. The POD technique decomposes the measured turbulent flow, with respect to its kinetic energy content, into a set of linear combination of proper orthogonal modes (POMs). Each orthogonal mode would contain the same number of velocity vector as the measured plane. Each of these velocity vectors, in a particular orthogonal mode, would contain amplitudes of similar kinetic

energy levels. The POD technique educes the different flow components of the turbulence systems, by sorting them into POMs, each corresponding to its kinetic energy levels. A more detailed description of the technique as well as its mathematical formulation is given in the next two subsections.

The POD technique allows the set of inputted data to be analysed into a set of linear combination Proper Orthogonal Modes (POM) whose summation constitutes the original set of input data. This is summarised in *Equation 5.1)*, where each POM consist of a non-dimensional temporal coefficient, *a(t)*, and a spatial orthogonal basis function, $\phi(x, y)$.

$$\vec{\mathbf{u}}(\boldsymbol{x}, \boldsymbol{y}, \boldsymbol{t}) = \sum_{i=1}^{T_N} a_i(t)\phi_i(x, y) \tag{5.1}$$

Each POM represents subspaces in the spatial Euclidean domain and is ranked in descending order in accordance to their eigenvalues. The first POM represents the subspace from which the mean squared distance of point from the input data is minimal. This occurs at the maximum eigenvalue in accordance to the spectral theory[148]. Subsequently, the next POMs represent the subspaces with the next minimal mean squared distance from each point of the input data and so forth. This makes the technique particularly effective in identifying temporal and/or spatial patterns as well as recognising its behaviour in the set of input data.

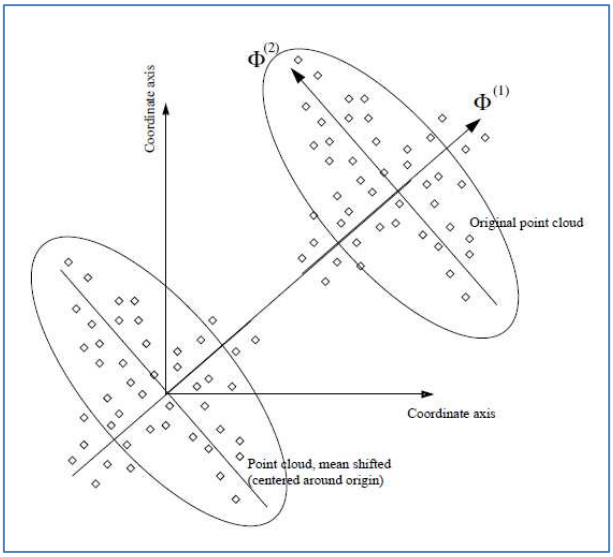

Figure 5-9: Physical Interpretation of the Proper Orthogonal Decomposition.

The input data for the POD analysis is the set of PIV plane velocity vector field measurements in the spatial domain, $\boldsymbol{\Omega}\ (\mathbf{x}, \mathbf{y})$ and recorded at time step intervals, t. The size of the velocity vector field is given by, $x_N \times y_N$, where x_N and y_N are the number of measured velocity vectors along the x-axis and the y-axis respectively. The total number of recorded time step is T_N. The PIV velocity vector results are given in terms of their x-axis and y-axis velocity components, and are denoted respectively by $\vec{u}_{x,y,t}$ and $\vec{v}_{x,y,t}$. The subscripts, x, y and t represent the spatial and temporal coordinates of the vectors respectively. The POD is computed by first assembling the velocity vector into the response matrix, $\overrightarrow{\mathbf{Vel}}$. The velocity vector components and position information for a single time step velocity vector field is appended into a single column. Each column in the $\overrightarrow{\mathbf{Vel}}$ matrix thus represents the velocity vector field information for each of the recorded time step. The row arrangement of the response matrix corresponding to the spatial domain is irrelevant.

$$\overrightarrow{\mathbf{Vel}} = \begin{bmatrix} u_{1,1,1} & \cdots & u_{1,1,T_N} \\ v_{1,1,1} & \cdots & v_{1,1,T_N} \\ u_{2,1,1} & \cdots & u_{2,1,T_N} \\ v_{2,1,1} & \cdots & v_{2,1,T_N} \\ \vdots & \ddots & \vdots \\ u_{x_N,y_N} & \cdots & u_{x_N,y_N,T_N} \\ v_{x_N,y_N} & \cdots & v_{x_N,y_N,T_N} \end{bmatrix} \tag{5.2}$$

POD is used to decompose the response matrix into the form shown in *Equation 5.1)*. For this application, the physical interpretation is where each POM contains the velocity vector components which have the most similar kinetic energy level as to its neighbouring vectors in the field. This allows the quantitative identification of explicit coherent structures as well as the eduction of implicit secondary flow component which may be obscured by the dominant primary flow. The kinetic energy levels of the POM are related to the eigenvalue component of the autocorrelation of the response matrix. Concurrently, the orthogonal basis function,$\phi_i(x, y)$, which describes the flow behaviour of each POM is related to the eigenvector of autocorrelation matrix. As such, the POD technique is simplified in solving the eigenvalue problem:

$$\boldsymbol{C}\mathbf{A}^{\boldsymbol{i}} = \boldsymbol{\lambda}^{\boldsymbol{i}}\mathbf{A}^{\boldsymbol{i}} \tag{5.3}$$

The auto-correlation matrix, **C**, can be computed either through spatial (topos) or temporal (chromos) correlation as shown in Equation (5.4) and (5.5).

$$\mathbf{C}_{topos} = \overrightarrow{\mathbf{Vel}} \cdot \overrightarrow{\mathbf{Vel}}^{\mathbf{T}} \tag{5.4}$$

$$\mathbf{C}_{chronos} = \overrightarrow{\mathbf{Vel}}^{\mathbf{T}} \cdot \overrightarrow{\mathbf{Vel}}. \tag{5.5}$$

Although both, $\mathbf{C}_{topos}$ and $\mathbf{C}_{chronos}$ are Hermitian matrices, the choice of correlation is important depending on the size of the measurement data set. The use of $\mathbf{C}_{topos}$ to compute the POD constitutes the classical POD approach introduced by Lumley[184] while using the $\mathbf{C}_{chronos}$ refers to the Snapshot approach introduced by Sirovich[191]. The eigenvalue for each POM is essentially the sum of the squared velocity vector field for each time-step in that mode.

$$\lambda^i = \sum_{l=1}^{T_N} \sum_{n=1}^{x_N} \sum_{m=1}^{y_N} [\, a_i(t_l)\phi_i(x_n, y_m)\,]^2 \tag{5.6}$$

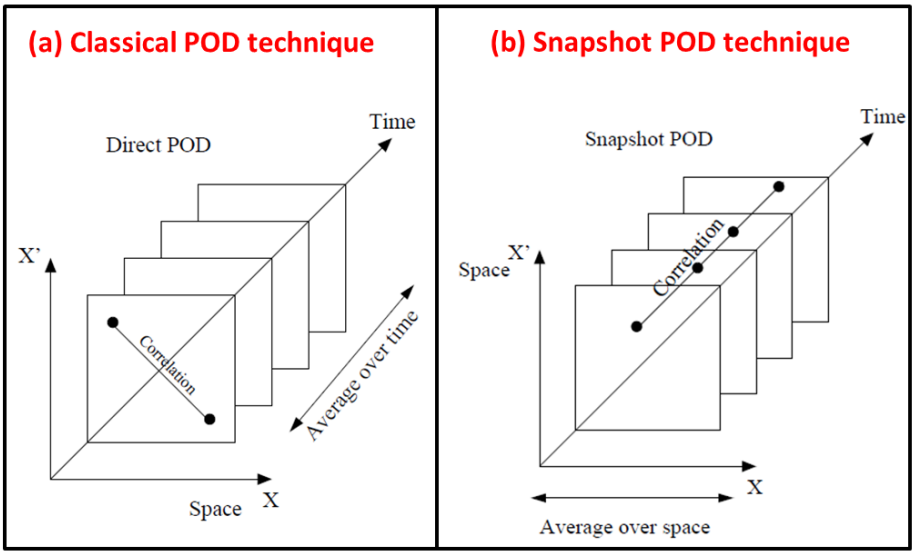

Figure 5-10: The two approach to the Proper Orthogonal Decomposition: (a) The Classical Approach takes the temporal average and correlates the data spatially over the domain (b) The Snapshot approach takes the spatial average over the domain correlates in over time. [156]

The eigenvector matrix, **A,** and diagonal eigenvalue matrix, **λ**, are obtained from solving the eigenvalue problem in *Equation* (5.3). It is of interest to rank the column of eigenvector matrix, **A**,

corresponding to their respective eigenvalues (diagonal elements of **λ**) in descending order: $\lambda_1 > \lambda_2 > \lambda_3 > \cdots > \lambda_N = 0$. The normalised orthogonal basis function matrix, ***Φ***, is thus given as:

$$\phi^i = \frac{\sum_{n=1}^{N} A_n^i u^n}{\left\| \sum_{n=1}^{N} A_n^i u^n \right\|} \tag{5.7}$$

Accordingly, the temporal coefficients, a_i, are thus given as:

$$\mathrm{a}^{\boldsymbol{i}} = \phi^i u^n \tag{5.8}$$

As such, the i^{th} Proper Orthogonal Modes can be computed:

$$\boldsymbol{i^{th}}\ \mathbf{POM} = a_i(t)\phi_i(x,y) \tag{5.9}$$

Both Classical and Snapshot approaches have their advantages. For PIV measurements, where the number of velocity vectors of the measured plane is much larger than the number of measured time steps, the snapshot POD is preferred[192]. However, for techniques such as hotwire and LDA/LDV measurements, where the number of time step far exceeds the number of measured velocity vector points, the classical POD approach would be more appropriate[193]. In this research, the number of velocity vectors measured for each time steps is (49 x 79). The minimum number of measured time step for each run is 4000. As such, it is computationally more efficient to use the Snapshot approach in analysing the PIV measurements.

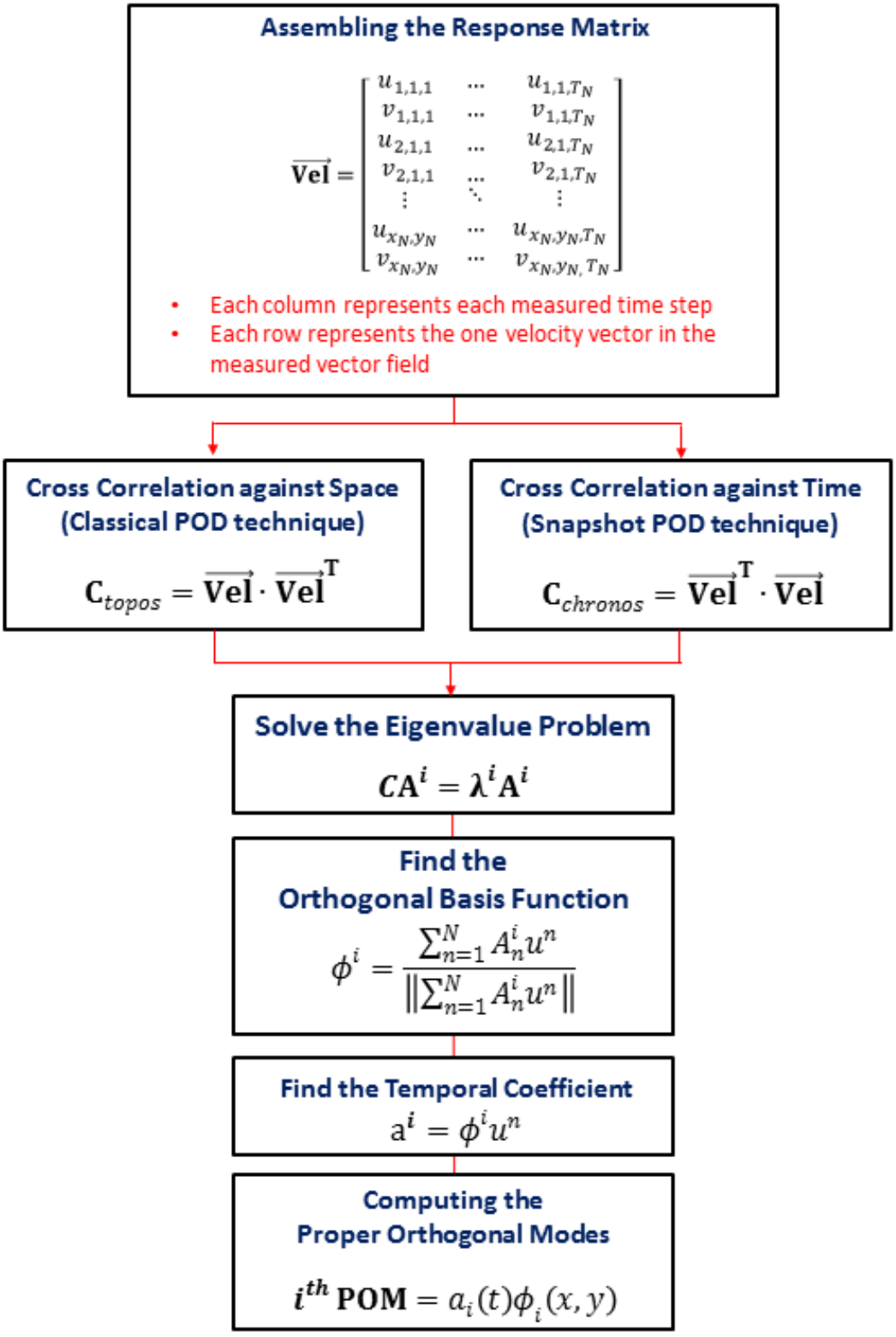

Figure 5-11: Summary of the Proper Orthogonal Decomposition Technique

5.6 POD computed using Singular Value Decomposition

It is of interest to compute the POD in terms of the SVD format because the MATLAB software has an inbuilt SVD function capable of decomposing high order matrices with computational ease. The PIV measured data can be represented in the Singular Value Decomposition equation given by:

$$\overrightarrow{\mathbf{Vel}} = \mathbf{U\Sigma V}^{\boldsymbol{T}} \tag{5.10}$$

$$\begin{bmatrix} \overrightarrow{\mathbf{Vel}} \\ ([x_{N\times}y_N] \text{ x } T_N) \end{bmatrix} = \begin{bmatrix} \mathbf{U} \\ Topos\ matrix \\ ([x_{N\times}y_N] \text{ x } [x_{N\times}y_N]) \end{bmatrix} \begin{bmatrix} \mathbf{\Sigma} \\ diagonal\ matrix \\ ([x_{N\times}y_N] \text{ x } T_N) \end{bmatrix} \begin{bmatrix} \mathbf{V}^{\boldsymbol{T}} \\ Chronos\ Matrix \\ (T_N \text{ x } T_N) \end{bmatrix} \tag{5.11}$$

Here, it is interesting to note that the matrix, **U**, denotes the spatial structure (also known as Topos) and the matrix, **V**, denotes the temporal structure (also known as Chronos)[190, 194]. The energy ranking is given by the singular values in the diagonal matrix, **Σ.** The matrix, **U,** is essentially the auto-correlation eigenvectors matrix $\mathbf{C}_{topos}$.

$$\overrightarrow{\mathbf{Vel}}\ \overrightarrow{\mathbf{Vel}}^{\mathbf{T}} = \mathbf{C}_{topos} = \mathbf{U\Sigma^2 U}^{\boldsymbol{T}} \tag{5.12}$$

$$\overrightarrow{\mathbf{Vel}}^{\mathbf{T}}\ \overrightarrow{\mathbf{Vel}} = \mathbf{C}_{chronos} = \mathbf{V\Sigma^2 V}^{\boldsymbol{T}} \tag{5.13}$$

It is important to note that the matrix $\mathbf{C}_{topos}$ and $\boldsymbol{C}_{chronos}$ are both Hermitian matrix. Hence *Equation (5.12)* and *(5.13)* can also be written as:

$$\mathbf{C}_{topos} = \mathbf{U}\,\mathbf{\Sigma^2}\,\mathbf{U^{-1}}$$

$$\mathbf{C}_{topos}\,\mathbf{U} = \mathbf{U}\,\mathbf{\Sigma^2} \tag{5.14}$$

This shows that the Topos Matrix, **U**, is essentially the eigenvector solution to the eigenvalue problem of the auto-correlation matrix, $\mathbf{C}_{topos}$. Similarly, the Chronos Matrix, V, is the eigenvector solution to matrix, $\mathbf{C}_{chronos}$.

$$\mathbf{C}_{chronos}\,\mathbf{V} = \mathbf{V}\,\mathbf{\Sigma^2} \tag{5.15}$$

Equation (5.14) and *(5.15)* also show that the squared of the diagonal singular values matrix, $\mathbf{\Sigma^2}$ corresponds to the eigenvalue matrix. This implicitly suggests that the square root of the singular values correspond to the eigenvalues of $\mathbf{C}$:

$$\lambda_i = \sqrt{\sigma_i} \tag{5.16}$$

The Singular Value Decomposition can also be written as a sum of its singular components:

$$\begin{aligned} \overrightarrow{\mathrm{Vel}} &= \mathrm{u}_1\sigma_1\mathrm{v}^T{}_1 + \mathrm{u}_2\sigma_2\mathrm{v}^T{}_2 + \cdots + \mathrm{u}_{T_N}\sigma_{T_N}\mathrm{v}^T{}_{T_N} \\ &= \sum_{i=1}^{T_N} \mathrm{u}_i\sigma_i\mathrm{v}^T{}_i \end{aligned} \tag{5.17}$$

Here, u_i, represents the i^{th} column of $\mathbf{U}$, σ_i the i^{th} x i^{th} element of the diagonal matrix $\mathbf{\Sigma}$ and $\mathrm{v}^T{}_i$, is the i^{th} row of matrix $\mathbf{V^T}$. Thus, $\mathrm{u}_i\sigma_i\mathrm{v}^T{}_i$ represents the i^{th} mode of the measured flow.

$$i^{th}\ \mathrm{Mode} = \mathrm{u}_i\sigma_i\mathrm{v}^T{}_i = \begin{bmatrix} {u_{1,1,1}}^i & \cdots & {u_{1,1,T_N}}^i \\ {v_{1,1,1}}^i & \cdots & {v_{1,1,T_N}}^i \\ {u_{2,1,1}}^i & \cdots & {u_{2,1,T_N}}^i \\ {v_{2,1,1}}^i & \cdots & {v_{2,1,T_N}}^i \\ \vdots & \ddots & \vdots \\ {u_{x_N,y_N}}^i & \cdots & {u_{x_N,y_N,T_N}}^i \\ {v_{x_N,y_N}}^i & \cdots & {v_{x_N,y_N,T_N}}^i \end{bmatrix} \tag{5.18}$$

The computation of the POD on the measured velocity vector field was conducted using the MATLAB software. The computation procedure is summarised in Figure 5-12.

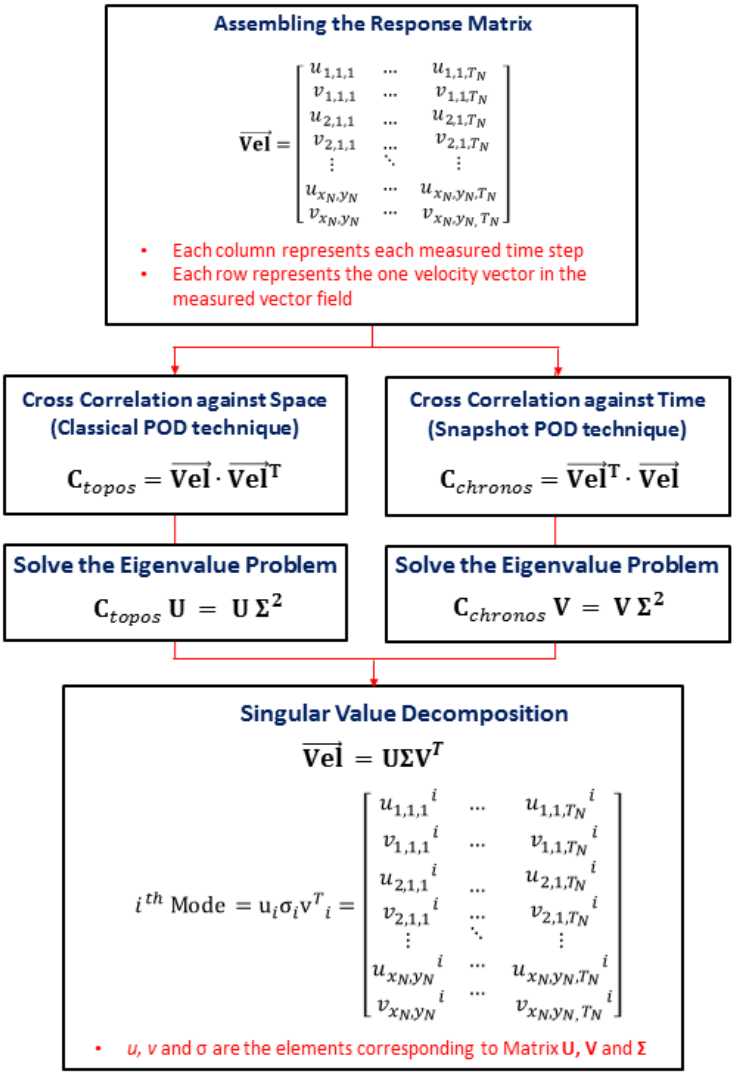

Figure 5-12: Summary of the POD computed via the Singular Value Decomposition technique.

5.7 Chapter Conclusion

The preliminary observation made on the secondary flow component through the mean flow and the phase aliasing technique provides a basis for which to compare the different oscillating flow behaviour of the various modes found in the POD analysis. From the observations made, it is shown that a double counter rotating vortex structure exists just upstream and downstream in the straight section before the curvature of the bend. The direction of circulation of these vortices encourages the flow towards the inner wall of the bend. This is in compliance with Lyne and other researchers who have studied oscillating flow systems through curved duct systems. The results of the POD technique will be discussed in Chapter 6.0 .

Chapter 6

Proper Orthogonal Decomposition

6.0 Result of POD analysis on the PIV measurements

The Snapshot POD technique decomposes the PIV measurement data set into the number of Proper Orthogonal Modes (POMs) equivalent to the number of PIV recorded time-steps. The POMs are ranked in descending order of their respective eigenvalues, λ. The eigenvalue for each POM is essentially the sum of the squared velocity vector field for each time-step in that mode.

$$\lambda^i = \sum_{l=1}^{T_N} \sum_{n=1}^{x_N} \sum_{m=1}^{y_N} [\, a_i(t_l)\phi_i(x_n, y_m)\,]^2 \tag{6.1}$$

The eigenvalues can thus be taken to be as a representative of the relative amount of kinetic energy stored within a particular POM. Figure 6-1 shows the first 50 POMs plotted against their respective percentage energy content for each of the investigated frequencies for the A1-Bend investigation. The percentage energy content plot helps to distinguish the dominant POMs within the dataset. A steep decline in the percentage energy content within the first 4 POMs before plateauing off implies that the first 3 POMs are the dominant modes, where approximately 99.75% of the total kinetic energy from the investigated velocity field vector resides within these 3 modes. The more dominant the modes would implies that a more defined flow pattern exists for that particular mode as compared to the other POMs, as shown in

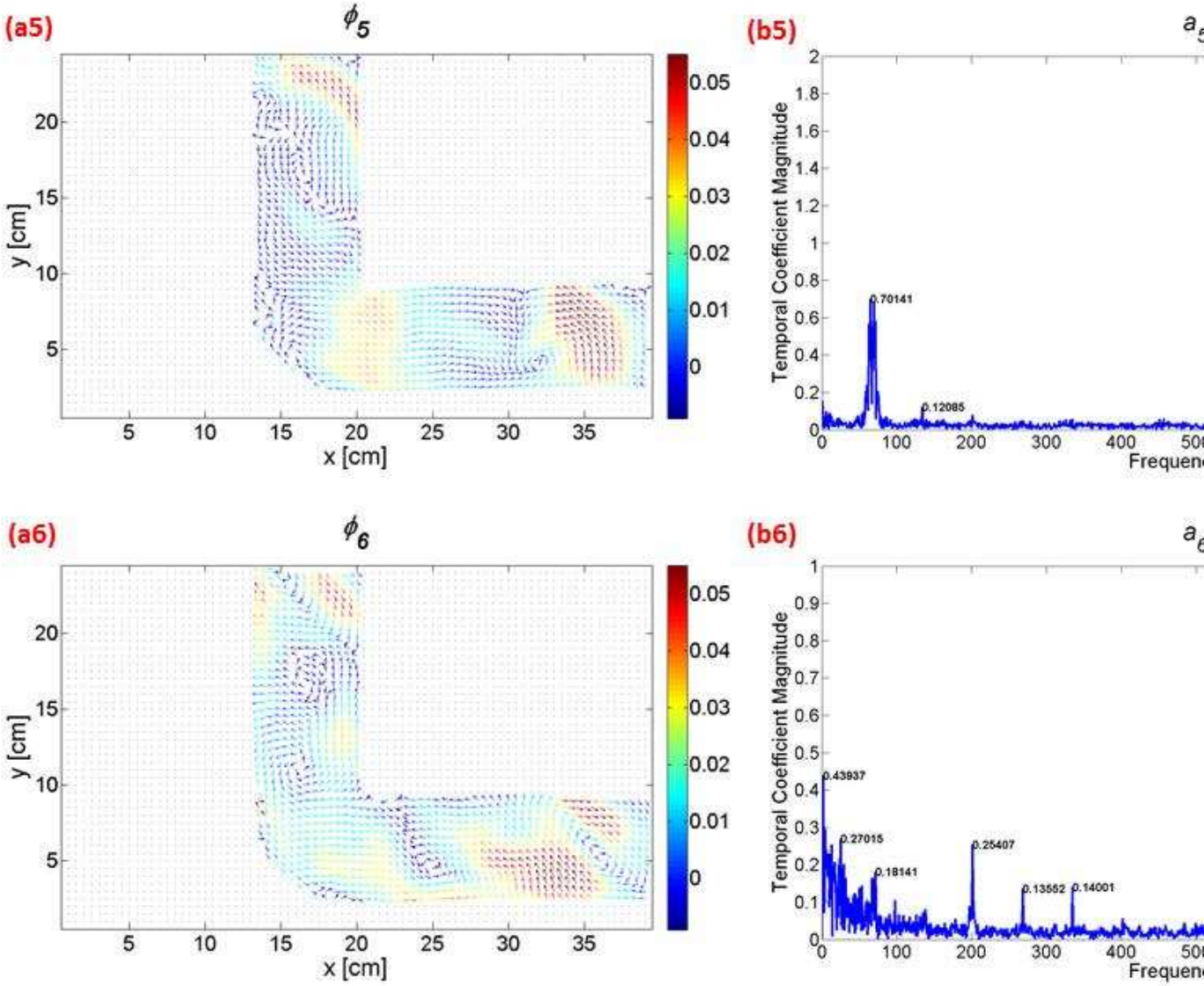
(a5)
ϕ_5
y [cm]
x [cm]
(b5)
Temporal Coefficient Magnitude
0.70141
0.12085
(a6)
ϕ_6
y [cm]
x [cm]
(b6)
Temporal Coefficient Magnitude
0.43937
0.27015
0.18141
0.25407
0.13552
0.14001

Figure 6-3.

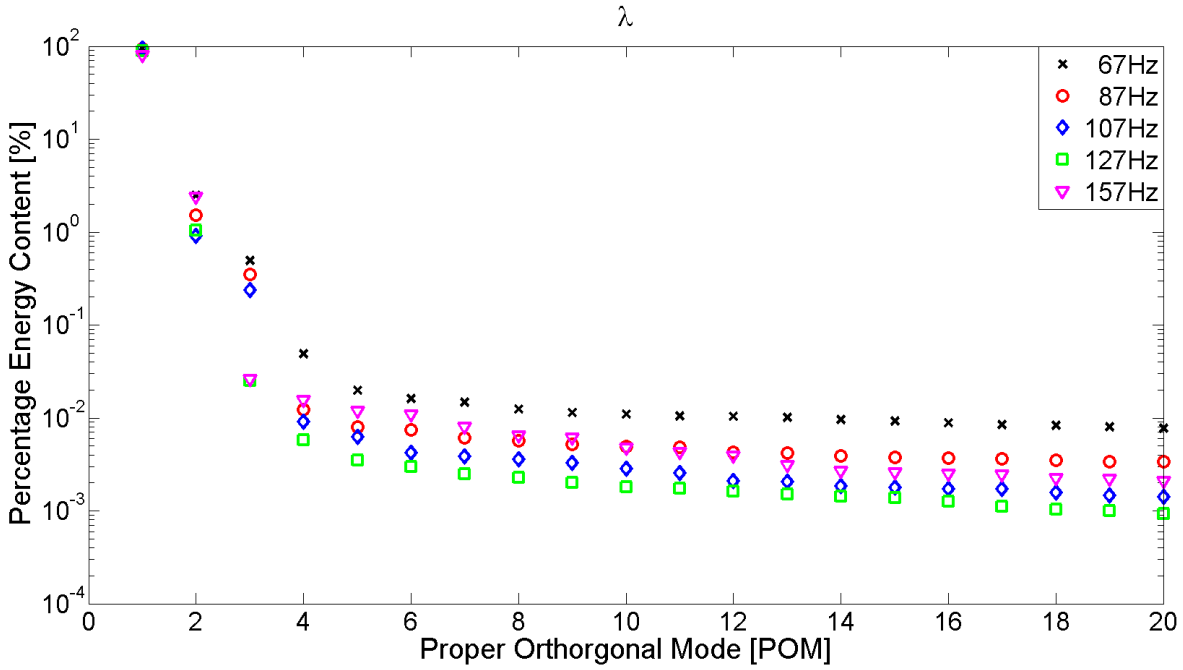

Figure 6-1: The Percentage Energy Level of the first 50 Proper Orthogonal Modes, in accordance to their respective eigenvalues, for Acoustic excitation of 200We at 67Hz to 157Hz. The percentage energy content for the first 6 POMs are labelled for comparison purposes.

As this investigation deals with measurement of an acoustic flow, the kinetic energy content of an acoustic wave can also be represented by the RMS value of the oscillation, which is incidentally the Standard Deviation of all the vector point in time and space for a particular POM:

By using the standard deviation energy profiling of the POMs, a comparison between the mean amplitude of oscillations between the modes can be made as shown in Figure 6-2. An added advantage of using the standard deviation energy profiling is that certain dominant non-oscillatory mode can be easily identified, such as in Mode 3 of Figure 6-2. In Figure 6-1, Mode 3 is shown to be follow the descending energy content trend together with the other POM modes. However, in Figure 6-2, the oscillating energy of Mode 3 is distinctively lower as compared to the other first 6 Modes. This implies that Mode 3 may essentially be a mean secondary flow component.

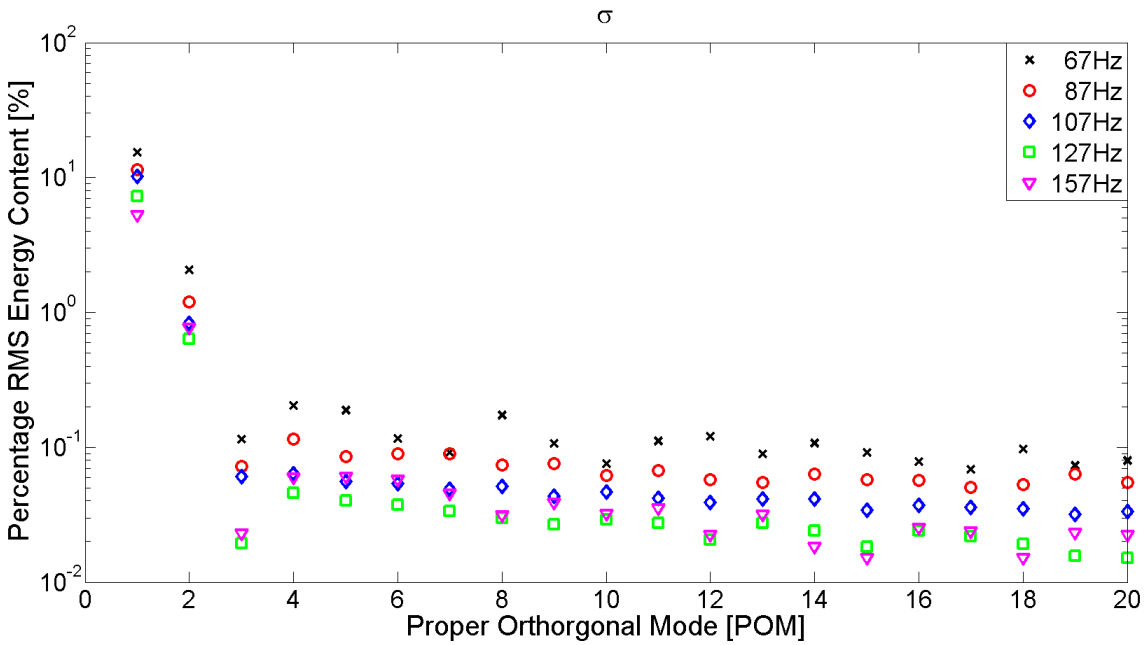

Figure 6-2: The Percentage Energy Level of the first 50 Proper Orthogonal Modes, in accordance to the standard deviation of the POM's oscillation, for Acoustic excitation of 200We at 67Hz. The percentage energy content for the first 6 POMs are labelled for comparison.

Each POM is the product of its orthonormal basis function, $\phi_i(x,y)$, with its temporal coefficient, $a_i(t)$, as shown in Equation(5.9). The orthonormal basis function, $\phi_i(x,y)$, is similar to the spatial eigenvector matrix for the velocity vector field of the i^{th} POM and serves to show the general flow pattern for that Mode. The temporal coefficients, $a_i(t)$, is a representative of the eigenvalue for orthonormal basis function for each timestep in that Mode. As such, each, $a_i(t)$, has 4000 timesteps corresponding to 100 measured acoustic oscillation periods. Thus, there are sufficient timesteps to represent the temporal coefficient in the frequency domain. The Fourier transform of the temporal coefficient will give a clear representation of the different wave components that exist in the investigated Mode.

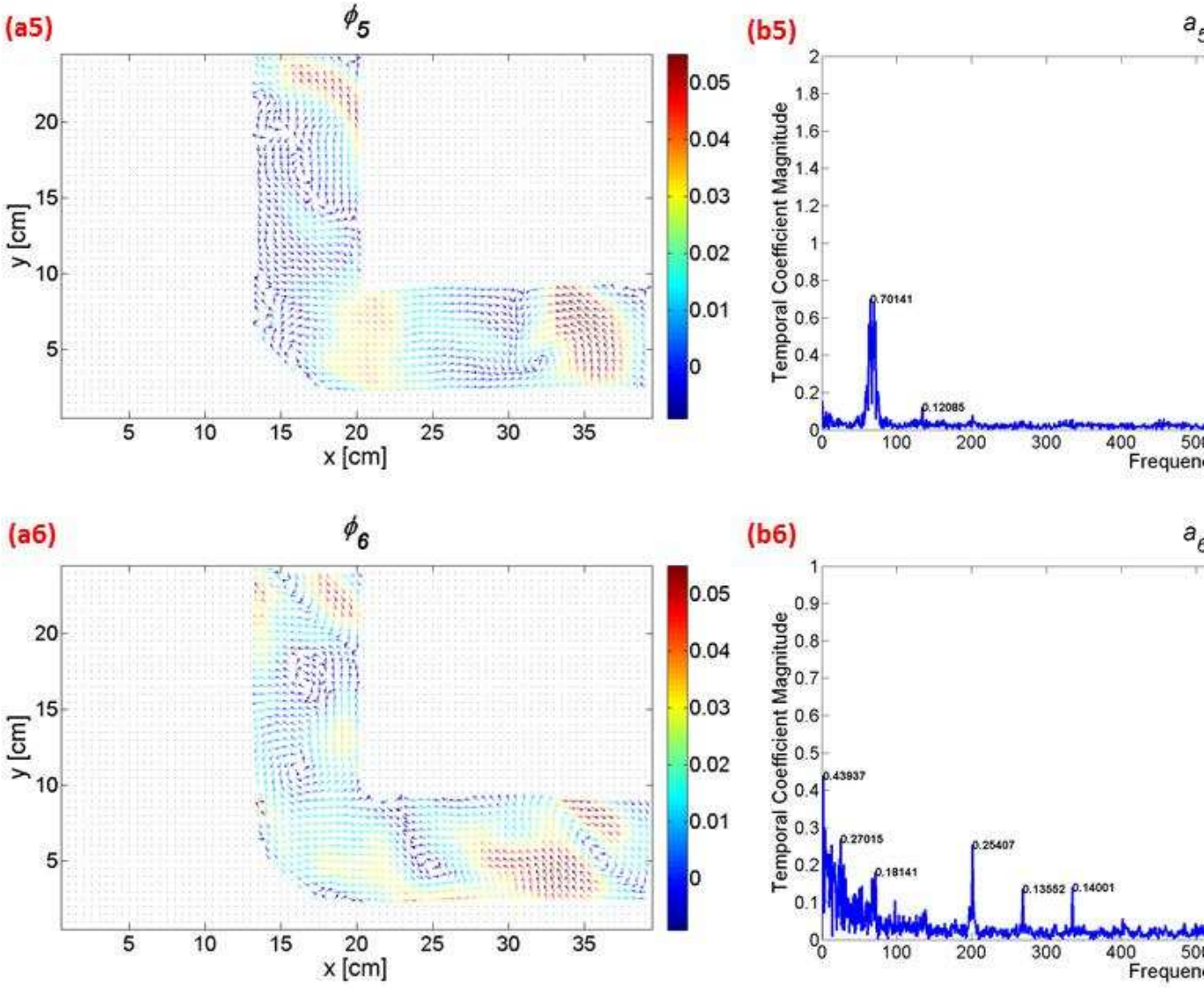

Figure 6-3 shows the first 6 POMs in terms of their orthonormal basis function, $\phi_i(x, y)$ and the temporal coefficient represented in the frequency domain, $a_i(f)$. Results in

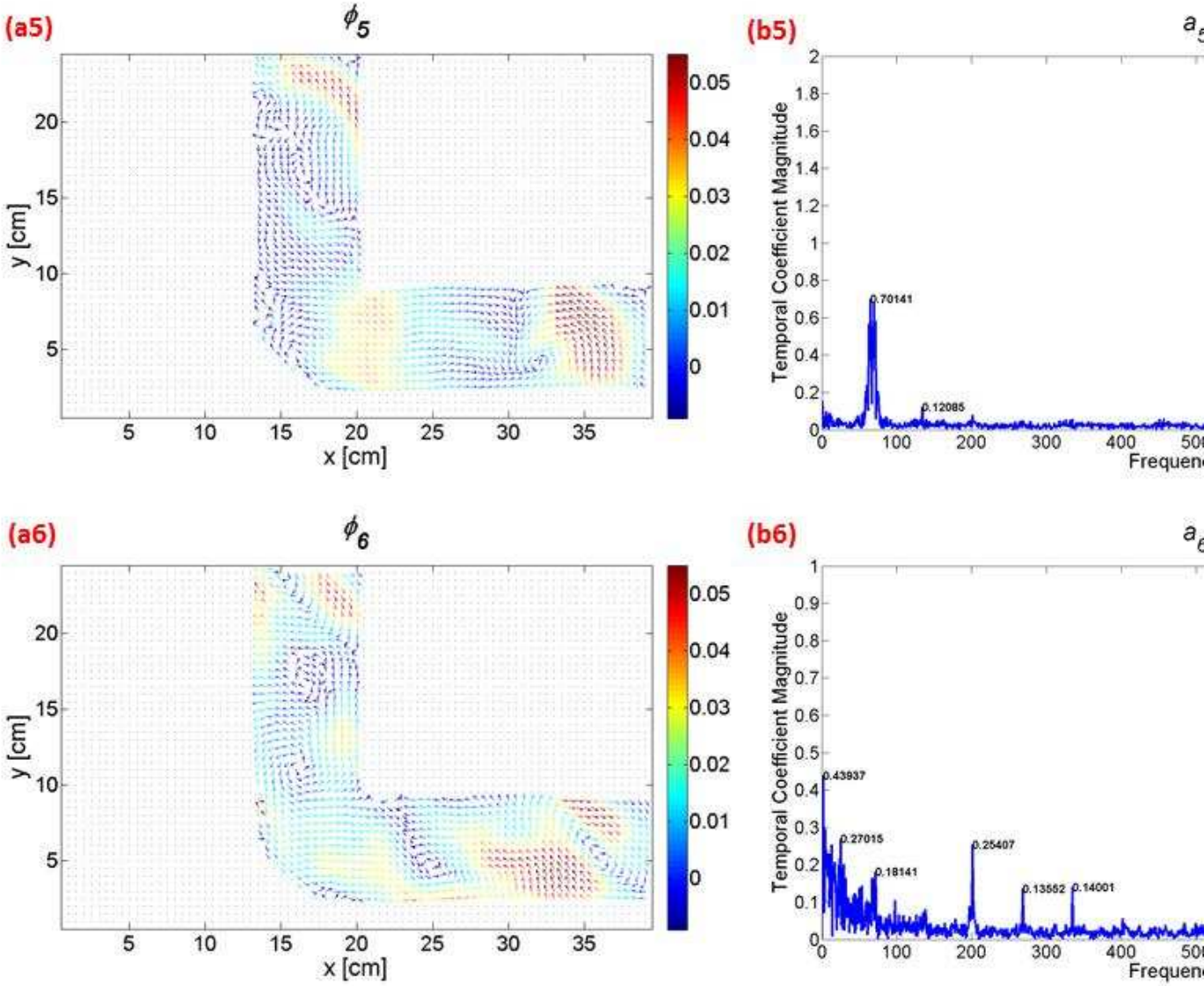

Figure 6-3, coincides with deductions made regarding the behaviour of the POM from the energy level plots of Figure 6-1 and Figure 6-2.

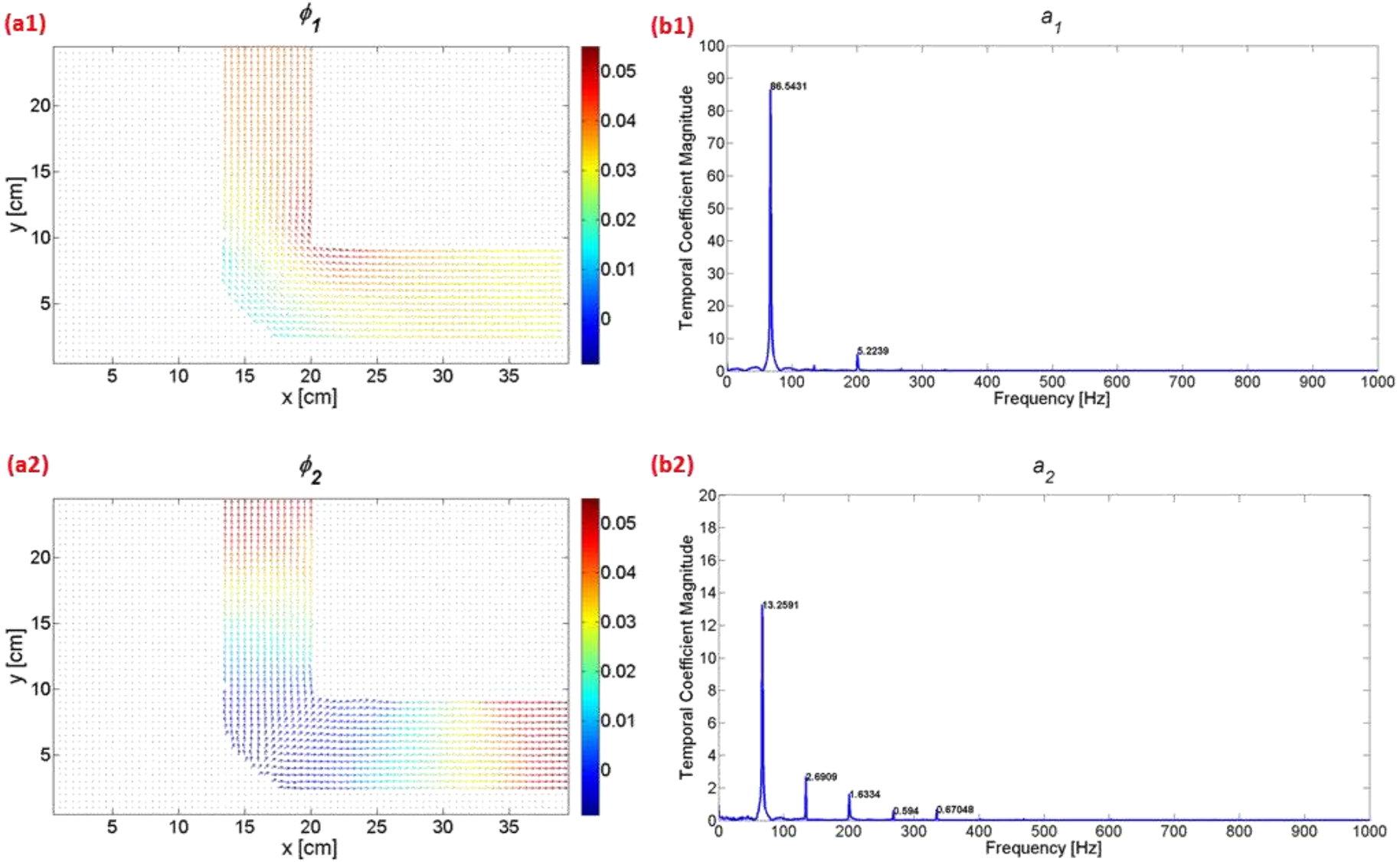

Figure 6-3[*(a)-(b)*]: For caption see pg.168.

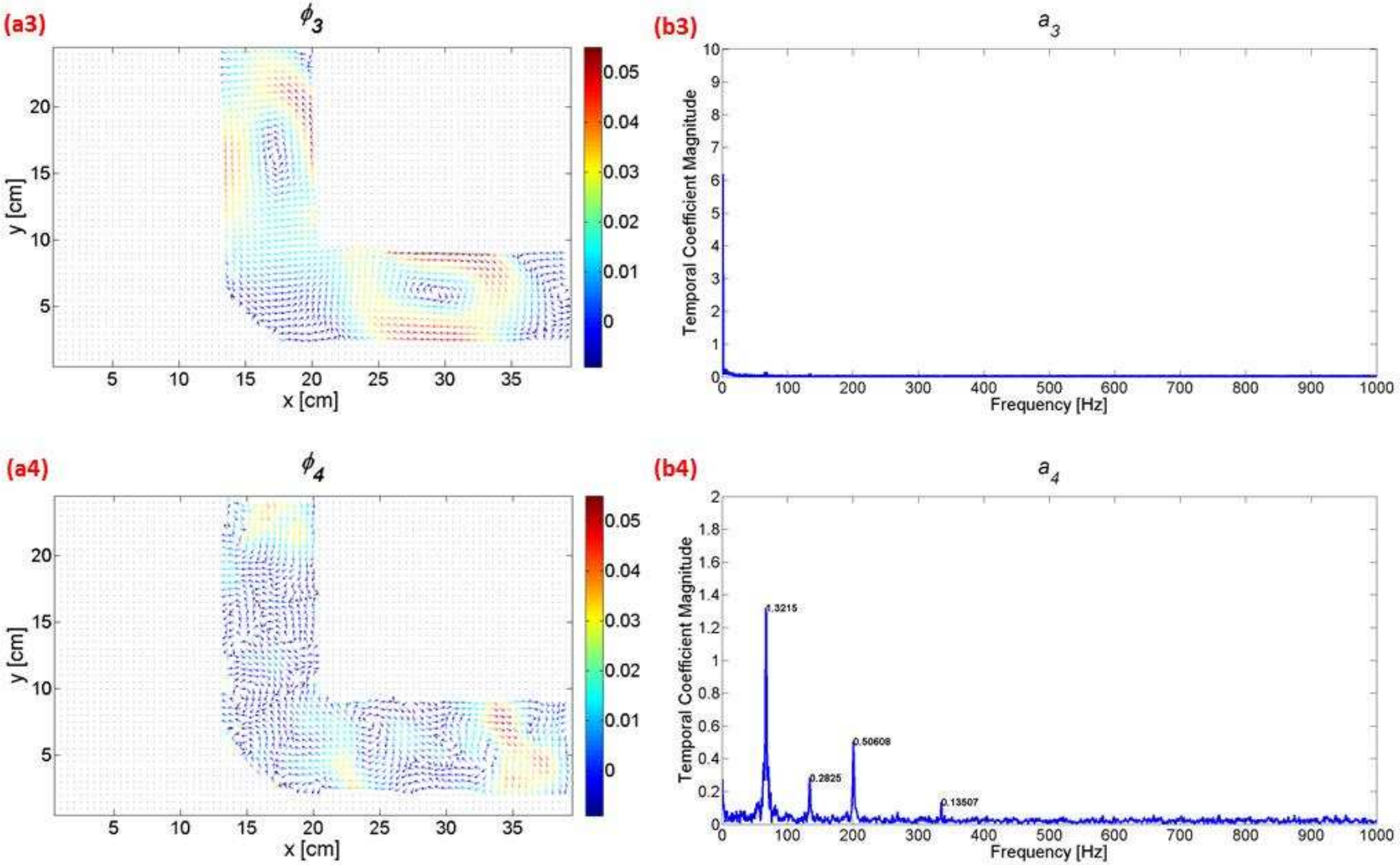

Figure 6-3[*(c)-(d)*]: For caption see pg.168.

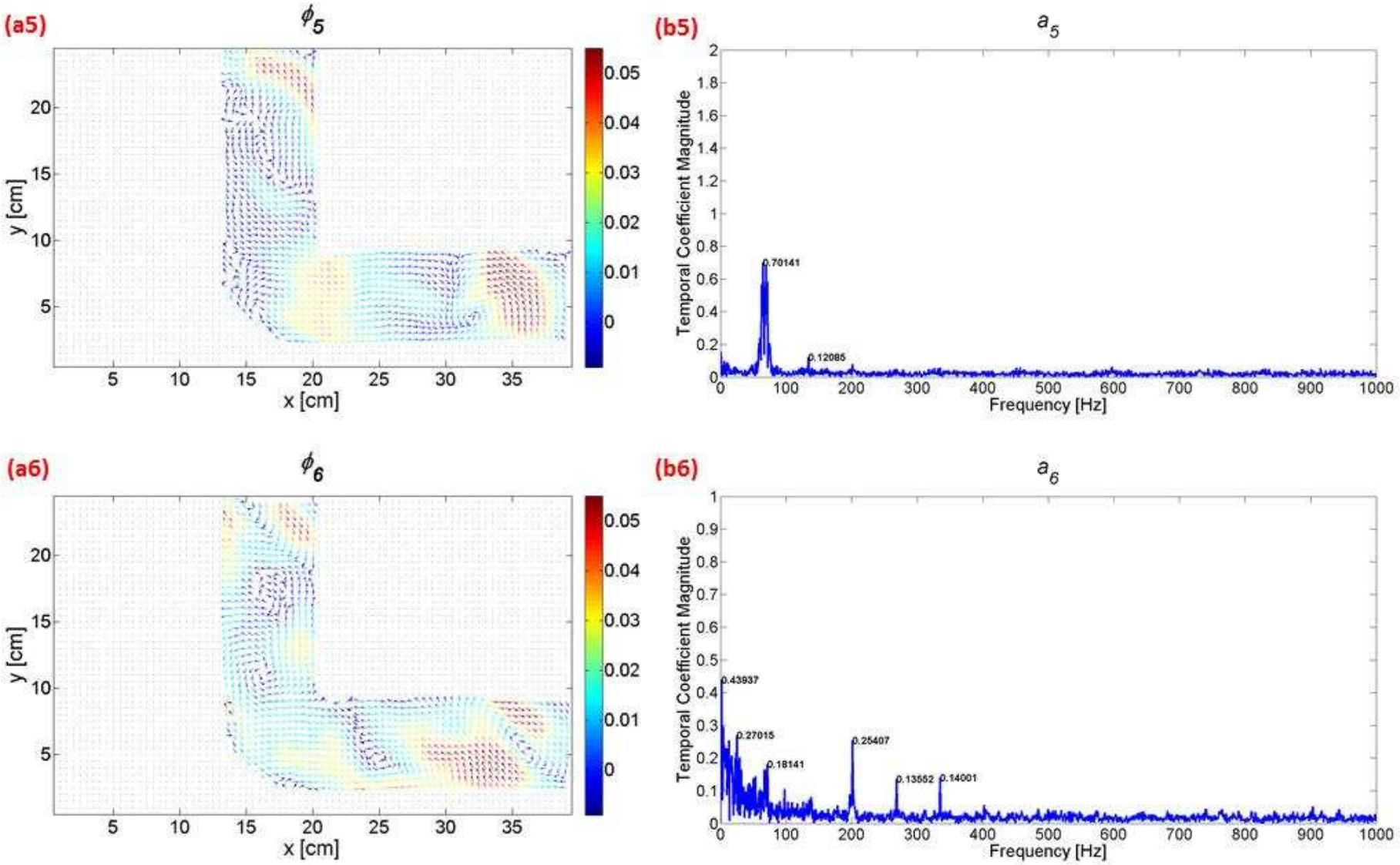

Figure 6-3: The First 6 Proper Orthogonal Modes (a1)-(a6) with their corresponding temporal coefficient (b1)-(b6) shown in terms of their spectral analysis for a Sharp Bend duct with acoustic excitation at 67Hz. The velocity amplitude of the vectors are represented by colours indicated by the colour scale (velocities given in ms^{-1}).

POM 1 and POM 2 cooresponding to Figure 6-3(1) & Figure 6-3(2) are shown to be pure oscillatory component (that has a high spectral peak corresponding to the investigated frequency) and a zero mean flow component. Both of these also show the highest kinetic energy content corresponding to the eigenvalue plots of Figure 6-1 and Figure 6-2. As such both POM 1 and 2 are taken to be the Primary Oscillating flow components these investigations. Sub-chapter 6.1 and 6.2 further discussed the properties of POM 1 and 2.

POM 3 corresponding to Figure 6-3(3) shows the same distinct pair of counter-rotating vortices as was previously observed using the mean flow and phase aliasing analysis. The spectral analysis shows that this Mode is a mean flow with no oscillatory component. This matches the result of Figure 6-2 in which this mode shows the lowest RMS energy content within the first 6 Modes. POM 3 however, has the highest kinetic energy content after POM 1 and 2 (Figure 6-1). The characteristics of POM 3 reaffirms the theory that these pair of counter-rotating vortices corresponds to the main acoustic energy dissipative mode. POM 3 is further discussed in sub-chapter 6.3.

The subsequent Modes after POM 3 corresponds to the smaller scale weaker secondary circulation. The formation of these smaller and weaker circulation are based on the energy cascaded from POM 3. The spectral analysis of POM 4, 5 and 6 corresponding to Figure 6-3(4-6) shows that these circulation are quasi-steady in nature containing both a mean component and an oscillatory component corresponding to the harmonics of th investigated frequency. This may explain why the phase aliasing technique was unable to detect the flow characteristiscs of these secondary components. The ability of the POD technique to educe these cascaded secondary flow component allows for a more complete investigation of the acoustic energy loss mechanism and will be further discussed in sub-chapter 6.4.

6.1 Primary Oscillating POD Modes [POM 1 and POM 2]

The Proper Orthogonal Decomposition analysis was able to separate out the different flow components into distinct Proper Orthogonal Modes. Based on the observation made from Figure 6-1, Figure 6-2 and

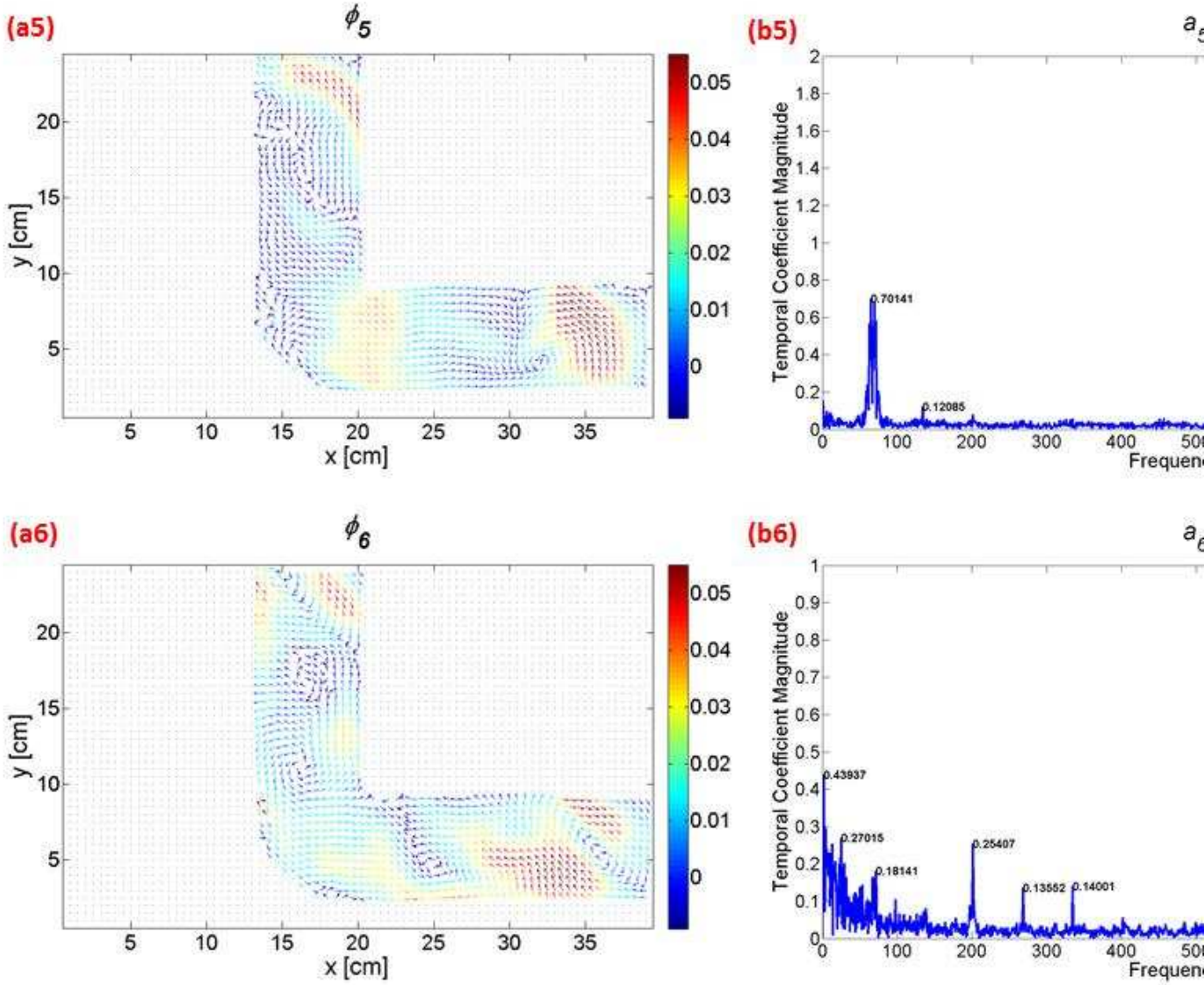

Figure 6-3 ,it can be deduced that POM 1 and POM 2 represent the primary oscillating components of the investigated wave. Both of these modes have large and distinct spectral peaks corresponding to the investigate frequency and its harmonics in the temporal coefficient, $a_i(f)$, frequency spectrum. These POMs also have matching high percentage kinetic energy and RMS energy levels based on their respective eigenvalue plots.

The PIV measurement was conducted via the Phase Locking recording technique. As such, it is possible to represent the temporal coefficients of these primary oscillating modes as single, phased averaged, oscillating period. Figure 6-4 shows the phased averaged temporal coefficient, a1 and a2. The amplitude vs. time waveform for both modes is represented clearly here. POM 1 shows a sine waveform with minimal harmonic distortion whereas POM 2 shows a negative cosine waveform with harmonic distortion. This is in accordance with the spectral temporal coefficient results in

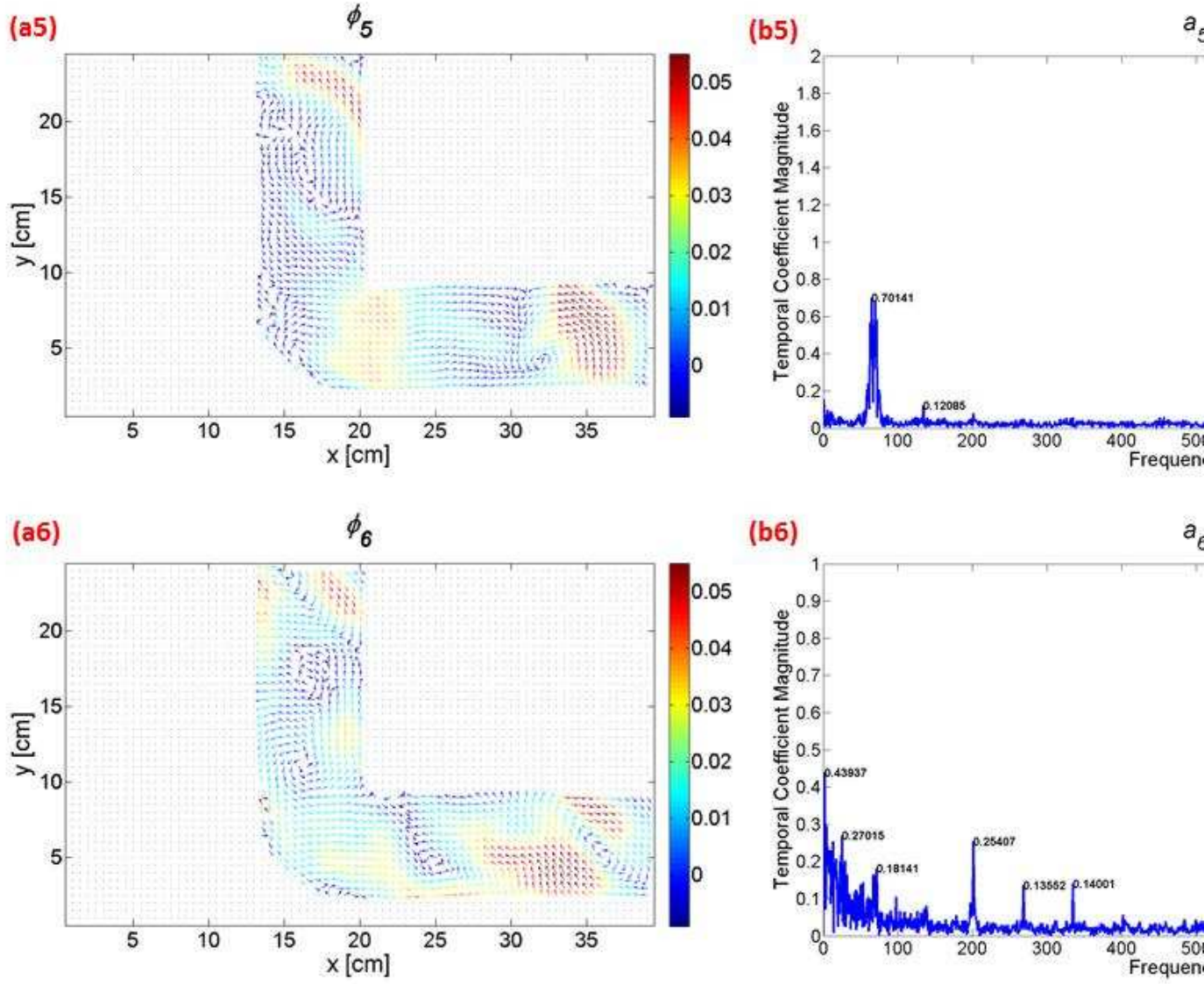

Figure 6-3 (b1) and (b2). Both POMs are shown to be pure oscillating modes about a zero mean and are approximately 90° out of phase with each other.

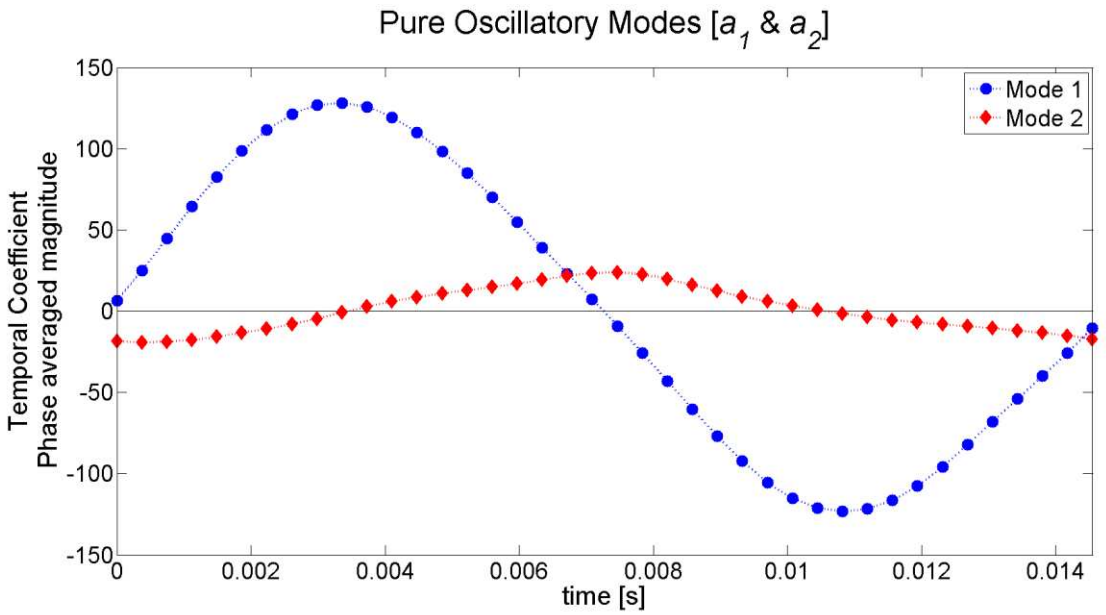

Figure 6-4: Phased average Temporal Coefficient for POD Modes 1 & 2 for Acoustic Excitation of 67Hz

The POD technique also allows the time step velocity vector field visualisation of each POM modes. The phased average oscillation of POM 1 and POM 2 are represented through 10 equally separated timesteps in Figure 6-5 and Figure 6-6 respectively. There are several deductions that can be made from observing the behaviour of these primary oscillating modes. It can be observe from POM 1:

1. The oscillation in the axial direction shows characteristics of a standing wave quarter wavelength system, where a slightly higher amplitude at the upstream of the bend and lower amplitude towards the downstream of the bend.

2. The higher axial oscillating velocity is concentrated close to the inner wall of the bend, causing a skewed axial oscillating velocity profile along the bend. This shows that the centripetal and not the centrifugal force dominate the acoustic flow through the bend.

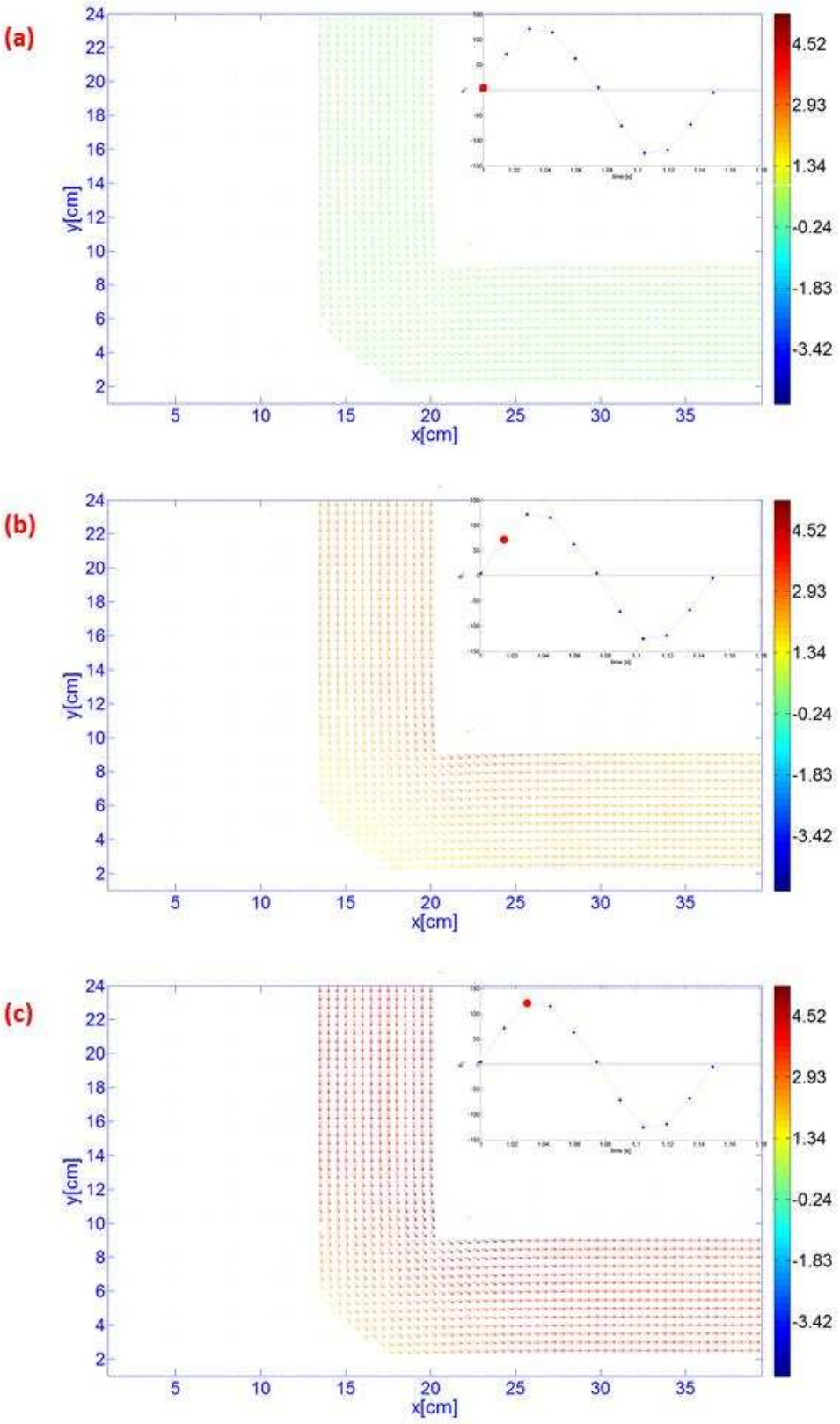

Figure 6-5[*(a)-(c)*]: For caption see pg.174.

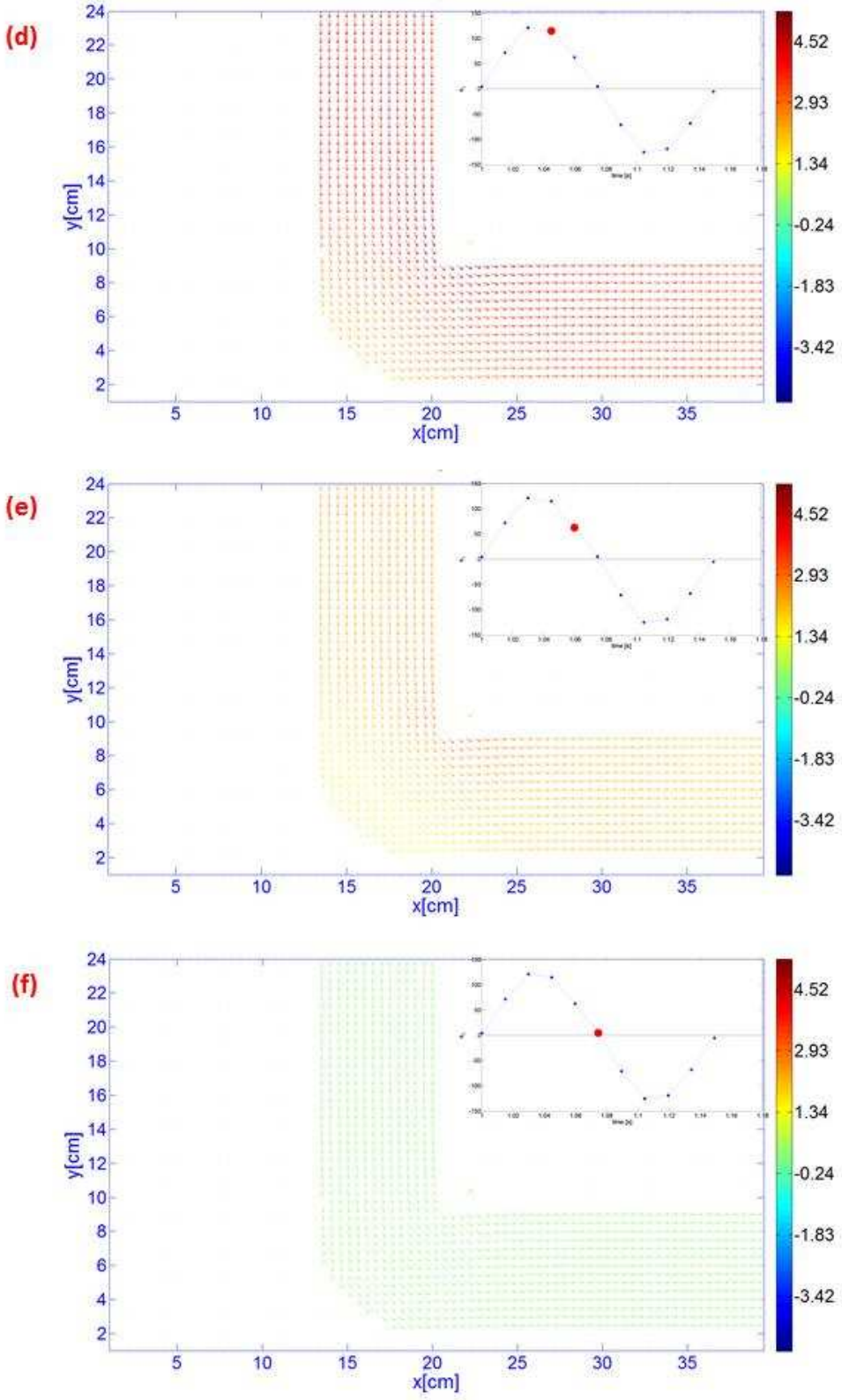

Figure 6-5[*(d)-(f)*]: For caption see pg.174.

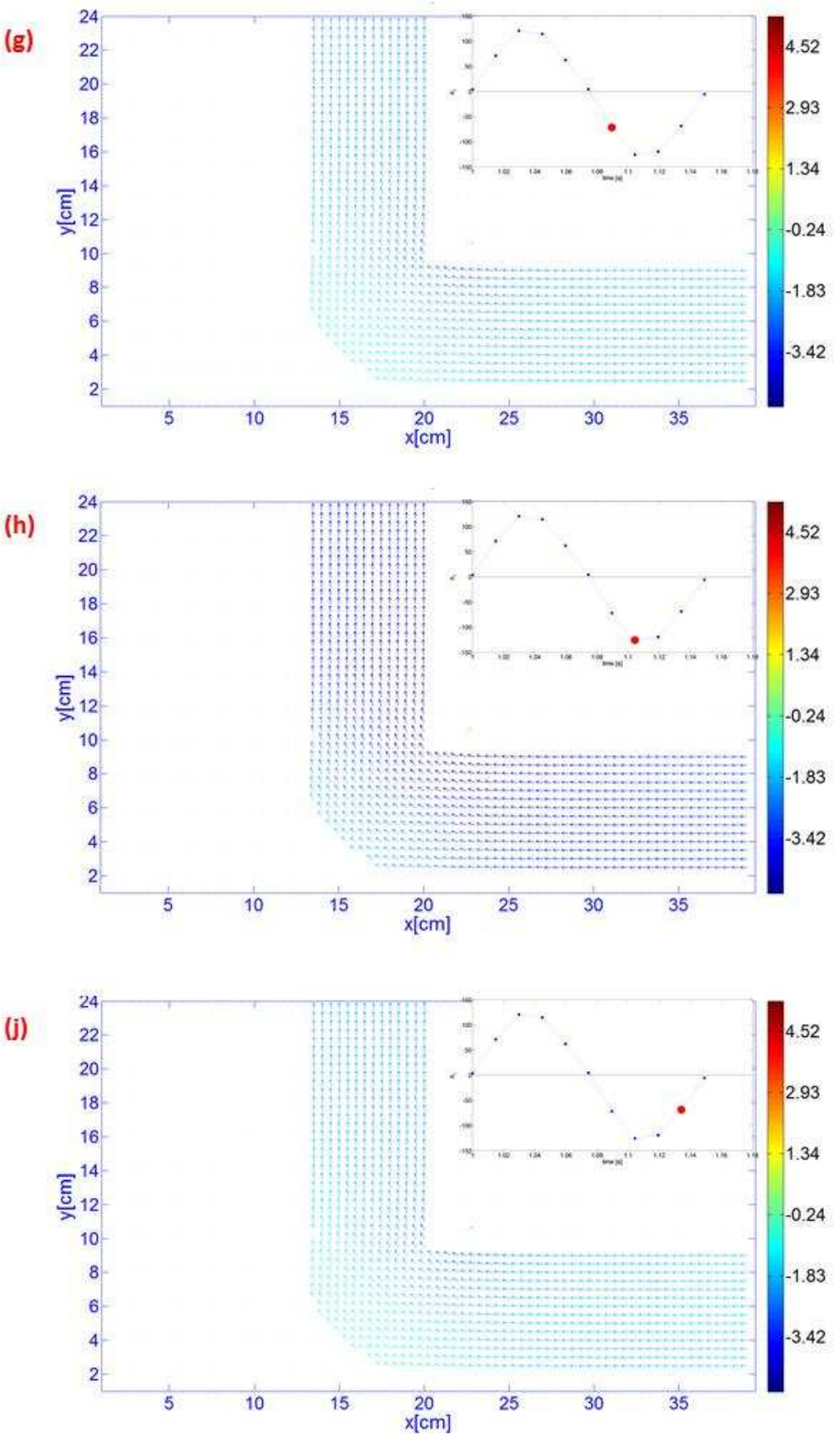

Figure 6-5: The timestep oscillation of POM 1 in a period under 200We excitation at 67Hz in the A1-Bend. The velocity amplitude of the vectors are represented by colours indicated by the colour scale (velocities given in ms^{-1})

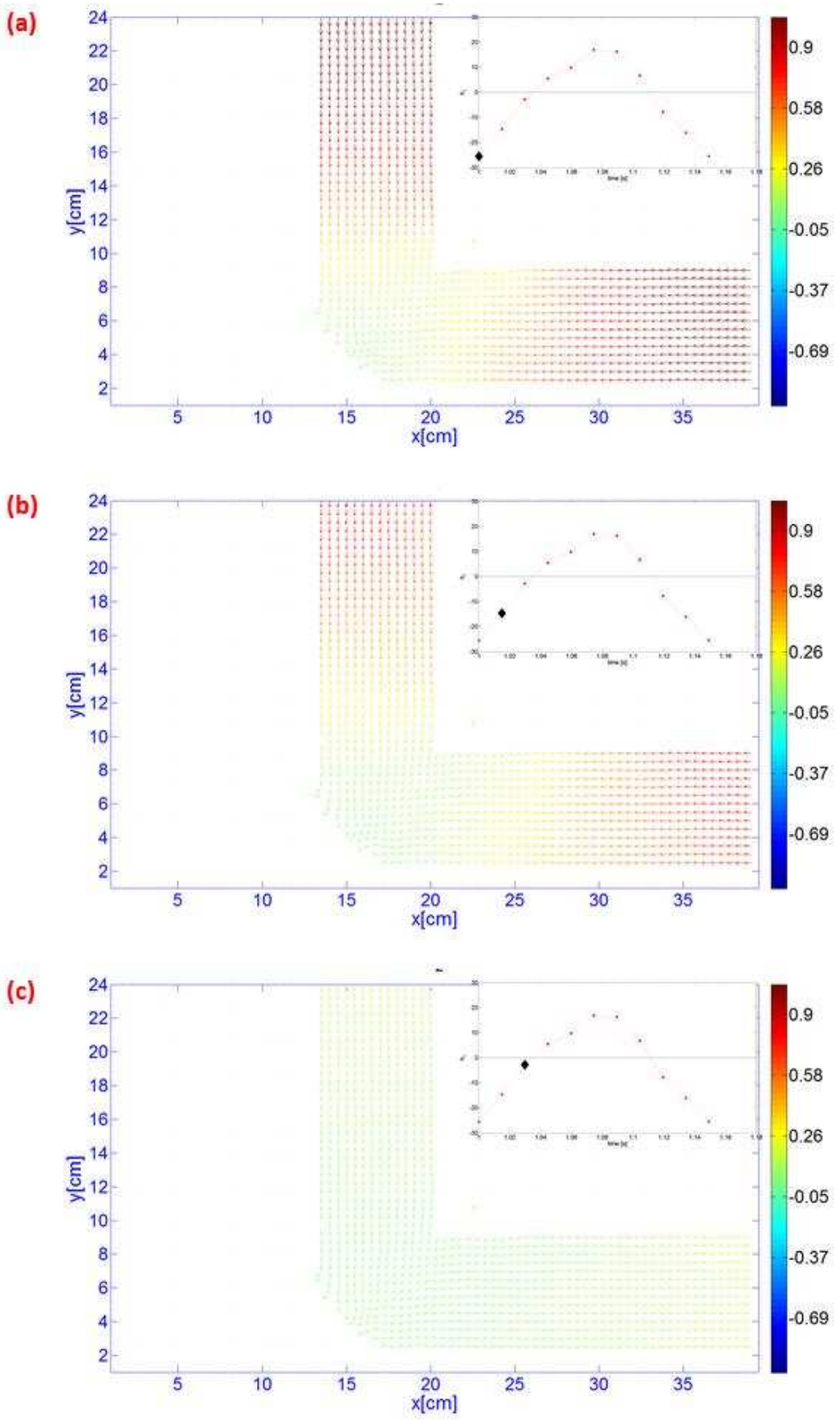

Figure 6-6[*(a)-(c)*]: For caption see pg.177.

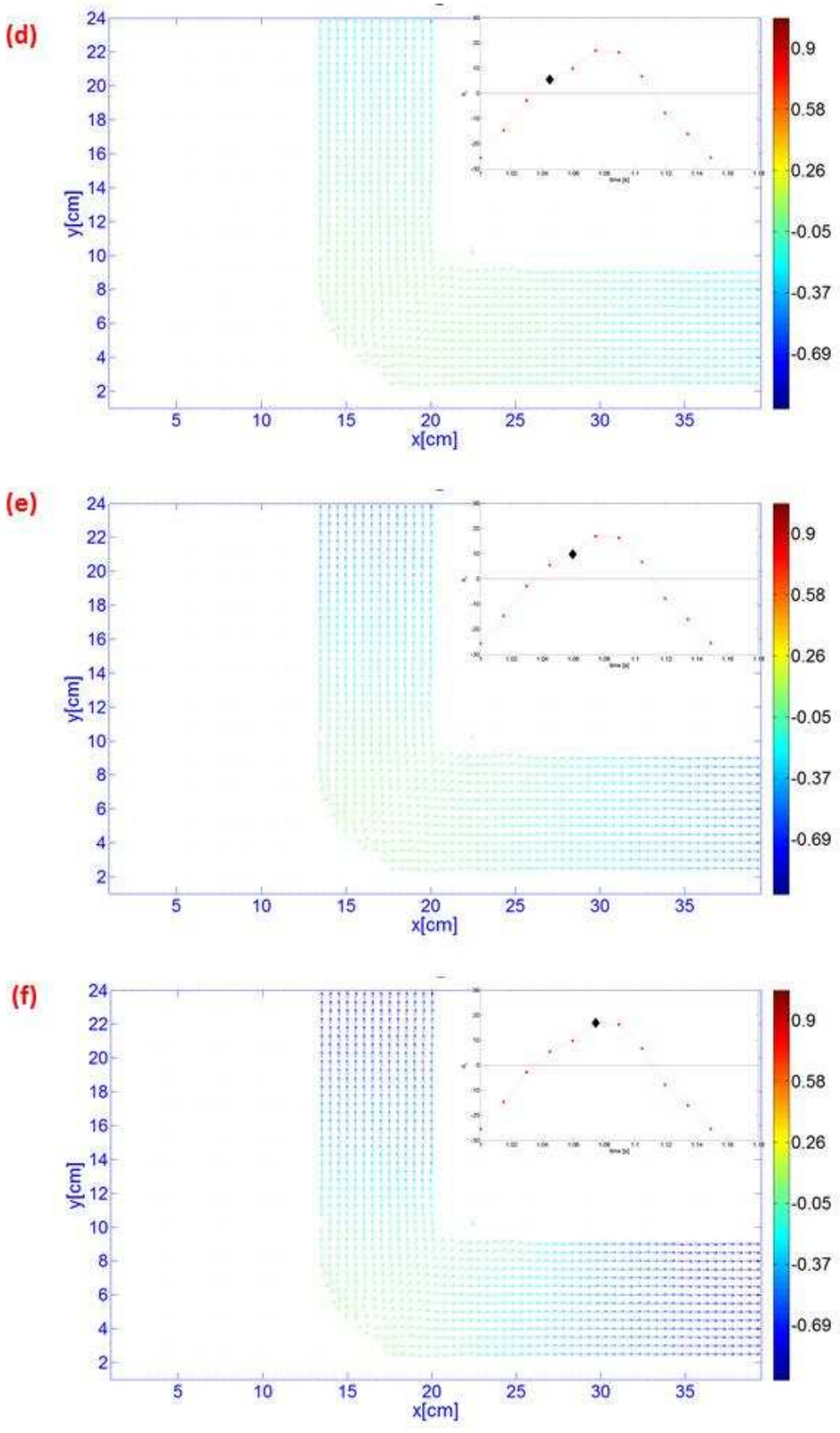

Figure 6-6[*(d)-(f)*]: For caption see pg.177.

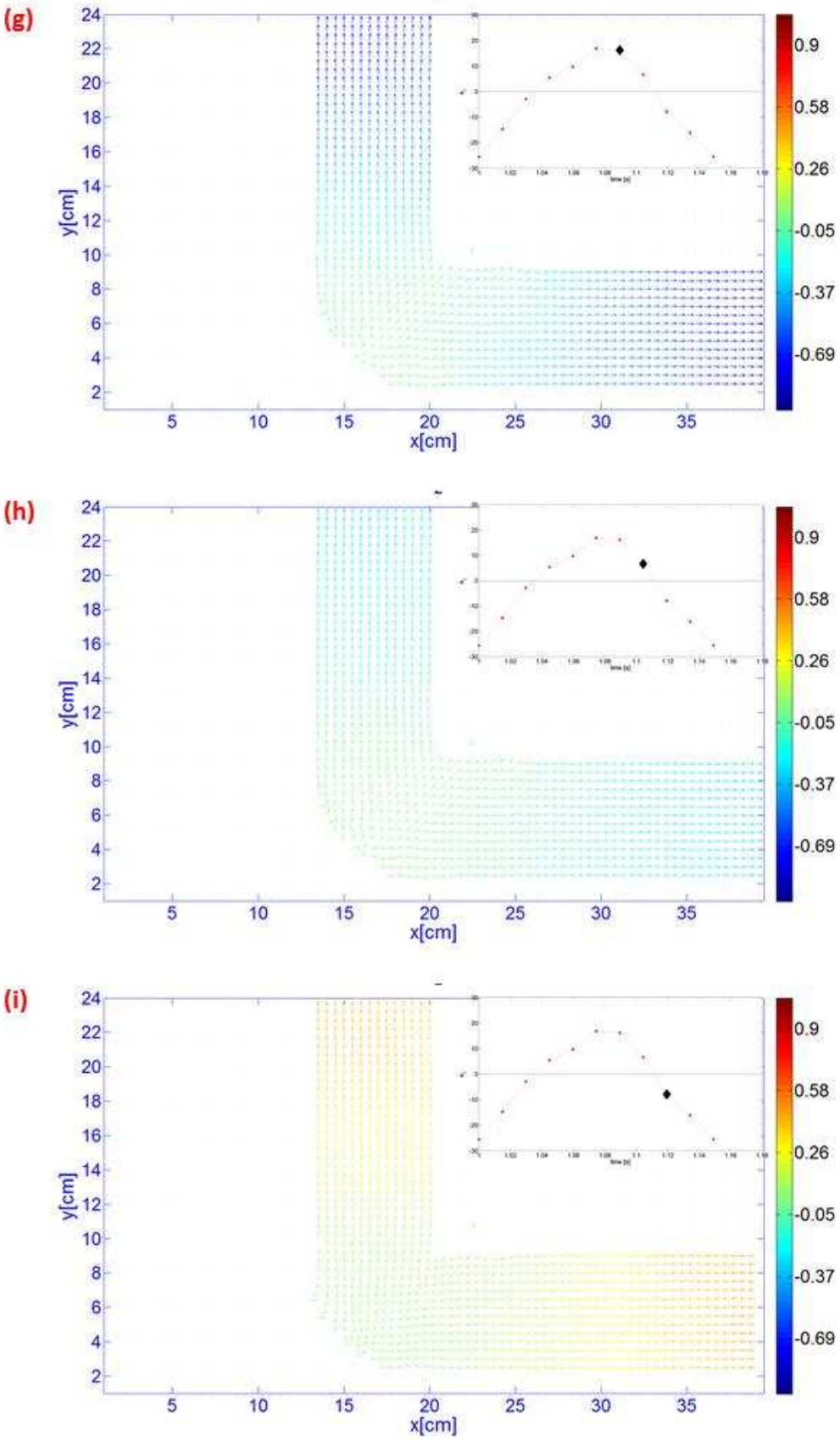

Figure 6-6: The timestep oscillation of POM 2 in a period under 200We excitation at 67Hz in the A1-Bend. The velocity amplitude of the vectors are represented by colours indicated by the colour scale (velocities given in ms^{-1})

The oscillating characteristics of POM 2 are vastly different from POM 1. The main observations that can be made from POM 2 are:

1. The oscillation shows characteristics of a half wavelength system. The acoustic velocity node appears to be right in the middle of the bend. The oscillating amplitude increases with the axial distance away from the node, both in the upstream and downstream directions.
2. The axial oscillating velocity profile in the duct bend is shown to be that of a plane wave mode of propagation, in both the straight and curved sections of the bend. POM 2 could probably be the representation of the acoustic propagation through the duct in the absence of the curve bend and thus the centripetal effects shown in POM 1.

It has previously been shown in

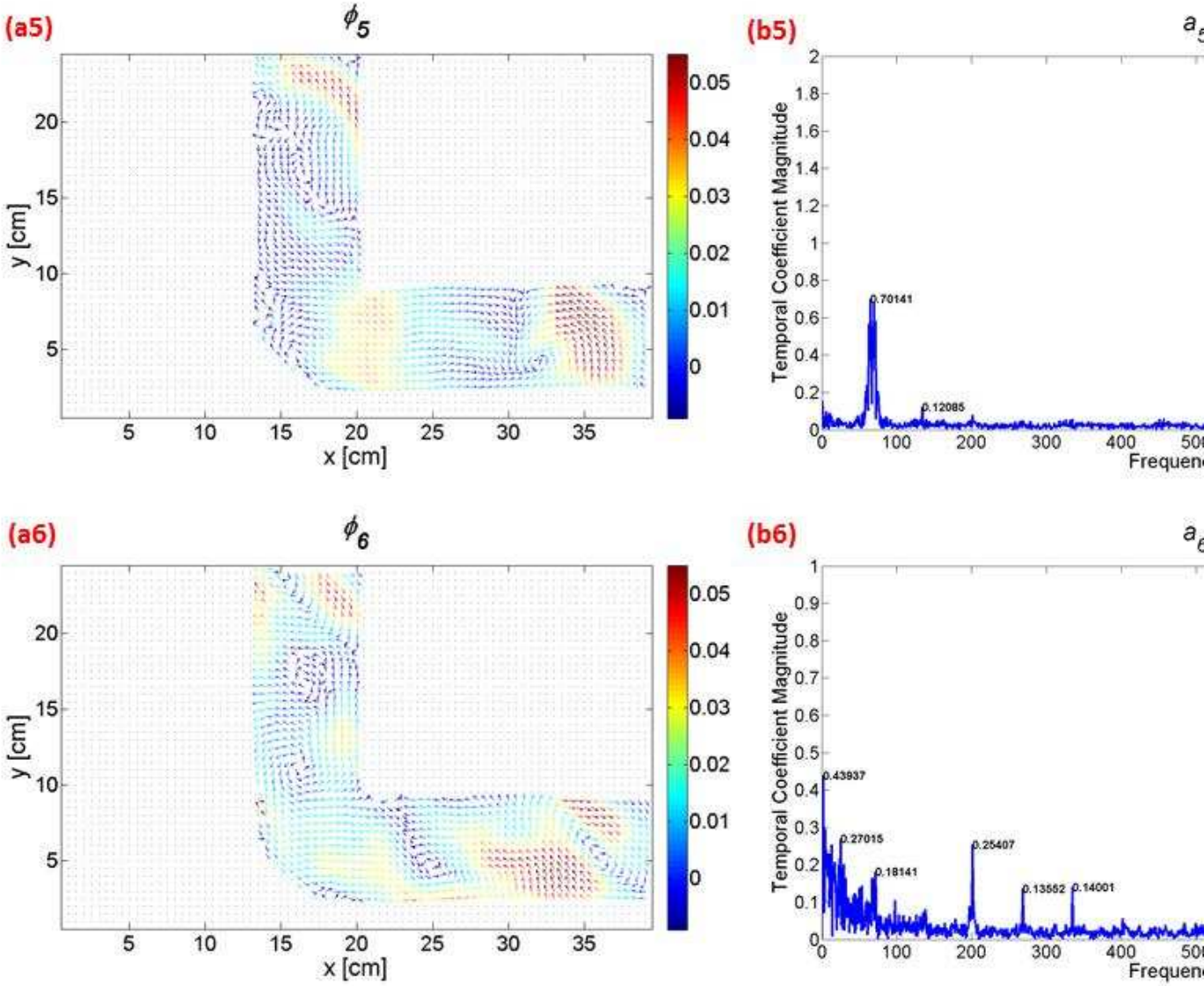

Figure 6-3, that there are sufficient timesteps in order to conduct a sufficiently accurate frequency spectral analysis. As such, since it is also possible to obtain the time varying component of the different points in the velocity vector field, the VWD technique can be used to further analyse the characteristics of these individual oscillating POD modes. The VWD technique has been carried out on the straight section of the bend prior (upstream) and after (downstream) the curved section. The VWD results for POM 1 and POM 2 are shown respectively in Figure 6-7 and Figure 6-8.

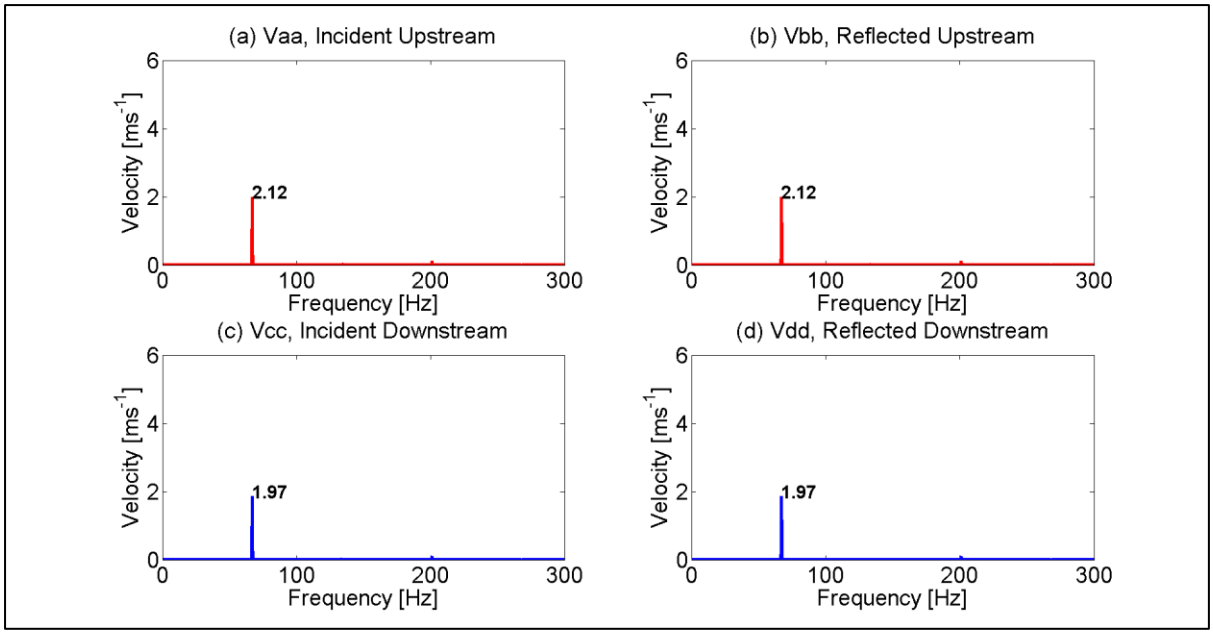

Figure 6-7: The VWD result of POM 1

The VWD results for both POM 1 and POM 2 shows an equal amplitude peak for the incident and reflected component for each of the measured sections. Since both the investigated upstream and downstream wave components of the two POD modes have $SWR = \infty$, it can be deduced that both POD modes are standing wave systems. The VWD spectral result also shows that POM 1 has only a minute peak in the 3rd harmonics (201Hz) while POM 2 has more distinct peak in the 2nd and 3rd harmonic (134Hz and 201Hz). These results verify the observations made in Figure 6-5 and Figure 6-6. It also explains the waveform distortion seen in Figure 6-4.

The VWD result also shows an overall reduction in standing wave amplitude as the wave propagates through the bend's curve section. By comparing the upstream incident component to the incident downstream component, there is an approximate 7% reduction in the wave amplitude for POM 1 and 23% reduction for POM 2.

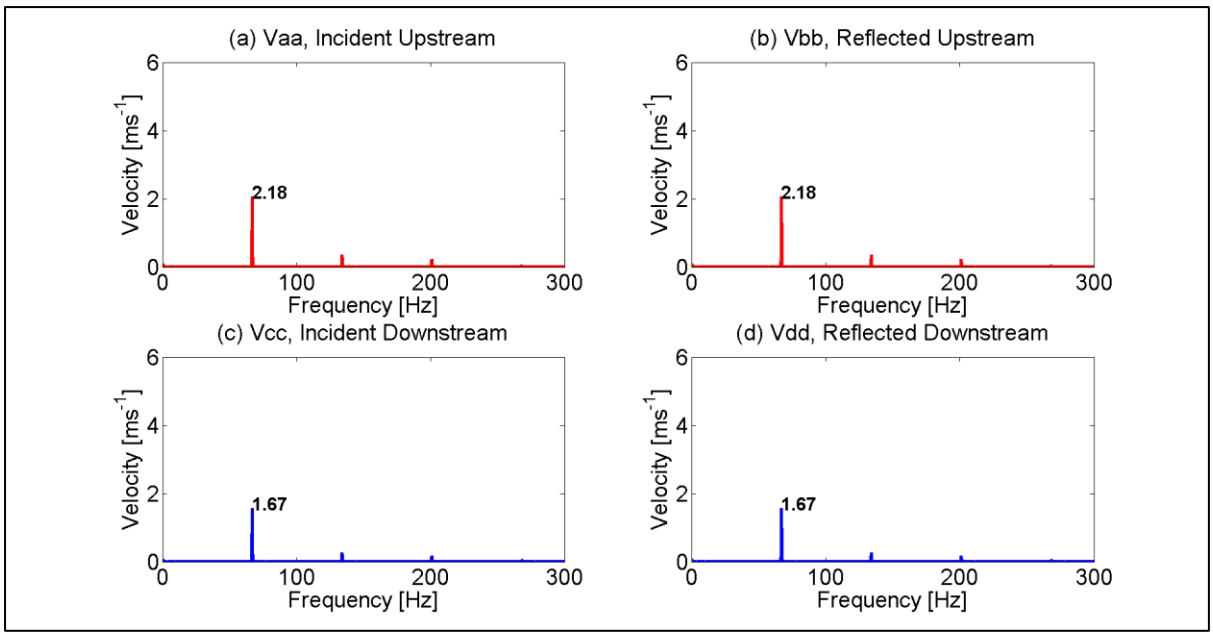

Figure 6-8: The VWD results for POM 2

The same primary oscillating flow characteristics for POM 1 and 2 is observed across the 5 investigated curved duct bends. The orthonormal basis function, ϕ, that illustrates the oscillating behaviour of POM 1 and 2 in each of the investigated curve duct bends are shown respectively in Figure 6-9 and Figure 6-10.

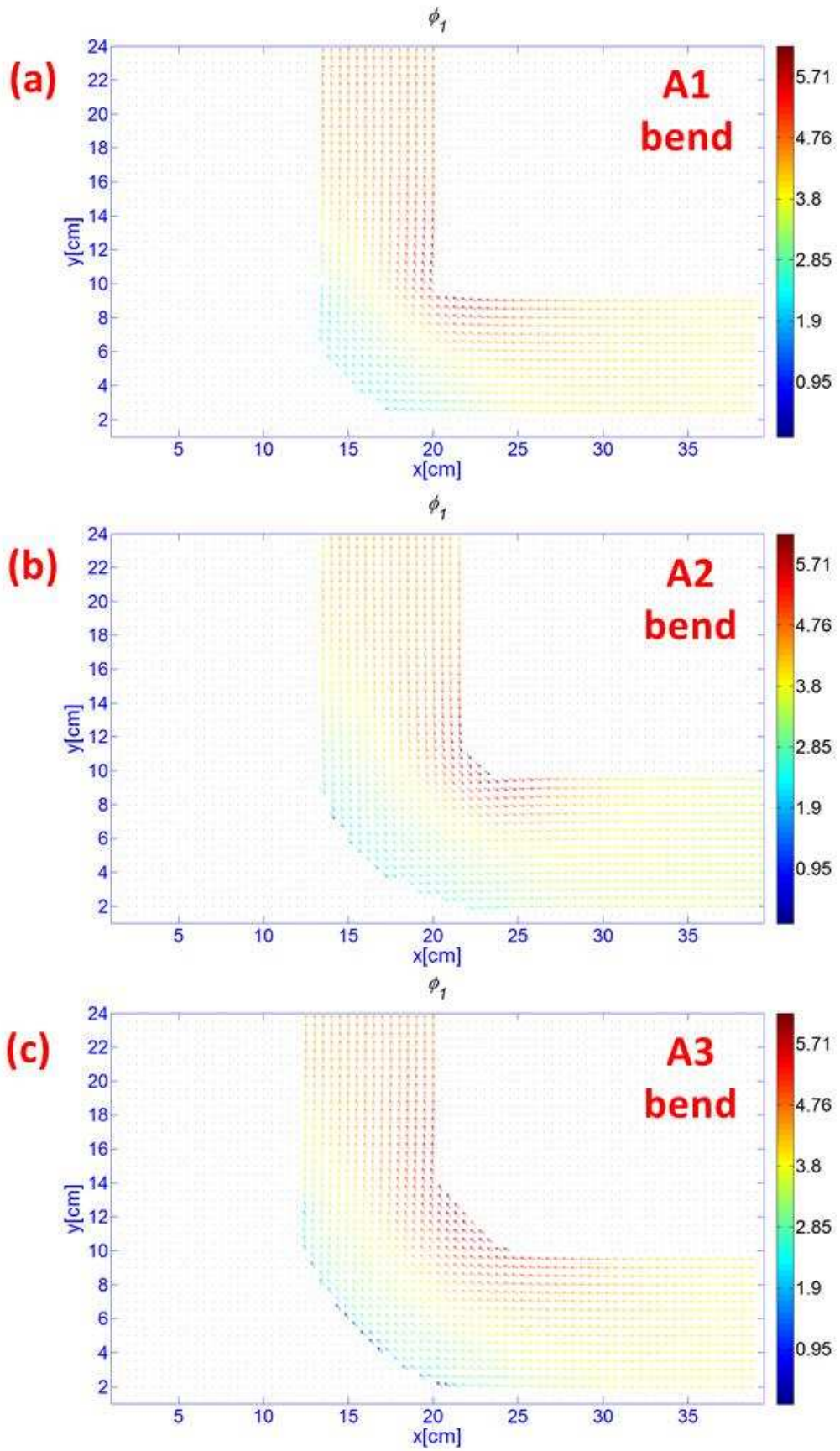

Figure 6-9[*(a)-(c)*]: For caption see pg.181.

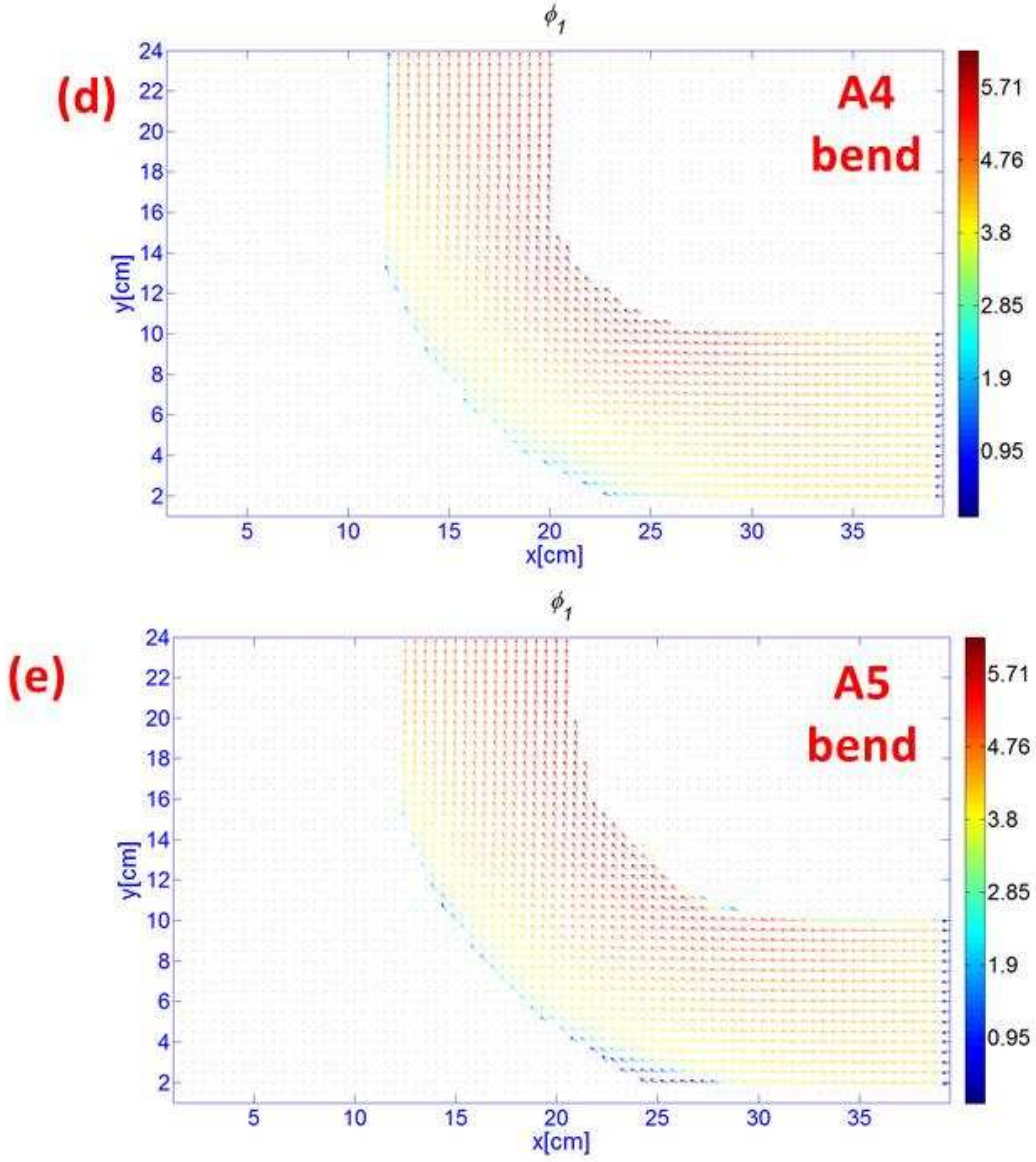

Figure 6-9: **The Orthonormal basis functions of POM 1 for bends A1 to A5 using 67Hz excitation at 200We. The velocity amplitude of the vectors are represented by colours indicated by the colour scale (velocities given in ms^{-1})**

The same quarter wavelength oscillating characteristics is observed for POM 1 across the 5 investigated curved duct bends. The higher oscillating axial velocity is shown to be concentrated on the inner wall of the curvature for all cases. POM 1 can be taken to represent the oscillating flow component of the primary oscillation that is influenced by the apparent centripetal affect due to the propagation through the duct curvature.

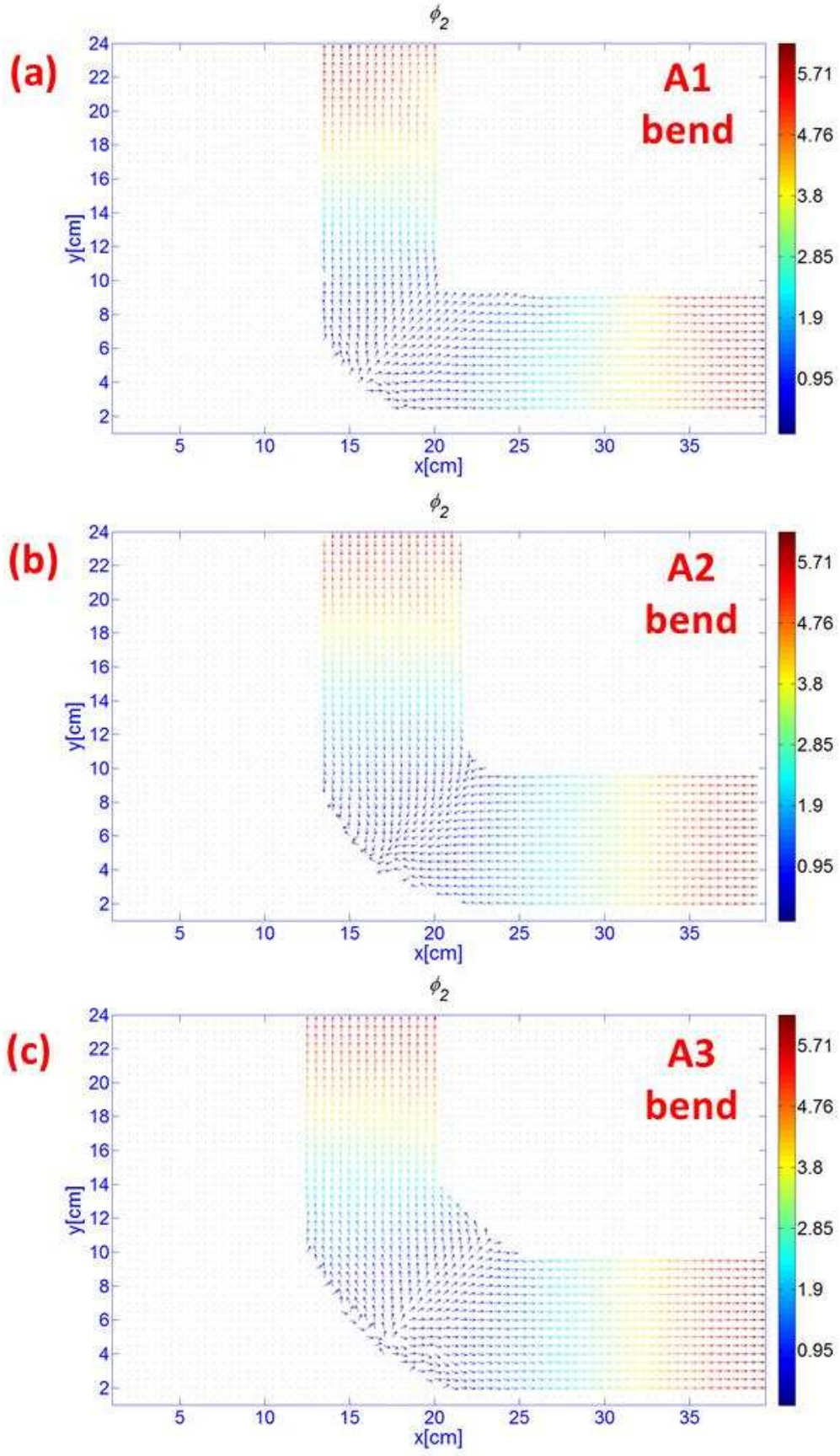

Figure 6-10[*(a)-(c)*]: For caption see pg.183.

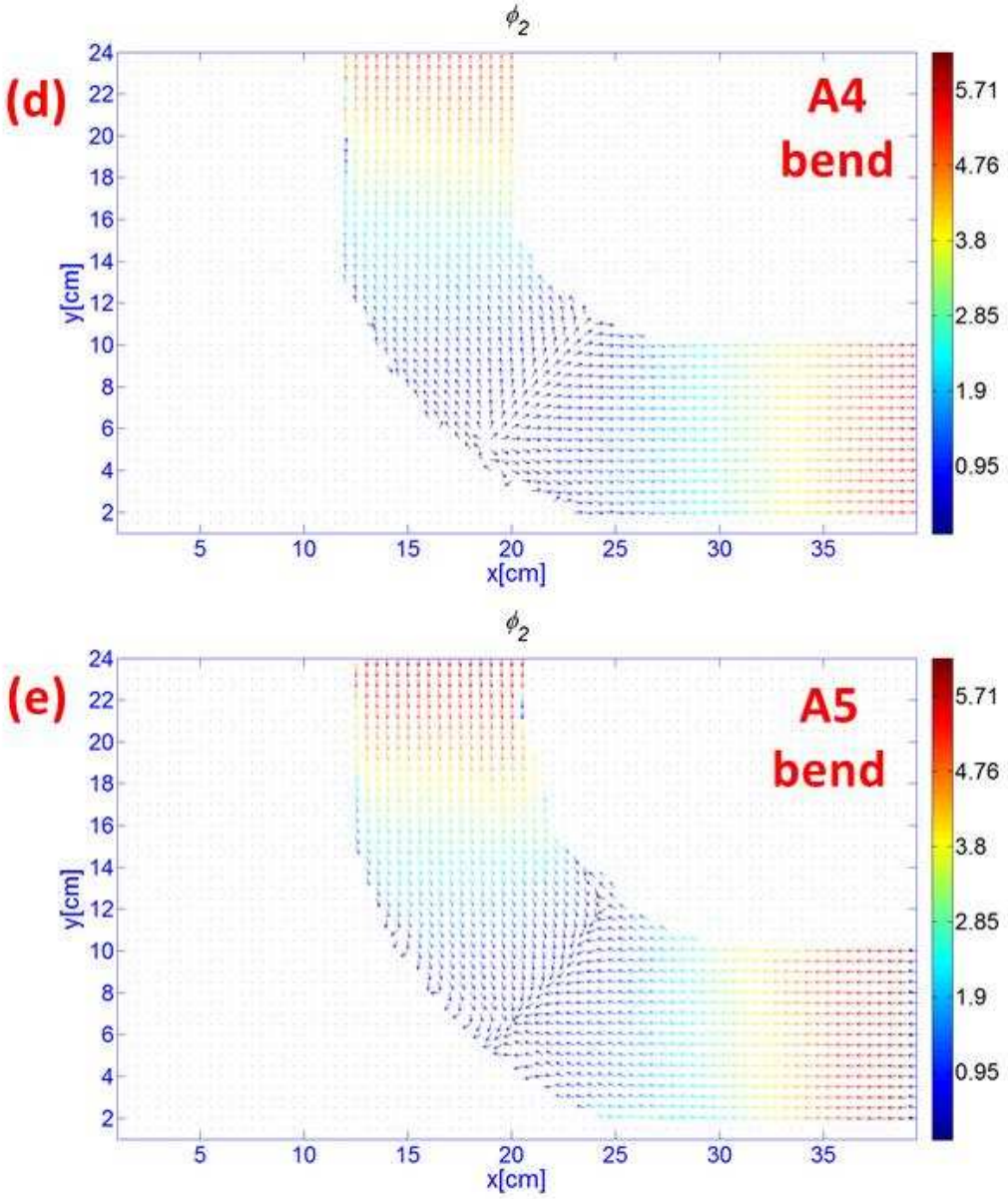

Figure 6-10: The Orthonormal basis functions of POM 2 for bends A1 to A5 using 67Hz excitation at 200We. The velocity amplitude of the vectors are represented by colours indicated by the colour scale (velocities given in ms^{-1})

POM 2 exhibits the same half wavelength oscillating characteristics across the the 5 investigated duct bends. In all cases the acoustic node is shown to be position in the mid section of the duct bend's curvature. POM 2 is shown to oscillate in the plane wave mode of propagation. POM 2 can thus be taken to represent the oscillating flow component of the primary oscillation that is not influenced by the radius of curvature of the duct bend.

6.2 Primary Oscillation [Linear Combination POM 1 – 2]

It is interesting to note that the POD technique from this investigation resulted in a pair of POM to represent the primary oscillating component of the system. Literature have shown that previous POD investigations on oscillating flows system have resulted in only a single POM to represent the primary oscillating component[195, 196]. The difference in number of POM taken to represent the primary oscillating component is attributed to the use of a predominant travelling wave system for this investigation as compared to the standing wave system used in previous works. The VWD technique has previously proven that each individual POM is only able to represent a standing wave oscillation. This is in accordance with the fundamentals of the POD technique, where each velocity vector for an oscillating POM is a product of a fixed spatial orthonormal basis value, $\phi_i(x,y)$, and a periodic temporal coefficient term, $a_i(t)$. As such, each point in the investigated velocity vector field will have fixed oscillating amplitudes for a given oscillating POM. A velocity vector field where the oscillating amplitude is fixed for a given position is characteristics of pure standing wave system.

Thus, in order for the POD technique to represent a travelling wave oscillating system, it would require the linear combination of two or more standing wave POMs to construct a travelling wave system through superposition. In this investigation, the POD analysis results in an orthonormal pair of standing wave oscillating modes (POM 1 and 2). To verify this, the linear combination of POM 1 and 2 were computed using equation:

$$\mathbf{POM\ 1-2}_{\boldsymbol{Primary\ Oscillation}}(x,y,t) = a_1(t)\phi_1(x,y) + a_2(t)\phi_2(x,y) \tag{6.2}$$

The phased averaged timesteps oscillation of the linear combination of POM 1 and 2 are given in Figure 6-11. The timesteps phased average oscillation shown in Figure 6-11 are of the same phase with those shown in Figure 6-5 and Figure 6-6. Hence, for example, the velocity vectors found in Figure 6-11(a) are actually the summation of the velocity vectors from Figure 6-5(a) and Figure 6-6(a) in accordance to the velocity vectors' respective positions. The oscillation of POM 1-2 shows characteristics of both POM 1 and POM 2 at different phases of the oscillation. In the straight

section upstream and downstream of the bend curvature, the wave is shown to have characteristics of POM 2 of a plane wave mode of propagation. As the wave propagates through the curved section, the influence of the centripetal force on the axial oscillating velocity profile is observed (characteristics of POM 1). The acoustic velocity node is shown to appear twice in an oscillating period (Figure 6-11(a) and (f)). This, together with the varying oscillating amplitude for a fixed position, suggests that the linear combination results in a predominant travelling wave system. The linear combined of POMs 1 and 2 shows similar propagation characteristics as the raw PIV velocity vector measurement shown in Figure 5-3. The VWD technique was also used to quantitatively verify the propagation characteristics of the linear combination of POMs 1 and 2. The VWD results are shown in Figure 6-12. The upstream and downstream components have SWR values of 1.9 and 1.5 respectively. This confirms the formation of a predominant travelling wave system through the linear combination of both standing wave POM 1 and POM 2. The VWD results also show the expected increase in the 2nd and 3rd harmonic peaks as a result of the summation from the two POD modes. Since the linear combination, POMs 1 and 2, is taken to represent the primary oscillating component of the system, it should show very similar characteristics with that of the raw PIV velocity vector measurements (approximately up to a 95% match as in accordance with Figure 6-1). The linear combination of POMs 1 and 2 is also written as POM 1-2.

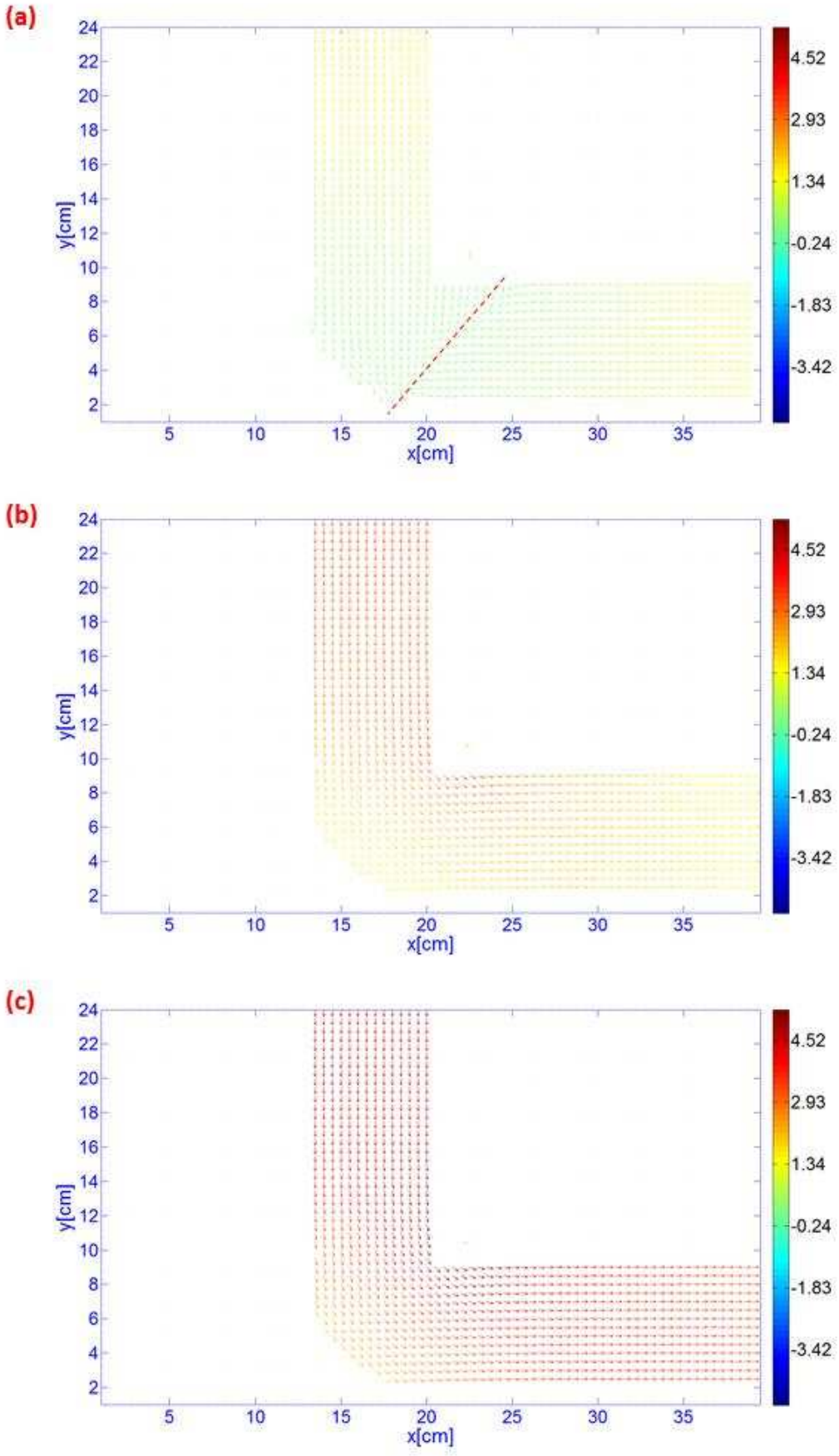

Figure 6-11[*(a)-(c)*]: For caption see pg.188.

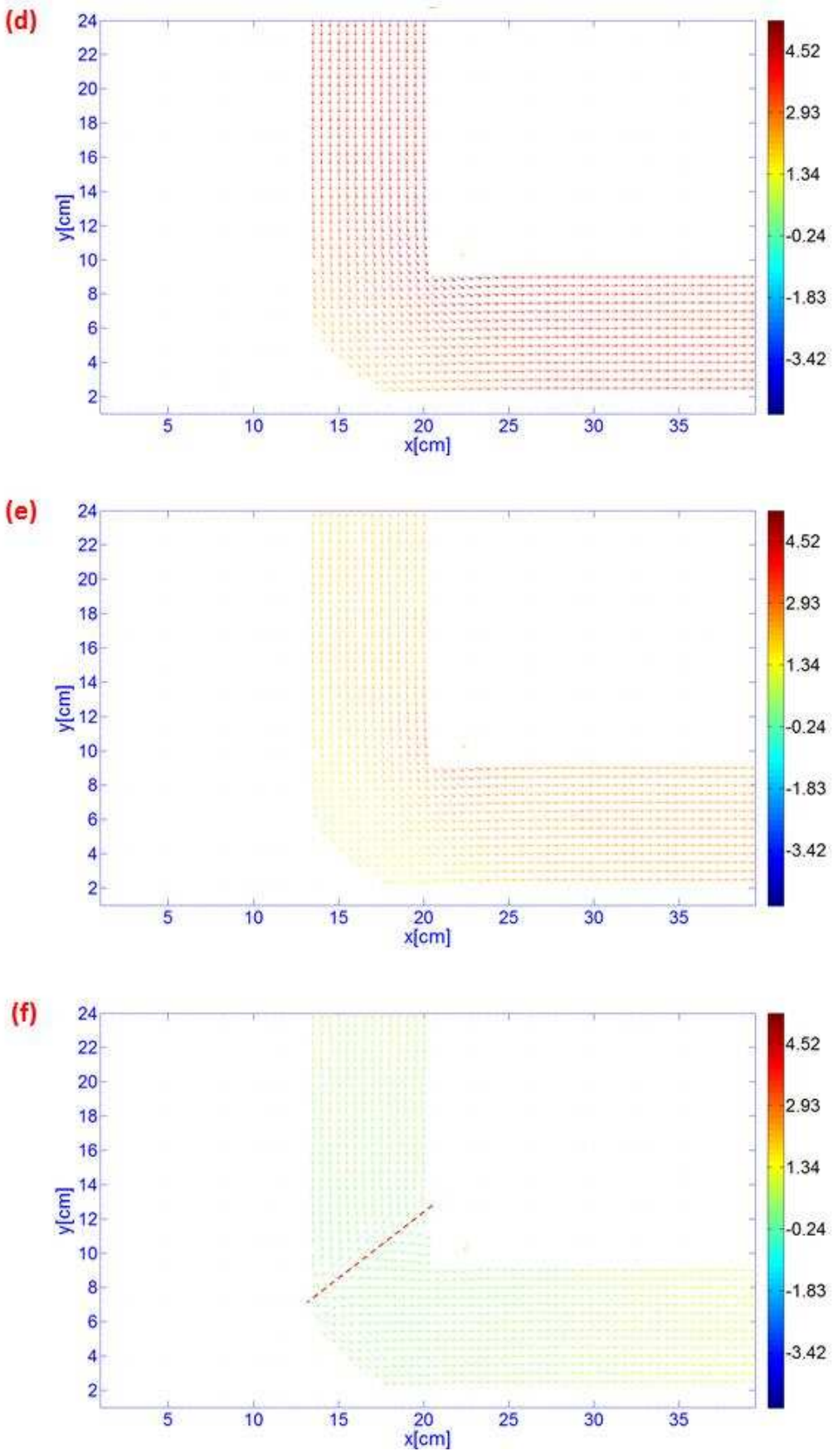

Figure 6-11[*(d)-(f)*]: For caption see pg.188.

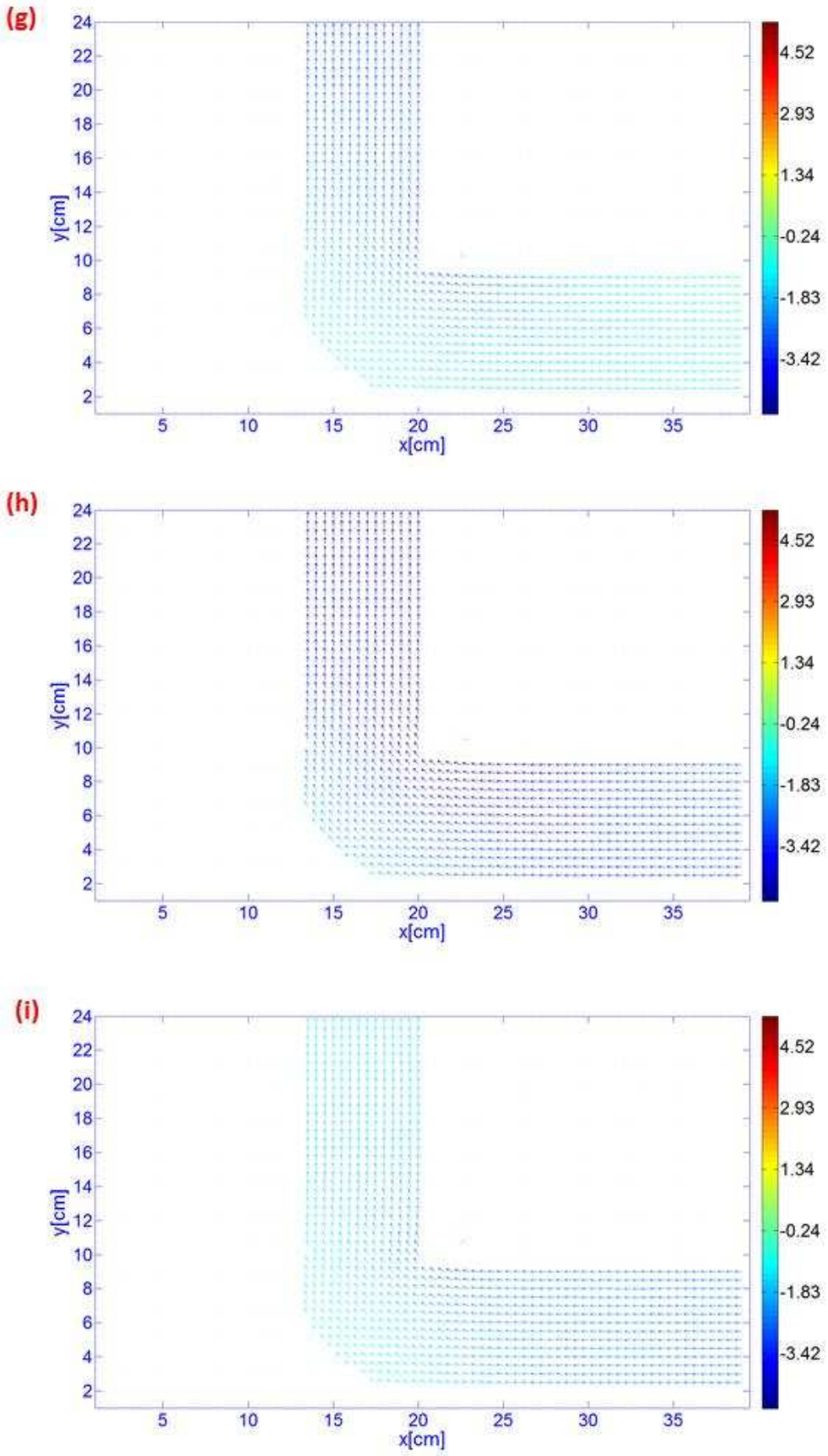

Figure 6-11: The linear combination of POM 1 and 2. The phase for each of the timestep (a)-(i), is the same as those in Figure 6-5 and Figure 6-6. The velocity amplitude of the vectors are represented by colours indicated by the colour scale (velocities given in ms^{-1}).

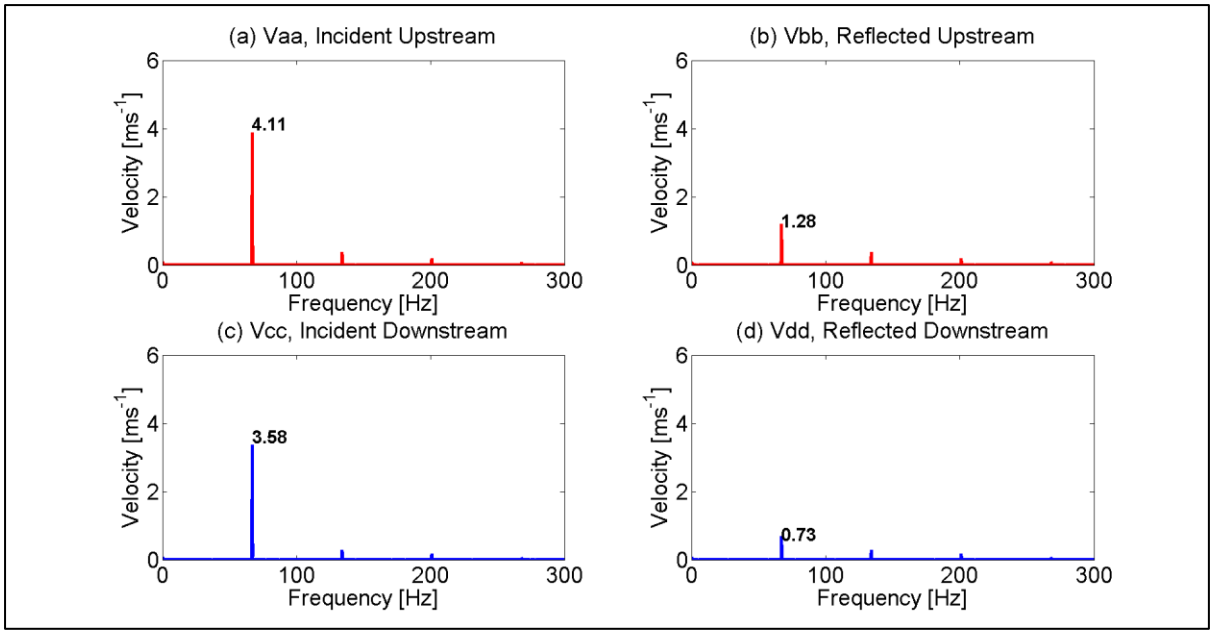

Figure 6-12: The VWD results for the linear combination of POM 1 & 2

The VWD analysis was also conducted on the raw PIV velocity vector measurements and the results are shown in Figure 6-13. The VWD results on the raw measurements have a noisier spectral floor level and show the existence of a mean flow component (peak at 0Hz). By comparison, POM 1-2 shows a cleaner spectral representation of the main oscillation, with the separation of the mean flow component, into POM 3 and other turbulent components, that makes up the noisy spectral floor level into higher POM modes. By comparing Figure 6-12 and Figure 6-13, POM 1-2 is shown to be a good representation of the primary oscillating component, as its VWD spectrum still shows the same amplitude peaks corresponding to the investigate frequency and its harmonics. The average percentage difference between the spectral peaks corresponding to the investigated frequency and its harmonics for POM1-2 and the raw PIV measurement is approximately 4.8%.

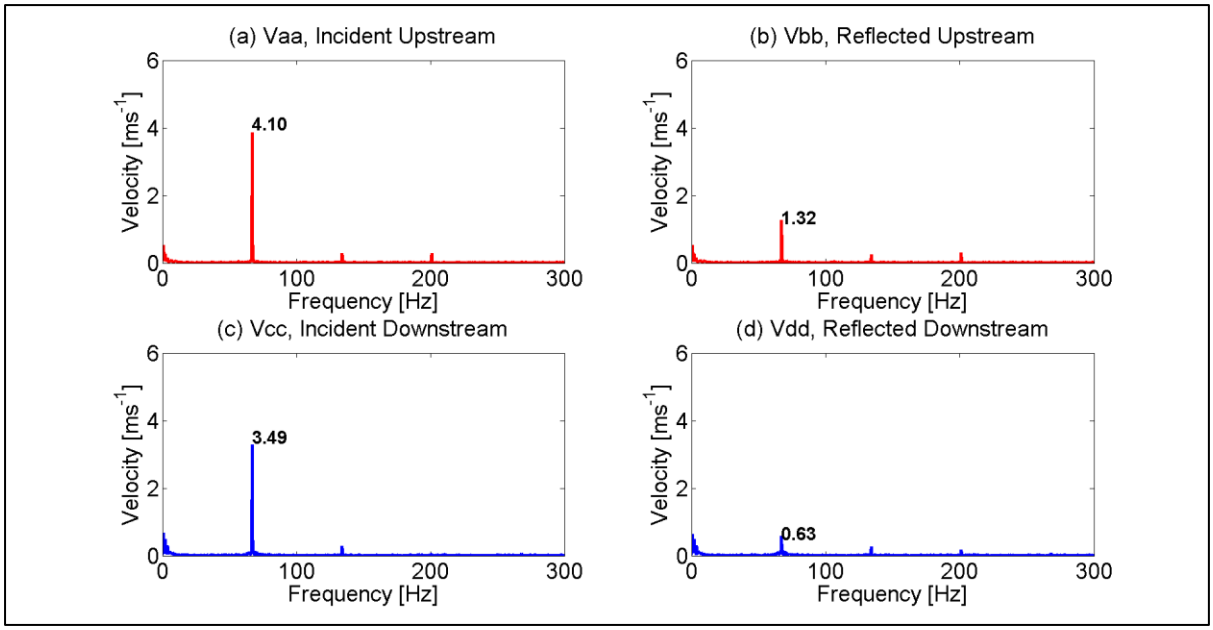

Figure 6-13: The VWD result for the raw PIV velocity vector field measurement

6.3 Secondary Flow [POM 3: Main Coherent Structure]

The POD results have shown that POM 3 has the largest peak in the zeroth frequency component in the temporal coefficient spectrum as compared to all the other POD modes. This trend has also been observed in all experimental run for varying frequency, radius of curvatures and amplitudes. The strong presence in the zeroth frequency component indicates that POM 3 represents the main secondary mean flow component of the system. It has also been shown in

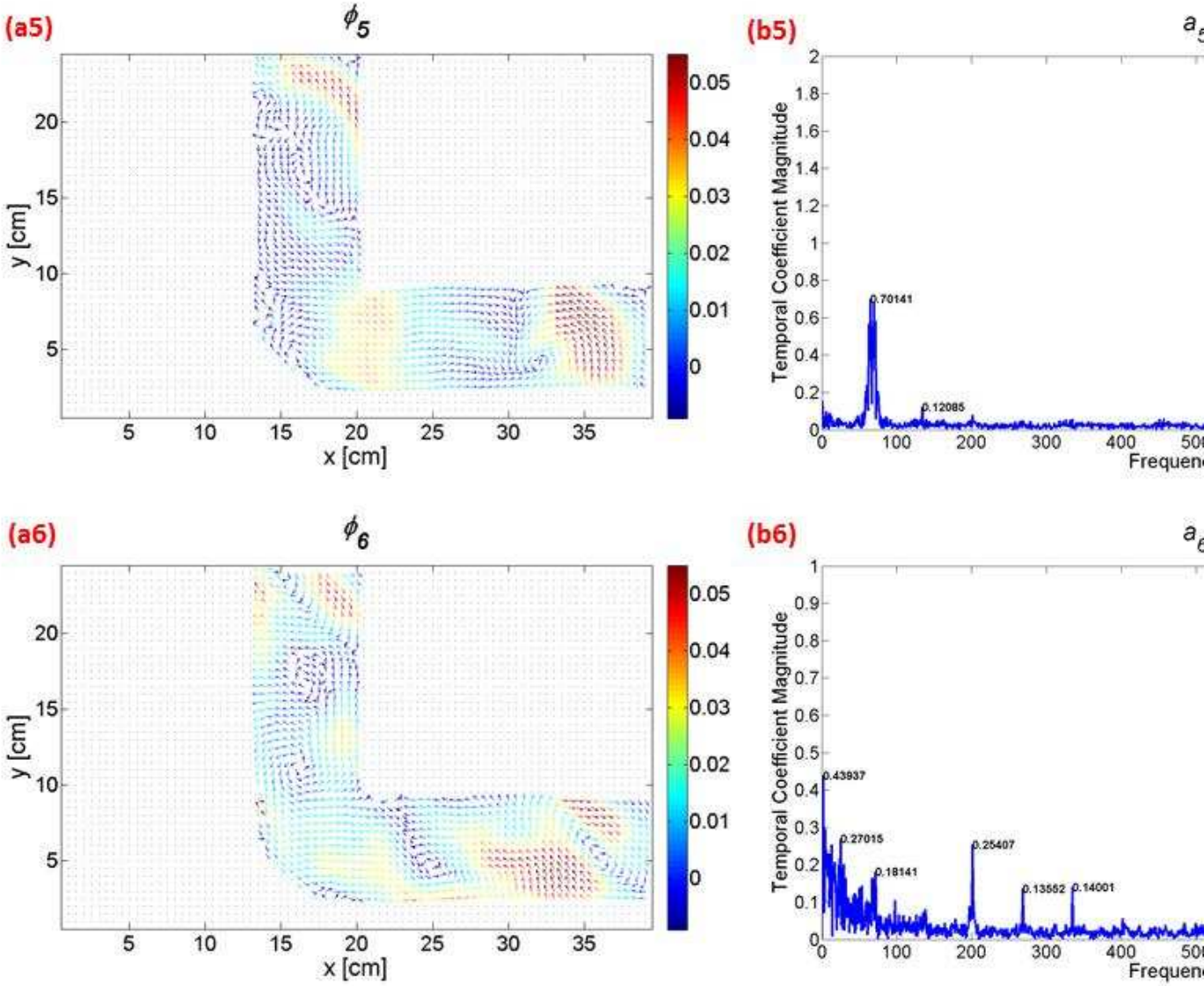

Figure 6-3, that POM 3 is a pure mean flow component with no oscillating component. The temporal coefficient, $a_3(t)$, however, shows the existence of random fluctuation about the mean flow value (Figure 6-14). Although this may be attributed to unsteady turbulent fluctuation, it must be noted that, as the radius of curvature is increased from A1 to A5, the oscillating component corresponding to the harmonics of the investigated frequency is shown to increase proportionally for $a_3(t)$ spectral component. The amplitude of these oscillating components are however, always lower than the mean flow amplitude for all POM 3.

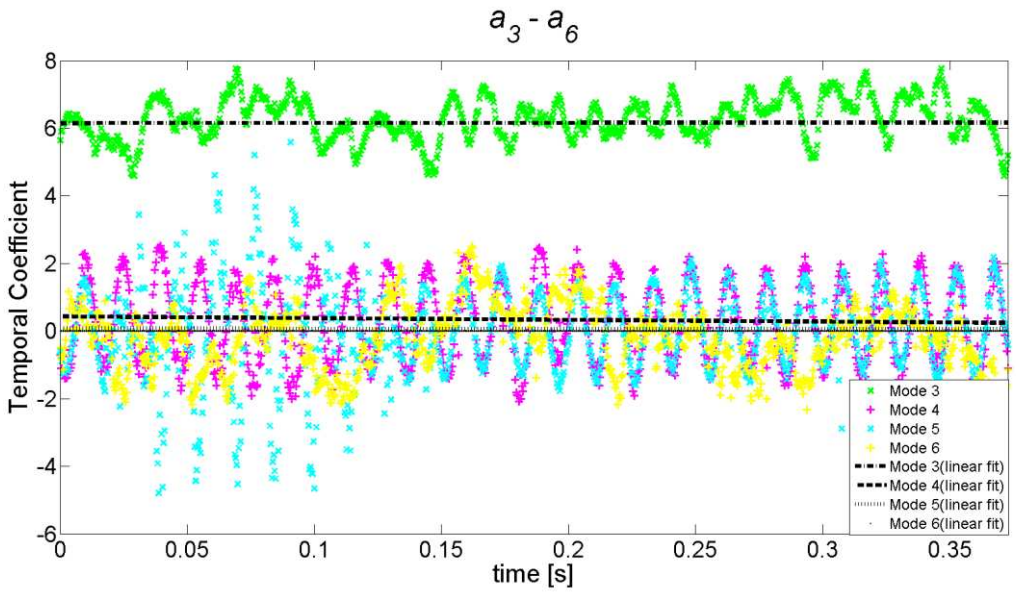

Figure 6-14: Temporal Coefficient for POD Modes 3 -6 for Acoustic Excitation of 67Hz at 200We

It is shown that for the sharper radius of curvature bends (A1-A3 Bends), the secondary mean flow circulation forms a distinct pair of counter rotating vortex structures: one in the upstream section, before the curvature of the bend, and the other, in the downstream section, after the curvature. Similar vortical structures have been observed by Bertelsen[197] in his experimental observation of oscillating flow through curve duct sections using colour dye.

The POD analysis shows that the pattern of these pairs of counter-rotating structures becomes less prominent with increasing radius of curvature. By observing the pattern of POM 3's Orthonormal basis function for radius of curvature A1 to A5 (Figure 6-15), it is predicted that as the radius of curvature increases, the vortex structure is shown to be elongated and finally dividing into smaller pairs of counter-rotating circulating structures (such as seen in A5).

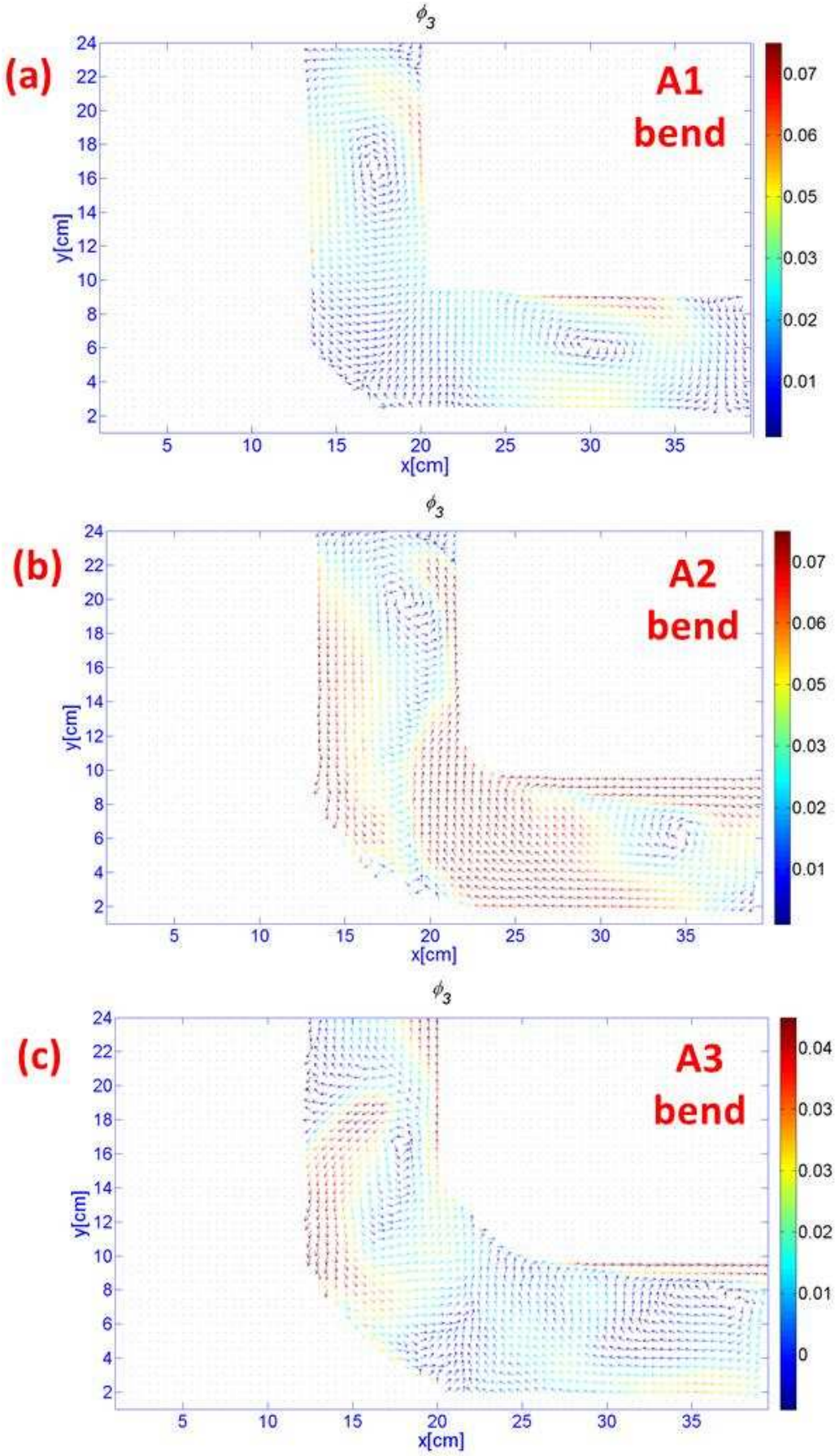

Figure 6-15[*(a)-(c)*]: For caption see pg.193.

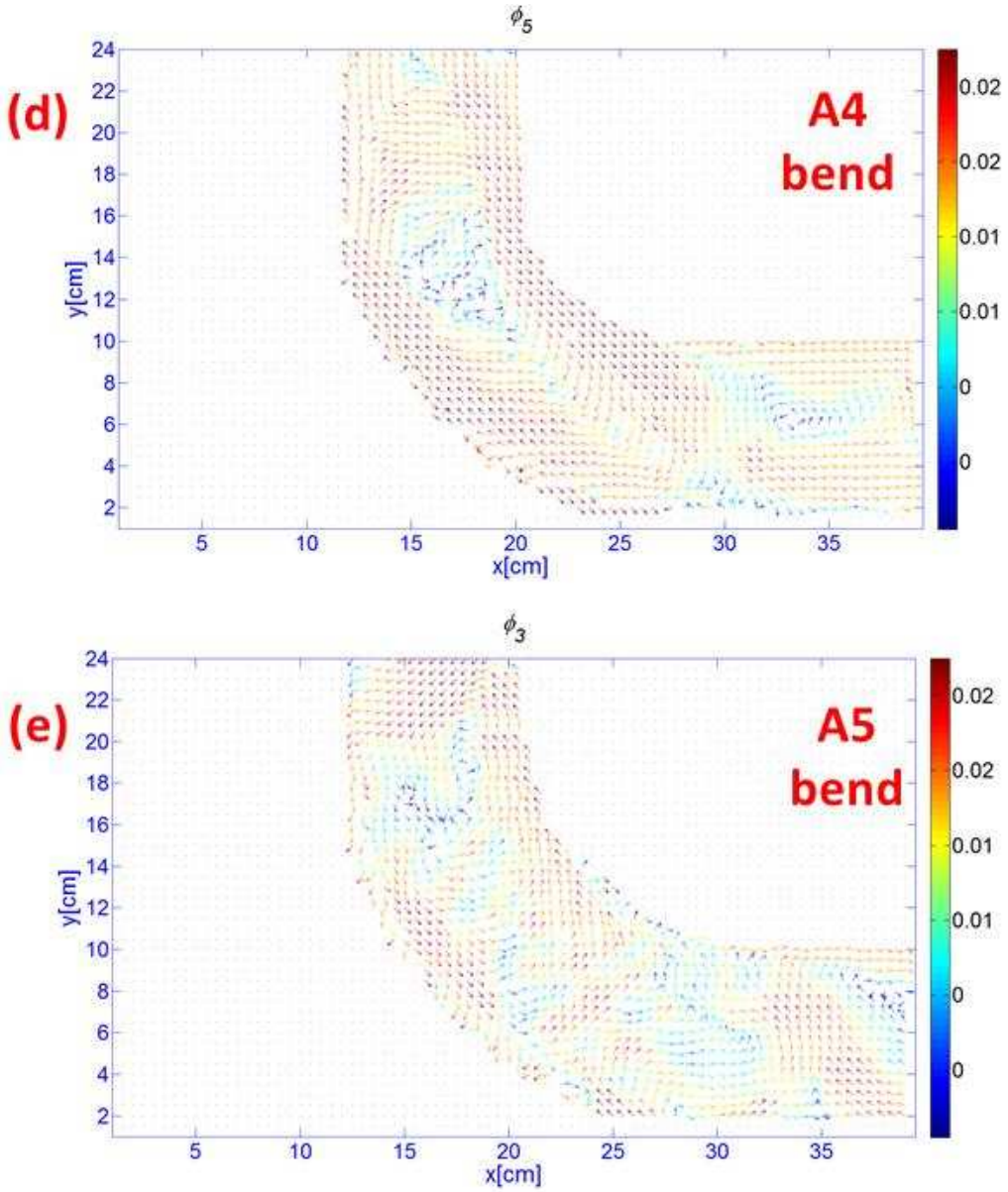

Figure 6-15 : The Orthonormal basis functions of POM 3 for bends A1 to A5 using 67Hz excitation at 200We. The velocity amplitude of the vectors are represented by colours indicated by the colour scale (velocities given in ms^{-1}).

These counter rotating vortices are shown to encourage the secondary flow from the outer wall of the curvature towards the inner wall of the curvature of the bend. The superposition of this secondary flow effect, on the primary oscillating flow component, may explain the cause of the skewed axial oscillating velocity profile, where the higher oscillating velocity is forced towards the inner wall of the bend's curvature. This skewed velocity profile, is in agreement with the Lyne type oscillating flow system through curved duct system. Although those researches focused on the secondary flow in the normal cross sectional plane, the secondary flow, in the axial plane observed in this investigation, complements those results, and helps complete the 3D flow characteristics of an oscillating flow through curved duct systems.

Besides explaining the centripetal effect on the primary oscillating flow component, POM 3 also plays an important role in understanding the acoustic energy dissipation mechanism of the system. The only source of excitation, provided for this investigation, is from the source speaker which provides a pure oscillating wave. As such, any mean flow component found within the system must have been convected from the acoustic wave propagating through the system. This is in accordance to the Kolmogorov turbulence dissipation theory where the kinetic energy from the primary flow component is convected into forming circulatory structures, such as eddies and vortices[198]. The presence of a discontinuity, such as a bend or a curvature in the duct system, helps to promote flow separation, and the formation of these circulatory structures. The sharper the radius of curvature of the curved elbow bend, the higher the probability for flow separation to occur. This explains the more defined vortex structures found for the sharper radius curvature bends. Since the primary flow component in this investigation is an oscillatory flow, it was easier to identify the main dissipative mean circulatory flow component in this investigation. Not only does POM 3 show the largest mean velocity amplitude but it also has the largest and most well defined vortex structure. As such, POM would represent the first level in which the acoustic kinetic energy is dissipated to form circulatory mean flow component. In the use of the POD technique to study turbulent flow systems, the circulating structures shown in POM 3 are also known as Coherent Structures[181,

182]. These coherent structures are the deterministic portion of a turbulent flow system and contain approximately 10% of the total turbulent energy of the system. The other 90% of the turbulence are contained within indeterministic, non-linear fluctuation of the flow.

6.4 Secondary Flow [Modes above POM 3]

It has previously been established, that the flow pattern and characteristics for the first three POD modes are the same for all the experimental runs. Unlike the first 3 modes however, POD modes above POM 3 may or may not show similar trends. The comparison for POM 4 and POM 5's Orthonormal basis function for the 67Hz at 200We investigation is shown in Figure 6-16 and Figure 6-17 respectively. It has been observed that these higher POD modes do not always exhibit characteristics of circulating structures on their own. However, the linear combination of these higher POD modes always shows a variety of unsteady circulating patterns. These circulatory structures represent the next level in the kinetic energy cascade mechanism. The higher POD modes show kinetic energy levels (in accordance to their eigenvalues) which are significantly lower than the first 3 POD modes. As such, in order to represent circulating structures at the higher levels of the energy cascade mechanism (those immediately after POM 3), the linear combination of these POD modes are required.

The turbulent loss mechanism predicts that, the energy convected into the main mean flow coherent structure is unstable, and will further divide, convecting energy to the generation of smaller circulation coherent structure systems. The energy from these smaller coherent circulation systems, will again be further cascaded into even smaller circulation structures, and so on until the smallest circulation level is reached. This level is known as the Kolmogorov scale where kinetic energy is finally dissipated as viscous heating in the boundary layer. There are two important factors to consider in identifying the different levels of the energy cascading loss mechanism:

- **PIV resolution**

  In this investigation, the priority was set for the qualitative and quantitative measurement of the overall trend of acoustic wave propagation through bend systems. At the resolution set for this investigation, only the larger coherent structures, corresponding to the higher levels of the energy cascade loss mechanism, are detectable. Higher resolutions are required for the identification of smaller circulation structures at the lower levels of the loss cascade mechanism. The identification of the Kolmogorov dissipation level requires the use of micro-PIV systems.

- **Vortex Identification Technique**

  As the loss cascading mechanism progress from the main coherent structure (given by POM 3) in to the lower dissipative levels, the number of circulating structures is predicted to increase. These circulating structures may or may not be steady with time. It is would be more practical to use a system that could automatically detect and accurately identify these circulating structures.

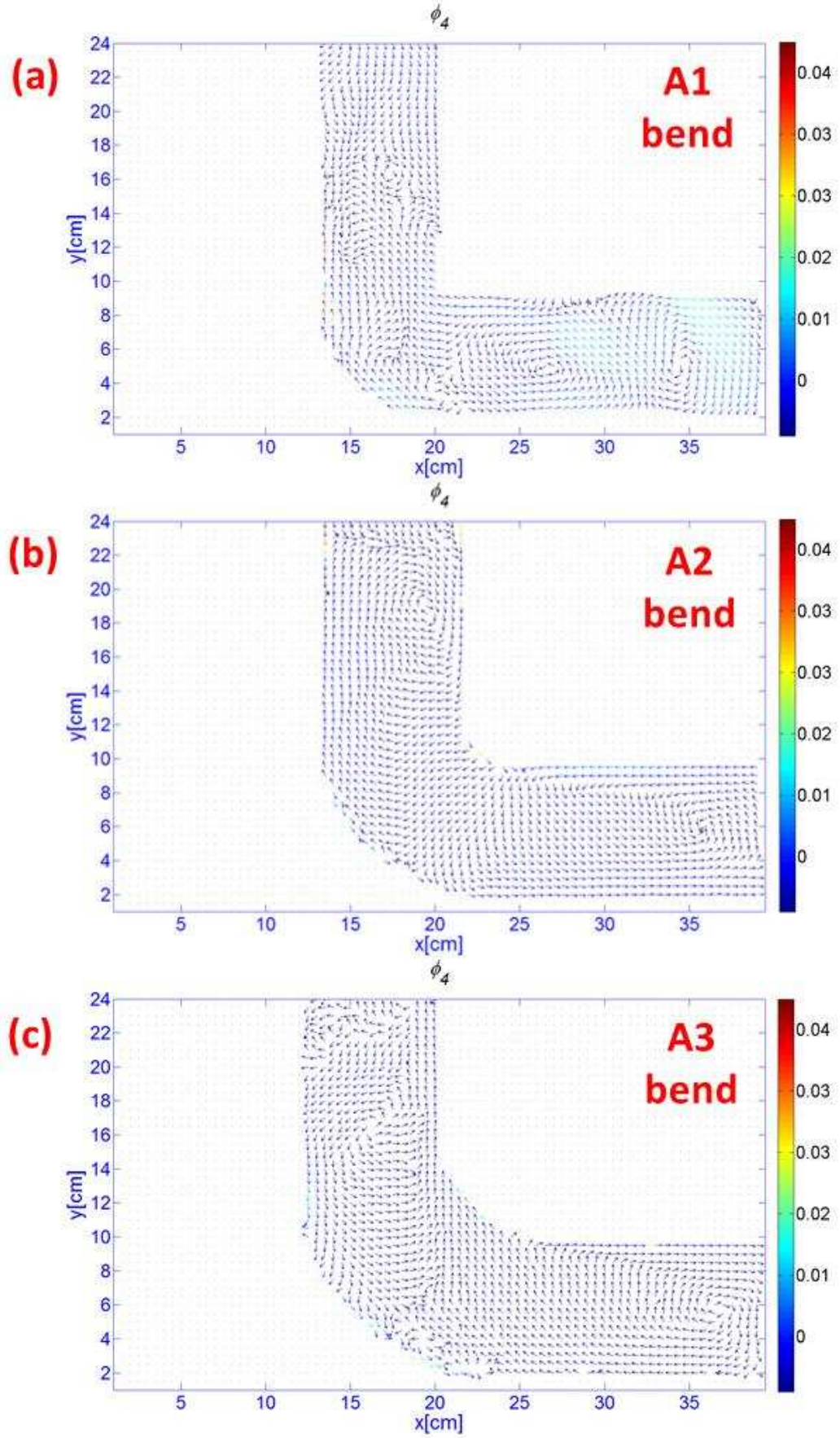

Figure 6-16[*(a)-(c)*]: For caption see pg.198

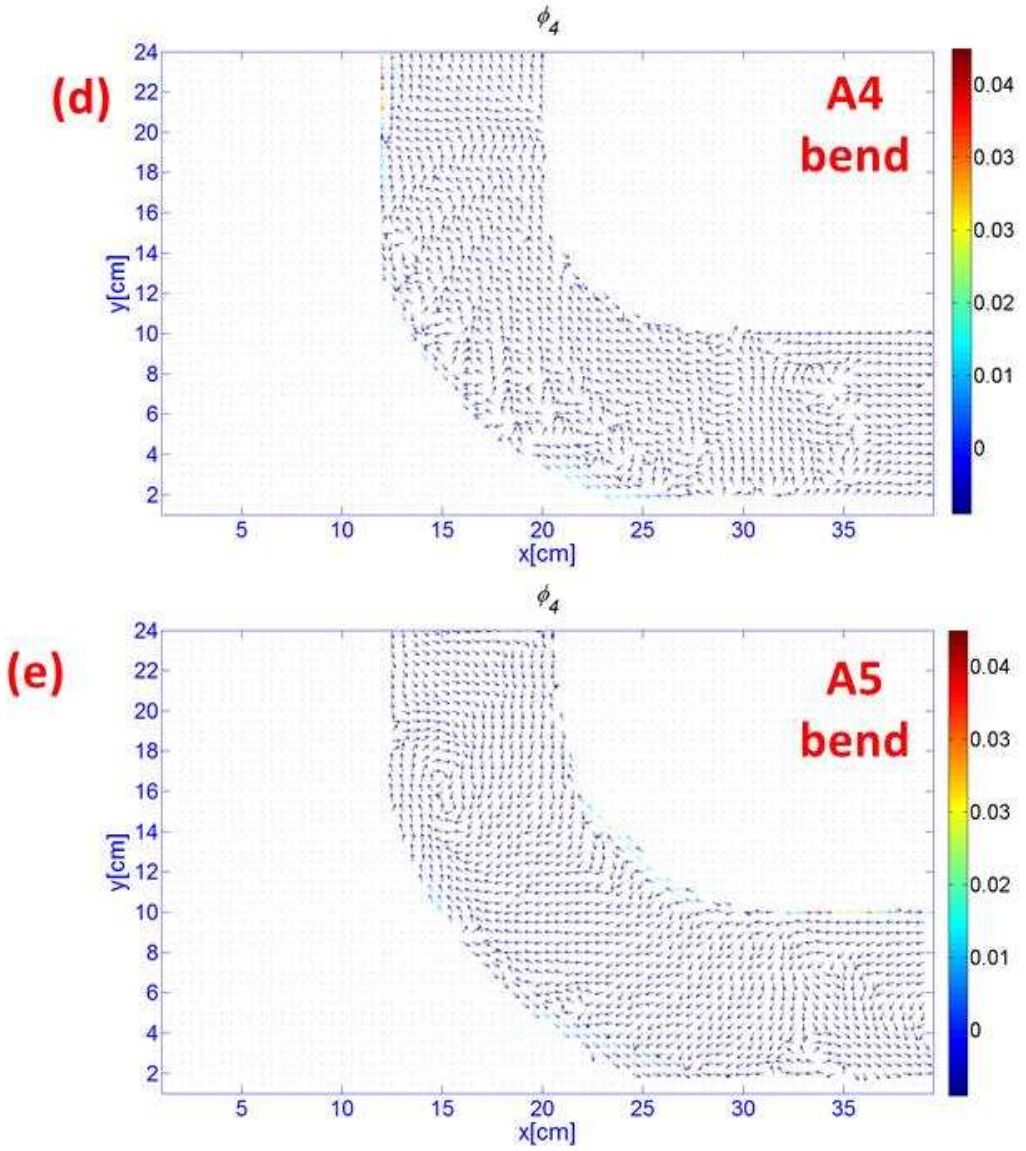

Figure 6-16: The Orthonormal basis functions of POM 4 for bends A1 to A5 using 67Hz excitation at 200We. The velocity amplitude of the vectors are represented by colours indicated by the colour scale (velocities given in ms^{-1}).

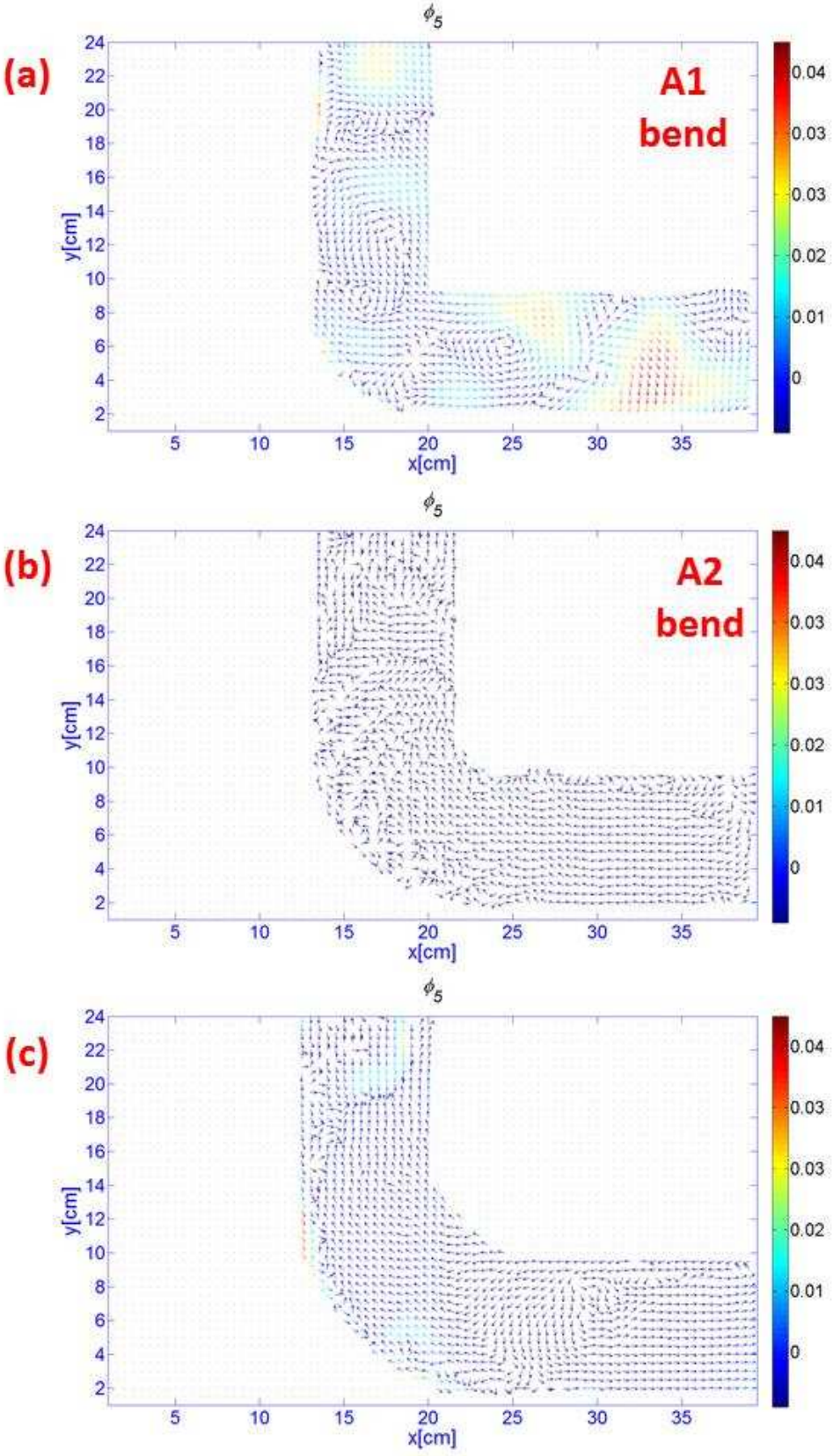

Figure 6-17[*(a)-(c)*]: For caption see pg.200

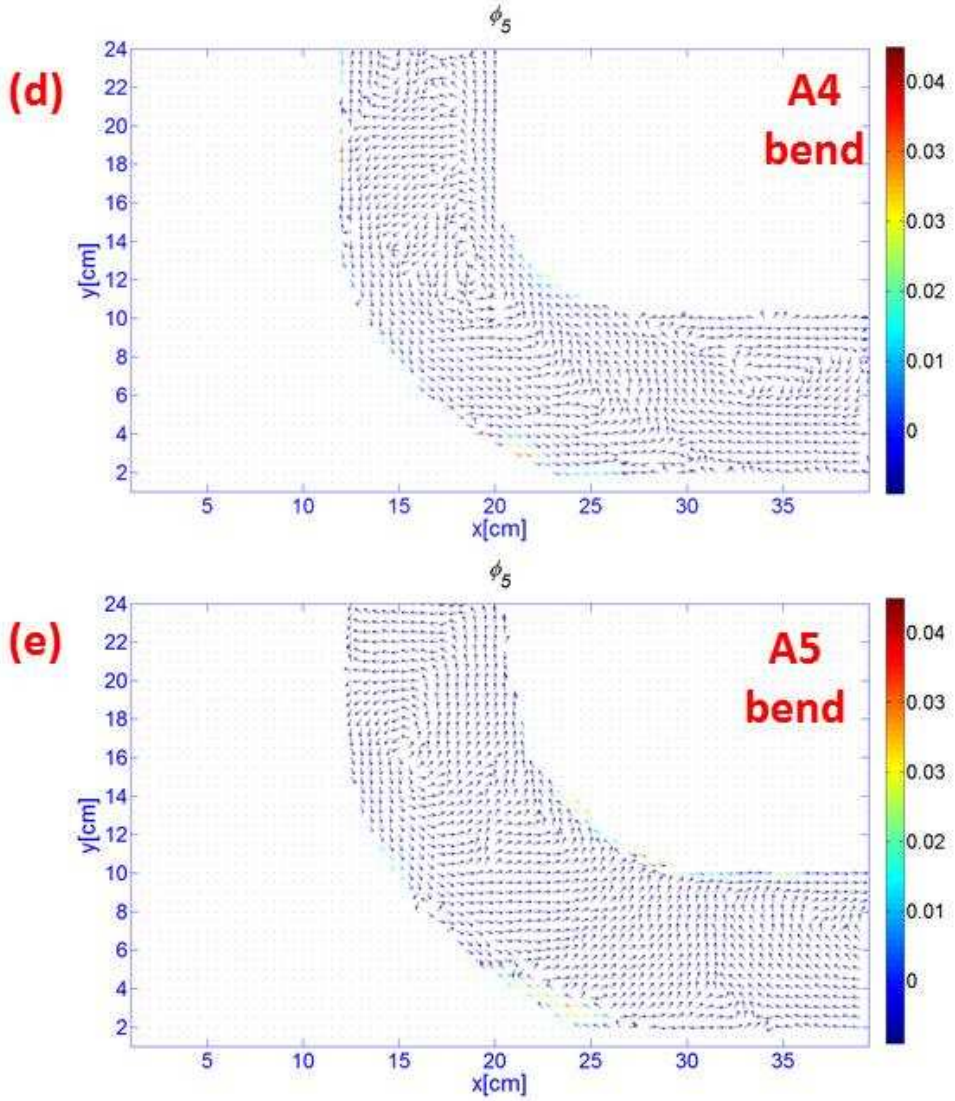

Figure 6-17: The Orthonormal basis functions of POM 5 for bends A1 to A5 using 67Hz excitation at 200We. The velocity amplitude of the vectors are represented by colours indicated by the colour scale (velocities given in ms^{-1}).

In order to facilitate the accuracy of this investigation, the vortex detection algorithm devised by Michard[199] and Graftieaux[200] was employed. This spatial algorithm operates by determining the strength of the circulation for each point in the velocity vector field, based on the direction and amplitude of the velocity vectors surrounding the investigated point. The circulation strength, $\Gamma_{centre}(x, y, t)$, for each point in the velocity vector field is computed using *Equation (6.3):*

$$\Gamma_{centre}(x, y, t) = \frac{1}{N}\sum_{S}\frac{(PM \otimes U_M)\cdot z}{\|PM\|\cdot\|U_M\|} = \frac{1}{N}\sum_{S}\sin(\theta_M) \tag{6.3}$$

Here, *P* denotes the investigated point in the velocity vector field; *S* denotes the region surrounding the point *P;* *N* represents the number of velocity vectors in the *S* region surrounding *P* (N=25, for this investigation); *z*, is the unit vector normal to the plane of measurement; U_M, is the magnitude of the velocity vector corresponding to point *M*; and θ_M is the angle between the velocity vector, U_M, and the vector, PM. This configuration is shown in Figure 6-18. The value of Γ_{centre} , for each point in the velocity vector field, ranges from 0 to unity, unity representing the strong presence of a circulation structure. The resultant Γ_{centre} field can be superimposed with the velocity vector quiver plot to give the location of the centre of these circulation structures.

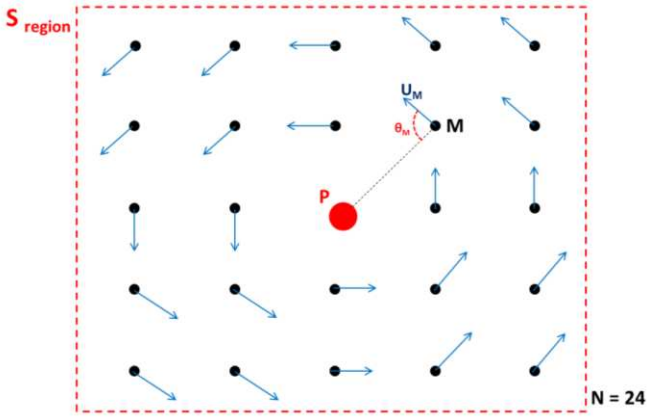

Figure 6-18: The layout for the Vortex Identification Algorithm

The vortex detection algorithm was applied to POM 3, the higher POD modes and their linear combinations. In Figure 6-19, column 1 shows the quiver plot of the POM 3 and the linear combination of higher POD modes depicting the cascading loss mechanism, and column 2 shows the resultant Γ_{centre} contour plots with respect to the column 1's quiver plots. Here, the progressive linear combination of the higher POD modes shows the increasing number in circulatory structures with decreasing sizes. Kolmogorov states that, it is possible for smaller circulating structures to exist within a larger circulatory one, in accordance to the different level of the cascading loss mechanism. The POD results in Figure 6-19 supports this theory and provides the visualisation of the cascading energy loss mechanism.

This investigation is however limited to the identification of the size of circulating structures shown in Figure 6-19. Attempts to find the next level of smaller circulation structure, through the linear combination of higher POD modes, resulted in the detection of random velocity vectors. This is due to the limitation of the set PIV resolution for this investigation, where the size of the circulation structures are predicted to be smaller than the size of the interrogation area; hence the resultant velocity vector appears to be random in nature.

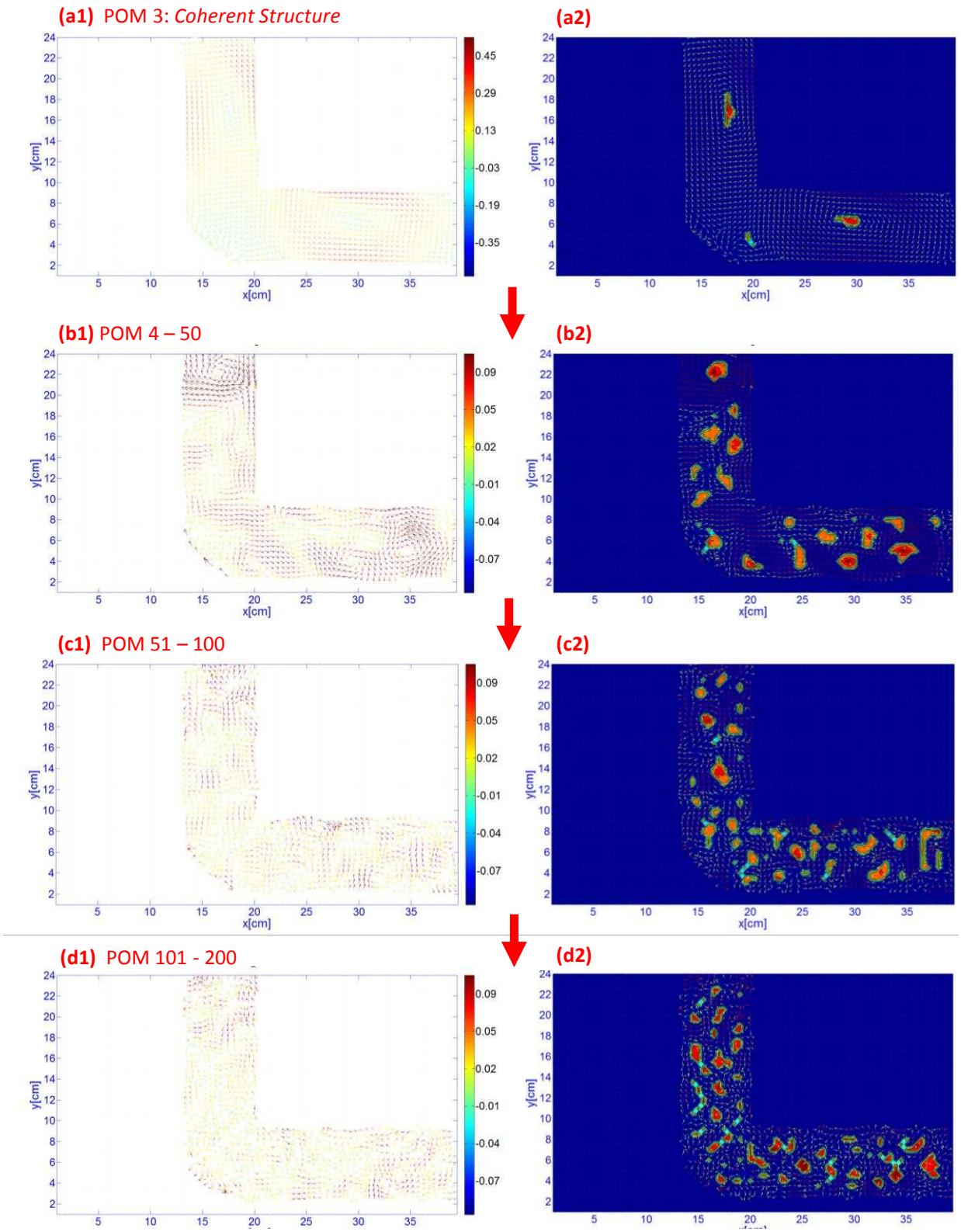

Figure 6-19: The cascade loss mechanism shown using the higher POD modes

6.5 Chapter Conclusion

The POD technique has successfully shown to be able to separate the investigated flow into its various investigated components. The first two modes correspond to the main oscillating component of the investigated acoustic wave. The POD technique is only able to represent a standing wave oscillation in each of its oscillating modes. As such, the POD technique requires the linear combination of 2 standing wave modes (POM 1 and 2) in order to represent the acoustic travelling wave system in this investigation. The oscillation in POM 1 shows a skewed axial oscillating velocity trend, where higher axial velocity appears to be closer to the inner wall of the curvature. This matches literature which has shown that the centripetal force is dominant in oscillating flow through curved duct systems. POM 2 shows a plane wave mode of propagation through the bend, unaffected by the curvature. This same trend is observed for both POM 1 and 2 in all experimental runs.

POM 3 is a predominant mean circulatory secondary flow system. The formation of these large vortex structures encourages flow towards the inner wall of the curvature in the bend. The superposition of this secondary flow on the primary oscillation may explain the skewed axial velocity profile. POM 3 also represents the main coherent structure in which the kinetic energy, from the acoustic wave, is first dissipated to form these mean secondary flow circulation structures. The linear combination of the higher POD modes has been shown to represent the subsequent level in the cascade energy loss mechanism. With progressing higher linear combination of POD modes, the number of secondary circulating flow structure increases and they are shown to be smaller in size. The circulating velocity of these structures also decreases with each dissipative level.

It has been established that the first two POD modes represent the main oscillating component of the acoustic wave and that subsequent POD modes represent the acoustic energy losses. The transmission of percentage kinetic energy of the acoustic energy through the bend may be computed from the

eigenvalue plots such as in Figure 6-1. The next chapter discusses the quantitative measurement of the acoustic transmission through the duct bends systems and its characterisation.

Chapter 7

Acoustic Transmission through Curved Duct Bend Systems

7.0 Acoustic Transmission through Duct Bend Systems

Farge[201] described turbulence as an open thermodynamic process, in which external energy is provided for its formation and perpetuation, while kinetic energy is slowly dissipated away from it, through viscous friction. This aptly describes the processes shown in the previous chapter. Due to instability, a minor portion of the kinetic energy from the primary oscillation (POM 1-2) is convected, in each periodic cycle, to form large scale, secondary flow, coherent structures (POM 3). These large coherent structures however, also proved to be unstable and are continuously dissipating energy through convection, forming smaller scale circulating structures as shown by the linear combinations of proper orthogonal modes above POM 3. As such, it can be concluded that the linear combination of POMs 1 and 2, would thus represent the remaining acoustic energy or rather the transmitted acoustic energy of the wave propagating through the duct bend system. This is important, as it gives a quantitative insight towards the transmission behaviour of the acoustic wave through these systems. This will then, allow the identification of a mathematical relationship of the geometric parameters of the duct bend and, the acoustic properties of the wave on the acoustic transmission of the system. This relationship in turn will be used in the optimisation of acoustic transmission through duct bend systems.

It has been shown earlier in *Equation (6.1)*, that the eigenvalue for each of the POD mode is given as the sum of the squared velocity vector values for each point in the investigated plane across the number of

timesteps used to compute the POD analysis. The squared incident acoustic velocity amplitude is proportional to the acoustic intensity, I_{aa}, and thus kinetic energy of the mode.

$$\mathrm{I}_{aa} = (V_{aa})^2 \rho c \tag{7.1}$$

The eigenvalues of each POD mode can thus be taken as the quantitative representation of the kinetic energy contained within each POD mode. Since the linear combination of the first two POMs are taken to represent the primary oscillating component of the incident acoustic travelling wave, the sum of the $\lambda_1$and λ_2 would thus give the acoustic energy content of the system. Consequently, POM 3 and the linear combination of higher modes corresponding to the secondary flow, coherent structure and the other vortical turbulent structures, represent the dissipated acoustic energy of the system. The acoustic transmission can thus be computed as the percentage ratio:

$$\text{Acoustic Transmission} = \frac{\sum_1^2 \lambda^i}{\sum_1^{T_N} \lambda^i} \times 100\% \tag{7.2}$$

The acoustic transmission for all the experimental run in the PIV investigation was found to be above 90%. As such, it would be more convenient to study the acoustic losses through the duct bend system.

$$Loss_{acoustic} = 1 - \text{Percentage Acoustic Transmission} \tag{7.3}$$

Based on this percentage acoustic transmission loss, their characteristics and transmission behaviour-are then investigated.

7.1 Characterisation of the Acoustic Transmission

The 3 varied parameters in this investigation include: the radius of curvature of the duct bends (as shown in Figure 5-2); the fundamental operating frequency; and the amplitude of the incident acoustic travelling wave that is injected into the system. Here, the incident velocity amplitude of the wave was not varied at constant intervals. The VWD analysis which is used to measure the incident acoustic velocity is a post processing technique. As such, the only means of controlling the acoustic wave

amplitude to be introduced into the system is to control the electrical power supply provided to the excitation speaker Owing to the characteristics impedance of the excitation speaker however, the amplitude of the acoustic wave that is introduced into the system varied slightly with each different investigated frequencies over a constant electrical power supply. Another challenge faced in keeping the incident acoustic amplitude constant is due to the limitation of the PRC technique itself. Although the PRC technique is able to generate travelling waves within the system below the SWR value of 1.3, the technique is unable to obtain a constant SWR value for all the investigated acoustic frequencies. The variation in SWR causes changes in the V_{aa} value as well. The limited ability to control the amplitude of the incident acoustic velocity however did not hinder the experiment from obtaining a good, even spread of results. The amplitude of the incident acoustic velocity is implicitly shown in the Reynolds number vs. Transmission loss plot of Figure 7-1. The Reynolds number here is computed from the amplitude of the incident acoustic velocity and is given as:

$$\mathrm{Re} = \frac{V_{aa}\, d_h}{\nu} \tag{7.4}$$

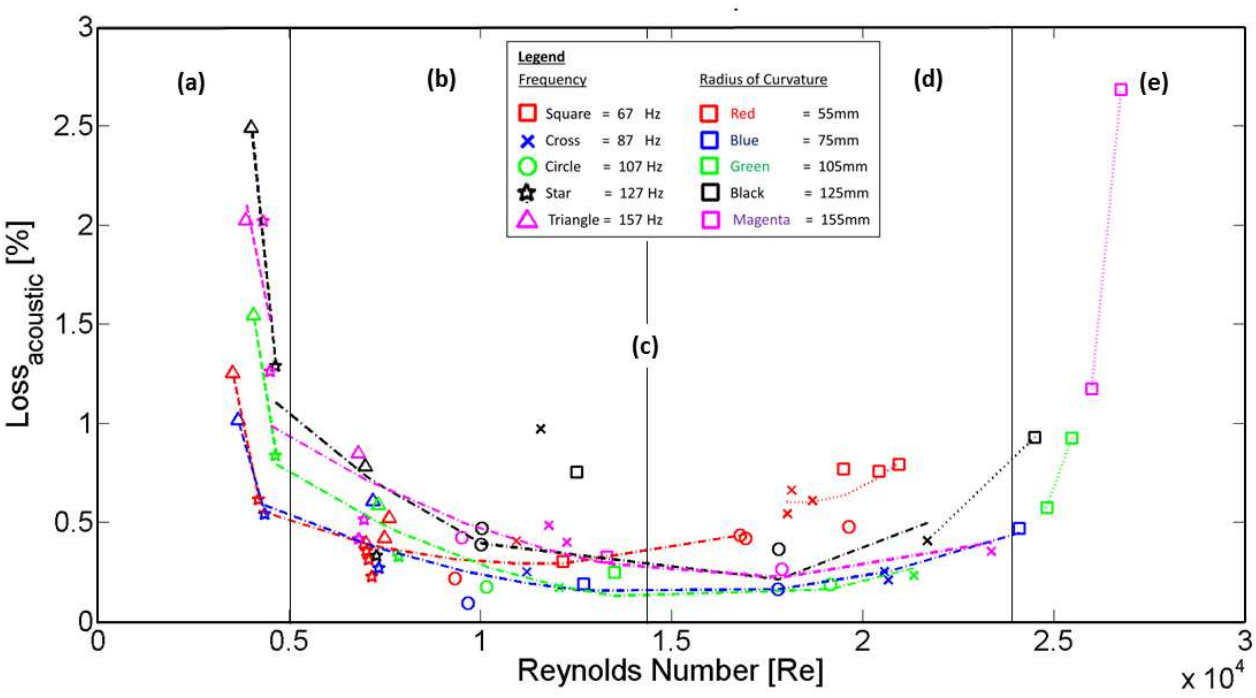

Figure 7-1: The Reynolds number plotted against the Acoustic Transmission Loss. The viscous dominated region is indicated by '- - -'trend lines, the transition region by '-.-.-'and inertia dominated, turbulent region by '….' trend lines.

The results showed that the trend for each runs corresponding to the 5 investigated radius of curvature are of the same "U" shaped acoustic transmission loss behaviour that divides the Reynolds number chart into 3 distinct regions: an initial high transmission loss region at approximately Re<7500 (Region **(a)**); an optimum oscillation transmission within the range of 7500<Re<25,000 (Region **(b), (c)** and **(d)**); and, a further increase in transmission loss at Re>25,000 (Region **(e)**). These acoustic transmission loss trend lines however, do not overlap each other, but show a small vertical offset between them. This is indicative that, an optimum point of minimum transmission loss exists for each investigated radius of curvature, and also, that an optimum radius of curvature exists for acoustic transmission through elbow duct bend systems. The POD results corresponding to one run in each region of Figure 7-1 are shown in Figure 7-4. The POD results are given as the Orthonormal basis function of POM 3 for each run and show the secondary flow characteristics in relation to the transmission loss behaviour of each region. The Reynolds number is essentially defined as the ratio of the inertia strength of the flow to its viscosity. As such, the initial high transmission losses region corresponding to 3500<Re < 5000 ($0.5ms^{-1} < V_{aa} <$

$1.25\ ms^{-1}$), may be attributed to large viscous frictional losses. These initial high losses, however, are shown to decrease exponentially for a small increase in Reynolds number. This is interesting since the viscous losses are generally expected to increase proportionally to square of the incident velocity for duct flow system[202].

This loss trend behaviour suggests that some form of viscous suppression process occurs with an increase in Reynolds number within Region **(a)**. Such behaviour has previously been observed in the transition flow regime, as well as the early stages of the turbulent flow regime[203]. It is thus postulated that the investigated oscillating flow range of this experiment spans over both of these flow regimes. The viscous frictional flow losses in the transition/turbulent flow regime are known to be much larger, as compared to the laminar regime. This has been attributed to the formation of streamwise vortices within the turbulent boundary layer. These streamwise vortices are formed due to the large velocity gradient formed within the viscous sublayer region of the boundary layer which eventually, leads to an inflection point and the turbulent bursting process[204]. The bursting process is a cyclic event, which involves the transport of momentum within the inner region of the viscous boundary layer[205, 206]. The cycle starts with the convection of low momentum fluid away from the wall, and out of the viscous sublayer, through a process known as “ejection”. This creates a low pressure region, in which high momentum fluid rushes down back towards the wall in a process known as ‘sweep’. In turn, the adverse pressure gradient formed above the viscous sublayer due to the sweep event sets the stage for the next ejection process of the cycle[207, 208]. This process has been illustrated in Figure 7-2. It has also been shown that, turbulence within the Stokes layer of an oscillating flow system undergoes the same turbulent formation processes, as described here[209]. The increase in viscous losses in transition/turbulent flow regime are caused by the sweep event, in which the high momentum fluid forced back towards the wall, intensifies the effects of skin friction[210].

The low Reynolds number at which the transmission losses reduction occurs in Region **(a),** suggests that this flow occurs within the transition regime, or the early stage of the turbulent flow regime. In this flow regime, these streamwise vortices are predicted to be largely confined within the Stokes boundary layer of the oscillation[211]. Figure 7-4(a) shows that the secondary flow component is relatively weak, and no distinct flow pattern is observed. This is indicative that the convective losses in this region is minimal, and supports the theory that the large transmission loss in Region **(a)** are predominantly caused by the high viscous losses in the Stokes turbulent boundary layer.

Studies have shown that by suppressing or disrupting the formation process of these streamwise vortices, the viscous friction of the system can be significantly reduced. Jung et el initially proposed the introducing of a spanwise oscillation of a wall bounded flow system in order to control its turbulence[205]. This could either be done through the oscillation of the wall in contact with the flow or the introduction of secondary cross flow in the spanwise direction. The spanwise oscillation perturbation was shown to form spanwise vortices which weaken the turbulence, causing sweep and ejection processes within the viscous sublayer near the wall[212, 213]. The experimental success of reducing turbulent viscous losses by up to 40% through spanwise wall oscillation have also sparked interest into investigation regarding other methods of introducing the spanwise perturbation. This include the introduction of cross-flow spanwise travelling wave oscillations[206, 214], the use of Lorentz forces through electromagnetism[210]and cold plasma[215].

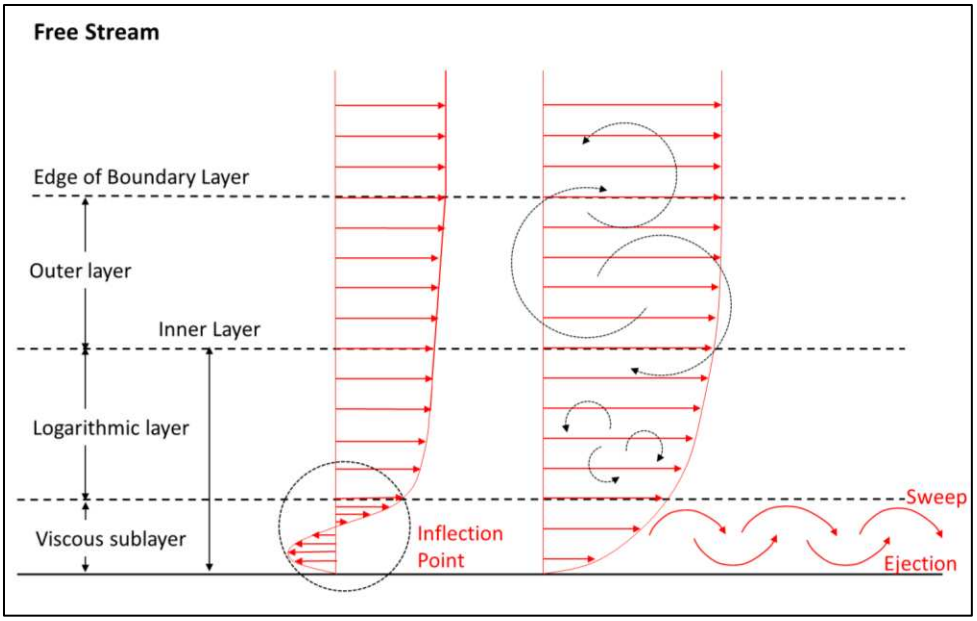

Figure 7-2: The development of turbulence in the viscous boundary layer

Here, it is speculated that the formation of the Lyne type secondary flow circulation within the curve section of the duct bend is one of such processes. This is especially since the secondary circulations in the cross section are akin to a spanwise DC flow along the perimeter of the duct. The formation of the Lyne type secondary circulation results in two pairs of counter rotating vortices. One of the two pairs of spanwise vortices is specifically confined within the viscous Stokes boundary layer of the duct. It is postulated that this pair of vortical circulation in the Stokes layer is responsible for the disruption of the turbulent streamwise generating processes. The indirect suppression of the sweep process in turn reduces the viscous losses of the oscillation and thus, the overall transmission losses of the system. This explains the sharp, almost exponential decrease in transmission loss shown in Figure 7-1 for the Region **(b)** corresponding to the range of 5000<Re < 12,500 ($1.5ms^{-1} < \mathrm{V}_{aa} < 2.0\,ms^{-1}$). Figure 7-4**(b)** also shows the formation of a pair of counter-rotating vortices in the axial plane of the bend. Since the formation of these vortical structures are assumed to be 3 dimensional, it is postulated that the growth in prominence of the secondary circulation in the streamwise axial plane is proportional to the growth in strength of the Lyne type secondary circulation in the spanwise cross sectional plane. This explains the suppression of the viscous losses within the system. The acoustic energy loss through convection for the

formation of these secondary circulations are offset by its viscous loss suppression and thus do not contribute to the net increase in the acoustic transmission loss of the system. The total transmission loss of the system is thus inversely proportional to the secondary circulation strength in Region **(b).**

Based on the observed trend, it is also predicted that an optimum transmission Reynolds number exists. This optimum Reynolds number corresponds to the oscillation which yields the largest viscous loss suppression without incurring additional convective and turbulent losses due to its formation. The optimum point is predicted to be in Region **(c)** of Figure 7-1 within the range of 7500<Re < 23,000 ($2.0\ ms^{-1} < \mathrm{V}_{aa} < 3.0\ ms^{-1}$). Figure 7-4**(c)** also shows the same pair of counter-rotating vortices as Figure 7-4**(b)** but with a large circulation magnitude and a more prominent circulation pattern. A further increase in Reynolds number beyond the optimum point corresponds to the onset of the secondary flow loss effect on the overall transmission of the system. Here in Region **(d)**, it is predicted that the formation of streamwise vortices has been completely suppressed by the high intensity secondary flow circulation. The amount of acoustic energy convected to form this high intensity secondary circulation is no longer negligible and contributes to the net acoustic transmission loss of the system. In addition to this, the high intensity secondary circulation is sufficiently large to generate its own viscous losses. As such, the increase in transmission losses in Region **(d)** is primarily attributed to both of these loss mechanisms. Figure 7-4**(d)** shows the most distinct secondary circulation pattern with the largest circulating intensity. It is also observed that the timestep flow of the secondary circulation corresponding to Region**(d)** corresponds to the most steady circulation as compared to that in Region **(b)** and **(c)** in which several forms of unsteady "pumping effects" were observed near the wall superimposed on the main pair of counter-rotating vortices. These pumping effects may be attributed to the remaining sweep and ejection process which have not been suppressed in those Regions.

Interestingly, the PIV results corresponding to Region **(e)** and Figure 7-4**(e)** shows a decrease in the Lyne type secondary flow circulation intensity in Region **(e)** as compared to Region **(d)**. In its place, a more random secondary flow is observed. The deterioration in Lyne type secondary circulation here means that the streamwise turbulent boundary layer suppression mechanism is weakened. This allows for the re-emergence of the unsteady streamwise turbulent vortices which is reflected in the exponential increase in transmission losses in Region **(e)** of Figure 7-1. It is postulated however, that the increase in transmission losses in this region is not purely attributed to the viscous losses (such as in Region **(a)**). The large Reynolds number indicates that this region of the flow is inertia dominated and thus has higher chances for flow separation to occur, especially in the curved section of the bend. These flow separation forms unsteady circulating structures which interact with each other causing turbulences in the freestream oscillation. This is representative of the more random nature of the secondary flow observed in Figure 7-4**(e)**. It is suspected that the turbulences formed in the freestream oscillation region of the duct are the main cause for the steep increase in acoustic transmission loss in this region.

The flow separation observation can be further verified from the percentage transmission loss plotted against the acoustic particle displacement shown in Figure 7-3. It is noted here, that while the Reynolds number was solely dependent on the acoustic incident velocity, the acoustic particle displacement takes into account both the amplitude and the frequency of the investigated acoustic wave and is given as:

$$\xi_{ac} = \frac{\mathrm{V}_{aa}}{2\pi f} \tag{7.5}$$

The acoustic particle displacement shows the same "U" shaped acoustic transmission loss trend as the Reynolds number plot. The acoustic particles' displacement length and oscillating velocity amplitude is proportional to the probability for the particle to leave its oscillating pathway, thus causing flow separation. Flow separation corresponding to low oscillating amplitude and displacement in acoustic flow process causes streaming or secondary flow circulations which could lead to the formation of the

streamwise circulation[204]. It is predicted that for, $\xi_{ac} < 1\,mm$ and Re < 0.5, flow separation is minimal and thus secondary flow circulation is either very weak or non-existent. As such, at this range, viscous turbulent losses dominate the system. The onset of secondary flow effect occurs when the particle displacement, $\xi_{ac} \geq 1\,mm$. Figure 7-3 shows that the optimum particle displacement and Reynolds number for transmission, from both Figure 7-1 and Figure 7-3 corresponds to the same incident velocity amplitude, Vaa. This indicates that the incident velocity is the dominating parameter for oscillating flow characteristics. It is shown here that the amplitude of the particle displacement is inversely proportional to the strength of the secondary flow for the region of large particle displacement ($\xi_{ac} > 9.5\,mm$). Here, it is postulated that the onset of the non-linear turbulent process in this region arises from the ejection of the unstable streamwise circulation in the Stokes layer into the free stream[129].

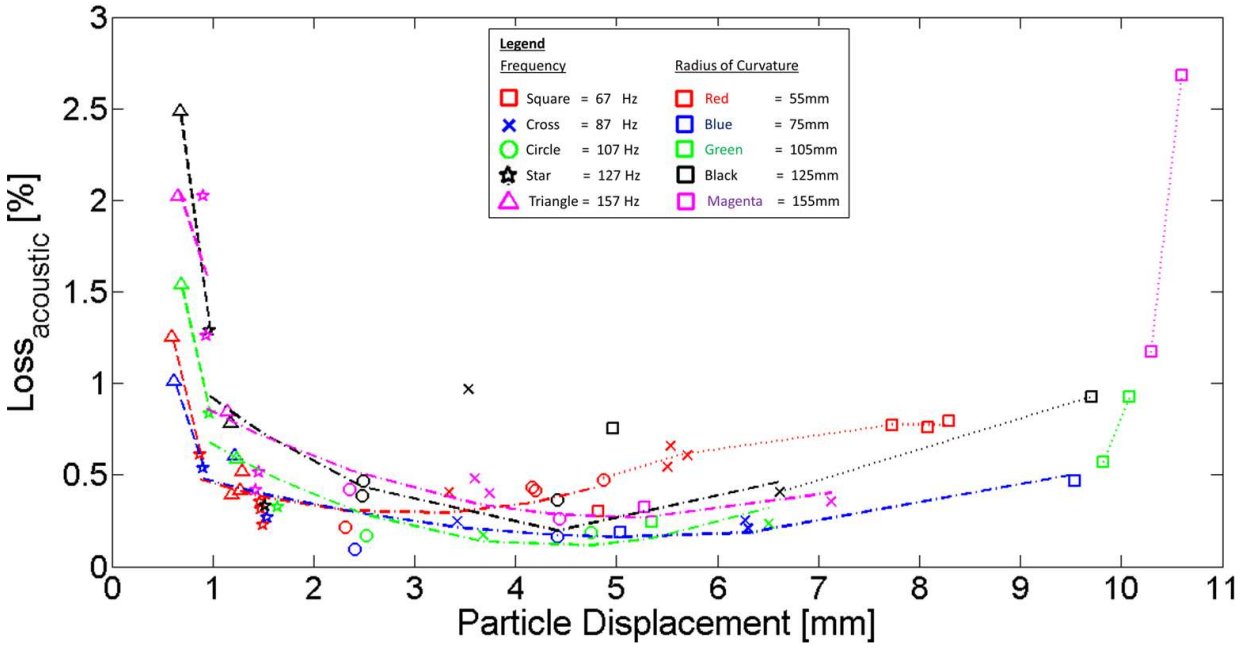

Figure 7-3: The Acoustic Particle Displacement in mm plotted against the acoustic transmission losses. The viscous dominated region is indicated by '- - -'trend lines, the transition region by '-.-.-'and inertia dominated, turbulent region by '….' trend lines.

The acoustic particle displacement shows the same "U" shaped acoustic transmission loss trend as the Reynolds number plot. The acoustic particles' displacement length and oscillating velocity amplitude is

proportional to the probability for the particle to leave its oscillating pathway, thus causing flow separation. Flow separation corresponding to low oscillating amplitude and displacement in acoustic flow process causes streaming or secondary flow circulations which could lead to the formation of the streamwise circulation[204]. It is predicted that for, $\xi_{ac} < 1\,mm$ and Re < 0.5, flow separation is minimal and thus secondary flow circulation is either very weak or non-existent. As such, at this range, viscous turbulent losses dominate the system. The onset of secondary flow effect occurs when the particle displacement, $\xi_{ac} \geq 1\,mm$. Figure 7-3 shows that the optimum particle displacement and Reynolds number for transmission, from both Figure 7-1 and Figure 7-3 corresponds to the same incident velocity amplitude, Vaa. This indicates that the incident velocity is the dominating parameter for oscillating flow characteristics. It is shown here that the amplitude of the particle displacement is inversely proportional to the strength of the secondary flow for the region of large particle displacement ($\xi_{ac} > 9.5\,mm$). Here, it is postulated that the onset of the non-linear turbulent process in this region arises from the ejection of the unstable streamwise circulation in the Stokes layer into the free stream[129].

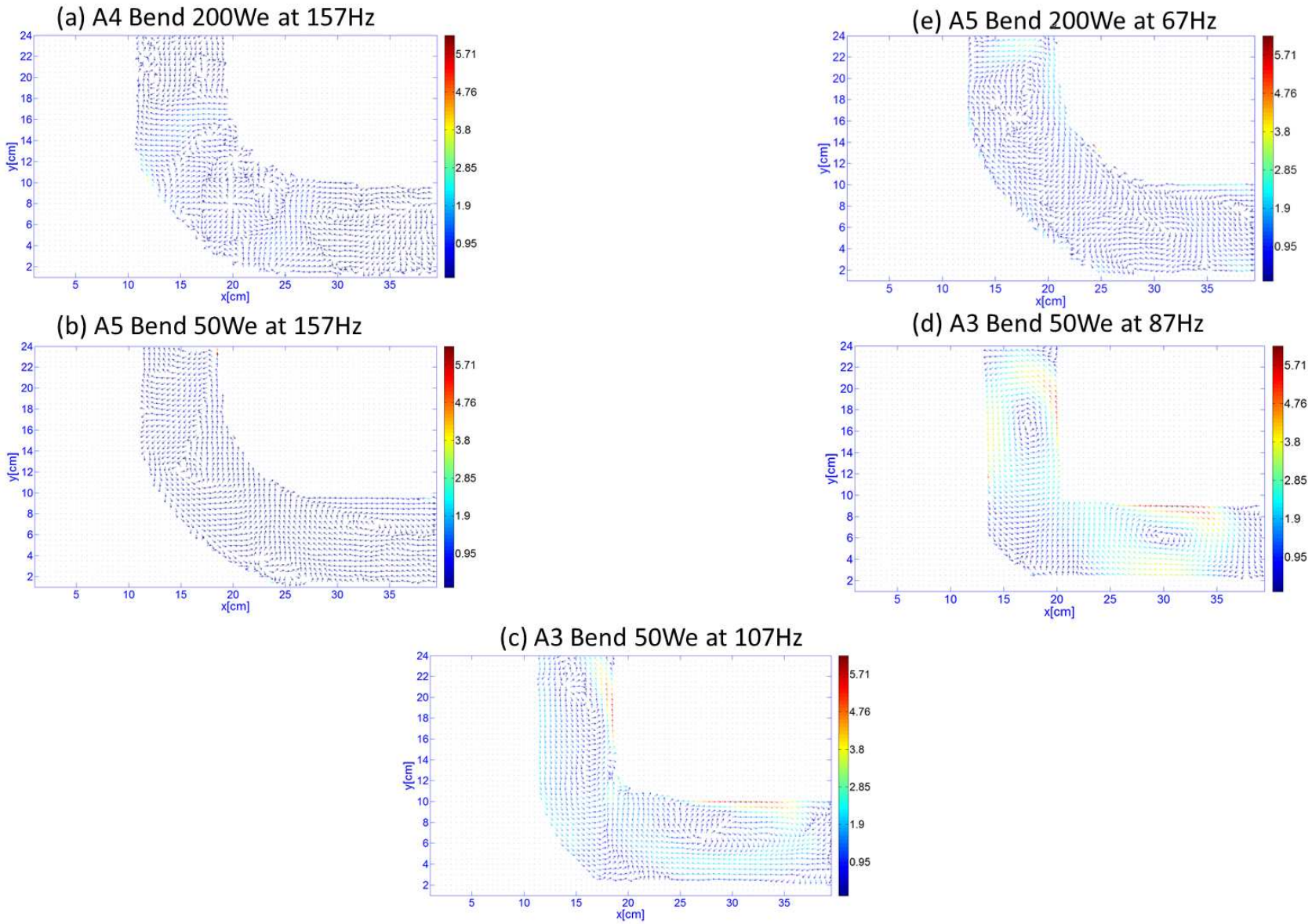

Figure 7-4: The Orthonormal basis function of POM 3 corresponding to the results taken from a single experimental run in each of the 5 Reynolds number transmission characterisation region as shown in Figure 7-1.

The transmission loss trend in the duct bend section is shown to be largely dependent on the balance between the strengths of the secondary Lyne type circulation and streamwise vortices. It is noted that the formation of the Lyne type circulation is attributed to the radius of curvature of the duct bend system. As such, in order to accurately characterise the oscillating flow, the radius of curvature of the bend has also to be taken into consideration numerically. In 1891, Strouhal conducted investigations on vortex shedding of a flow pass circular wire strips. He introduced a non-dimensional parameter in order to predict the frequency of the vortex generated. The non-dimensional number has since been known as the "Strouhal" number and has been used extensively in fluid dynamics to study the vortex formation for a flow pass bluff bodies. In the past century, the Strouhal number has also been used to characterise the effects of rounding the edges of sudden expansion and constriction discontinuities in unidirectional duct flow systems, as well as with oscillating flow systems[195, 196]. Since the acoustic transmission losses is suspected to be due to the loss attributed to flow separation, the Strouhal number was adopted in an effort to characterise the acoustic transmission loss behaviour. The Strouhal number is given as:

$$St = \frac{2\pi f \cdot ROC}{\mathrm{V}_{aa}} = \frac{ROC}{\xi_{aa}} \tag{7.6}$$

The Strouhal number plotted against the Acoustic Transmission Ratio is shown in Figure 7-5.

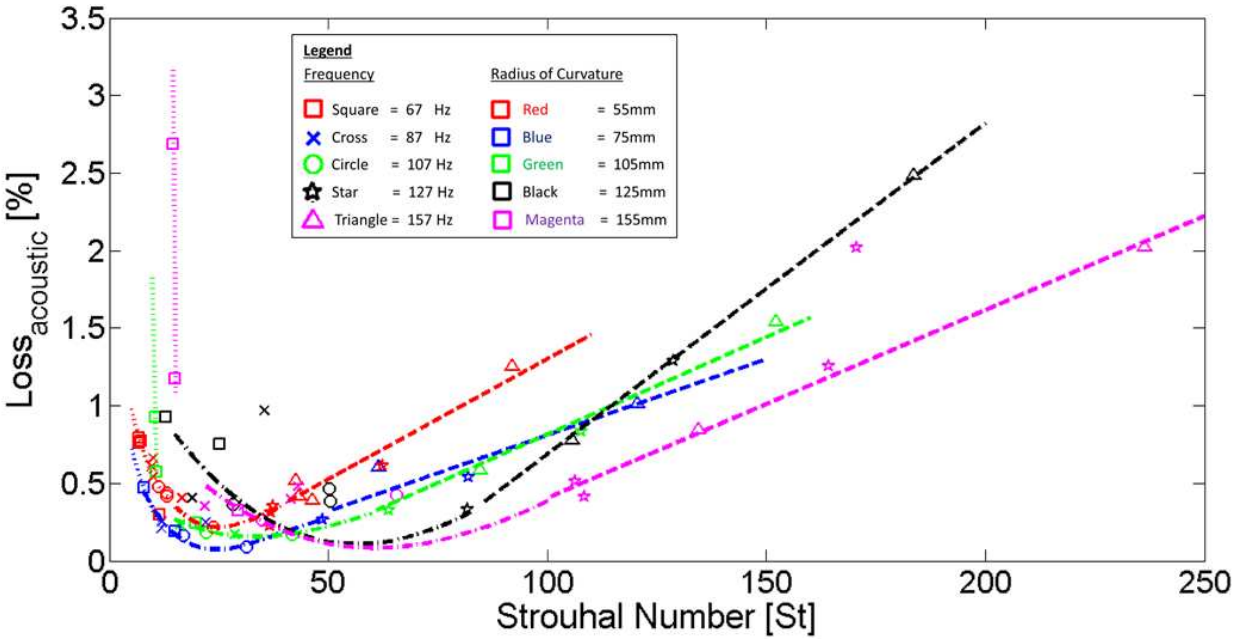

Figure 7-5: The acoustic transmission losses vs. the Strouhal number. The viscous dominated region is indicated by '- - - 'trend lines, the transition region by '-.-.-'and inertia dominated, turbulent region by '….' trend lines.

The Strouhal number can also be interpreted as the ratio of the radius of curvature of the duct bend to the acoustic particle displacement. As such, the results are the reversed of Figure 7-1 and Figure 7-3, in which smaller Strouhal number would correspond to the inertia dominated region (Region **(d)** and **(e)** in Figure 7-1) and larger Strouhal number to the viscous dominated region (Region **(a)** and **(b)** in Figure 7-1). The Strouhal number shows a minimum "U" shape transmission loss trend that is skewed towards the inertia dominated region. It is found that this skew is a function of the radius of curvature of the bend. Sharp bends such as A1, A2 and A3 shows a narrower "U" shaped transmission loss trends while larger radius of curvature bend (A4 and A5) have wider "U" shaped transmission loss trends. This Strouhal transmission loss behaviour divides the investigated range of Strouhal number into 3 regions:

Region 1: The inertia dominated region: The transmission loss behaviour shows a steep linear increase in transmission loss for a decrease in Strouhal number. Here the steep increase in transmission losses is attributed to non-linear turbulence.

Region.2: The transitional region: The transmission loss trend shows a minimum parabolic curved section in which the optimum acoustic transmission Strouhal number exists

Region.3: The viscous dominated region: The increase in transmission loss behaviour is linearly proportional to the increase in Strouhal number.

The skewed velocity profile is reflective of the effects of different radius of curvature on the transmission loss behaviour. In the viscous dominated region, it is shown that the decrease in viscous losses is linearly proportional to the decrease in Strouhal number. This linear relationship is brought about from the balance between the secondary Lyne type circulation and the formation of Streamwise vortices. As the Strouhal value decrease passed the viscous region into the transitional Region 2, it is shown that an increasing V_{ac} or ξ_{ac}(represented by a decrease in Strouhal number) results in a large increase in the secondary Lyne type circulation strength resulting in the parabolic decrease in transmission loss until the optimum transmission point is reached. The optimum transmission point for each radius of curvature duct bend is shown to be different. By Increasing the V_{ac} or ξ_{ac} till it passes the optimum transmission point has resulted in the increment of the transmission loss due to the convected energy loss for the generation of the secondary Lyne type flow circulation itself.

Figure 7-5 also shows that in the transition region, the longer bends (A4 and A5) have a much wider parabolic transmission loss curve as compared to the sharper bends (A1, A2 and A3). The width of the parabolic transmission loss curve is indicative of the bend's radius of curvatures effectiveness in promoting flow separation and convecting energy from the primary oscillating flow for the formation of secondary circulating structures. Duct bends with smaller radius of curvature have sharper discontinuities, often leading to only one point of flow separation in the mid axial length of the bend's curvature. This leads to the formation of two strong, counter-rotating circulation structures located at both the upstream and downstream of the flow separation point. The strength of these secondary

circulations is shown to be closely related to the amplitude of oscillation. This close convective relationship is reflected by the narrow width of the Strouhal-transmission loss parabolic trend for sharper bends. In larger radius of curvature duct bends however, the oscillating is similar to that over a bluff body. Flow separation may occur at multiple tangential points along the longer radius of curvature of the bend. This in turn may lead to the formation of multiple, weak secondary circulating structures. The duller discontinuity coupled with the spread of the convected energy into the multiple secondary circulations causes the relationship between the oscillating amplitude and the strength of the secondary circulation to be weaker. This is again reflected by the wider parabolic transmission loss curve for the longer bends in this regime.

Figure 7-5 also shows that a critical Strouhal number exists for each radius of curvature that divides the transitional Region 2 from the non-linear turbulent Region 1. The "trip" to non-linear turbulence occurs when V_{ac} or ξ_{ac} exceeds a certain threshold for a given radius of curvature. It is interesting to observe that secondary flow strength are more sensitive towards the change in oscillating amplitude; the "trip" to non-linear turbulence occurs at a much larger value of V_{ac} or ξ_{ac}. It is shown that the "trip" to turbulence occurs first in the oscillation in duct bends with larger radius of curvature. It is postulated that as the oscillating amplitude increases, the multiple secondary circulation grows in size and intensity. These secondary circulation acts as energy "pathways" for kinetic energy to be convected from the primary oscillation into these secondary circulations. As such, the convective transmission losses are proportional to the number of secondary circulations. It is also suspected that as these secondary circulations grow larger, they tend to interact with each other causing mixing and other non-linear turbulent effects. Both the additional convection and non-linear turbulence cause the steep gradient of acoustic transmission loss in this Region 1.

It is observed that the optimum Strouhal number occurs around 55-60 for the larger radius of curvature bend (A4–A5) and at approximately 25-30 for the sharper bends (A1-A3). Since the investigated acoustic particle displacement range was the same for the 5 investigated bend (as shown in Figure 7-3) and that the increment of radius of curvature was kept at a nearly constant interval, the irregular intervals of optimum Strouhal number for the 5 investigated bend suggest that an optimum acoustic transmission radius of curvature exists. This suggests that the Strouhal number is not the optimum non-dimensional parameter for characterising the acoustic transmission through duct elbow bend systems. One possible reason for this is because the hydraulic radius of the duct was not taken into consideration.

It is noted here, that the hydraulic radius and the radius of curvature of the bend play an important role in the dynamics of flow through curve ducts. The ratio of the hydraulic radius to the radius of curvature is known as the slender ratio. In his investigation of flow systems through curved ducting sections, Dean used the product of the Reynolds number with the square root of the slender ratio in order to characterise the flow regimes. This non-dimensional number became known as the “Dean” number. In taking inspiration from the Dean number, the product of the Strouhal number and different powers of the slender ratio was investigated in order to find the best fit for the acoustic loss transmission behaviour for all of the investigated radii of curvature of duct bends.

Similar to the Dean number, it was found that the non-dimensional number that gives the best fit for the acoustic transmission loss trend is given by the product of the square root of the slender ratio with the Strouhal number. This new parameter shall be referred to as the “Strouhal-Dean” number and is given as:

$$St_{Dean} = \frac{2\pi f \cdot ROC}{V_{aa}} \times \left[\frac{r_h}{ROC}\right]^{\frac{1}{2}} \tag{7.7}$$

This trend is plotted in Figure 7-6. Here, it is shown that the results of the experimental runs on the 5 duct bends, with different radius of curvature, have been approximately aligned together. This is observed more so in the transition region (similar to Region 2 of Figure 7-5) where the optimum transmission point lies. There are still slight divergences observed in between the acoustic transmission loss trends for the different radius of curvature in the non-linear turbulent region and the viscous dominated region. It is shown in the inertia dominated region that the critical Strouhal-Dean number in which the oscillation trips into the non-linear turbulent region is different for bends with different radius of curvature. The increase in acoustic transmission loss in this region is shown to approximately have the same linear gradient. In the dominated viscous region of Figure 7-6 however, the increase in linear acoustic loss trends shows a divergence in gradient. This implies that there are better non-dimensional parameters which can be used to characterise the oscillation in the inertia dominated, nonlinear turbulent region and the viscous dominated region respectively. There are a number of hypothesis made in interpreting the acoustic transmission loss trends given by the chosen non-dimensional numbers. The results from this investigation will be compared against the results and characterisation obtained from literature in order to verify the results obtained here.

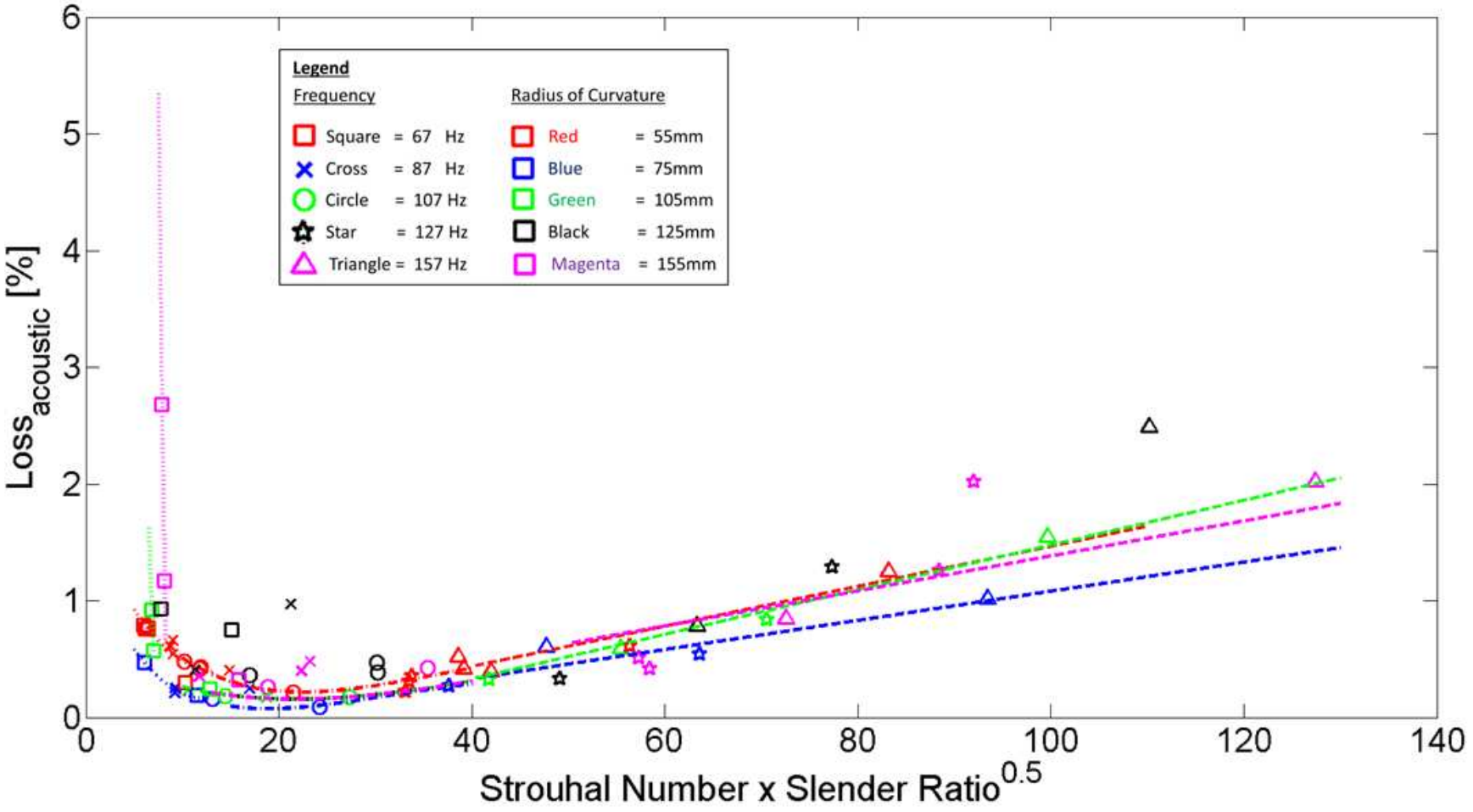

Figure 7-6: (Strouhal Number x Slender Ratio^0.5) vs. Acoustic transmission loss. The viscous dominated region is indicated by '- - -'trend lines, the transition region by '-.-.-'and inertia dominated, turbulent region by '….' trend lines.

7.2 Results Comparison with Literature Review

In has previously been noted in Chapter 4, that an acoustic wave propagating through a duct section below the first cut-off frequency, propagate only in the plane wave mode of propagation. In this case, the cut-off frequency for a square cross section is given by:

$$f_{c,square} = \frac{\mathrm{c}}{2d_h} \approx 3.8\ \mathrm{kHz} \tag{7.8}$$

The cut-off frequency for this investigation is approximately 250 times larger than the highest investigated frequency. As such, the primary oscillating component of the flow should show characteristics of a 2-D plane wave system. The flow visualisation of the bends in which the straight sections of the duct was also recorded in the PIV measurement shows the investigated wave to exhibit almost plane wave like behaviours just upstream and downstream of the bend (Figure 5-3). This plane wave mode of propagation gets distorted the closer it gets to the bend's curvature. It has also been observed that the onset distance for the distortion of the acoustic plane wave mode of propagation both in the upstream and downstream sections of the duct is equivalent to the duct's hydraulic diameter. This is also in agreement with Rostafinski[56] prediction for the distance required for an acoustic flow to return to its original mode of propagation after passing through a discontinuity. The confirmation of the plane wave mode of propagation justifies the use of the VWD technique as well as the PWD technique in the acoustic transmission investigation. It also shows that the wave propagating in the straight duct section can be modelled as a one dimensional wave and that the straight square cross section of the duct has negligible contribution to the distortion caused by the curved section of the bend.

The PIV results show that the acoustic wave propagating through the curved section of the bend is definitely not a plane wave. The effects of the skewed velocity profile combined with POM 3's coherent

structure circulation suggest that the velocity profile of the acoustic propagation through the curved section is possibly 3 dimensional in nature. It is also observed that the secondary flow circulation promotes the skewed behaviour of the velocity profile. The combination of these behaviours matches the Lyne type secondary circulation found in the cross sectional plane of oscillating flows through curved duct systems. Since these secondary coherent structures are also known to be 3 dimensional in nature, it is believed that the results in this investigation are a reflection of the Lyne type secondary circulation in the axial cross sectional plane. This may serve to give a more holistic understanding of these 3-dimensional, secondary coherent structures. It is also noted, that since this is the first time acoustic wave transmission have been made in the axial cross section plane of curved duct systems, the match in secondary flow behaviour would also give a basis for which to compare the results obtained in this investigation with those in literature of the spanwise cross sectional plane.

The first literature comparison is made with oscillating flow propagating through straight duct. This comparison is made in order to identify the effects of the flow in straight ducts systems for the investigated range that will provide a basis for differentiating the effects of the flow through the curved section of the bend. Literature on oscillating flow through straight duct systems are numerous covering different regions corresponding the amplitude and wavelength of the oscillation as well as the different duct sizes[216-219]. Ohmi et al sought to compile these findings and characterise the different behaviours of the secondary flow in the cross section of the duct[215]. They introduced the Womersley Number vs Dean Number chart. The oscillation characterisation of the different regions in the chart was based on exhaustive experimentation, numerical simulation and comparison with the previous works done[220]. The full characterisation of the chart has previously been shown in Chapter 1.3.2. The results from this investigation have also been plotted in the Womersley number vs. Reynolds number Chart shown in Figure 7-7. Here, it is shown that the range of acoustic waves used in this investigation corresponds to the Weakly turbulent region of the chart. The Weakly turbulent region however, is

indicative that the turbulence persist throughout the oscillating period, unlike the conditionally turbulent region where the secondary flow only appear in certain phase of the oscillation. It also shows that the oscillating amplitude and the hydraulic diameter used in this investigation are both sufficiently large to allow for weak turbulent behaviour, even without the presence of the bend's discontinuity. The weak turbulence is suggestive of the formation and propagation of streamwise vortices within the acoustic Stokes layers. This reaffirms the explanations given in the previous chapter regarding Figure 7-1, Figure 7-3, Figure 7-5 and Figure 7-6 for the transitional and viscous dominated regions of the oscillation. It must be noted here, that neither the Womersley number nor the Reynolds number takes into account the radius of curvature of the bend which will predictably promote the "trip" to turbulent flow at lower Reynolds numbers. It is predicted that the oscillations closer to the turbulent boundary (Re=400α) were tripped into the turbulent region due to the bend's radius of curvature discontinuity.

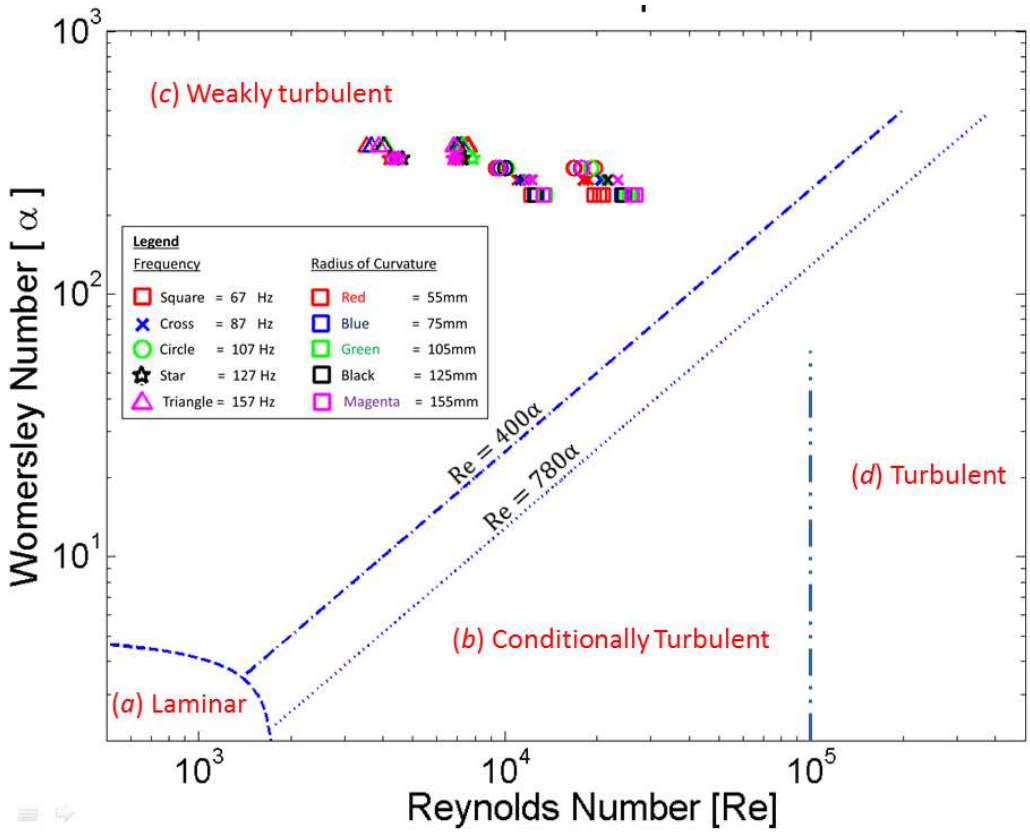

Figure 7-7: Womersley vs. Reynolds Number Oscillation Flow Characterisation for Acoustic Resonator Duct systems[221]

Literature shows that the investigated range of acoustic oscillation corresponds to Weakly turbulent regime in which turbulence is confined within the Stokes boundary layer. The distortion of the velocity profile thus only occurs in the Stokes layer. The freestream oscillating velocity profile remains largely plug like (plane wave mode of propagation). Based on this, the investigation results are now compared with literature for oscillating flow through duct bends. The literature review on acoustic transmission through duct bends systems have been given in Chapter 1. It has also been shown that there has yet to be any investigation done for the range of investigated oscillation and for duct systems with such a relatively large hydraulic diameter. As such, literature comparison is better made with investigation of oscillating flow through curved and/or coiled ducting systems which have similar oscillating amplitude and duct size[78, 85, 86]. It is interesting to note, that a large part of this literature on this subject focussed on the secondary circulation in the spanwise cross section of the curved duct. Yamane et al began a compilation on previous studies of oscillating flow through curved duct systems[85]. In addition, they also conducted numerical analysis and limited experimentation to determine the transition between Dean and Lyne type secondary flow circulation in the cross section of the curved ducting systems. In an effort to compile the results of oscillating flow through curved ductings, Yamane et al emulated Ohmi's characterisation technique[220] by introducing the Womersley vs Dean number chart in order to characterise the cross sectional secondary flow behaviour of oscillating flow in curved/coiled duct systems.

The range of investigated acoustic oscillation is shown to correspond to the Lyne type secondary circulation $\left[\frac{\alpha^3}{De} > 30\right]$. The Lyne type secondary circulation consists of two pairs of counter-rotating vortices; the first pair confined within the oscillation's Stokes layer, and the second pair in the core, mid-section of the duct. The Lyne type secondary circulation behaviour is in agreement with all of the PIV investigation results which show skewed velocity profile as the flow propagates through the curved

section of the duct bend. The effects of viscosity were found to be confined within the thin Stokes boundary layer, leaving the oscillation in the core region of the duct to be nearly inviscid. Since a large portion of the oscillating flow was shown to be within the inviscid core region of the duct, this oscillating region is also known as "inertia dominated" region. The boundary for the inertia dominated region is given by:

$$\frac{\alpha^2}{De} = 0.655 \tag{7.9}$$

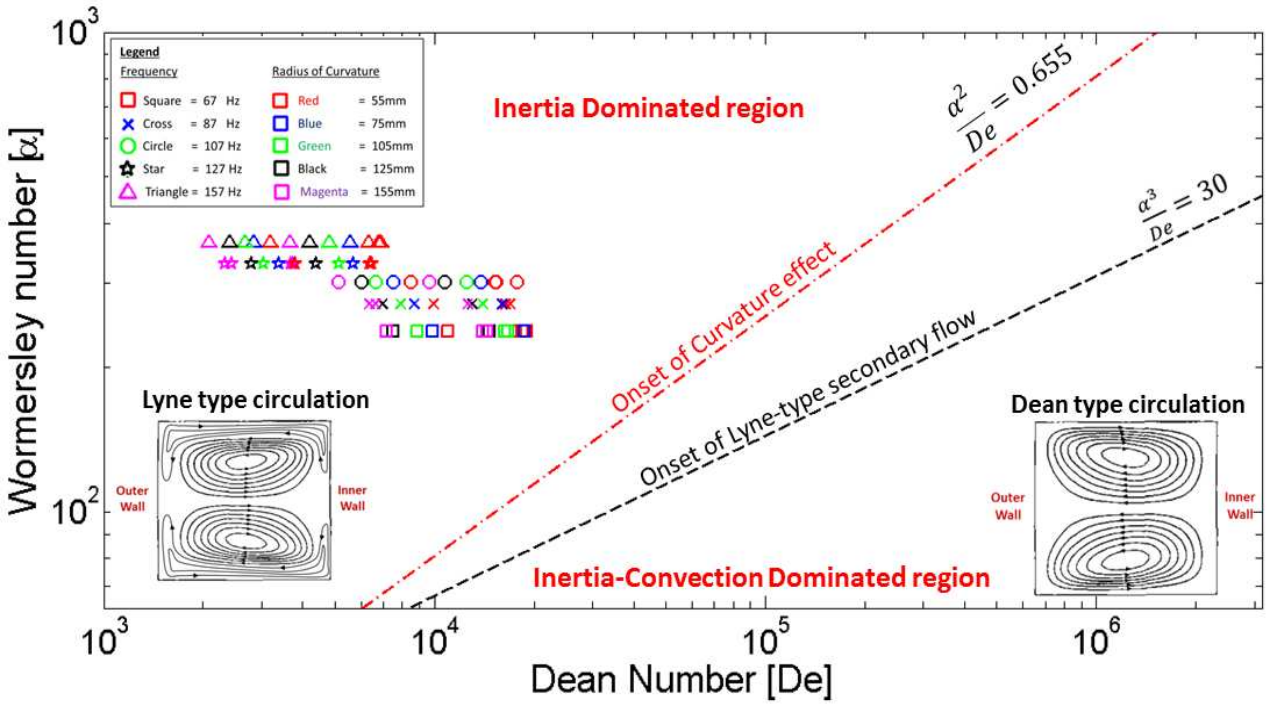

Figure 7-8: Flow characterisation based on Yamane et al's Womersley vs Dean number chart[85]

This non-dimensional number is representative of the ratio of inertia to the convection of energy in forming secondary flow systems. Sudo et al, continued Yamane's works[85] by conducting extensive experimentations and flow visualisation investigations in order to verify their numerical analysis[86]. This resulted in a more comprehensive Womersley vs. Dean number chart. Sudo et al's chart successfully identified the Dean and Lyne secondary flow oscillating regions as well as the three complex transitional regions between them. In addition to this, Sudo et al, also included contour lines indicating

the intensity of the secondary flow into the Womersley vs. Dean chart. The intensity of the secondary circulation is computed from the circulation's kinetic energy content based on numerical simulations. This represents the close quantitative comparison that would allow the verification of the streamwise viscous vortices vs. the Lyne secondary suppression circulation theory described in the previous sub-chapter. Figure 7-9 shows the result from this investigation, superimposed on the extrapolated Sudo et al's Womersley vs. Dean number chart.

The Figure 7-9 chart shows only a minor change in the Womersley number across the range of investigated frequencies. The incident velocity amplitude and the duct's radius of curvature are thus taken to be the determining factor for the strength and intensity of the Lyne type secondary circulation. It is thus shown, that the Lyne type secondary circulation is proportional to the Dean number for the investigated range of oscillations. The Lyne type secondary circulation intensity for optimum acoustic transmission is shown to be approximately, $\Psi \approx 70$. By matching the magnitude of transmission loss found in Figure 7-6 with secondary circulation intensity in Figure 7-9, it is shown that by increasing the Dean number just pass the optimum transmission value corresponds to a sudden increase in acoustic transmission loss. The maximum transmission loss corresponding to the inertia dominated region occurs when the secondary circulation strength is approximately $\Psi = 120$. By further increasing the Dean number past $\Psi = 100.$, the acoustic transmission loss is shown to decrease again. This can be explained by the number of secondary flow circulation in accordance to the radius of curvature of the duct bend and the amplitude of the oscillation as shown in Figure 7-10

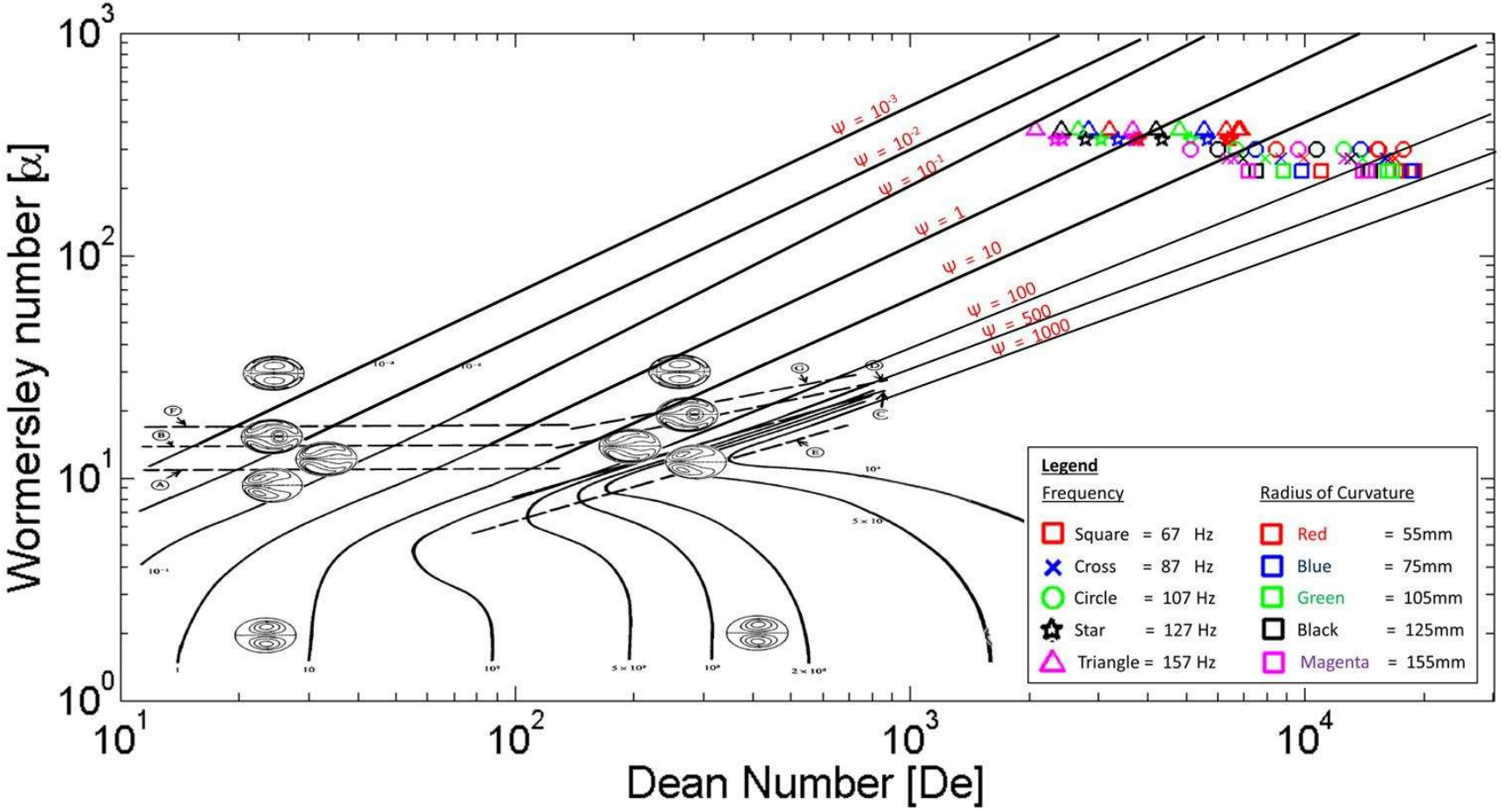

Figure 7-9: The PIV investigation results plotted in the Womersley vs. Dean number characterisation chart. The contour lines denotes the strength of the Secondary flow for each region of the chart.

In this inertia dominated region (Region **(e)** of Figure 7-1), it is suspected that for longer duct bends, flow separation occurs at various tangential angles along the radius of curvature of the bend. This causes the formation of multiple secondary circulation structures. The number of separation points is also dependent on the displacement amplitude of the oscillation. Large displacement amplitude has less flow separation points but tend to form stronger, larger circulating structures (Figure 7-10(c)). Smaller displacement amplitudes tend to have more flow separation points with smaller, weaker circulating structures (Figure 7-10(d)). The strength of secondary circulation intensity is inversely proportional to the number of secondary circulation structures formed. The convective losses are thus determined by both the number of secondary circulating structures as well as their circulation intensities. These secondary circulating structures may interact and mix with each other causing the turbulent oscillation to be more non-linear in nature, creating a large increase in transmission losses.

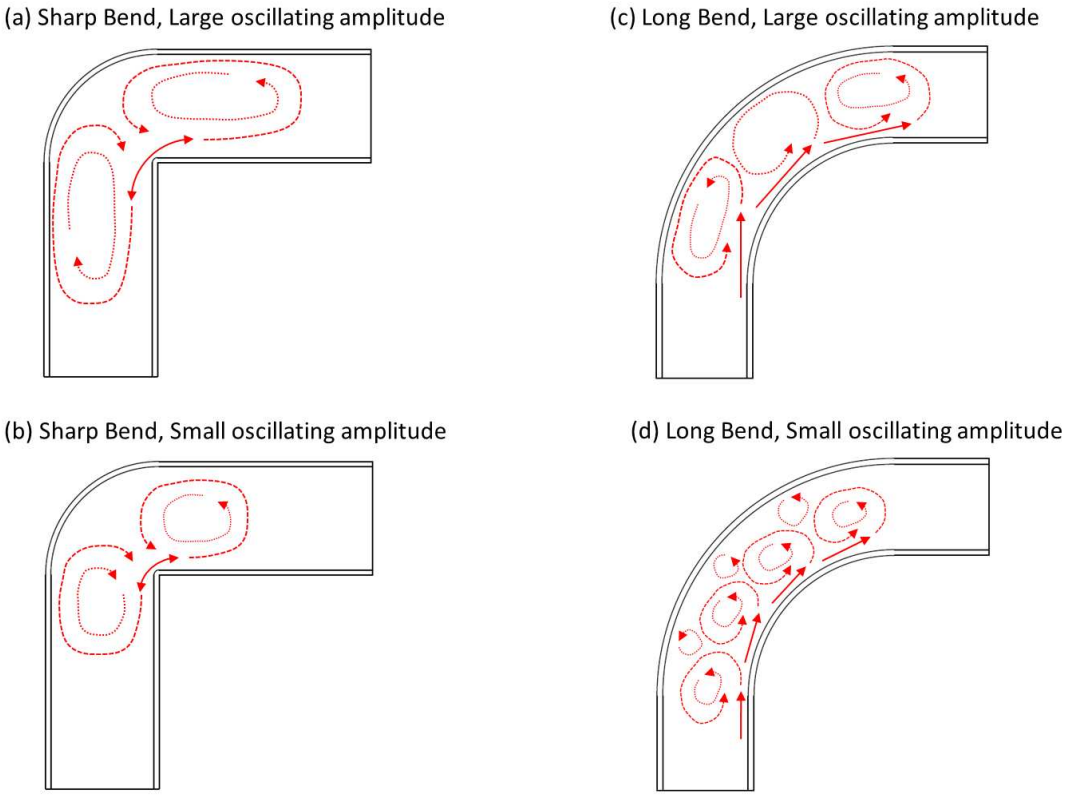

Figure 7-10: The formation of different secondary flow structures based on the amplitudde of oscillation an the radius of curvature of the bend.

The largest acoustic transmission loss that occurs in Region **(a)** and Region **(e)** of Figure 7-1 corresponds to the bends with the larger radius of curvatures (A4 & A5 Bend). In the viscous Region **(a)**, the formation of these multiple secondary circulation constitutes the weakening of the Lyne type secondary circulation, and hence the increase in streamwise vortices and viscous transmission losses. In Region **(e)** however, the large transmission loss is due to both the increase in convective losses due to the formation of multiple circulating structures and the interaction of these structures leading to the non-linear loss effects.

Flow separation in sharper bends occurs close to the middle of the bend's radius of curvature (Figure 7-10(a) & (b)). The flow separation in turn is shown to form two large, strong coherent structures which can be seen in the axial plane (refer to Figure 7-4 **(d)**). These coherent structures are shown to promote the Lyne secondary circulation in the cross sectional plane and, as such, correspond to the increase in secondary flow intensity. The maximum secondary circulation intensity is shown to occur along the line:

$$\frac{\alpha^2}{De} = 0.41 \tag{7.10}$$

It is found that the Dean number does not give the best representation for the inertia dominated region of the oscillation through the duct bend systems. Based on this investigation, the Reynolds number (Figure 7-1) and the Strouhal-Dean number (Figure 7-6) give a better fit for the transmission loss behaviour in the inertia dominated region.

7.3 Transmission Loss Characterisation

This research has identified 3 main loss mechanisms that determine the overall acoustic transmission through duct bend systems for this "high amplitude, low frequency" investigated range. These losses include

1. The viscous frictional losses encouraged by turbulences in the Stokes boundary layer.
2. Kinetic energy convection to form secondary circulation structures that is ultimately dissipated through the energy cascade mechanism.
3. Non-linear turbulence caused by high inertia flow separation and the flow distortion through the mixing of several secondary circulations system.

The POD analysis of the PIV investigation has successfully produced a flow visualisation that identifies both the convective and non-linear turbulent loss mechanism. The resolution used for this PIV investigation however, was unable to identify the viscous loss mechanism visually. This turbulent boundary layer driven loss mechanism however, is evident from the numerical analysis of the acoustic transmission loss behaviour, and from the comparison of results with that of literature. The acoustic oscillation range in this investigation however, proved to be unique. As such, the quantitative comparison of results with that from literature relied heavily on the use of non-dimensional parameters in order to characterise the acoustic transmission loss behaviour. The non-dimensional parameter found to best represent the acoustic transmission into a single trend line was found to be the product of the Strouhal number with the square root of the slender ratio. This non-dimensional parameter was mathematically found to coincide with twice the ratio of the Womersley number squared to the Dean number.

$$\frac{\alpha^2}{De} = \frac{St_{Dean}}{2}$$

$$= \frac{\omega}{2 \cdot V_{aa}} [r_h \times ROC]^{\frac{1}{2}} \quad (7.11)$$

These parameters also represent the ratio of the inertia strength of the oscillation to the convection of kinetic energy away from the oscillation. Here Inertia and convection represents 2 of the 3 main loss mechanism of the oscillation. Based on literature, the entire investigated range of acoustic oscillation lies within the Weakly turbulent flow regime. This corresponds to turbulence confined within the Stokes boundary layer of the oscillation which contributes to an increase in skin friction and thus viscous loss. It was found previously that an increase in Lyne type secondary flow circulation corresponds to a decrease in acoustic transmission loss. Literature has shown that spanwise flow circulation have been known to suppress streamwise turbulent circulations and thus viscous losses. As such, the acoustic transmission loss is strongly dependent on the balance between convection of energy to generate these viscous suppression secondary circulations and the inertia force which can cause flow separation at the bend's discontinuity leading to non-linear turbulences, thence leading to large transmission losses. The selection of the St_{Dean} not only gives a good a fit for the acoustic transmission loss trend, but also represents the balance between two main opposing loss mechanisms. $\frac{\alpha^2}{De}$ is plotted against the percentage acoustic transmission loss and is shown in Figure 7-11. Although, St_{Dean} is twice the value of the, $\frac{\alpha^2}{De}$., the acoustic transmission loss trend behaviour remains exactly the same for both of these parameters. This can be seen by comparing Figure 7-6 and Figure 7-11 . As such, in order to standardise the use of non-dimensional parameters, $\frac{\alpha^2}{De}$ will be noted as the "new Strouhal Dean"number and is represented by:

$$St_{0.5\,Dean} = \frac{St_{Dean}}{2} = \frac{\alpha^2}{De} \quad (7.12)$$

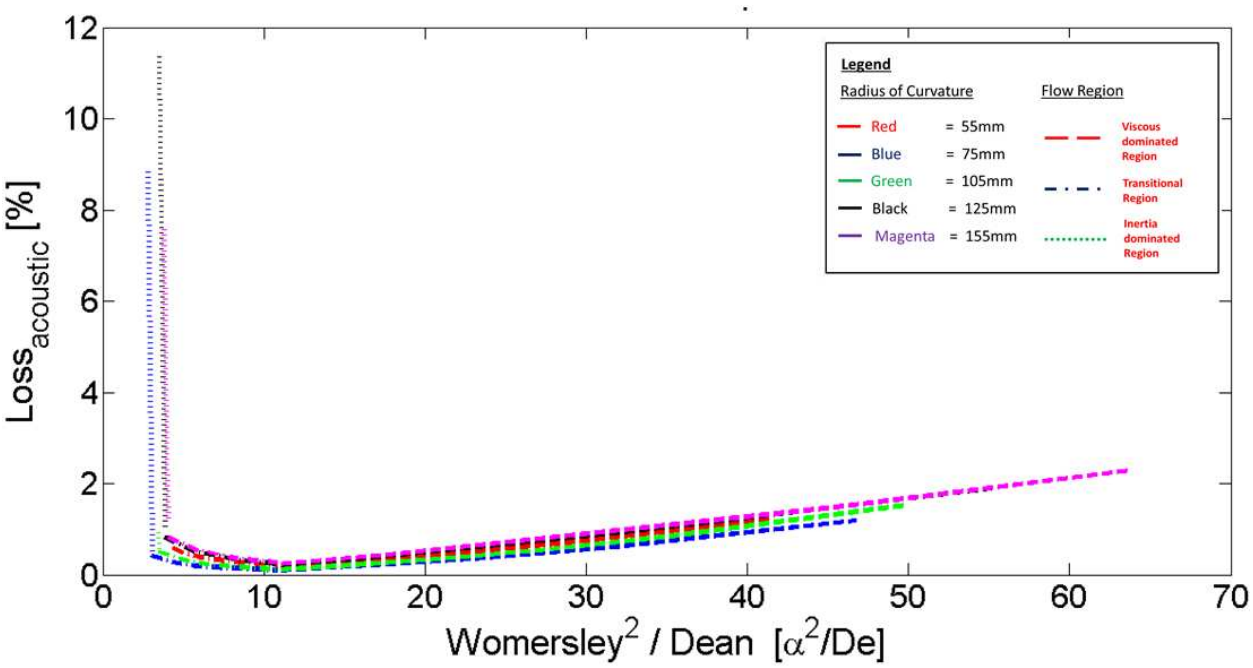

Figure 7-11: The percentage acoustic transmission loss plotted against the (Womerley number^2/ Dean number). The viscous dominated region is indicated by '- - -'trend lines, the transition region by '-.-.-'and inertia dominated, turbulent region by '….' trend lines.

Figure 7-11 also shows the extrapolated results in both extremes of the inertia dominated region and the viscous dominated regions based on the linear trend line behaviour of each respective region. This linear acoustic transmission loss trendline behaviour are expected to hold true, as long as the investigated oscillation falls within the Weakly turbulent regime, corresponding to the Womerley-Reynolds number chart shown in Figure 7-7. This allows for a limited prediction of the acoustic transmission loss outside the investigated range of this experiment.

It was found that the logarithmic plot of the $St_{0.5\,Dean}$ vs. acoustic transmission loss gives a much clearer representation of the trends in each loss region discussed previously. Figure 7-12 shows this logarithmic plot as well as the secondary circulation behaviour expected in each of the discussed loss regions.

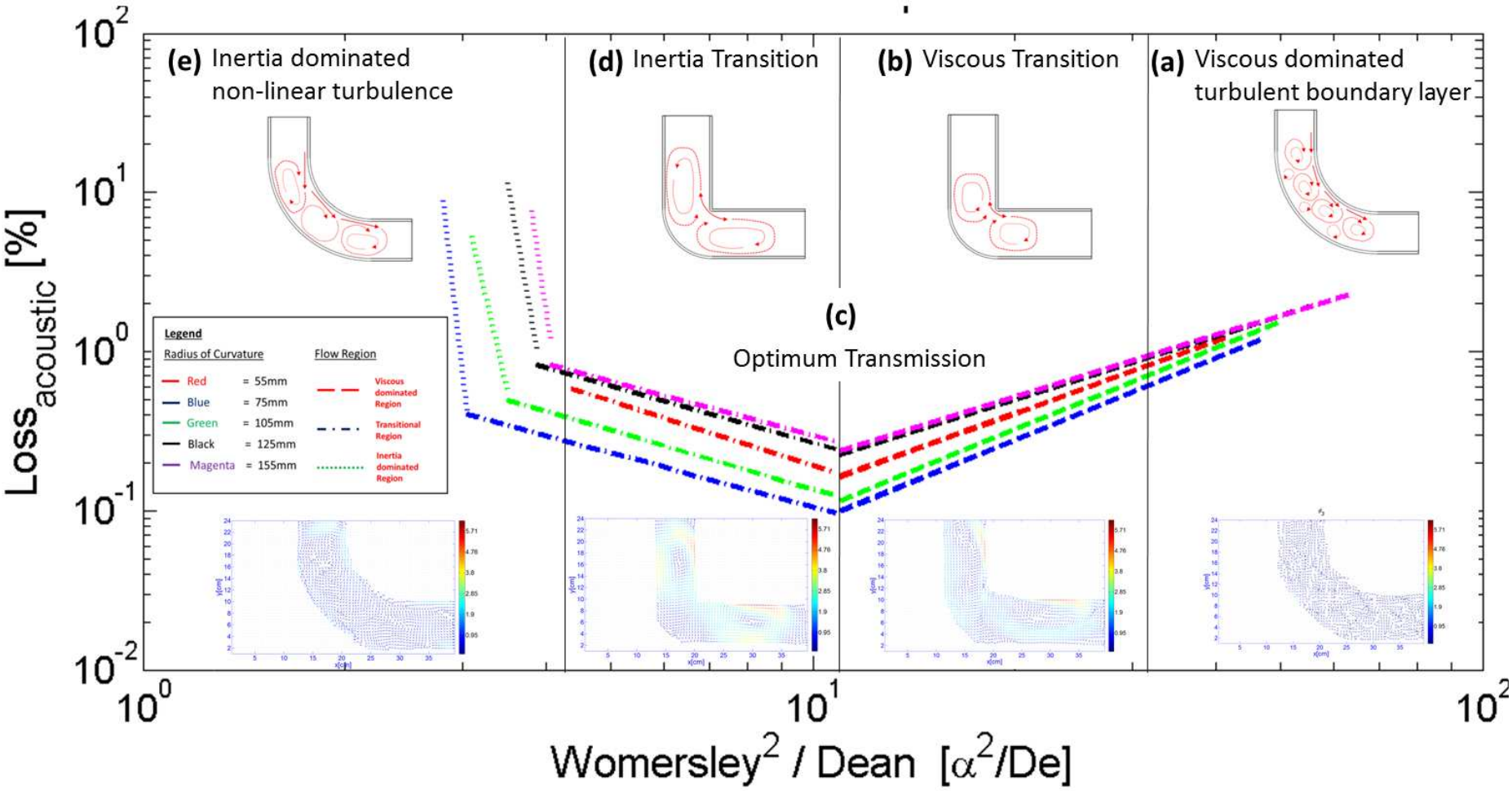

Figure 7-12: The loglog plot of the percentage acoustic transmission loss plotted against the (Womerley number^2/ Dean number). The viscous dominated region is indicated by '- - -'trend lines, the transition region by '-.-.-'and inertia dominated, non-linear turbulent region by '….' trend lines.

Here, the log-log plot of the acoustic transmission loss vs. $St_{0.5\,Dean}$ can again be divided in to the same 5 regions described by the Reynolds number vs. acoustic transmission loss plot. The behaviour of each of these 5 regions are summarised below:

Region (a)

This is the viscous dominated region containing low amplitude and high frequency oscillations. The oscillations in this region belong to the Weakly turbulent regime in which turbulence is confined within the Stokes boundary layer. The unsteady conditions within the boundary layer induce the sweep and ejection processes which promote the formation of streamwise vortical structures within the boundary layer itself. These streamwise circulations in the boundary layer are known to increase skin friction and thus viscous flow losses of the system. In the axial plane, it is shown that oscillating velocity profile is larger at the inner wall of the duct bend. This promotes flow separation at several tangential angles of the bend, based on the amplitude of the oscillating particle displacement. Flow separation in turn, causes the formation of weak secondary circulating structures which are observed in the axial plane. The formation and characteristics of these secondary circulations are shown in Figure 7-13 which gives the 3rd POD mode (POM 3) for two examples of oscillating flow in this region. In longer bends, the formations of multiple secondary circulations are observed. The circulation structures in longer bends are shown to interact with each other, thus causing an increase in turbulence (Figure 7-13[a1 & b1]) . This observation in the axial plane is indicative that the Lyne type secondary circulation is either not formed or is too weak to suppress the formation of the streamwise circulations. The oscillation in this region is thus dominated by the turbulent Stokes boundary layer's viscous losses. In addition to this, the turbulence generated by the unsteady circulation, shown in the axial plane of the longer bends, also contributes to the acoustic transmission loss. This explains the higher transmission losses in this region of the longer bends. Figure 7-13[a2 & b2] shows the transitional flow between Region(a) and Region(b).

[A5 Bend] 57Hz (POD Mode 3)

(a1)

(a2)

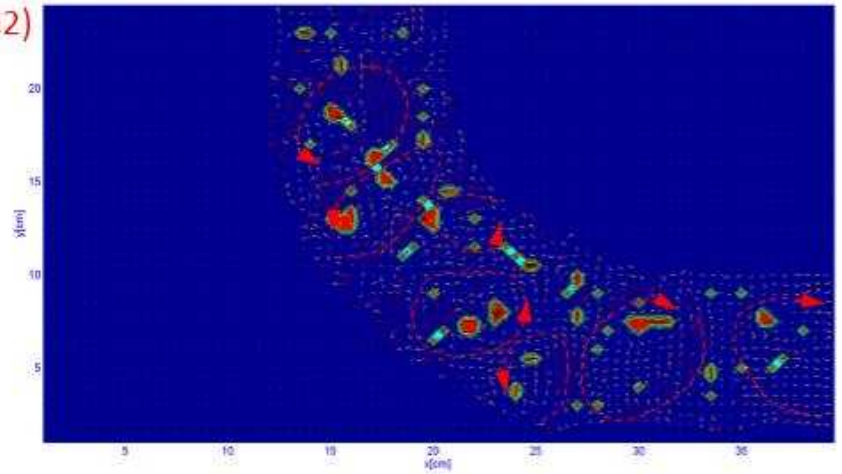

[A4 Bend] 127Hz (POD Mode 3)

(b1)

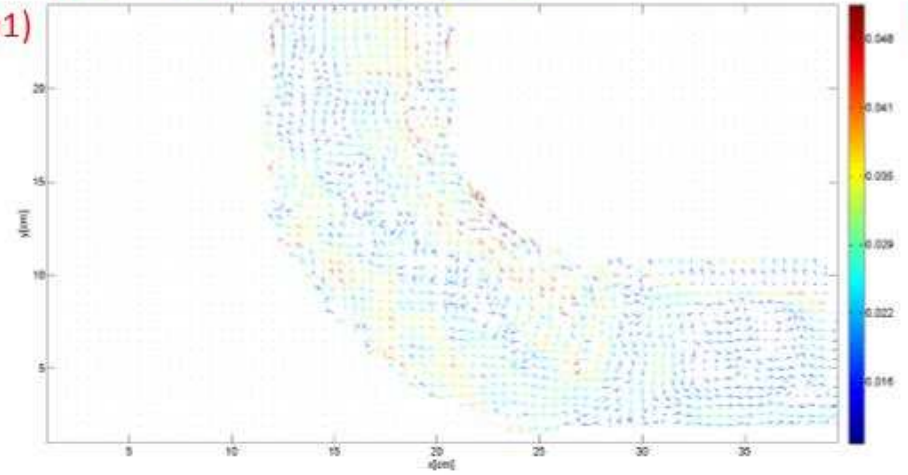

(b2)

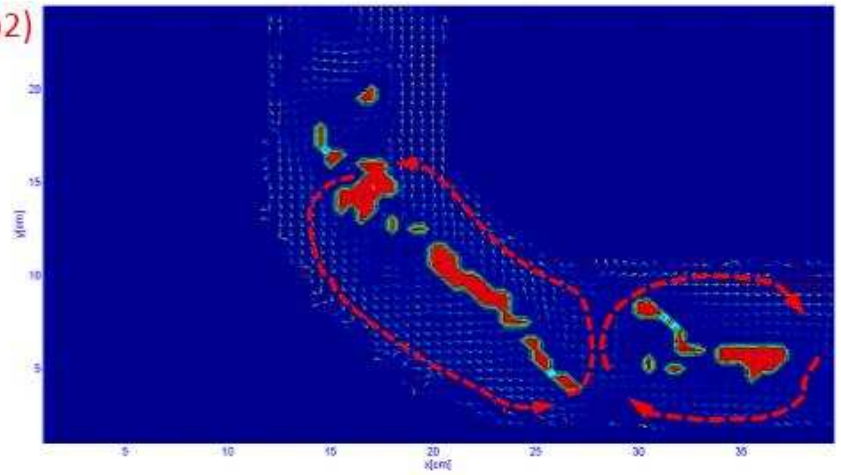

Figure 7-13: Region (a) – Examples of Proper Orthogonal Mode 3 for oscillating flows found in Region (a) of *Figure 7-12.* The velocity amplitude of the vectors shown in (a) are represented by colours indicated by the colour scale (velocities given in ms^{-1}). (b) shows the result of the vortex detection technique discussed in Sub-Chapter 6.4.

Region (b)

In continuation from Figure 7-13[a2 & b2] to Figure 7-14, it is observed that the secondary circulation starts to form larger circulating structures that are more defined and steadier with time. The pair of counter-rotating vortical structures shown in Figure 7-14, corresponds to the Lyne circulation in the axial plane. The acoustic transmission loss in this region is determined by the strength of these Lyne type secondary circulation in order to suppress the increase in skin friction caused by the Streamwise vortices in the turbulent boundary layer. The strength of the secondary flow is dependent on the conditions which promotes flow separation. It is can be deduced from Figure 7-12, Figure 7-13 and Figure 7-14 that the number of flow separation points, along the curvature of the bend, is inversely proportional to the oscillation's amplitude, wavelength and bend's radius of curvature. As the value of $St_{0.5\,Dean}$ decreases along this region, it is shown that the secondary flow in the axial plane becomes more prominent and steadier with time. This transition is shown from Figure 7-13[a2 & b2] to Figure 7-14 [a1 & b1]and finally to Figure 7-14 [a2 & b2]. The sharper bends (A1, A2 and A3) are shown to have only one flow separation point in the middle of the curvature. This produces two large circulation structures which are coherent in time. These circulations induce higher axial velocity amplitudes near towards the inner wall of the bend's curvature. Such oscillating behaviour matches the characteristics of the spanwise Lyne type circulation in curved ductings. These observed secondary circulations are thus taken to be the axial plane representation of the spanwise Lyne type secondary circulations. It is shown that as these axial circulation increases in intensity, the acoustic transmission loss is reduced. This confirms that the Lyne type secondary circulation acts as a suppressive mechanism for the formation of the streamwise vortices. As such, the increase in intensity of the Lyne type secondary circulation in this region, leads to further suppression of the streamwise vortices which, in turn, reduces the viscous losses of the system and thus the overall acoustic transmission loss of the system.

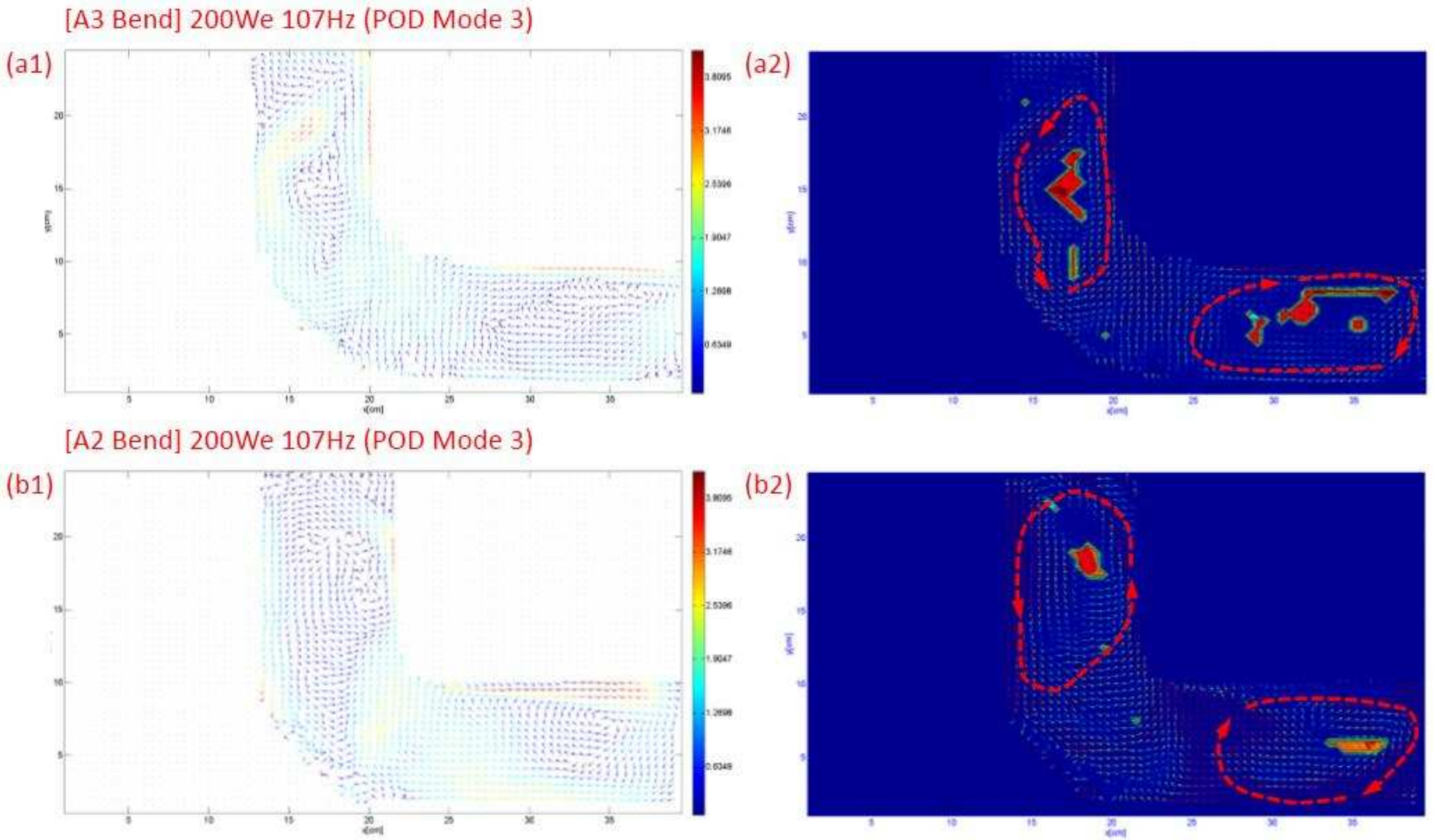

Figure 7-14: Region (b) – Examples of Proper Orthogonal Mode 3 for oscillating flows found in Region (b) of *Figure 7-12.* The velocity amplitude of the vectors shown in (a) are represented by colours indicated by the colour scale (velocities given in ms^{-1}). (b) shows the result of the vortex detection technique discussed in Sub-Chapter 6.4.

Region (c)

This is the optimum region for acoustic transmission through duct bends for Weakly turbulent oscillations. It is noted that while the Lyne type circulation acts as a viscous suppression mechanism, the convection of kinetic energy away from the primary oscillation to form these secondary circulation, also contributes to the acoustic transmission loss of the system. Region **(c)** represents the $St_{0.5\,Dean}$ value in which the optimum amount of kinetic energy is convected for the formation of the Lyne type secondary circulation for viscous loss suppression, without incurring additional convective losses. This balance allows for the loss possible acoustic transmission loss through the duct bend system.. Figure 7-6, Figure 7-11 and Figure 7-12 all show the that although the trend lines for all the investigated radius of curvatures are a match, they are not aligned together. Again the acoustic transmission loss offset between the radii of curvature trend lines suggests that an optimum radius of curvature exists for the Weakly turbulent oscillation region. The lowest percentage transmission point is taken for each of the bend's radius of curvature and plotted against their respective slender ratio. This is shown in Figure 7-15.

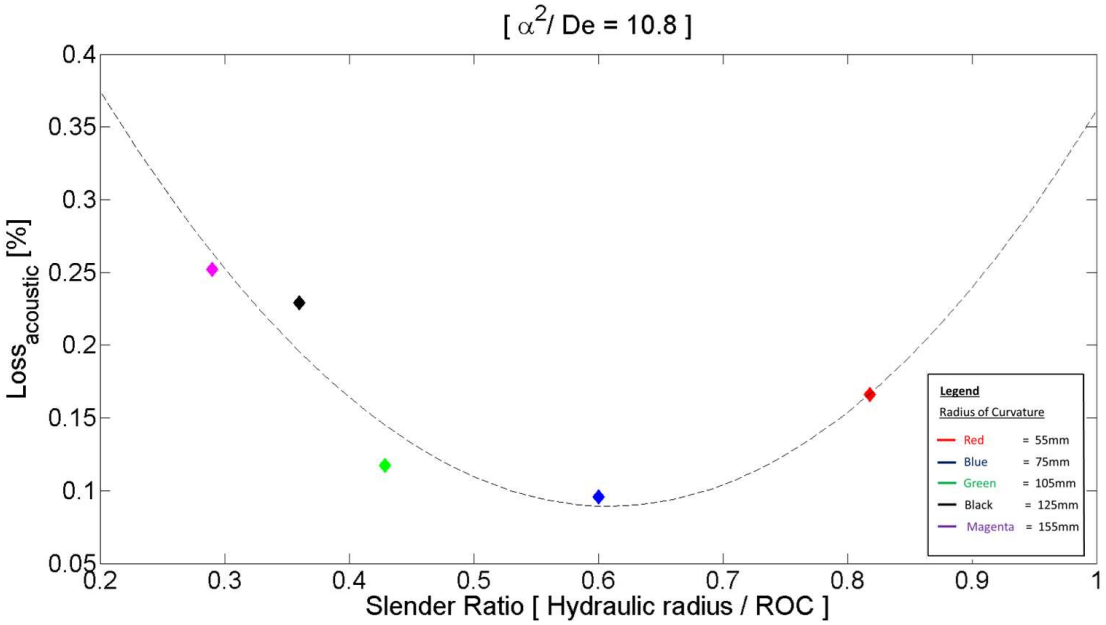

Figure 7-15: Optimum radius of curvature for acoustic transmission in the Weakly turbulent oscillation regime.

The optimum acoustic transmission slender ratio is shown to be approximately 0.6. This corresponds to the A2 Bend with radius the radius of curvature of 75mm. The lowest attainable acoustic transmission loss from this setup is approximately 0.1%.

Figure 7-14 gives the POM 3 for two examples of oscillating flow in this region. Figure 7-14[a1 & b1] corresponds to the oscillating flow with the lowest transmission losses amongst all the investigated runs. The pair of counter-rotating vortices are shown to be strong and well defined. It is theorised that these pair of counter-rotating vortices found in POM 3, corresponds to the main secondary circulation component which acts as a gateway for convective losses through the Kolmogorov's cascading loss mechanism discussed in Chapter 6. In the optimum region, it is shown that the secondary circulation is limited to only a pair of strong secondary circulation vortices as shown in Figure 7-14. This incidentally limits the number of gateway in which acoustic energy can be convected away from the oscillation. The circulating strength of the pair of vortices also limits the amount of energy convected to form smaller secondary circulations. As such minimal convective losses occurs in this region; the acoustic energy lost to the formation of the main pair of secondary vortices are offset by the viscous suppression it induces.

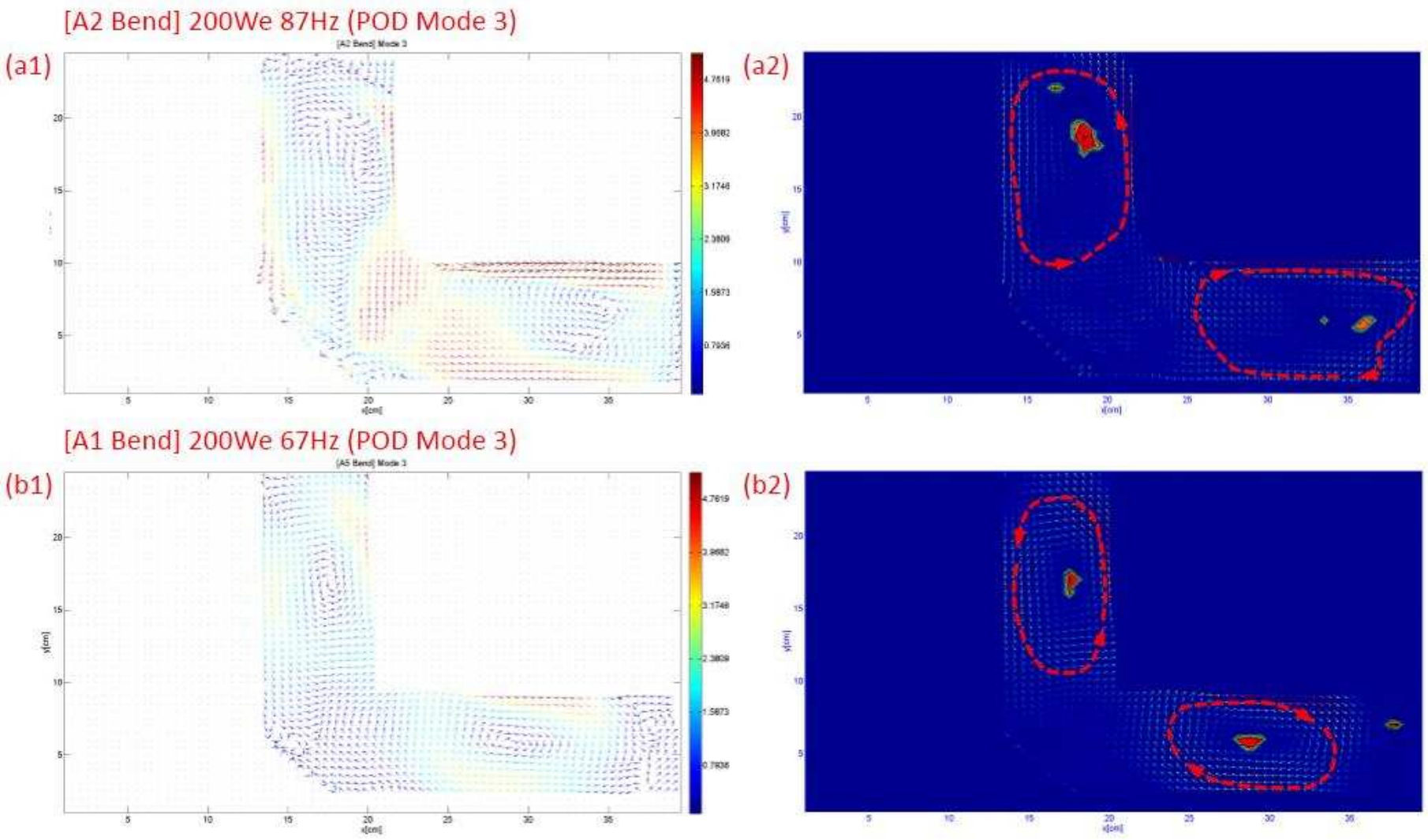

Figure 7-16: Region (c) – Examples of Proper Orthogonal Mode 3 for oscillating flows found in Region (c) of *Figure 7-12.* The velocity amplitude of the vectors shown in (a) are represented by colours indicated by the colour scale (velocities given in ms^{-1}). (b) shows the result of the vortex detection technique discussed in Sub-Chapter 6.4.

Region (d)

This region corresponds to the convection transition loss region. The further increase in secondary flow circulation strength passes the optimum at Region **(c),** corresponds to an increase in convective loss which offsets the viscous suppression it causes. This causes a net increase in acoustic transmission loss for an decrease in $St_{0.5\,Dean}$, in this region. Figure 7-16[a2 & b2] proceeding to Figure 7-17[a1 & b1], shows the increase in circulation strength of the main pair of vortices. The strongest Lyne type secondary circulation is observed to occur in this region (Figure 7-9). The large circulating structures are shown to be almost steady with time. As the $St_{0.5\,Dean}$ value is further decreased in this region, the pair of vortical structure is observed to be stretched in the axial direction(Figure 7-17[a1 & b1] to Figure 7-17[a2 & b2]),. The deformation of the main pair of counter-rotaing vortices increases the probability for the formation of smaller secondary circulations as observed in Figure 7-17[a2 & b2]. The formation of these smaller secondary circulation increase the gateway for convective acoustic losses to occur. The main pair of secondary vortices still provides viscous suppression and as such the increase in convective losses only causes a gradual increase in the net percentage of acoustic losses, for decreasing $St_{0.5\,Dean}$ value in this region.

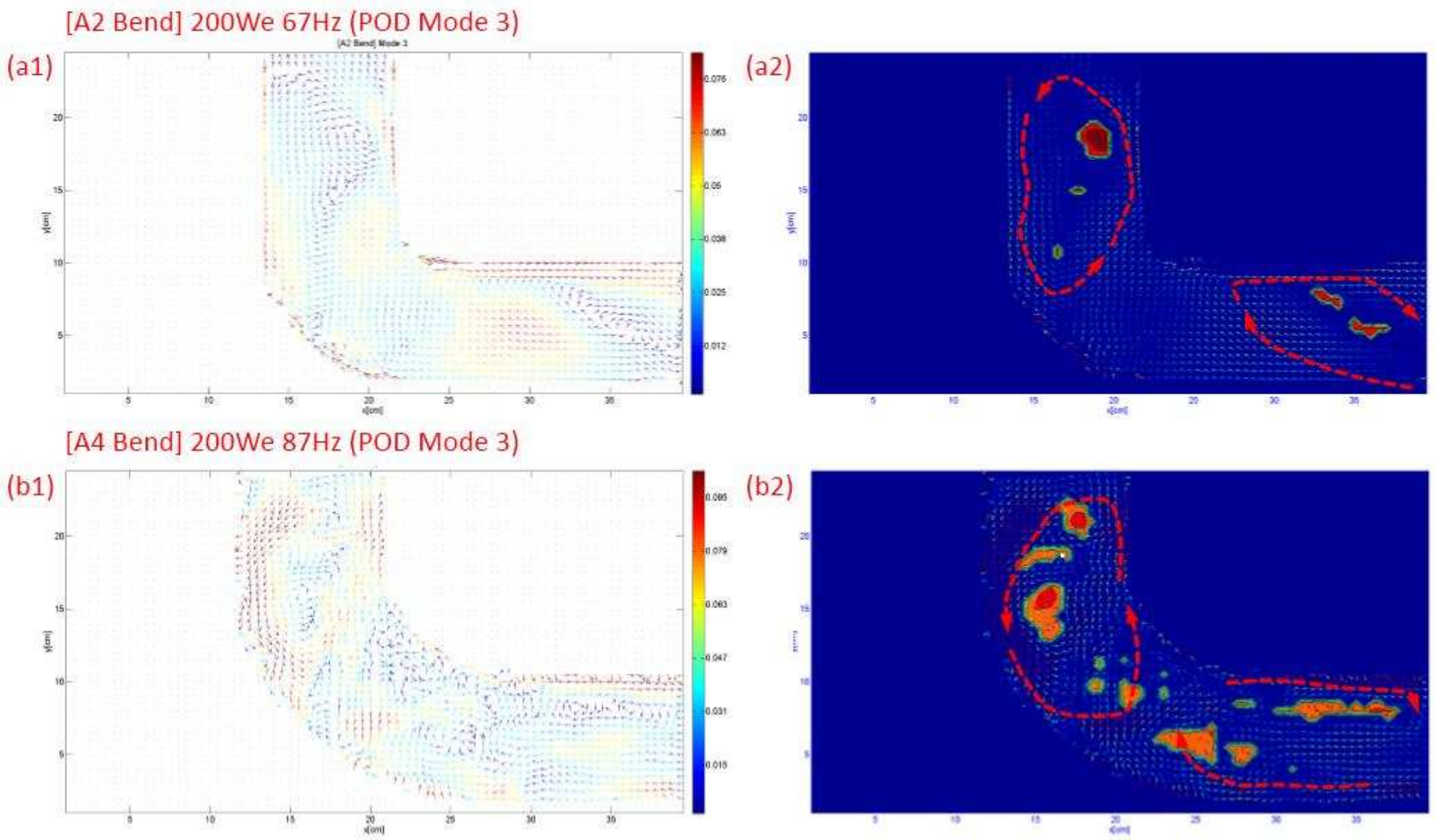

Figure 7-17: Region (d) – Examples of Proper Orthogonal Mode 3 for oscillating flows found in Region (d) of *Figure 7-12.* The velocity amplitude of the vectors shown in (a) are represented by colours indicated by the colour scale (velocities given in ms^{-1}). (b) shows the rdesult of the vortex detection technique discussed in Sub-Chapter 6.4

Region (e)

This region is inertia dominated with oscillation corresponding to the largest investigated amplitude and frequency. Interestingly, the oscillation found in this region corresponds only to the longer bends (A4 and A5). Figure 7-18 gives the 3rd POD mode for two examples of oscillating flow in this region. It is shown that the large particle displacement in this region contributes to multiple flow separation points along the bend's curvature. The number of flow separation points are less than those found in Region **(a)** due to the large inertia of the oscillations in this region. The secondary circulations caused by the flow separation points are also shown to be strong and semi-coherent with time (Figure 7-18[a1 & b1]). These circulations are however, weaker than the circulations in Region **(d)**. The production of multiple secondary circulations increases the convective transmission loss of the system. It is also observed that these secondary circulations becomes increasing unsteady and interact with each other to produce turbulent flow effects such as observed in Figure 7-18[a2 & b2] with decreasing $St_{0.5\,Dean}$ value. Both the increase in number of secondary circulating structures and their interaction to produce non-linear turbulent effects contribute to a larger increase in acoustic transmission loss for a decrease in $St_{0.5\,Dean}$ value in this region.

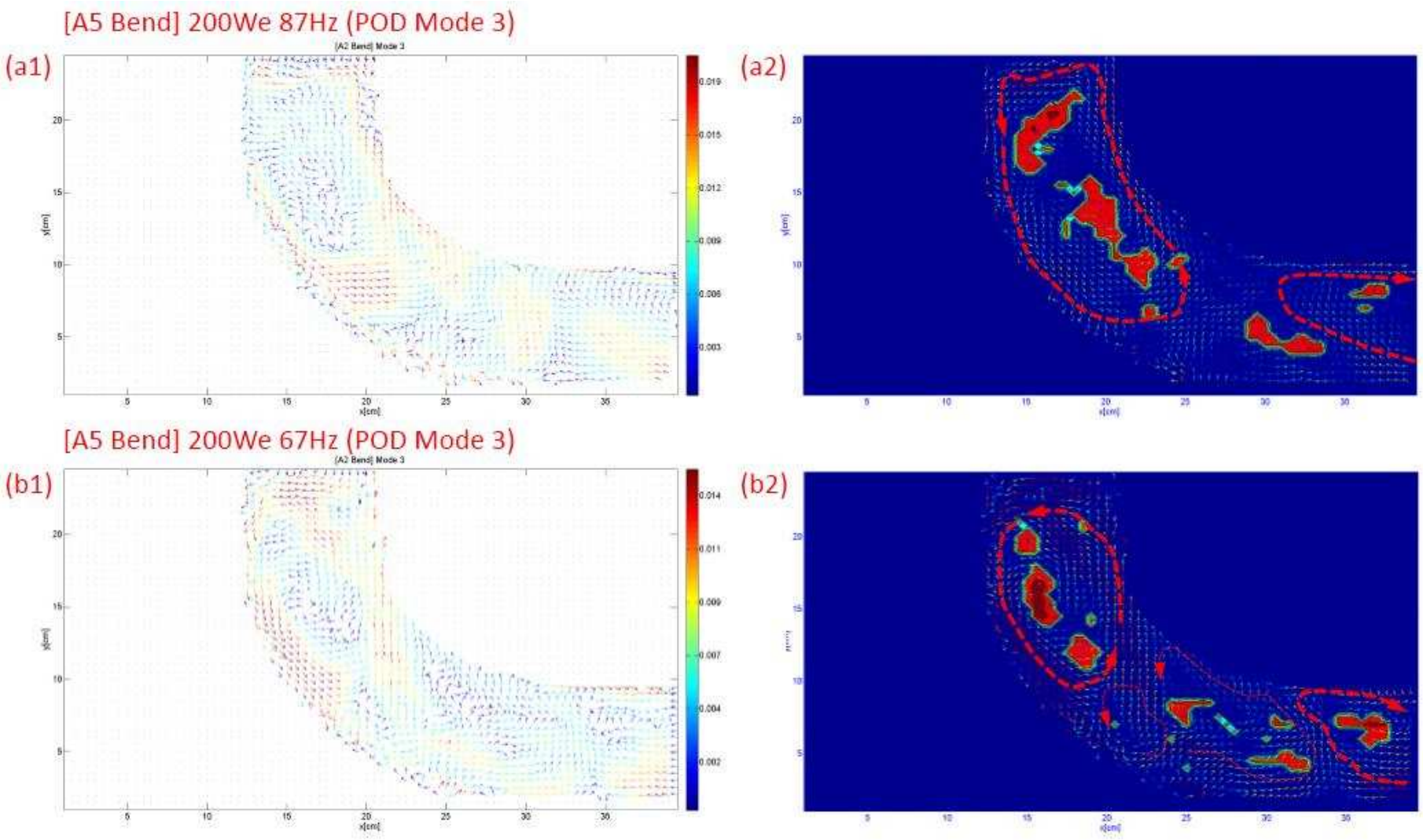

Figure 7-18: Region (e) – Examples of Proper Orthogonal Mode 3 for oscillating flows found in Region (e) of *Figure 7-12*. The velocity amplitude of the vectors shown in (a) are represented by colours indicated by the colour scale (velocities given in ms^{-1}). (b) shows the result of the vortex detection technique discussed in Sub-Chapter 6.4.

It is interesting to note that the largest transmission loss that occurs at the extreme of both the inertia and viscous dominated region of the $St_{0.5\,Dean}$ range corresponds to oscillation in large radius of curvature bends. The main difference observed between the sharper bends (A1, A2 and A3) and the longer bends (A4 and A5) are the number of flow separation points and the associated number of secondary circulating structures they produced. It is shown that the sharp bends (A1 and A2) have only one flow separation point leading to a pair of secondary circulating structures, regardless of the amplitude and wavelength of the oscillation. The larger bends (A4 and A5) have two or more flow separation points, depending on the amplitude and wavelength of the oscillation. It is shown that the radius of curvature is the largest determining factor for the number of flow separation points along the curvature of the bend. Longer bends have larger number of tangential angles for flow separation to occur. In terms of acoustic transmission, the number of secondary circulating structures represents the number of channels in which kinetic energy can be convected away from the primary flow. As such, it is of interest to minimise the number of flow separation points. Here, it is found that the sharper bend limits the number of secondary circulating structures down to two. It is thus shown that increasing the $St_{0.5\,Dean}$ value to that of Region **(e)**, the acoustic transmission loss will still follow the acoustic transmission loss trend line corresponding to that in Region **(d)**, (as shown for the A2 and A3 Bend of Figure 7-12). The Strouhal-Dean number at which the transmission loss trips into the non-linear turbulent region is plotted against the slender ratio for each of the investigated bends, and is shown in Figure 7-19.

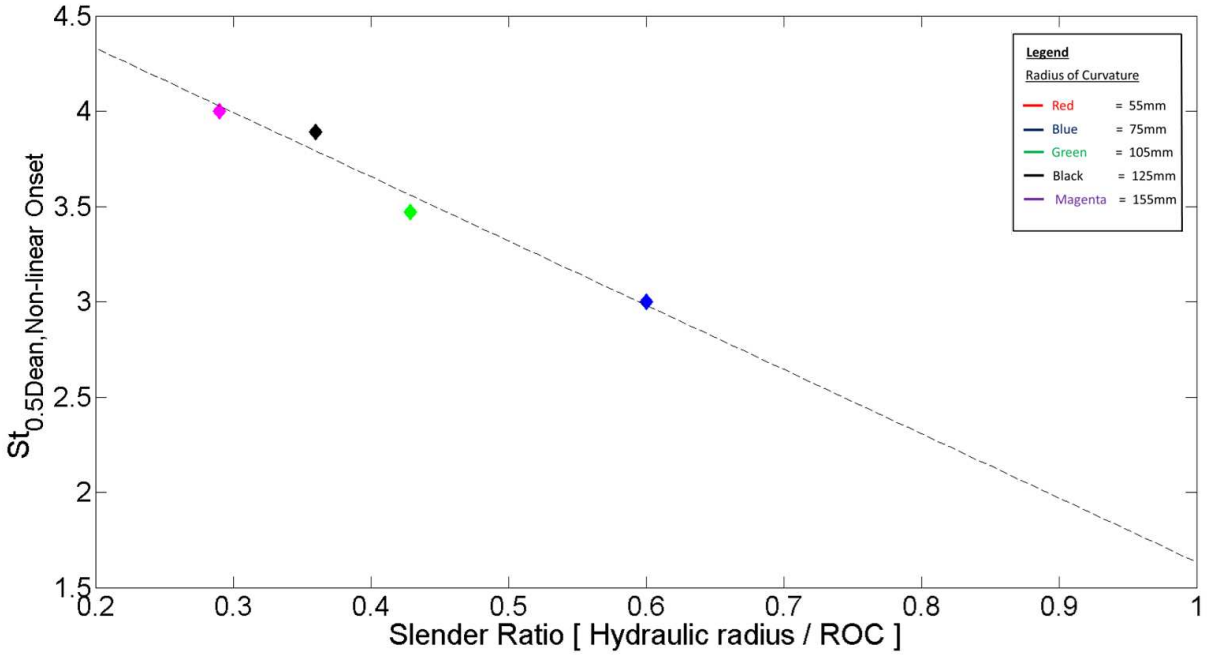

Figure 7-19: The Strouhal-Dean number for the onset of Non-linear losses with respect to the slender ratio for Bend A2 –A5.

The Strouhal-Dean number for the onset of non-linear turbulent losses can be approximated based on the slender ratio of the duct bend system using *Equation (7.13)*.

$$St_{\,0.5\,Dean,Nonlinear\ Onset} = -3.37\left[\frac{r_h}{ROC}\right] + 5.00 \tag{7.13}$$

Figure 7-11 shows that the percentage acoustic transmission loss in the non-linear turbulent region is linearly related to the Strouhal-Dean number. As such, the acoustic transmission loss above the $St_{\,0.5\,Dean,Nonlinear\ Onset}$ value can be approximated using *Equation (7.14)*.

$$Loss_{\,acoustic,Nonlinear} = -28\,St_{\,0.5\,Dean} - 92.17\left[\frac{r_h}{ROC}\right] + 140.12 \tag{7.14}$$

7.4 Chapter Conclusion

This objective of this chapter is to quantitatively characterise the acoustic transmission loss behaviour in duct bend systems. The eigenvalue for each POM are taken to represent the percentage kinetic energy content of that mode itself. POM 1 & 2 are pure oscillatory modes and their linear combination represents the acoustic wave propagating through the system. POM 3 and the higher modes are, thus representative of the energy dissipated away from the acoustic wave. The Strouhal-Dean number is shown to be the best non-dimensional parameter to model the acoustic transmission loss behaviour of the oscillating flow through curved duct bend systems. In order to understand the characteristics of the oscillation however, other well established non-dimensional number such as the Reynolds number and Strouhal number were also used.

The percentage acoustic transmission loss plotted against both the Reynolds number revealed a "U" shaped graph. Since the Reynolds number is representative of the ratio of inertia to viscosity, the curve to the left of the minimum point is attributed to be the viscous dominated region, and the curve to the right of the minimum point, to be inertia dominated. Comparison with literature has revealed that the investigated range of oscillation corresponds to the Weakly turbulent oscillation regime. The transmission losses in this regime are mainly attributed to the turbulent viscous losses within the Stokes boundary layer. Literature has shown that these losses are caused by the formation of streamwise vortices within the Stokes layer due to the bursting processes. Streamwise vortices are responsible for the increase in viscous losses in the system at low Reynolds number.

It is shown however, that an increase in Reynolds number below the minimum transmission loss point leads to a decrease in transmission losses. Literature has also shown that the introduction of a spanwise Stokes layer perturbation can suppress the formation of these streamwise vortices and ultimately reduce the viscous transmission losses in the system. The increase in Reynolds number can thus be

taken to represents the increase in the inertia component of the flow, thus allowing the formation of these spanwise circulations in the curvature of the bend. The PIV results were compared with the oscillating flows in curved duct systems. It is shown that the investigated range of oscillation corresponds to the Lyne type spanwise secondary circulation Region 1. Although the PIV investigation was done on the axial cross sectional plane, the results of the primary oscillation (POM 1-2) and POM-3 both shows characteristics with matches that of the Lyne type secondary circulation in the spanwise plan. The results were thus taken as the axial plane representative of the Lyne type circulation. Comparison from literature also shows that as the strength of the secondary flow is increased from its minimum up to $\Psi \approx 70$, the net acoustic transmission loss through the system is reduced. It is thus postulated that the Lyne type circulation within the boundary acts to suppress the formation of the streamwise vortices and thus the net transmission losses in the system. The optimum transmission region corresponds to a Reynolds number range of 0.5 to 2.4 with the optimum point at approximately 1.4.

The increase in Reynolds number above the optimum transmission point corresponds to the increase in inertia energy of the oscillation, leading to non-linear turbulent effects and a further increase in acoustic transmission loss. The magnitude of acoustic transmission loss in this region is shown to correspond largely to the acoustic particle displacement and the radius of curvature of the bend. The Strouhal-Dean number takes into account both of these factors and gives a good representation of the acoustic transmission loss trend. The Strouhal-Dean number is essentially the product of the inverse of the particle displacement with the square root of the slender ratio. The percentage transmission loss plotted against the Strouhal-Dean number reveals a skewed “U” shape trend. The Strouhal-Dean number is inversely proportional to the oscillating amplitude, as such the “U” shape trend is inverted, where Strouhal-Dean number above the optimum point is representative of viscous dominated region, and the Strouhal-Dean number range below the optimum point corresponds to the inertia dominated

region. The skewed acoustic transmission loss profile, towards the inertia dominated region, is representative of the influence of the duct bend's radius of curvature on the transmission loss of the system. The optimum acoustic transmission Strouhal-Dean number is 10.8. For Strouhal-Dean number value below this optimum region, the trip to non-linear turbulent losses can be ascertained using Equation (7.13). It is thus recommended to use acoustic duct bend system within the optimum transmission point of 10.8 obtained from Equation (7.13). If larger oscillating amplitudes are propagated through the acoustic duct bend system (below the Strouhal-Dean number specified by Equation (7.13)), the acoustic transmission loss can be predicted by using Equation (7.14).

Chapter 8

The Application of the Research for Optimising Thermoacoustic Systems

8.0 The Application of the Research for the Optimisation of the Thermoacoustic system

This research has successfully studied the acoustic transmission through curved duct bend systems. As such, this chapter discusses the application of the research results in order to optimise the travelling wave thermoacoustic system. The four main parameters that determine the Strouhal-Dean number are:

- The duct's hydraulic radius and the bend's radius of curvature.
- The acoustic wave's amplitude and operating frequency;

Each of these parameters affects the acoustic transmission line circuit of the travelling wave thermoacoustic resonator system. As such, careful considerations have to be taken to ascertain the values of these parameters in relation to obtaining the desired Strouhal-Dean Number. This chapter aims at discussing the consideration that could be taken to obtain the Strouhal-Dean that would help optimise the thermoacoustic system.

Figure 7-12 and Figure 7-15 both indicate the optimum slender ratio value to be approximately 0.6. This slender ratio value gives the lowest acoustic transmission loss in both the transitional region (mid oscillating amplitude range) and inertia dominated region (high oscillating amplitude range). The slender ratio here is the ratio between the hydraulic radius and the radius of curvature of the bend. The hydraulic radius, is a function of the acoustic impedance, which is an important parameter related to the

acoustic transmission in waveguide network systems, such as the thermoacoustic resonators. The acoustic impedance is the ratio of the acoustic wave's pressure to its volumetric velocity. Since, the velocity is proportional to viscous losses, high acoustic impedances are generally preferred for the resonator ductings. The radius of curvature of the bend can then be determined from the selected hydraulic radius and the optimum slender ratio value.

The amplitude of the acoustic wave is a dependent variable since it represents both the parameter to be optimised as well as that which determines the Strouhal-Dean number. It is noted that the amplitude of the excited wave varies from 0 to its maximum, at stable operation condition. The amplitude used to compute the Strouhal-Dean number is taken when the engine achieves steady oscillating amplitudes. The other acoustic wave property that can be used to influences the Strouhal-Dean number is the operating frequency of the travelling wave thermoacoustic system. In this case, there are two considerations to determine the operating frequency of the system:

- The optimal frequency for the operation of the linear alternator
- Keeping the Strouhal-Dean number value as close as possible to $St_{0.5\,Dean} = 10.8$, in order to minimise acoustic transmission through the duct bend system.

Therefore, the axial length of the thermoacoustic resonator, which will determine the operating frequency of the system, will thus be a compromised factor between these two parameters. Another important factor is the viscous losses incurred by the acoustic wave propagating along the axial length of the resonator loop. This is again related to the design of the hydraulic radius and the acoustic impedance. In travelling wave thermoacoustic systems, which have relatively low operating temperature, and thus relatively small oscillating amplitudes, it is recommended to keep the value of the Strouhal-Dean number of the resonator duct bends to be as close as possible to, $St_{0.5\,Dean} = 10.8$. This is to ensure the maximum suppression of the acoustic transmission loss mechanisms which could

otherwise attenuate the oscillation. Thermoacoustic systems, which can acquire sufficiently high operating temperature without problems with the initial start-up excitation of the engine, can be designed for a lower Strouhal Dean number.

In the inertia dominated region (Strouhal-Dean number value <10.8), sharper bends are preferred since it limits the number of the secondary circulating structures formed, and thus constricting the convection of kinetic energy away from the acoustic wave. It is shown that although the secondary circulations are stronger in the sharper bends, the overall acoustic transmission losses are larger for the longer bends which have multiple circulating structures. In order to avoid non-linear turbulent losses however, the Strouhal-Dean number value has to be kept above the non-linear onset value given by the *Equation (7.13):*

$$St_{\,0.5\,Dean,Nonlinear\ Onset} = -3.37\left[\frac{r_h}{ROC}\right] + 5.00 \tag{7.13}$$

Figure 7-11 shows that the percentage acoustic transmission loss in the non-linear turbulent region is linearly related to the Strouhal-Dean number. In the case where the acoustic amplitude generated causes the Strouhal-Dean number value to be below that of the respective $St_{\,0.5\,Dean,Nonlinear\ Onset}$ value, the acoustic transmission losses can be approximated using *Equation (7.14).*

$$Loss_{\,acoustic,Nonlinear} = -28\,St_{\,0.5\,Dean} - 92.17\left[\frac{r_h}{ROC}\right] + 140.12 \tag{7.14}$$

Chapter 9

Thesis Summary and Conclusion

9.0 Thesis Summary and Conclusion

Summary

This research aims to optimise the SCORE-stove travelling wave thermoacoustic engine, expressly, by investigating the acoustic transmission through its curved elbow bends that are used to coil and compact its feedback resonator loop.

Preliminary investigations have shown that the traditional method of using flush mounted pressure transducers in order to compute the acoustic transmission does not work effectively. The SCORE-stove resonator ducting has a relatively large hydraulic diameter and the amplitude of the wave propagating through the resonator are also large. The combination of both of these factors causes the oscillation to be in the Weakly turbulent regime. Turbulence in this regime originates from the bursting process in the boundary layer of the oscillation. This complicates the measurements made by the flush mounted pressure transducers. In addition to this, the resolutions of the pressure transducers are also limited, causing inaccuracies in the pressure wave decomposition technique.

This research thus relies on the use of Particle Image Velocimetry for both the quantitative measurements of the acoustic velocity as well as the flow observation in order to qualitatively understand the oscillation flow behaviour in curved duct section of the bend. A new wave decomposition (WD) technique, developed based on the adaptation of the established pressure wave decomposition technique, was introduced in order to analyse the impedance and transmission of the

wave based on the velocity measurements obtained from PIV. The velocity vector field obtained from each timestep measurement allows for:

- The confirmation that the wave propagating through the duct is that of a plane wave. Measurements for the computation of the VWD were taken from the middle of the duct in the free stream region of the oscillations; and
- The use of interpolation technique in order to reconstruct the wave's amplitude along the propagation direction of the wave in the duct.

Careful use of the interpolation technique has helped in increased accuracy of the measurement as well as increasing the resolution of the measurement; hence the overall accuracy of the VWD technique as a whole. This technique has been verified experimentally as well as through the use of simulated PIV measurements.

The VWD technique was used to measure the amplitude of the incident travelling wave component propagating into the bend. Preliminary PIV results have shown that in some cases, the secondary circulations have extended to the straight duct section downstream of the bend. Undoubtedly, this would affect the downstream computation of the VWD technique.

The Proper Orthogonal Decomposition (POD) technique was thus employed to analyse the PIV results. The technique decomposes the measurement into the number of Proper Orthogonal Modes (POMs) equal to the number of timestep used. Each POM contains the velocity vector components which have the closest kinetic energy content within them. Each POM thus represents the different flow systems within the measured oscillation. POM 1 and 2 are demonstrate to have the largest percentage energy content and are the only pure oscillation modes amongst the other POMs. Due to the mathematical nature of the POD technique, both POM 1 and 2 are pure standing wave oscillations. The linear combination of both POM 1 and 2 however, resulted in the travelling wave component similar to that of

the raw PIV velocity vector field measurements. POM 1 and 2 are thus taken to be the primary travelling wave component of the system.

POM 3 shows the largest non-oscillatory flow component in all of the investigated bends. This mode shows the formation of two large vortical structures, both upstream and downstream from the midsection of the bend. These almost steady secondary flow circulations are also known as coherent structures and acoustic streaming with reference to literature. They correspond to the initial stage of the loss mechanism in which the kinetic energy is first convected from the primary oscillating component to form these steady secondary flow circulations. The flow behaviour of POMs above POM 3 becomes less distinct and appears to be random velocity vectors fields. The linear combination of POM 4 and the subsequent 50 POMs revealed the existence of additional weaker secondary vortical structures which are smaller in size from that of POM 3, but larger in number. The progressive linear combination of subsequent 50 POMs shows the existence of progressively weaker secondary vortical structures of smaller size but with increasing number. This observation matches the turbulence energy loss cascade mechanism theory described in literature.

The acoustic transmission can thus be taken as the ratio of the kinetic energy content of POM 1 and 2 over the total energy of all the POMs. The VWD technique was used to compute the amplitude of the incident travelling wave component entering the bend. Based on these quantitative results, a new non-dimensional number was developed in order to predict the acoustic transmission behaviour in duct bend systems. This non-dimensional parameter is known as the Strouhal-Dean number and is the product of the Strouhal number with the square root of the slender ratio.

$$St_{0.5\ Dean} = \frac{(r_h \times ROC)^{\frac{1}{2}}}{2\,\xi_{aa}} \tag{9.1}$$

Similar to the Strouhal number, this new parameter is also the ratio of a characteristic length to the acoustic particle displacement. In this case, the characteristic length is the square root of the product of the hydraulic radius and the radius of curvature of the investigated duct bend. The investigated range of acoustic waveguide propagation system corresponds to the Weakly turbulent oscillation flow regime. In this flow regime, non-linear effects are confined within the boundary layer of the oscillating flow. The Strouhal-Dean number divides the investigated acoustic transmission loss range into 3 regions: The viscous dominated region, the inertia dominated region, and the optimum transitional region between them.

The viscous dominated region is the range of Strouhal-Dean number, $St_{0.5\,Dean} > 20$. The large viscous losses in this region are attributed to the turbulent bursting process which occurs in the boundary layer of the oscillation. The turbulent bursting process is cyclic and involves the convection of fluid momentum away from the solid boundary for the first half of the cycle (ejection processes) and the down rush of fluid back onto the solid boundary during the next half of the cycle (sweep process). This in turn leads to the formation of the streamwise vortices. This causes the formation of the self-sustaining streamwise vortices. The sweep process is responsible for the increase in the effect of skin friction leading to greater viscous losses. The increase in viscous losses is balanced by the formation of spanwise vortices supressing it. The propagation of the acoustic wave within the curved section of the duct causes higher oscillating velocity amplitudes to be skewed towards the inner wall of the bend's curvature. This uneven axial velocity distribution causes the formation of secondary circulations within the cross section region of the plane – these secondary circulations are known as the "Lyne type" circulation. Literature has shown that spanwise perturbation can suppress the formation of streamwise vortices and thus reduces viscous losses in duct systems. The PIV results have qualitatively and quantitatively shown that the stronger and more prominent the Lyne type secondary circulation becomes, the lower the transmission losses becomes in the viscous dominated region. It is noted, that

the convection of acoustic energy for the formation of these spanwise secondary Lyne type circulation is offset by the larger viscous loss suppression it causes, and thus does not contribute to any additional transmission loss in the viscous dominated region.

The range of Strouhal-Dean number between $4 < St_{0.5\,Dean} \leq 20$ corresponds to the transitional region between the viscous dominated region and the inertia dominated region. This transitional region also represents the optimum Strouhal-Dean number range for acoustic transmission through duct bend systems. The optimum Strouhal-Dean number is representative of the secondary Lyne type circulation strength that gives the maximum viscous loss suppression before incurring additional convection losses of its own. Here the optimum Strouhal-Dean number is,

$$St_{0.5\,Dean,\ Optimum} = 10.8 \tag{9.2}$$

Above this optimum point, the increase in transmission loss is due to the increase in convectional losses for the formation of these spanwise secondary Lyne-type circulations and the residual turbulent viscous losses.

The acoustic transmission in both the viscous dominated region and transitional region are based on the balance between the viscous and convective losses of the system. In the inertia dominated region (Strouhal-Dean number, $St_{0.5\,Dean} \leq 4$), the transmission losses are primarily due to convective losses which are the precursor to non-linear turbulent losses. It is found that the tripping to non-linear turbulent losses occurs at different Strouhal-number for bends with different radius of curvatures. The transition to non-linear turbulent losses occur at a much lower Strouhal-Dean number for sharper bends (A2 and A3) as compared to longer bends (A4 and A5). The POD results shows that the sharper bends in this region have only two well defined, larger secondary circulating structures. These structures appear to originate from a single point of flow separation in the middle of the bend's curvature. In longer bends however, the three or more large secondary circulating structures are observed. These structures

appear to be unsteady with time and are less defined in nature. The larger radius of curvature bend provides a longer curvature with more tangential points for flow separation to occur as compared to the sharper bends. As such, more secondary circulations are formed in longer bends. These secondary circulations act as "pathway" for the convection of kinetic energy away from the acoustic wave. Although the two secondary circulations are stronger in the sharper bends, the overall acoustic transmission losses are larger for the longer bends which have multiple weaker circulating structures. The number of secondary circulation form within the axial plane of the bend is thus proportional to the acoustic transmission loss of the system. The number of secondary circulations is also proportional to the magnitude of Strouhal number at which the acoustic transmission loss trips to the non-linear loss region. In the sharper bends, the circulations are physically separated by the sharp corner of the bend. The two circulations have little chance of mixing. In the longer bends however, there are no defined boundaries that separates the secondary circulation structures. As such, there are higher chances for these vortical circulations to collide and mix causing further non-linear turbulence effects. The longer bends thus trip to the non-linear turbulent at loss region at a higher Strouhal-Dean number (lower oscillating amplitude) as compared to the sharper bends.

Equation (7.13) was developed in order to predict the Strouhal-Dean number in the inertia dominated range at which the oscillation trips in to the non-linear turbulent loss region. It is shown that the different in this $St_{0.5\,Dean,Nonlinear\,Onset}$ value is based on the different slender ratio of the curved duct bend used. Equation (7.14) was in turn developed to predict the transmission losses incurred in the non-linear turbulent range of the oscillation. The qualitative assessment for these high oscillating amplitude regions is essential to the design and development of new thermoacoustic devices, as it is the continuous striving to achieve larger operating amplitudes, within the acoustic resonator, at lower temperature gradients.

With these, the research objectives of qualitatively understanding the different acoustic transmission loss in curved duct bend system and the quantitative measurement and characterisation of these transmission losses trends have been reached. The results from this research is for the optimisation of the SCORE-stove in particular, and applicable to travelling wave thermoacoustic engines in general. The application of the results from this research has been discussed in Chapter 8.0. This concludes the thesis.

10.0 References

1. Belcher, J.R., et al., *Working gases in thermoacoustic engines.* The Journal of the Acoustical Society of America, 1999. **105**: p. 2677.
2. Kinsler, L.E., et al., *Fundamentals of acoustics.* 1999.
3. Gifford, W.E. and R.C. Longsworth, *PULSE TUBE REFRIGERATOR*, 1963, SYRACUSE UNIV NY.
4. Merkli, P. and H. Thomann, *Thermoacoustic effects in a resonance tube.* Journal of Fluid Mechanics, 2006. **70**(01): p. 161-177.
5. Feldman Jr, K.T., *Review of the literature on Sondhauss thermoacoustic phenomena.* Journal of Sound and Vibration, 1968. **7**(1): p. 71-82.
6. Gases, L., *7.9. THERMAL OSCILLATIONS.*
7. Rayleigh, J.W.S.B., *The Theory of Sound, vol. II*, 1878, Macmillan.
8. Rott, N., *Thermoacoustics.* Advances in Applied Mechanics, 1980. **20**: p. 135-175.
9. Ceperley, P.H., *A pistonless Stirling engine—the traveling wave heat engine.* The Journal of the Acoustical Society of America, 1979. **66**: p. 1508.
10. Hofler, T.J., *Thermoacoustic refrigerator design and performance.* 1986.
11. Wheatley, J.C., G.W. Swift, and A. Migliori, *The natural heat engine.* Los Alamos Science, 1986. **14**: p. 2-33.
12. Swift, G.W. and S.L. Garrett, *Thermoacoustics: A unifying perspective for some engines and refrigerators.* The Journal of the Acoustical Society of America, 2003. **113**: p. 2379.
13. Garrett, S.L., *Resource Letter: TA-1: Thermoacoustic engines and refrigerators.* American Journal of Physics, 2004. **72**: p. 11.
14. Atchley, A.A. and F.m. Kuo, *Stability curves for a thermoacoustic prime mover.* The Journal of the Acoustical Society of America, 1994. **95**: p. 1401.
15. Yu, Z. and A.J. Jaworski, *Optimization of thermoacoustic stacks for low onset temperature engines.* Proceedings of the Institution of Mechanical Engineers, Part A: Journal of Power and Energy. **224**(3): p. 329-337.
16. Qiu, L., et al., *Numerical simulation of the onset characteristics in a standing wave thermoacoustic engine based on thermodynamic analysis.* International Journal of Heat and Mass Transfer, 2011.
17. Migliori, A. and G.W. Swift, *Liquid sodium thermoacoustic engine.* Applied physics letters, 1988. **53**: p. 355.
18. Swift, G.W. *Malone refrigeration*. 1993.
19. Yu, Z., P. Saechan, and A.J. Jaworski, *A method of characterising performance of audio loudspeakers for linear alternator applications in low-cost thermoacoustic electricity generators.* Applied acoustics, 2011. **72**(5): p. 260-267.
20. Yu, Z., A.J. Jaworski, and S. Backhaus, *Travelling-wave thermoacoustic electricity generator using an ultra-compliant alternator for utilization of low-grade thermal energy.* Applied Energy, 2012.
21. Smoker, J., et al., *Energy harvesting from a standing wave thermoacoustic-piezoelectric resonator.* Journal of Applied Physics, 2012. **111**(10): p. 104901-104901-11.

22. Wekin, A.B.E., *Characterization and Comparison of Piezoelectric Materials for Transducing Power from a Thermoacoustic Engine*, 2008, Washington State University.
23. Wollan, J.J., et al., *Development of a thermoacoustic natural gas liquefier.* 2002.
24. Yu, Z. and A.J. Jaworski, *Impact of acoustic impedance and flow resistance on the power output capacity of the regenerators in travelling-wave thermoacoustic engines.* Energy conversion and management. **51**(2): p. 350-359.
25. Backhaus, S. and G.W. Swift, *A thermoacoustic-Stirling heat engine: Detailed study.* The Journal of the Acoustical Society of America, 2000. **107**: p. 3148.
26. Yu, G., et al., *Study on energy conversion characteristics of a high frequency standing-wave thermoacoustic heat engine.* Applied Energy, 2012.
27. Kongtragool, B. and S. Wongwises, *A review of solar-powered Stirling engines and low temperature differential Stirling engines.* Renewable and Sustainable energy reviews, 2003. **7**(2): p. 131-154.
28. Backhaus, S. and G.W. Swift. *New varieties of thermoacoustic engines*. 2002.
29. Kolin, I., *The evolution of the heat engine.* 1972.
30. Radebaugh, R. *A review of pulse tube refrigeration*. 1990.
31. Senft, J.R., *Ringbom stirling engines*. 1993: Oxford University Press, USA.
32. Walker, G. and J.R. Senft, *Free piston Stirling engines*. 1985: Springer-Verlag.
33. West, C.D., *Liquid piston Stirling engines*. 1983: Van Nostrand Reinhold, New York.
34. Walker, G., *Cryocoolers*. 1983.
35. Sugita, H., et al., *Experimental study on thermally actuated pressure wave generator for space cryocooler.* Cryogenics, 2004. **44**(6-8): p. 431-437.
36. Gardner, D.L. and G.W. Swift, *A cascade thermoacoustic engine.* The Journal of the Acoustical Society of America, 2003. **114**: p. 1905.
37. De Blok, C.M. and N. Van Rijt, *Thermo-acoustic system*, 2001, Google Patents.
38. Yazaki, T., et al., *Traveling wave thermoacoustic engine in a looped tube.* Physical Review Letters, 1998. **81**(15): p. 3128-3131.
39. Garrett, S.L. and S. Backhaus, *From" The Power of Sound.* Sound and electromagnetic waves: an anthology of current thought, 2005: p. 126.
40. Kang, H., G. Zhou, and Q. Li, *Thermoacoustic effect of traveling–standing wave.* Cryogenics, 2010. **50**(8): p. 450-458.
41. Qiu, L., et al., *Effect of pressure disturbance on onset processes in thermoacoustic engine.* Energy conversion and management, 2006. **47**(11): p. 1383-1390.
42. Sun, D., et al., *Novel Helmholtz resonator used to focus acoustic energy of thermoacoustic engine.* Applied Thermal Engineering, 2009. **29**(5): p. 945-949.
43. Swift, G. and S. Garrett, *Thermoacoustics: A unifying perspective for some engines and refrigerators.* The Journal of the Acoustical Society of America, 2003. **113**: p. 2379.
44. Luo, E., et al., *A high pressure-ratio, energy-focused thermoacoustic heat engine with a tapered resonator.* Chinese Science Bulletin, 2005. **50**(3): p. 284-286.
45. Sugita, H., et al., *Experimental study on thermally actuated pressure wave generator for space cryocooler.* Cryogenics, 2004. **44**(6): p. 431-437.
46. Wu, Z., et al., *A solar-powered traveling-wave thermoacoustic electricity generator.* Solar Energy, 2012. **86**(9): p. 2376-2382.
47. Yu, G., et al., *An energy-focused thermoacoustic-Stirling heat engine reaching a high pressure ratio above 1.40.* Cryogenics, 2007. **47**(2): p. 132-134.
48. De Blok, K., *Low operating temperature integral thermo acoustic devices for solar cooling and waste heat recovery.* Journal of the Acoustical Society of America, 2008. **123**(5): p. 3541-3541.
49. Gedeon, D., *DC gas flows in Stirling and pulse-tube cryocoolers.* Cryocoolers, 1997. **9**: p. 385-392.

50. Qiu, L., et al. *Investigation on Gedeon streaming in a traveling wave thermoacoustic engine*. in *Advances in Cryogenic Engineering: Transactions of the Cryogenic Engineering Conference*. 2006.
51. Sanchez, D.T., *Lessons from project implementation on cook stoves and rural electrification, the Practical Action Experience*, 2008, Practical Action: Rugby.
52. Miles, J.W., *The Diffraction of Sound Due to Right-Angled Joints in Rectangular Tubes.* The Journal of the Acoustical Society of America, 1947. **19**(4): p. 572-579.
53. Berger, S.A., L. Talbot, and L.S. Yao, *Flow in curved pipes.* Annual Review of Fluid Mechanics, 1983. **15**(1): p. 461-512.
54. ITO, H., *Flow in curved pipes.* JSME international journal: bulletin of the JSME, 1987. **30**(262): p. 543-552.
55. Rayleigh, J., *The Theory of Sound, vols. 1 and 2*, 1945, Dover, New York.
56. Rostafinski, W. and F. Buckens, *Propagation of Long Waves in Curved Ducts.* J Acoust Soc Am, 1972. **51**: p. 154.
57. Miles, J.W., *The Diffraction of Sound Due to Right Angled Joints in Rectangular Tubes.* The Journal of the Acoustical Society of America, 1947. **19**: p. 572.
58. Miles, J.W., *The analysis of plane discontinuities in cylindrical tubes. Part I.* The Journal of the Acoustical Society of America, 1946. **17**: p. 259.
59. Miles, J.W., *The analysis of plane discontinuities in cylindrical tubes. Part II.* The Journal of the Acoustical Society of America, 1946. **17**: p. 272.
60. Lippert, W., *Wave transmission around bends of different angles in rectangular ducts.* Acustica, 1955. **5**(5): p. 274-278.
61. Lippert, W. and CSIRO., *The measurement of sound reflection and transmission at right-angled bends in rectangular tubes*. 1954: Commonwealth Scientific and Industrial Research Organization.
62. Dequand, S., et al., *Acoustics of 90 degree sharp bends. Part I: Low-frequency acoustical response.* Acta Acustica united with Acustica, 2003. **89**(6): p. 1025-1037.
63. Dequand, S., *Duct aeroacoustics: from technological applications to the flute.* 2001.
64. Rostafinski, W., *Analysis of propagation of waves of acoustic frequencies in curved ducts.* The Journal of the Acoustical Society of America, 1974. **56**: p. 11.
65. Cummings, A., *Sound transmission in curved duct bends.* Journal of sound and vibration, 1974. **35**: p. 451-477.
66. Cabelli, A., *The acoustic characteristics of duct bends.* Journal of sound and vibration, 1980. **68**(3): p. 369-388.
67. El-Raheb, M. and P. Wagner, *Acoustic propagation in rigid sharp bends and branches.* The Journal of the Acoustical Society of America, 1980. **67**: p. 1914.
68. Rostafinski, W., *Monograph on propagation of sound waves in curved ducts.* Unknown, 1991. **1**.
69. Eustice, J., *Flow of water in curved pipes.* Proceedings of the Royal Society of London. Series A, 1910. **84**(568): p. 107.
70. Dean, W. and J. Hurst, *Note on the motion of fluid in a curved pipe.* Mathematika, 1959. **6**(01): p. 77-85.
71. White, C., *Streamline flow through curved pipes.* Proceedings of the Royal Society of London. Series A, 1929. **123**(792): p. 645-663.
72. Dean, W., *Fluid motion in a curved channel.* Proceedings of the Royal Society of London. Series A, 1928. **121**(787): p. 402-420.
73. Dyke, M.V., *Extended Stokes series: laminar flow through a loosely coiled pipe.* Journal of Fluid Mechanics, 1978. **86**(01): p. 129-145.
74. Itō, H., *Laminar flow in curved pipes.* ZAMM-Journal of Applied Mathematics and Mechanics/Zeitschrift für Angewandte Mathematik und Mechanik, 2006. **49**(11): p. 653-663.

75. Bara, B., K. Nandakumar, and J. Masliyah, *An experimental and numerical study of the Dean problem: flow development towards two-dimensional multiple solutions.* Journal of Fluid Mechanics, 1992. **244**(1): p. 339-376.
76. Womersley, J., *Method for the calculation of velocity, rate of flow and viscous drag in arteries when the pressure gradient is known.* The Journal of physiology, 1955. **127**(3): p. 553-563.
77. Loudon, C. and A. Tordesillas, *The use of the dimensionless Womersley number to characterize the unsteady nature of internal flow.* Journal of theoretical biology, 1998. **191**(1): p. 63-78.
78. Lyne, W., *Unsteady viscous flow in a curved pipe.* J. Fluid Mech, 1971. **45**(part 1): p. 13-31.
79. Zalosh, R. and W. Nelson, *Pulsating flow in a curved tube.* Journal of Fluid Mechanics, 1973. **59**(04): p. 693-705.
80. Munson, B.R., *Experimental results for oscillating flow in a curved pipe.* Physics of Fluids, 1975. **18**(12): p. 1607-1609.
81. Mullin, T. and C. Greated, *Oscillatory flow in curved pipes. Part 1. The developing-flow case.* Journal of Fluid Mechanics, 1980. **98**(02): p. 383-395.
82. Eckmann, D.M. and J.B. Grotberg, *Oscillatory flow and mass transport in a curved tube.* Journal of Fluid Mechanics, 1988. **188**(1): p. 509-527.
83. Bertelsen, A.F., *An experimental investigation of low Reynolds number secondary streaming effects associated with an oscillating viscous flow in a curved pipe.* Journal of Fluid Mechanics, 1975. **70**: p. 519-527.
84. Boiron, O., V. Deplano, and R. Pelissier, *Experimental and numerical studies on the starting effect on the secondary flow in a bend.* Journal of Fluid Mechanics, 2007. **574**: p. 109-130.
85. YAMANE, R., et al., *Study of Oscillatory Flow in Curved Channel.* Bulletin of JSME, 1985. **28**(237): p. 428-435.
86. Sudo, K., M. Sumida, and R. Yamane, *Secondary motion of fully developed oscillatory flow in a curved pipe.* Journal of Fluid Mechanics, 1992. **237**(1): p. 189-208.
87. Tada, S., S. Oshima, and R. Yamane, *Classification of pulsating flow patterns in curved pipes.* Journal of biomechanical engineering, 1996. **118**(3): p. 311.
88. Uchida, S., *The pulsating viscous flow superposed on the steady laminar motion of incompressible fluid in a circular pipe.* Zeitschrift für angewandte Mathematik und Physik ZAMP, 1956. **7**(5): p. 403-422.
89. Uchida, S., *The pulsating viscous flow superposed on the steady laminar motion of incompressible fluid in a circular pipe.* Zeitschrift für Angewandte Mathematik und Physik (ZAMP), 1956. **7**(5): p. 403-422.
90. Clark, J.P., W.C. Ward, and G.W. Swift, *Design environment for low-amplitude thermoacoustic energy conversion (DeltaEC).* Acoustical Society of America Journal, 2007. **122**: p. 3014.
91. B. M. Chen, P.H.R., Y. A. Abakr, K.Pullen, D.B.Hann and C.M.Johnson., *Design and Development of a Low-Cost, Electricity-Generating Cooking Score-Stove™*, in *Low cost, micro-electrically generating heat engines for rural areas*2012: The East Midlands Conference Centre, Nottingham UK.
92. Cunniff, P.F., *Environmental noise pollution*. 1977: John Wiley & Sons Inc.
93. Tao, Z. and A. Seybert, *A review of current techniques for measuring muffler transmission loss.* 2003.
94. Félix, S., J.P. Dalmont, and C. Nederveen, *Effects of bending portions of the air column on the acoustical resonances of a wind instrument.* The Journal of the Acoustical Society of America, 2012. **131**(5): p. 4164-4172.
95. Félix, S. and J.P. Dalmont, *Effects of bending portions of the air column on the acoustical properties of a wind instrument.* 2011.

96. Scott, R., *An apparatus for accurate measurement of the acoustic impedance of sound-absorbing materials.* Proceedings of the Physical Society, 1946. **58**: p. 253.
97. Selamet, A., I.J. Lee, and N.T. Huff, *Acoustic attenuation of hybrid silencers.* Journal of Sound and Vibration, 2003. **262**(3): p. 509-527.
98. Lippert, W. and CSIRO., *The measurement of sound reflection and transmission at right-angled bends in rectangular tubes*, 1954, Commonwealth Scientific and Industrial Research Organization.
99. Rostafinski, W. and F. Buckens, *Propagation of Long Waves in Curved Ducts.* The Journal of the Acoustical Society of America, 1972. **51**: p. 154.
100. Åbom, M., *Measurement of the scattering-matrix of acoustical two-ports.* Mechanical systems and signal processing, 1991. **5**(2): p. 89-104.
101. Bonfiglio, P. and F. Pompoli, *A single measurement approach for the determination of the normal incidence transmission loss.* J Acoust Soc Am, 2008. **124**: p. 1577.
102. Chung, J. and D. Blaser, *Transfer function method of measuring in duct acoustic properties. I. Theory.* The Journal of the Acoustical Society of America, 1980. **68**: p. 907.
103. Ho, K.M., et al., *Measurements of sound transmission through panels of locally resonant materials between impedance tubes.* Applied Acoustics, 2005. **66**(7): p. 751-765.
104. Johnston, J. and W. Schmidt, *Measurement of acoustic reflection from an obstruction in a pipe with flow.* The Journal of the Acoustical Society of America, 1978. **63**: p. 1455.
105. Katz, B.F.G., *Method to resolve microphone and sample location errors in the two-microphone duct measurement method.* The Journal of the Acoustical Society of America, 2000. **108**: p. 2231.
106. Munjal, M. and A. Doige, *Theory of a two source-location method for direct experimental evaluation of the four-pole parameters of an aeroacoustic element.* Journal of Sound and Vibration, 1990. **141**(2): p. 323-333.
107. Salissou, Y. and R. Panneton, *A general wave decomposition formula for the measurement of normal incidence sound transmission loss in impedance tube.* The Journal of the Acoustical Society of America, 2009. **125**: p. 2083.
108. Song, B.H. and J.S. Bolton, *A transfer-matrix approach for estimating the characteristic impedance and wave numbers of limp and rigid porous materials.* J Acoust Soc Am, 2000. **107**: p. 1131.
109. Desoer, C.A. and E.S. Kuh, *Basic circuit theory*. 1984: Tata McGraw-Hill Education.
110. Tao, Z. and A.F. Seybert, *A review of current techniques for measuring muffler transmission loss.* 2003.
111. Pierce, A.D., *Acoustics: an introduction to its physical principles and applications*. 1989: Acoustical Society of Amer.
112. Attia, J.O., *Electronics and circuit analysis using MATLAB*. 2004: CRC.
113. Munjal, M.L., *Acoustics of ducts and mufflers with application to exhaust and ventilation system design*. 1987: Wiley-Interscience.
114. Fahy, F., *Foundations of engineering acoustics*. 2001: Academic Press.
115. Seybert, A. and D. Ross, *Experimental determination of acoustic properties using a two-microphone random-excitation technique.* J. Acoust. Soc. Am, 1977. **61**(5): p. 1362-1370.
116. Seybert, A., *Two sensor methods for the measurement of sound intensity and acoustic properties in ducts.* The Journal of the Acoustical Society of America, 1988. **83**: p. 2233.
117. Chung, J. and D. Blaser, *Transfer function method of measuring in duct acoustic properties. II. Experiment.* The Journal of the Acoustical Society of America, 1980. **68**: p. 914.
118. Seybert, A., *Two-sensor methods for the measurement of sound intensity and acoustic properties in ducts.* J. Acoust. Soc. Am, 1988. **83**(6): p. 2233-2239.

119. Riley, P., C. Saha, and C. Johnson, *Designing a Low-Cost, Electricity-Generating Cooking Stove.* Technology and Society Magazine, IEEE, 2010. **29**(2): p. 47-53.
120. Holmberg, A., M. Åbom, and H. Bodén, *Accurate experimental two-port analysis of flow generated sound.* Journal of sound and vibration, 2011.
121. Abom-KTH, M., *Aeroacoustics of Duct Branches-With Application to Silencers.* 2011.
122. Dequand, S., et al., *Acoustics of 90 degree sharp bends. Part II: Low-frequency aeroacoustical response.* Acta Acustica united with Acustica, 2004. **90**(1): p. 13-23.
123. Adrian, R., *Twenty years of particle image velocimetry.* Experiments in Fluids, 2005. **39**(2): p. 159-169.
124. Willert, C. and J. Kompenhans, *PIV Analysis of Ludwig Prandtl's Historic Flow Visualization Films.* Arxiv preprint arXiv:1010.3149, 2010.
125. Melling, A., *Tracer particles and seeding for particle image velocimetry.* Measurement Science and Technology, 1997. **8**: p. 1406.
126. Adrian, R.J. and C.S. Yao, *Pulsed laser technique application to liquid and gaseous flows and the scattering power of seed materials.* Applied optics, 1985. **24**(1): p. 44-52.
127. Raffel, M., C. Willert, and J. Kompenhans, *Particle image velocimetry*. Springer Series on Experimental Fluid Mechanics. Springer, Berlin, 2001.
128. PAPOULIS, A., *Probability, random variables and stochastic processes.*
129. Papoulis, A. and J.G. Hoffman, *Probability, Random Variables, and Stochastic Processes.* Physics Today, 1967. **20**: p. 135.
130. Adrian, R.J., *Particle-imaging techniques for experimental fluid mechanics.* Annual Review of Fluid Mechanics, 1991. **23**(1): p. 261-304.
131. Magnan, P., *Detection of visible photons in CCD and CMOS: A comparative view.* Nuclear Instruments and Methods in Physics Research Section A: Accelerators, Spectrometers, Detectors and Associated Equipment, 2003. **504**(1): p. 199-212.
132. Keane, R.D. and R.J. Adrian. *Theory and simulation of particle image velocimetry*. in *Proc. SPIE*. 1993.
133. Olsen, M.G. and R.J. Adrian, *Measurement volume defined by peak-finding algorithms in cross-correlation particle image velocimetry.* Measurement Science and Technology, 2001. **12**(2): p. N14.
134. Adrian, R., *Statistical properties of particle image velocimetry measurements in turbulent flow.* Laser anemometry in fluid mechanics, 1988. **3**: p. 115-129.
135. Willert, C. and M. Gharib, *Digital particle image velocimetry.* Experiments in Fluids, 1991. **10**(4): p. 181-193.
136. Keane, R.D. and R.J. Adrian, *Optimization of particle image velocimeters: II. Multiple pulsed systems.* Measurement Science and Technology, 1999. **2**(10): p. 963.
137. Keane, R.D. and R.J. Adrian, *Theory of cross-correlation analysis of PIV images.* Applied scientific research, 1992. **49**(3): p. 191-215.
138. Westerweel, J., *Fundamentals of digital particle image velocimetry.* Measurement Science and Technology, 1999. **8**(12): p. 1379.
139. Rosenfeld, A. and A.C. Kak, *Digital picture processing. Volumes 1 & 2//(Book).* New York, Academic Press, 1982, 1982.
140. Adrian, R.J. and J. Westerweel, *Particle image velocimetry*. Vol. 30. 2010: Cambridge University Press.
141. Westerweel, J., *Digital particle image velocimetry: theory and application.* 1993.
142. Dynamics, D., *2D PIV Reference Manual*, ed. S. Edition. 2006, Denmark: Dantec Dynamics.

143. Westerweel, J., D. Dabiri, and M. Gharib, *The effect of a discrete window offset on the accuracy of cross-correlation analysis of digital PIV recordings.* Experiments in Fluids, 1997. **23**(1): p. 20-28.
144. Hart, D.P., *Super-resolution PIV by recursive local-correlation.* Journal of Visualization, 2000. **3**(2): p. 187-194.
145. Wereley, S.T. and C.D. Meinhart, *Second-order accurate particle image velocimetry.* Experiments in Fluids, 2001. **31**(3): p. 258-268.
146. Lecordier, B., J. Lecordier, and M. Trinite. *Iterative sub-pixel algorithm for the cross-correlation PIV measurements*. in *International Workshop on PIV'99- Santa Barbara, 3 rd, Santa Barbara, CA*. 1999.
147. Scarano, F. and M. Riethmuller, *Advances in iterative multigrid PIV image processing.* Experiments in Fluids, 2000. **29**: p. 51-60.
148. Riesz, F. and B.S. Nagy, *Functional Analysis, Frederick Ungar Pub.* Co., New York, 1955.
149. Alexander, B.F. and K.C. Ng, *Elimination of systematic error in subpixel accuracy centroid estimation [also Letter 34 (11) 3347-3348 (Nov1995)].* Optical engineering, 1991. **30**(9): p. 1320-1331.
150. Cholemari, M.R., *Modeling and correction of peak-locking in digital PIV.* Experiments in Fluids, 2007. **42**(6): p. 913-922.
151. Okamoto, K., et al., *Standard images for particle-image velocimetry.* Measurement Science and Technology, 2000. **11**(6): p. 685.
152. Raffel, M., C. Willert, and S. Wereley, *Particle image velocimetry: a practical guide*. 2007: Springer Verlag.
153. Landreth, C. and R. Adrian. *Measurement and refinement of velocity data using high image density analysis in particle image velocimetry*. in *4th International Symposium on Applications of Laser Anemometry to Fluid Mechanics*. 1988.
154. Hart, D.P. *The elimination of correlation errors in PIV processing*. in *Proc. 9th International Symposium on Applications of Laser Techniques to Fluid Mechanics*. 1998.
155. Westerweel, J., *Efficient detection of spurious vectors in particle image velocimetry data.* Experiments in Fluids, 1994. **16**(3): p. 236-247.
156. Tropea, C., A. Yarin, and J. Foss, *Springer handbook of experimental fluid mechanics*. 2007: Springer Verlag.
157. Tijani, M., J. Zeegers, and A. de Waele, *Prandtl number and thermoacoustic refrigerators.* The Journal of the Acoustical Society of America, 2002. **112**: p. 134.
158. Belcher, J., et al., *Working gases in thermoacoustic engines.* The Journal of the Acoustical Society of America, 1999. **105**: p. 2677.
159. Boguslavskii, Y. and O. Eknadiosyants, *Physical mechanism of the acoustic atomization of a liquid.* Sov Phys Acoust, 1969. **15**: p. 14-21.
160. Taylor, G., *The instability of liquid surfaces when accelerated in a direction perpendicular to their planes. I.* Proceedings of the Royal Society of London. Series A, Mathematical and Physical Sciences, 1950. **201**(1065): p. 192-196.
161. Rajan, R. and A. Pandit, *Correlations to predict droplet size in ultrasonic atomisation.* Ultrasonics, 2001. **39**(4): p. 235-255.
162. Avvaru, B., et al., *Ultrasonic atomization: effect of liquid phase properties.* Ultrasonics, 2006. **44**(2): p. 146-158.
163. Hann, D. and C. Greated, *Particle image velocimetry for the measurement of mean and acoustic particle velocities.* Measurement Science and Technology, 1997. **8**: p. 656.
164. Hann, D. and C. Greated, *Measurement of acoustic particle velocity using particle image velocimetry techniques.* Acta Acustica united with Acustica, 1997. **83**(2): p. 354-358.

165. Seybert, A. and D. Ross, *Experimental determination of acoustic properties using a two-microphone random-excitation technique.* J Acoust Soc Am, 1977. **61**: p. 1362.
166. Rienstra, S.W. and A. Hirschberg, *An introduction to acoustics.* Eindhoven University of Technology, 2003.
167. Snyder, W.H. and J. Lumley, *Some measurements of particle velocity autocorrelation functions in a turbulent flow*, 1969, Cambridge Univ Press.
168. Westerweel, J., *Theoretical analysis of the measurement precision in particle image velocimetry.* Experiments in Fluids, 2000. **29**: p. 3-12.
169. Baur, T. and J. Köngeter. *PIV with high temporal resolution for the determination of local pressure reductions from coherent turbulence phenomena*.
170. Fujisawa, N., et al., *Pressure field evaluation in microchannel junction flows through PIV measurement.* Microfluidics and Nanofluidics, 2006. **2**(5): p. 447-453.
171. Fujisawa, N., S. Tanahashi, and K. Srinivas, *Evaluation of pressure field and fluid forces on a circular cylinder with and without rotational oscillation using velocity data from PIV measurement.* Measurement Science and Technology, 2005. **16**: p. 989.
172. Gurka, R., et al. *Computation of pressure distribution using PIV velocity data*. 1999.
173. Hosokawa, S., et al., *PIV measurement of pressure distributions about single bubbles.* Journal of Nuclear Science and Technology ( ), 2003. **40**(10): p. 754-762.
174. Yoshioka, S., S. Obi, and S. Masuda. *Momentum transfer in the periodically perturbed turbulent separated flow over the backward-facing step*. 1999.
175. Liu, J., *Contributions to the understanding of large-scale coherent structures in developing free turbulent shear flows.* Advances in applied mechanics., 1988. **26**: p. 183-309.
176. Roshko, A., *Experiments on the flow past a circular cylinder at very high Reynolds number.* J. Fluid Mech, 1961. **10**(3): p. 345-356.
177. Cantwell, B.J., *Organized motion in turbulent flow.* Annual Review of Fluid Mechanics, 1981. **13**(1): p. 457-515.
178. Dernoncourt, B., J.-F. Pinton, and S. Fauve, *Experimental study of vorticity filaments in a turbulent swirling flow.* Physica D: Nonlinear Phenomena, 1998. **117**(1): p. 181-190.
179. Hussain, A., *Coherent structures and turbulence.* Journal of Fluid Mechanics, 1986. **173**(303-356): p. 125.
180. Townsend, A., *Entrainment and the structure of turbulent flow.* Journal of Fluid Mechanics, 1970. **41**(01): p. 13-46.
181. Townsend, A., *The structure of turbulent shear flow*. 1980: Cambridge University Press.
182. Holmes, P., et al., *Turbulence, Coherent Structures, Dynamical Systems and Symmetry*. 2012: Cambridge university press.
183. Bertelsen, A.F., *An experimental investigation of high Reynolds number steady streaming generated by oscillating cylinders.* Journal of Fluid Mechanics, 1974. **64**: p. 589-597.
184. Lumley, J.L., *Stochastic Tools in Turbulence. Volume 12. Applied Mathematics and Mechanics*, 1970, DTIC Document.
185. Hotelling, H., *Analysis of a complex of statistical variables into principal components.* Journal of educational psychology, 1933. **24**(6): p. 417.
186. Kosambi, D., *Statistics in function space.* J. Indian Math. Soc, 1943. **7**(1): p. 76-88.
187. Loeve, M., *Probability Theory, Vol. II.* Graduate texts in mathematics, 1978. **46**: p. 0-387.
188. Berkooz, G., P. Holmes, and J.L. Lumley, *The proper orthogonal decomposition in the analysis of turbulent flows.* Annual Review of Fluid Mechanics, 1993. **25**(1): p. 539-575.
189. Liang, Y., et al., *PROPER ORTHOGONAL DECOMPOSITION AND ITS APPLICATIONS--PART I: THEORY.* Journal of sound and vibration, 2002. **252**(3): p. 527-544.

190. Hémon, P. and F. Santi, *Simulation of a spatially correlated turbulent velocity field using biorthogonal decomposition.* Journal of wind engineering and industrial aerodynamics, 2007. **95**(1): p. 21-29.
191. Sirovich, L. and J. Rodriguez, *Coherent structures and chaos: a model problem.* Physics Letters A, 1987. **120**(5): p. 211-214.
192. Sirovich, L., *Turbulence and the dynamics of coherent structures. I-Coherent structures. II-Symmetries and transformations. III-Dynamics and scaling.* Quarterly of applied mathematics, 1987. **45**: p. 561-571.
193. M., C.L.B., *Proper Orthogonal Decomposition: An Overview* in *Lecture series 2002-04 and 2003-04 on post-processing of experimental and numerical data*. 2002-04, Von Karman Institute for Fluid Dynamics. p. 46.
194. Aubry, N., *On the hidden beauty of the proper orthogonal decomposition.* Theoretical and Computational Fluid Dynamics, 1991. **2**(5): p. 339-352.
195. Macdonald, R., et al., *PIV and POD Applied to High Amplitude Acoustic Flow at a Tube Termination.* 10ème Congrès Français d'Acoustique, 2010.
196. Marx, D., H. Bailliet, and J.-C. Valiere, *Analysis of the acoustic flow at an abrupt change in section of an acoustic waveguide using particle image velocimetry and proper orthogonal decomposition.* Acta Acustica united with Acustica, 2008. **94**(1): p. 54-65.
197. Bertelsen, A.F. and L.K. Thorsen, *Experimental investigation of oscillatory flow in pipe bends.* Journal of Fluid Mechanics, 1982. **118**(1): p. 269-284.
198. Pope, S.B., *Turbulent flows*. 2000: Cambridge university press.
199. Michard, M., et al. *Identification of vortical structures by a non local criterion- Application to PIV measurements and DNS-LES results of turbulent rotating flows*. 1997.
200. Graftieaux, L., M. Michard, and N. Grosjean, *Combining PIV, POD and vortex identification algorithms for the study of unsteady turbulent swirling flows.* Measurement Science and Technology, 2001. **12**(9): p. 1422.
201. Farge, M., et al., *Wavelets and turbulence.* Proceedings of the IEEE, 1996. **84**(4): p. 639-669.
202. Moody, L.F., *Friction factors for pipe flow.* Trans. Asme, 1944. **66**(8): p. 671-684.
203. Miyake, Y., K. Tsujimoto, and M. Takahashi, *On the mechanism of drag reduction of near-wall turbulence by wall oscillation.* JSME international journal. Series B, fluids and thermal engineering, 1997. **40**(4): p. 558-566.
204. Kline, S., et al., *The structure of turbulent boundary layers.* Journal of Fluid Mechanics, 1967. **30**(04): p. 741-773.
205. Kim, H., S. Kline, and W. Reynolds, *The production of turbulence near a smooth wall in a turbulent boundary layer.* Journal of Fluid Mechanics, 1971. **50**(01): p. 133-160.
206. Jukes, T.N., *Turbulent drag reduction using surface plasma*, 2007, University of Nottingham.
207. Robinson, S.K., *Coherent motions in the turbulent boundary layer.* Annual Review of Fluid Mechanics, 1991. **23**(1): p. 601-639.
208. Kravchenko, A.G., H. Choi, and P. Moin, *On the relation of near-wall streamwise vortices to wall skin friction in turbulent boundary layers.* Physics of Fluids A: Fluid Dynamics, 1993. **5**: p. 3307.
209. Costamagna, P., G. Vittori, and P. Blondeaux, *Coherent structures in oscillatory boundary layers.* Journal of Fluid Mechanics, 2003. **474**: p. 1-33.
210. Orlandi, P. and J. Jiménez, *On the generation of turbulent wall friction.* Physics of Fluids, 1994. **6**: p. 634.
211. Kim, J., P. Moin, and R. Moser, *Turbulence statistics in fully developed channel flow at low Reynolds number.* Journal of Fluid Mechanics, 1987. **177**(1): p. 133-166.
212. Choi, K.-S., J.-R. DeBisschop, and B.R. Clayton, *Turbulent boundary-layer control by means of spanwise-wall oscillation.* AIAA journal, 1998. **36**(7): p. 1157-1163.

213. Choi, K.-S., *Near-wall structure of turbulent boundary layer with spanwise-wall oscillation.* Physics of Fluids, 2002. **14**: p. 2530.
214. Du, Y., V. Symeonidis, and G. Karniadakis, *Drag reduction in wall-bounded turbulence via a transverse travelling wave.* Journal of Fluid Mechanics, 2002. **457**: p. 1-34.
215. OHMI, M., M. IGUCHI, and I. URAHATA, *Flow patterns and frictional losses in an oscillating pipe flow.* Bulletin of JSME, 1982. **25**(202): p. 536-543.
216. Eckmann, D. and J. Grotberg, *Experiments on transition to turbulence in oscillatory pipe flow.* Journal of Fluid Mechanics, 1991. **222**: p. 329-350.
217. Hino, M., M. Sawamoto, and S. Takasu, *Experiments on transition to turbulence in an oscillatory pipe flow.* Journal of Fluid Mechanics, 1976. **75**(02): p. 193-207.
218. Merkli, P. and H. Thomann, *Transition to turbulence in oscillating pipe flow.* Journal of Fluid Mechanics, 1975. **68**(03): p. 567-576.
219. Sergeev, S., *Fluid oscillations in pipes at moderate Reynolds numbers.* Fluid dynamics, 1966. **1**(1): p. 121-122.
220. Ohmi, M., et al., *Transition to turbulence and velocity distribution in an oscillating pipe flow.* Bulletin of JSME, 1982. **25**(201): p. 365-371.
221. Olson, J.R. and G.W. Swift, *Energy dissipation in oscillating flow through straight and coiled pipes.* The Journal of the Acoustical Society of America, 1996. **100**: p. 2123.